TECHNISCHE UNIVERSITÄT MÜNCHEN

Lehrstuhl für Halbleitertechnologie
am
Walter Schottky Institut

Detection schemes, algorithms and device modeling for tunable diode laser absorption spectroscopy

Andreas Hangauer

Vollständiger Abdruck der von der Fakultät für Elektrotechnik und Informationstechnik der Technischen Universität München zur Erlangung des akademischen Grades eines

Doktor-Ingenieurs (Dr.-Ing.)

genehmigten Dissertation.

Vorsitzender: Univ.-Prof. Dr.-Ing. N. Hanik

Prüfer der Dissertation:

1. Univ.-Prof. Dr.-Ing. M.-Chr. Amann
2. Hon.-Prof. Dr. rer. nat. habil. M. Fleischer,
   Universität Budapest/Ungarn

Die Dissertation wurde am 14.08.2012 bei der Technischen Universität
München eingereicht und durch die Fakultät für Elektrotechnik und Informationstechnik
am 08.03.2013 angenommen.

Contents

1. Introduction and conceptional considerations

1.1. Spectroscopy

With the invention of the spectroscope[1] by Joseph Fraunhofer in 1814 a series of discoveries started leading ultimately to the development of modern spectroscopy and quantum physics. The same year he discovered black lines in the sun spectrum – which are now called Fraunhofer lines – and he was the first to realize that these lines are part of the light itself (see Fig. 1.1). Around 1860 Kirchhoff and Bunsen recognized that there are two dual, molecule or atom specific processes: emission and absorption, which show this discrete line structure. They concluded that the Fraunhofer lines are caused by absorption of gaseous species in the solar and earth's atmosphere. Due to their characteristic fingerprints of elements and molecules, many new elements like He, Cs and Rb have been discovered since. The way to a theoretical explanation of the observed phenomena was long and ultimately resulted in the development of quantum mechanics in 1925 and the Schrödinger equation in 1926.

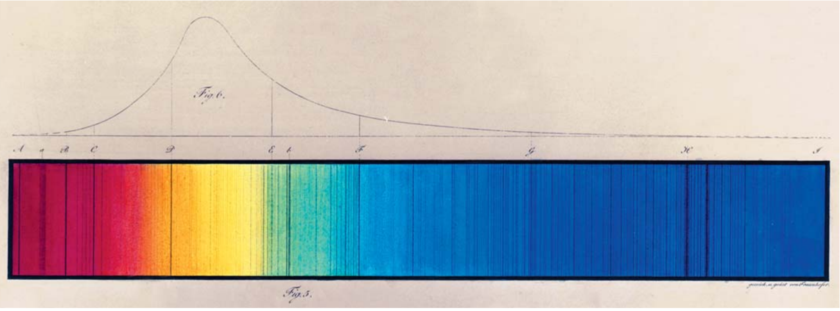

Fig. 1.1: *The original 1814 drawing by Fraunhofer showing black lines in the sun spectrum – which are absorption lines and called Fraunhofer lines today ([2], image taken from [3]). Today it is known that the black lines are caused by absorption of atmospheric species such as* O_2 *and elements such as Na, H, He, Fe, etc. in the solar atmosphere.*

A further key step in understanding molecule spectra was the development of the Born-Oppenheimer separation and, based on this, the Born-Oppenheimer approximation [4,

---

[1] According to the IUPAC [1], a spectroscope is for observation of a spectrum with the eye (usually employing a grating or prism), a spectrograph is a combination of a spectroscope and a device for photographic recording of the spectrum and spectrometer a general term for an apparatus allowing for quantitative recording of spectra including measurement of wavelength and intensity. For historical reasons spectroscopy refers to the whole field dealing with light matter interactions including measurement and theory. Spectrometry on the contrary is specific to measurement of spectra.

5]. It rigorously explains that electron and nucleus motion can be separated due to the strongly different electron and nucleus mass. The separability of these different types of motion is also observed by the band-type appearance of gas spectra shown in Fig. 1.2. For a molecule with mass of electrons m and mass of the nuclei M the

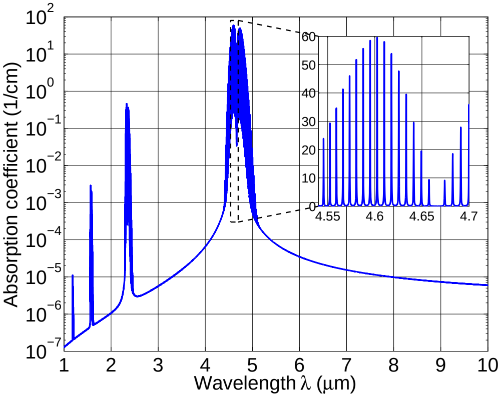

Fig. 1.2: *Computed absorption spectrum of the* $^{12}C^{16}O$ *molecule [6] at standard conditions. Vibrational transition bands with rotational fine structure are observed (fundamental band* $(v = 0) \rightarrow (v = 1)$ *at* $\lambda = 4.6\,\mu\mathrm{m}$*, first overtone band* $(v = 0) \rightarrow (v = 2)$ *at* $\lambda = 2.3\,\mu\mathrm{m}$ *and so on). Resolution of the rotational fine structure requires spectrometers with very high resolution – which can be provided by laser spectrometers.*

energy separation between electronic and nuclear (vibrational) levels as well as between rotational and vibrational energy levels is approximately

$$\Delta E_{\mathrm{nucl}} \approx \Delta E_{\mathrm{el}}\kappa^2 \qquad\qquad \Delta E_{\mathrm{rot}} \approx \Delta E_{\mathrm{vib}}\kappa^2 \tag{1.1}$$

with

$$\kappa = \sqrt[4]{m/M} \qquad\qquad \text{(in the order of 0.1)} \tag{1.2}$$

This is because in the Born-Oppenheimer separation, electronic energy, molecule vibration energy and rotation energy naturally appear as zeroth, second and fourth order term for an expansion in terms of κ. The first and third order energies vanish. The Schrödinger equation then can be split into three equations to treat all effects separately. Although this is only yields approximate solutions, this procedure completely defines the quantum numbers. Mixing or coupling terms are small and only affect energy levels and wavefunctions. Hence, the separate treatment of all three effects, i.e., the Born-Oppenheimer approximation, gives correct qualitative and, for molecules in electronic ground state, good quantitative results. For the latter the Schrödinger equation for electron movement is solved with the nuclei fixed in space, and by variation of the nuclear distance potential curves are obtained. These potential curves, which may also be determined semi-empirically, then enter the Schrödinger equations for molecule vibration and rotation.

Hence, in the near and mid-infrared only vibration-rotation transitions are relevant because electronic transitions occur – due to higher energies – in the visible or ultra-violet wavelength range.

Since then spectroscopic observations provided many insights and scientific advances. Almost all astronomical knowledge, e.g., existence of chemical elements, temperatures and even magnetic field strengths in space is obtained from spectroscopic observations. Another second major scientific application is atmospheric science. The developments in both fields involved modeling, collection of data and computation of spectral lines for many elements and molecules. Hence, consolidated knowledge is available including large databases with molecule and atom parameters. Using these, the absorption and emission spectra of different molecules, atoms and ions are predictable with very high accuracy.

In principle spectra can be measured using monochromators or dispersive elements, but those measurements are limited in terms of spectral resolution. For example the "lines" A and B Fraunhofer recognized, correspond to the now called oxygen A and B bands at 761 nm and 687 nm wavelength, which are not single lines but contain a multitude of lines – the rotational fine structure. Substantial improvement in terms of spectral resolution can only be achieved by use of tunable lasers with their ultra-narrow emission linewidth.

1.2. Lasers

Although the principle of stimulated emission was predicted by Einstein in 1915, the technical application of this effect for light generation was first realized in 1960 by Maiman. Lasers (Light amplification by stimulated emission of radiation) have a significantly higher spectral brightness than thermal emitters at technical relevant temperatures which is their fundamental advantage for spectroscopic applications. Laser operation is usually achieved by placing an optical gain medium in a resonator (e.g., two mirrors that form a resonant cavity). Due to the cavity, a feed-back loop oscillator is realized which emits monochromatic light (or nearly monochromatic, because of a finite linewidth).

After the successful realization of a semiconductor laser in 1962 by Nathan and Hall [7, 8] the application of tunable lasers for gas sensing was first demonstrated by Hinkley around 1970 [9, 10]. The utilized lasers were lead-salt lasers which had to be operated at liquid nitrogen or liquid helium temperatures.

Nowadays the availability of room-temperature single-mode tunable semiconductor lasers simplify the laser spectrometer apparatus significantly. Notable developments from the spectroscopic perspective are spectrally single-mode lasers such as edge-emitting distributed feed-back (DFB) lasers in 1972 [11] and the vertical-cavity surface-emitting laser (VCSEL) in 1979 [12]. Presently, there are single-mode continuous-wave room-temperature tunable semiconductor lasers available covering almost the complete NIR and MIR from 0.62 µm to 12 µm wavelength. Early realization of cw operation at RT of DFB lasers were for GaAs in 1975 [13] for InP in 1982 [14] and for DFB-QCLs in 2006 [15]. For VCSELs efficient RT cw single-mode emission was achieved for GaAs around 1993 [16], for InP in 2000 [17] and for GaSb in 2008 [18].

VCSELs have several advantages over DFB edge-emitters like perpendicular, circularly shaped emission, inherent longitudinal single-mode operation, low power consumption and on-wafer testability. Furthermore, they have a larger current tuning range. In mass production spectroscopically suitable VCSELs are more cost effective as the example of the laser mouse indicates.

1.3. Tunable diode laser absorption spectroscopy (TDLAS)

Spectroscopic gas sensing strongly benefits from scientific achievements in spectroscopy and the development of lasers especially semiconductor lasers. Spectrometry or spectroscopy using tunable semiconductor lasers is called tunable diode laser absorption spectroscopy (TDLAS).

1.3.1. Working principle

TDLAS is the method for the measurement of the absorption or transmission spectrum of substances (usually gases). The emission frequency of the spectrally single-mode laser can be tuned to a certain extent and the power of the light that passes though the sample is determined with a photodetector (for schematic see Fig. 1.3a). The emission frequency or wavelength is varied around the absorption line of interest according to the spectroscopic detection method. Subsequent processing together with the data extraction determines the physical gas properties, e.g., concentration, pressure or temperature. Using room-temperature operated tunable semiconductor lasers, rather compact sensors can be constructed.

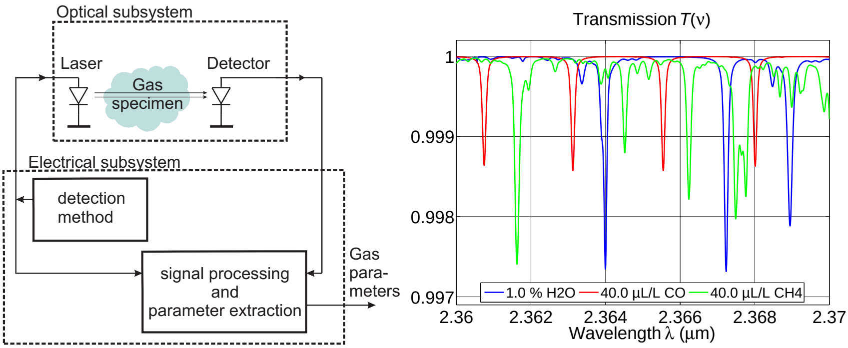

(a) Schematic

(b) Example gas transmission spectra (1 m optical path length)

Fig. 1.3: *Abstract schematic of a TDLAS system showing the important system components. The optical subsystem contains a tunable laser, a detector and the gas cell. The electrical subsystem contains the detection method, the signal processing and the parameter extraction unit from measured signals. The right plot shows as an example the characteristic "fingerprint" character of the gas spectra.*

1.3.2. Wavelength of operation

The positions and strengths of absorption lines are given by the molecule and suitable lasers have to be chosen accordingly to the quantum physical properties of the target gas. The peak line strength of absorption bands of several important gases and the typically achievable sensing resolution is shown in Fig. 1.4. Since the line strength decreases with the order of the vibrational transition (cf. Fig. 1.2), absorption strength typically increases with wavelength. The strongest IR absorption bands are in the mid-infrared (fundamental vibrational bands). The narrow gas absorption lines (half-width at half maximum (HWHM) around 1 GHz to 2 GHz at atmospheric conditions with $\lambda = 1\,\mu\text{m}$ corresponding to $\nu = 300\,000\,\text{GHz}$) explains the fingerprint character of spectra (cf. Fig. 1.3b) and the need for lasers with single-mode emission for proper sampling of the lines (laser linewidth below 100 MHz). Multi-mode lasers like those frequently employed in CD and DVD players and laser pointers are not suitable for spectroscopic applications.

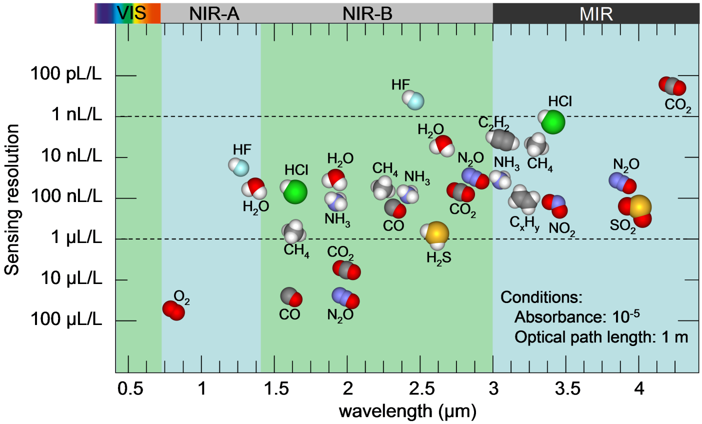

Fig. 1.4: *Line strength of important gas absorption bands in the NIR and the typically achievable gas sensing resolution at* 1 m *optical path length and absorbance resolution of* 10^{-5}. *(Data taken from HITRAN [19])*

1.3.3. Advantages of TDLAS for industrial and medical applications

For industrial, safety or medical applications, e.g., exhaust-gas monitoring, fire detection, workplace monitoring or breath analysis, reliable and long term stable sensors are required. Spectroscopic gas sensors are known to have the lowest possible cross-sensitivity to other gases due to the spectroscopic measurement and due to the characteristic spectral fingerprints of gases. Furthermore, TDLAS enables fail-safe operation of the sensor as it allows for self-monitoring due to the dynamic characteristic of the optical output signal during each single scan. The signature in the recorded signals corresponding to gas absorption lines is only obtained if laser, detector and driver/receiver electronics are working correctly. This is because the absorption line signal is a very narrow and unique feature that can not be simulated by malfunction of any component.

The measurement itself is inherently insensitive to attenuation in the optical path by contamination, since the absorption features of the gas are spectrally very narrowband compared to the wideband spectrum of typical contamination. The attenuation can rise by several orders of magnitude until reliable measurements become impossible. Furthermore, contamination, complete blockage of the optical path, failures of the laser, failures of the detector or failure of the corresponding electronic circuits can be detected by comparing the absolute signal voltage from the detector circuit with the voltage applied to the laser driver. These mentioned advantages predestine TDLAS for sensors in safety applications or those where real-time and/or in-situ measurement is required.

Note, that no other gas sensing method combines all of these advantages. This together with the high sensitivity and selectivity makes laser spectroscopic gas sensors unique and attractive for industrial and medical applications.

1.4. Frame of the work, aim and desired results

The complexity and price of such sensors is still very high for consumer and high-volume applications, because existing systems are not cost-optimized as there are only small production quantities. The mentioned advances in semiconductor lasers, especially recent developments in the field of VCSELs provide new perspectives for sensor realization at lower cost than currently. Hence, optimization and miniaturization of the other sensor components is a current research topic. Important developments are digital implementation of the sensor hardware for complexity and cost reduction. However an exploration of new possible detection methods has not been done so far.

The question is whether increased performance over traditional TDLAS methods can be achieved using novel methods. The focus should be on, but is not limited to, methods which fully exploit the flexibility of digital hardware. For an illustration of the latter see Fig. 1.5b.

One idea is wavelength modulation spectrometry (WMS) with multi-harmonic detection. Using digital hardware the constraints which limited the analog WMS realization to single harmonic detection [20] are no longer present.

An important issue is the performance quantification of designated methods both experimentally and theoretically. For theoretical comparison adequate metrics have to be developed and suitable computer simulation models have to be developed.

This will solve – among others – the unanswered question, whether direct spectroscopy or wavelength modulation spectroscopy is fundamentally better or if it is just limits in the technical implementation that cause the differences.

The above statements essentially specify the aim of this thesis:

- Development of a computer simulation model of TDLAS sensors, including the laser (VCSEL).
- Development of new methods to enable high precision sensors with compact design.

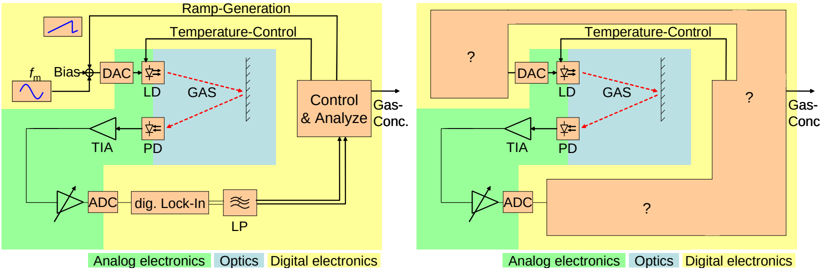

(a) Traditional realization (single harmonic detection wavelength modulation spectrometry)

(b) Scheme to be developed

Fig. 1.5: *Block diagrams of the digital realization of a traditional TDLAS sensor (left) and a (yet unknown) method, which fully exploits the flexibility and high performance of digital hardware (right). (ADC: Analog to digital converter, DAC: Digital to analog converter, LD: Laser diode, PD: Photodetector, TIA: Transimpedance amplifier, µC: Microcontroller)*

- Development and identification of high performance operating and evaluation methods. The focus should be on, but is not limited to, methods that make best possible use digital signal processing equipment with special emphasis on the wavelength modulation spectroscopy framework. Specific questions are for example:
  - Is there a benefit of detection of multiple harmonics, and how to implement it?
  - Is direct spectrometry fundamentally better in terms of performance than wavelength modulation spectrometry?
  - What parameters influence sensor performance (e.g., spectral region, gas pressure, etc.)?
- How to realize a fair comparison of methods? What are suitable metrics?

1.5. Approach

Suitable laser models – modeling the low frequency operation regime accurately – do not exist in literature. This issue is presented in chapter 2: the frequency and amplitude modulation behavior of the laser is thoroughly analyzed both theoretically and experimentally (section 2.2 and section 2.3). A combined model for laser emission wavelength and intensity is finally derived (section 2.4).

A fundamental reduction of the spectral background of multi-mode hollow capillary fiber based gas cells, would be an important advance in the field of compact gas sensors. Therefore an analysis of a highly multi-mode fiber using a mode-matching technique is presented. It confirms that back-scattering from the end of a waveguide can create a weak pseudo-random interference pattern, even if the waveguide and free space have the same refractive index (section 3.2.3). Another approach, which was found to solve the fiber background problem, is application of Zeeman spectroscopy to hollow fiber based gas cells (section 4.3). It combines the fringe insensitivity of Zeeman spectroscopy with the compactness of hollow fiber based gas sensing.

The wavelength modulation spectrometry method is modeled and analyzed in depth in section 3.3. It serves as basis for the improved methods in chapter 4.

In literature the signal processing or parameter extraction from spectra is often not included in the published performance specification for new methods. This problem is solved by modeling the data extraction by curve-fitting for the first time (section 3.4). This allowed for development of suitable metrics to assess the performance of the entire sensor with respect to noise and optical interference (section 5.1.1).

Three promising new methods with experimental demonstration will be presented in chapter 4. These are multi-harmonic detection, the Zeeman modulation spectrometry with hollow capillary fibers and laser wavelength stabilization with an in-line reference cell.

In the last chapter, application of the developed tools and knowledge will provide design guidelines for future sensor realizations (section 5.2). Many answers to the above specific questions will be given in section 5.1. An air quality sensor and a CO sensor based fire detector, which partly implement the obtained design guidelines, will be presented in section 5.3 and section 5.4 and their practical suitability is tested under realistic conditions.

2. Laser Modeling

Computer simulation of a TDLAS sensor requires appropriate models for all electrical and optical hardware components of the sensor. For hardware components like amplifiers, photodetector, the gas sample, optical beamsplitters models exist, which describe the behavior sufficiently exact for TDLAS sensor applications. The laser diode and gas cells with highly multipath propagation are exceptions where suitable models do not exist in the literature.

A suitable laser model has to precisely reproduce the laser amplitude modulation and frequency modulation behavior in the lower frequency range from DC to a few MHz. Existing models usually target high-speed communication applications and hence do not model the relevant thermal effects precisely enough.

So unfortunately, the few models and experimental data that is available from literature suitable for laser spectroscopic applications are not applicable for the VCSEL case. Hence, in course of this work experimental characterization of VCSEL behavior with respect to their low frequency ($< 100\,\mathrm{MHz}$) properties has been carried out. Some expectations from prior model theoretical considerations could be verified, and some others not and appropriate models have been developed. The purpose of this chapter is to summarize the experimental findings and the peculiarities of device behavior that were uncovered by experiment together with theoretical analysis and explanation.

The questions that originally motivated the research in this chapter are the following:

- How is the static and dynamic low frequency ($< 100\,\mathrm{MHz}$) behavior of the VCSEL and how to describe it?
- What is the strength of the plasma effect?
- What is the effect of self-heating to overall VCSEL behavior?

In course of this work, the following subsequent questions turned up.

- What is the origin of the weak process that contributes a few percent to the tuning with cutoff frequencies in the 10 Hz to 100 Hz range?
- Is it possible to determine the tuning phase-shift from the tuning coefficient amplitude (i.e., is there a relationship à la Kramers-Kronig)?
- Is there difference between the average cavity temperature and the junction (active region) temperature?

The chapter is partly based on the following publications

- A. Hangauer, J. Chen, and M.-C. Amann, “Vertical-cavity surface-emitting laser light-current characteristic at constant internal temperature”, *IEEE Photon. Technol. Lett.*, vol. 23, no. 18, pp. 1295–1297, Sep. 2011. DOI: `10.1109/LPT.2011.2160389`
- A. Hangauer *et al.*, “The frequency modulation response of vertical-cavity surface-emitting lasers: experiment and theory”, *IEEE J. Sel. Topics Quantum Electron.*, vol. 17, pp. 1584–1593, Nov. 2011. DOI: `10.1109/JSTQE.2011.2110640`

- A. Hangauer, J. Chen, and M. C. Amann, “Comparison of plasma-effect in different InP-based VCSELs”, in *Conference on Lasers and Electro Optics (CLEO)*, San Jose, USA, 2010, CMO4
- A. Hangauer *et al.*, “High-speed tuning in vertical-cavity surface-emitting lasers”, in *CLEO Europe - EQEC 2009*, Jun. 2009, CB13.5. DOI: `10.1109/CLEOE-EQEC.2009.5193616`
- A. Hangauer, J. Chen, and M.-C. Amann, “Square-root law thermal response in VCSELs: experiment and theoretical model”, in *Conference on Lasers and Electro Optics (CLEO)*, May 2008, JThA27

2.1. Fundamentals: definitions and basic assumptions

The following assumptions were found sufficient to describe the laser behavior for spectroscopically suited lasers.

- **Time invariant behavior:** From experience and long term experiments it is known that time-variant behavior like laser aging (i.e., slow variation of laser properties over time) or hysteresis effects (i.e., the behavior depends on previously applied operation conditions) are negligible on time scales of typical spectroscopic measurements (seconds to hours). This applies to lasers with stable single-mode emission over the operation range and lifetimes $> 10\,\mathrm{a}$, which is a typical value for commercial grade laser diodes.
- **Constant far-field:** Possible variations of the laser far-field emission characteristic are not relevant. Usually imaging optics are used in TDLAS applications, and, hence light is completely focused on detector. For gas-cells based on non-imaging components like hollow core fibers [26], integrating spheres [27] or diffuse reflectors [28] a dominant far-field influence on the overall transmission characteristic has not been experimentally observed so far.
- **Single-mode emission and stable polarization:** The light emitted by single-mode lasers has a pre-determined polarization (from crystallographic direction). Note that multi-mode lasers, which may show spurious mode-flips (either polarization mode or transverse mode flip), are not suitable for spectroscopic applications and, hence, no attempt is made to model behavior of these.
- **No optical feedback:** The lasers response to optical feedback or light injected into the cavity is neglected. Laser linewidth or intensity noise is typically unaffected for feedback amplitudes smaller than -25 dB [29]. In sensors the interference effects from these feedback amplitudes disturb the measurements much stronger.
- **No influence from ambient conditions (e.g., convection, humidity or radioactive radiation):** Laser chips for spectroscopic applications are usually mounted in a sealed housing to protect the laser chip from contamination with reactive gases (e.g., humidity, NH_3, HCl) and to prevent strong convection on the laser chip surface. If the operation temperature of the laser chip is much higher than the ambient temperature, convection may have a strong influence on the laser internal temperature and emission wavelength. The effect of convection can be neglected for lasers mounted in a sealed housing.

  Additionally, gamma ray or radioactive radiation can be neglected under typical ambient operation conditions. This has to be reconsidered for important but specific applications, e.g., in space, in nuclear power plants or in high-energy physical experiments. Although VCSELs tend to be quite robust against these radiation (slightly better than DFBs, due to their smaller active volume), the aging or laser performance deterioration can be significant with strong gamma ray or radioactive radiation present [30, 31].

As usual for spectrally single-mode lasers an instantaneous frequency and instantaneous power is defined. This can be done because all technically relevant laser modulation frequencies (up to several 10 GHz) are much lower than the optical frequency ($\lambda_0 = 1\,\mu\mathrm{m}$ corresponds to $\nu_0 = 300\,\mathrm{THz}$). The electrical field $E_\mathrm{L}(t)$ of the single-mode laser is separated into a slowly varying envelope $\sqrt{P_\mathrm{L}(t)}$ (slow compared to optical frequency ν_0) and the "rest" – described by a varying phase term:

$$E_\mathrm{L}(t) = \sqrt{\frac{Z_w}{A}}\sqrt{P_\mathrm{L}(t)}\cos\left(2\pi\nu_0 t + \phi(t)\right), \tag{2.1}$$

with Z_w the wave impedance (unit: Ω) of the material and A the cross section (unit: m^2) over which the emission power $P_\mathrm{L}(t)$ (unit: W) is determined. The instantaneous emission frequency is then given by

$$\nu(t) = \nu_0 + \frac{1}{2\pi}\frac{\partial\phi(t)}{\partial t} \qquad \text{(in Hz)}. \tag{2.2}$$

2.1.1. Static behavior

Under the mentioned basic and general assumptions, the lasers static electro-optical behavior is completely described by the following variables:

- Injection current I (unit: mA)
- Heat-sink temperature T_S (unit: K)
- Emitted light power P (unit: mW)
- Emitted wavelength λ (unit: µm), or emitted frequency ν (unit: Hz)
- Laser voltage U (unit: V)

All variables are connected by generally non-linear relationships. For convenience, the variables light power, wavelength and voltage are considered as functions of I and T_S:

$$P = P(I, T_\mathrm{S}), \qquad \lambda = \lambda(I, T_\mathrm{S}), \qquad U = U(I, T_\mathrm{S}). \tag{2.3}$$

When these relationships are known the static laser behavior under all operation conditions (e.g., constant current, constant voltage or with certain source impedance) can be obtained.

2.1.2. Dynamic small-signal behavior

In the non-static (i.e., time dependent) case, the system can be described with regard to its small-signal behavior. The dynamic large signal behavior can not be described without further assumptions on the origin of the non-linearities in the device. This is because there is, in contrast to linear systems, no general mathematical model for dynamic non-linear systems.

From experimental results and experience it is known that the single-mode laser behavior below and above threshold is continuous and smooth so that for small changes of I the device response is linear.

The behavior of a linear time-invariant system is completely described by its frequency response (i.e., its response to sinusoidal excitations, see section B.6 for reason). For a sinusoidal injection current $I_{\mathrm{L}}(t)$ around bias point (I, T_{S}) with small amplitude ΔI, i.e.,

$$I_{\mathrm{L}}(t) = I + \Delta I \cos(2\pi f t), \qquad T_{\mathrm{S}}(t) = \text{const}, \tag{2.4}$$

the following responses for wavelength, power, and voltage are expected:

$$\lambda_{\mathrm{L}}(t) \approx \lambda(I, T_{\mathrm{S}}) + \mathrm{Re}\left\{\Delta\lambda(I, T_{\mathrm{S}}, f)\, \mathrm{e}^{2\pi \mathrm{i} f t}\right\}, \tag{2.5}$$

$$P_{\mathrm{L}}(t) \approx P(I, T_{\mathrm{S}}) + \mathrm{Re}\left\{\Delta P(I, T_{\mathrm{S}}, f)\, \mathrm{e}^{2\pi \mathrm{i} f t}\right\}, \tag{2.6}$$

$$U_{\mathrm{L}}(t) \approx U(I, T_{\mathrm{S}}) + \mathrm{Re}\left\{\Delta U(I, T_{\mathrm{S}}, f)\, \mathrm{e}^{2\pi \mathrm{i} f t}\right\}. \tag{2.7}$$

The maximum value of ΔI for the approximation to be valid, depends on the smoothness of the steady state laser characteristics $P(I, T_{\mathrm{S}})$, $\lambda(I, T_{\mathrm{S}})$ and $U(I, T_{\mathrm{S}})$. The amplitudes $\Delta P(I, T_{\mathrm{S}}, f)$, $\Delta\lambda(I, T_{\mathrm{S}}, f)$ and $\Delta U(I, T_{\mathrm{S}}, f)$ are complex and depend on operation point and modulation frequency f. The magnitude and angle of the complex amplitude specify the amplitude and phase-shift of the sinusoidal variation:

$$\mathrm{Re}\left\{\Delta Z \mathrm{e}^{2\pi \mathrm{i} f t}\right\} = R \cos(2\pi f t - \phi), \qquad \text{with } \Delta Z = R\,\mathrm{e}^{-\mathrm{i}\phi}. \tag{2.8}$$

This justifies that the magnitude $|\Delta Z(f)|$ $(= R)$ is also called amplitude response and the angle $\angle \Delta Z(f)$ $(= \phi)$ is called phase response (with $Z \in \{P, U, \lambda\}$).

If these complex frequency responses are known, responses of the laser to small but arbitrarily shaped current excitation signals (e.g., rectangular, triangular, non-periodic) can be computed.

Because the amplitudes are proportional to ΔI the ratio is the proper variable to describe the small-signal behavior. The quantities

$$\eta_{e,\mathrm{S}}(I, T_{\mathrm{S}}, f) = \frac{e}{h\nu} \frac{\Delta P(I, T_{\mathrm{S}}, f)}{\Delta I}, \qquad R_d(I, T_{\mathrm{S}}, f) = \frac{\Delta U(I, T_{\mathrm{S}}, f)}{\Delta I}, \tag{2.9}$$

$$k_\lambda(I, T_{\mathrm{S}}, f) = \frac{\Delta\lambda(I, T_{\mathrm{S}}, f)}{\Delta I}, \tag{2.10}$$

are called **external quantum efficiency at constant heat-sink temperature** ($\eta_{e,\mathrm{S}}$), the **differential impedance** (R_d) and **tuning coefficient** (k_λ). These definitions are more general than in the literature where usually only an averaged value at DC conditions is specified. Here the definition is also extended to the dynamic case which causes these quantities to become frequency dependent and complex for $f > 0$. This has the advantage that special symbols for the frequency dependency can be avoided.

These values approach for $f = 0$ the derivatives of the static characteristics:

$$\eta_{e,\mathrm{S}}(I, T_\mathrm{S}, 0) = \frac{e}{h\nu}\frac{\partial P(I, T_\mathrm{S})}{\partial I}, \qquad R_d(I, T_\mathrm{S}, 0) = \frac{\partial U(I, T_\mathrm{S})}{\partial I}, \tag{2.11}$$

$$k_\lambda(I, T_\mathrm{S}, 0) = \frac{\partial \lambda(I, T_\mathrm{S})}{\partial I}. \tag{2.12}$$

As a consequence, the values of $\eta_{e,\mathrm{S}}$, R_d and k_λ must approach 0° or 180° at zero frequency, which is an important check of measurement data consistency.

The normalized frequency response of the differential quantum efficiency and the tuning coefficient are called **IM response** and **FM response**, respectively:

$$H_\mathrm{IM}(I, T_\mathrm{S}, f) = \frac{\eta_{e,\mathrm{S}}(I, T_\mathrm{S}, f)}{\eta_{e,\mathrm{S}}(I, T_\mathrm{S}, 0)}, \qquad H_\mathrm{FM}(I, T_\mathrm{S}, f) = \frac{k_\lambda(I, T_\mathrm{S}, f)}{k_\lambda(I, T_\mathrm{S}, 0)}. \tag{2.13}$$

2.2. P-I-characteristic at constant internal temperature

It is well known, that self-heating strongly influences the observed behavior of the laser diode. The bending of the P-I-characteristics including the roll-over and laser turn-off at high currents is usually attributed to self-heating. It is also the dominant effect that causes wavelength tuning.

The results of this section have been published in IEEE Photonics Technology Letters [21] in frame of this thesis.

For laser modeling it is of fundamental importance to quantify the amount of self-heating and the device behavior without self-heating. The advantage of knowing the (average) junction temperature T_jcn is that a general model for the static output power P at injection current I of semiconductor lasers can be stated [32]:

$$P(I) = \frac{h\nu}{e}\eta_\mathrm{e}(T_\mathrm{jcn}) \cdot \left(I - I_\mathrm{th}(T_\mathrm{jcn})\right), \quad I > I_\mathrm{th}, \tag{2.14}$$

with $I_\mathrm{th}(T_\mathrm{jcn})$ the laser threshold current and $\eta_e(T_\mathrm{jcn})$ the external quantum efficiency[1] that to a first approximation only depend on the active region temperature T_jcn. In addition to Eq. (2.14) the (average) junction temperature can be expressed by

$$T_\mathrm{jcn} = T_\mathrm{S} + R_\mathrm{thm}(UI - P), \tag{2.15}$$

with U the laser voltage and T_S the laser heat-sink temperature.

In section A.1.4 two continuous-wave measurement methods for the laser P-I-characteristic at constant internal temperature are developed. It is then expected that the power $P(I)$ curve can be described by the linear Eq. (2.14).

The two methods give approximations to the cavity and junction/active region temperature. The first employs a high speed modulation to keep the junction temperature during modulation constant and the other uses the emission wavelength as indicator for the average cavity temperature. The methods are used to correctly quantify the

---

[1] Not to confuse with the external quantum efficiency at constant heatsink temperature $\eta_{e,\mathrm{S}}$. This is the slope of the measured P-I-characteristic and approaches η_e at modulation frequencies above the thermal cut-off and below the region where dynamic effects of the intrinsic laser diode set in. This fact is exploited by characterization method 2 in section A.1.4

temperature dependence of threshold current and differential quantum efficiency without need for pulsed measurements. Furthermore the effective thermal resistance can be determined (see Eq. (2.15)).

The determined trajectories of constant internal temperature using both methods are shown in Fig. 2.1 and the resulting P-I-characteristics are shown in Fig. 2.2.

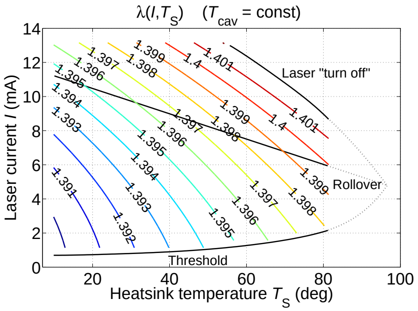

(a) T_{cav} = const (method 1) (b) T_{jcn} = const (method 2)

Fig. 2.1: *Trajectories of constant cavity temperature (i.e., constant wavelength) and junction temperature in the* (I, T_S) *plane. If* η_e *is close to* $\mathrm{d}P/\mathrm{d}I$ *method 2 becomes inexact, which makes extrapolation to* $I = 0$ *more difficult.*

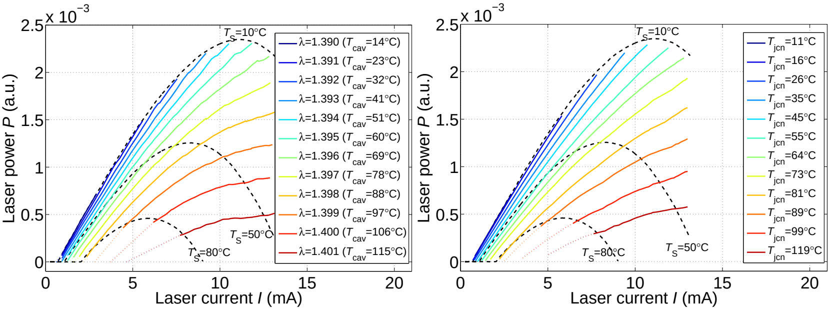

(a) T_{cav} = const (method 1) (b) T_{jcn} = const (method 2)

Fig. 2.2: *Laser power at constant cavity temperature and junction temperature, corresponding to the trajectories in Fig. 2.1. For comparison some ordinary* P-I-*characteristics are also shown (dashed, black).*

The absolute internal temperature corresponding to the curves is estimated by extrapolating the trajectories to $I = 0$, because there $T_{\mathrm{jcn,cav}} = T_{\mathrm{S}}$.

The slope and threshold of the P-I-characteristic is plotted against internal temperature in Fig. 2.3. Recalling Eq. (2.14), it is apparent that the rise in threshold only contributes

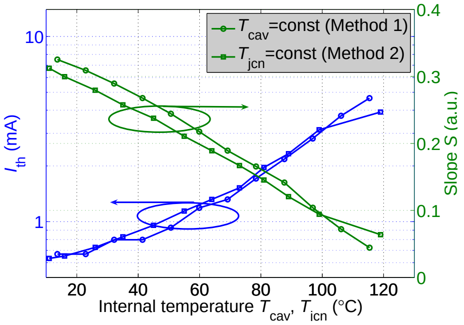

Fig. 2.3: *The threshold current I_{th} and the slope η_e of the curves in Fig. 2.2a versus internal temperature T_{jcn} or T_{cav}. Extrapolating to about 130 °C the laser turns off (η_e becomes zero).*

partly to the nonlinearity of the ordinary P-I-characteristic, because also the slope S is strongly decreasing with internal temperature. This very nicely explains the fact that the laser turns off at a specific internal temperature: The turn-off happens at approximately the temperature where the slope reaches zero and according to Eq. (2.14) no light is generated. The actual value of 130°C is obtained by extrapolation in Fig. 2.3. This effect is also found in GaAs-based VCSELs [33] and in edge-emitting lasers where the differential quantum efficiency ("slope") reaches zero at a certain temperature. This is either due to lower internal efficiency, i.e. less current is flowing through the active region or increased absorption losses. For the latter free-carrier absorption or inter-valence band absorption are typically dominant contributions when the carrier density rises with temperature. Note, that if laser turn-off was caused by the threshold current $I_{\text{th}}(T_{\text{jcn}})$ to reach I (see Eq. (2.14)) the laser-turn off would not happen at a constant internal temperature. Such a behavior is for instance observed for the laser rollover (cf. Fig. 2.1) which happens at different internal temperatures.

Fitting the empirical model

$$\eta_e(T_{\text{cav/jcn}}) = \eta_e(0)(1 + \alpha T_{\text{cav/jcn}}), \tag{2.16}$$

$\alpha = -0.0074\ \text{K}^{-1}$ (Method 1) and $\alpha = -0.0070\ \text{K}^{-1}$ (Method 2) is obtained with deviation less than 12 %. The deviation is attributed to $T_{\text{cav}} \neq T_{\text{jcn}}$, which is indicated by the different curvature of the characteristics for $T_{\text{cav}} = \text{const}$ and $T_{\text{jcn}} = \text{const}$. For currents around I_{th} or around 12 mA $T_{\text{cav}} \approx T_{\text{jcn}}$, while around 5-7 mA $T_{\text{jcn}} \approx T_{\text{cav}} + 5$ K can be estimated from superimposing Fig. 2.2a and Fig. 2.2b.

The experimental finding of a linear and exponentially quadratic dependence of the quantum efficiency and threshold, respectively (cf. Fig. 2.3), motivated the development of a simplified thermal laser model which will be presented in section 2.4.

2.3. Theory and experiment for the FM response

The laser tuning behavior is predominantly defined by thermal effects. Hence, analysis of the FM response (i.e., the dynamics of the current to wavelength tuning behavior) will reveal important information on the dynamics of the lasers internal temperature variation (or dynamics of self-heating). Furthermore, the analysis will give information about the contribution of the non-thermal plasma effect to the overall tuning behavior.

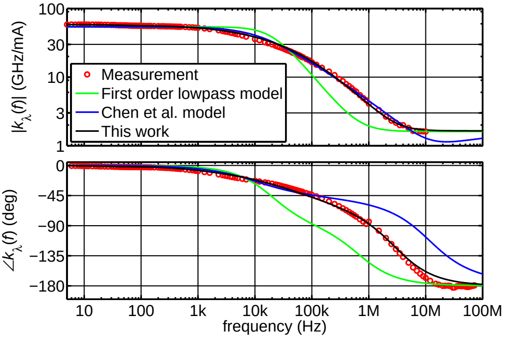

Fig. 2.4: *Comparison of models (thermal and plasma effect contributions) known from the literature and the experimental FM response data for the* 2.3 µm *VCSEL (red). The frequently used first order lowpass model (green) is very inaccurate. Significant improvement is achieved by the Chen model (blue), which is extended in this work (black) to correctly reproduce the phase-shift.*

Besides presentation of measurements, a major part in this section is the extension of the thermal model by Chen et al. [34] to include a heat source with non-zero thickness. It turned out that this is necessary to correctly reproduce the experimentally observed tuning phase-shift (see Fig. 2.4).

2.3.1. The FM response and its characteristic components

In Fig. 2.5 measurement data for a 2.3 µm VCSEL [35, 36] is shown. At frequencies of several MHz a constant tuning coefficient is observed and a phase-shift of $-180°$ is approached. Between the cutoff starting at ~ 10 kHz and this constant region a behavior $1/f^n$ with n around 0.5 is observed in the magnitude response (visible as slope -1/2 in the log-log plot). At low frequencies (see the insets in Fig. 2.5) a small but characteristic dip in the phase-shift and a small step in the tuning coefficient response is found. It is a small effect but was found to be present in all examined VCSELs in this work. A model for the FM response for VCSELs that accounts for these three effects (summarized in Tab. 2.1) is developed in the next section.

2.3.2. Analysis and physical model of the FM response

From the measurement it can be concluded that the frequency dependent tuning coefficient $k_\lambda(f)$ is a superposition of three contributions:

$$k_\lambda(f) = k_{\text{thm}} H_{\text{thm}}(f) + k_{\text{pl}} H_{\text{pl}}(f) + k_{\text{chip}} H_{\text{chip}}(f), \tag{2.17}$$

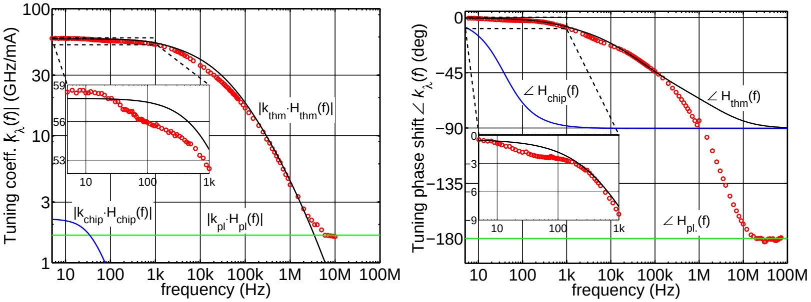

(a) Tuning coefficient amplitude

(b) Tuning phase-shift

Fig. 2.5: *The amplitude (a) and phase (b) of the tuning coefficient for a* 2.3 µm *VCSEL (circles). The individual additive contributions from the intrinsic thermal tuning* H_{thm} *(black), interaction between laser chip and submount* H_{chip} *(blue) and plasma effect* H_{pl} *(green) in the laser are shown as solid lines.*

Effect	Observation	Symb.	Section
Intrinsic thermal	Amplitude behavior is f^{-n} ($n \approx 0.5$) between cutoff and constant region	H_{thm}	2.3.2.i
Plasma	Amplitude constant at $> 1-5$ MHz, phase reaches $-180°$	H_{pl}	2.3.2.ii
Chip-submount	Additional step in amplitude and peak in phase response around 100 Hz	H_{chip}	2.3.2.iii

Tab. 2.1: *Overview of the characteristic components observed in VCSEL FM responses (see Fig. 2.5 for a graphical representation).*

with coefficients k_{thm}, k_{pl} and k_{chip} modeling contributions from the intrinsic thermal tuning, the plasma effect and the interaction between laser chip and the submount. The normalized functions $H_{\mathrm{thm}}(0) = H_{\mathrm{pl}}(0) = H_{\mathrm{chip}}(0) = 1$ model the respective frequency dependency. For all examined VCSELs typical values are in the range $k_{\mathrm{thm}} \approx k_\lambda(0)$, $k_{\mathrm{pl}} \approx -0.02 \ldots -0.1 k_\lambda(0)$ and $k_{\mathrm{chip}} \approx 0.03 k_\lambda(0)$. The 3 dB frequencies for H_{thm} are in the several kHz to 100 kHz range, for H_{pl} in the 1 GHz to 20 GHz range and for H_{chip} around 5 Hz to 100 Hz.

i. Intrinsic thermal tuning

The current tuning behavior is dominantly a thermal effect at low frequencies. It is caused by the temperature dependence of the effective optical length (geometric length times refractive index) of the cavity resulting in an increasing wavelength with temperature. The dominant contribution comes from the refractive index increase with temperature. The thermal expansion of the cavity only contributes approximately 10 % of the overall thermal wavelength tuning [37, section 3.2.3].

The first order low-pass model is unsuited for the intrinsic thermal model because it does not reproduce the slope of $n \approx 0.5$ above the thermal cutoff (cf. Fig. 2.4). The analytic VCSEL FM response model by Chen et al. [34] is better suited because it reaches an asymptotic slope of -1/2 ($1/\sqrt{\mathrm{i}f}$, "square root behavior"). However, its phase-shift only reaches -45° which does not allow for the combined model (thermal and plasma effect) to reach the high phase-shift that is practically observed. The model [34] is based on the assumption of an infinitely thin heat source and mode distribution. In section B.6.3 it is explained that if a plane or line heat source has a nonzero thickness h, a transition from square root behavior ($1/\sqrt{\mathrm{i}f}$) to $1/(\mathrm{i}f)$ behavior will occur at a frequency given by approximately $\kappa/(\pi h^2)$ with κ being the thermal diffusivity. It is clear that in a real device the heat source has some thickness even if it is expected to be very thin in VCSELs. Then the modeled FM response can both reproduce the slope of $-1/2$ after the cutoff and an asymptotic slope of -1 with a -90° phase-shift. The "transition frequency" from slope $-1/2$ to slope -1 is adjusted by the thickness of the heat source and light mode.

The refined model is based on the following approximations:

- The material inside the laser is homogeneous but non-isotropic, i.e. has different thermal conductivities in r and z direction.
- The substrate, located at distance D below the active region, is kept at constant temperature:

$$T(x, y, -D) = 0. \tag{2.18}$$

- The heat is generated in the active region with radius R_Q and is radially Gaussian distributed. The heat source has a thickness of Z_Q with also Gaussian distribution in longitudinal direction. Hence the distribution $Q(x, y, z)$ is given by

$$Q(x, y, z) = \frac{1}{(2\pi)^{3/2} R_Q^2 Z_Q} \mathrm{e}^{-\frac{x^2}{2R_Q^2} - \frac{y^2}{2R_Q^2} - \frac{z^2}{2Z_Q^2}}. \tag{2.19}$$

- The wavelength is determined by the average temperature in the laser (average with respect to mode distribution). The light mode $M(x, y, z)$ is laterally and longitudinally Gaussian distributed with radius R_M and thickness Z_M:

$$M(x, y, z) = \frac{1}{(2\pi)^{3/2} R_M^2 Z_M} \mathrm{e}^{-\frac{x^2}{2R_M^2} - \frac{y^2}{2R_M^2} - \frac{z^2}{2Z_M^2}}. \tag{2.20}$$

The laser model including the approximations are illustrated in Fig. 2.6. The Chen et al. model [34] is then contained as a special case with $Z_M = Z_Q \to 0$. In appendix A.1.5 it is shown that only the combined radii or thicknesses of heat source of light mode are relevant. The impulse response of the intrinsic thermal tuning behavior $h_{\mathrm{thm}}(t)$ is proportional to the evolution of the average temperature over time in response to a temporal heat pulse of unit strength (appendix A.1.5):

$$h_{\mathrm{thm}}(t) \propto \frac{1}{\sqrt{t + \frac{1}{2\pi f_Z}} \left(t + \frac{1}{2\pi f_R}\right)} \left(1 - \exp\left(-\frac{1/(2\pi f_D)}{t + \frac{1}{2\pi f_z}}\right)\right), \tag{2.21}$$

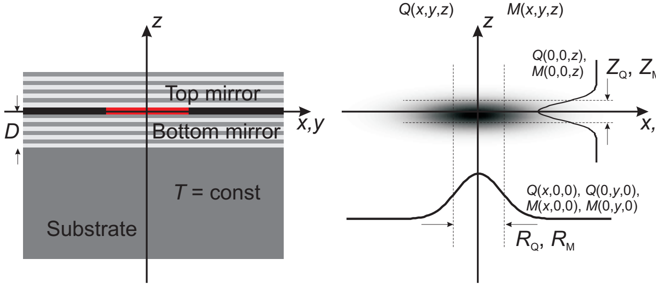

Fig. 2.6: *Schematic of the laser model (left) and the internal heat source Q and mode distribution M (right). Both Q and M are assumed to be Gaussian with radii (R_Q, R_M) and thicknesses (Z_Q, Z_M). The distance of the active region (at the coordinate origin) to the substrate (assumed as an ideal heat-sink) is D.*

with characteristic frequencies that directly relate to distances in the laser

$$f_R = \frac{\eta_R \kappa_{\text{bulk}}}{\pi(R_Q^2 + R_M^2)}, \qquad f_Z = \frac{\eta_Z \kappa_{\text{bulk}}}{\pi(Z_Q^2 + Z_M^2)}, \qquad f_D = \frac{\eta_D \kappa_{\text{bulk}}}{2\pi D^2}, \tag{2.22}$$

were $\eta_R \kappa_{\text{bulk}}$, $\eta_Z \kappa_{\text{bulk}}$, $\eta_D \kappa_{\text{bulk}}$ are the relevant thermal diffusivities of the active region material in lateral direction, longitudinal direction and the "effective" diffusivity of the material between active region and heat sink, respectively. Since such an "effective" or average diffusivity is difficult, if not impossible, to obtain a priori, the η values are used as fit parameters. The bulk diffusivity κ_{bulk} depends on the laser material system and is given by 0.31 cm^2/s for GaAs, 0.372 cm^2/s for InP and 0.23 cm^2/s for GaSb. The η values are typically much smaller than one because of several effects:

- For the ternary or quaternary material the laser contains, the thermal conductivity (and so the diffusivity) can drop by one to two orders of magnitude compared to the bulk value (binary material).
- In layered structures such as an DBR the multitude of interfaces can cause the diffusivity in growth direction to drop to about 30 % of the bulk value [38].
- Uncertainties in the width or height of the mode or heat source distribution.

The FM response is given as the Fourier transform of Eq. (2.21):

$$H_{\text{thm}}(f) \propto \int_0^\infty \frac{1 - \exp\left(-\frac{1/(2\pi f_D)}{t + \frac{1}{2\pi f_z}}\right)}{\sqrt{t + \frac{1}{2\pi f_Z}}\left(t + \frac{1}{2\pi f_R}\right)} \mathrm{e}^{-2\pi \mathrm{i} f t} \mathrm{d}t. \tag{2.23}$$

Note that the proportionality constant is chosen so that $H_{\text{thm}}(0) = 1$. Note that a closed form expression for Eq. (2.23) only exists in the case $f_Z \to \infty$ (i.e., mode and heat source are infinitely thin: $Z_Q = Z_M \to 0$) [34, Eq. 8 with $f_0 = f_R$ and $d = \sqrt{f_R/f_D}$]. Efficient numerical evaluation of Eq. (2.23), where the desired frequency points are distributed over several orders of magnitude, is explained in section B.3.

ii. Plasma effect

The plasma effect is the dominant effect that causes a dependency of the refractive index on the carrier density in lasers [39, section 4.5]. Since the carrier density in the active region is very high, even a small relative modulation of the carrier density will also cause a laser wavelength modulation. Compared to thermal tuning the tuning by the plasma effect is broad band with cutoff frequencies in the GHz range and acts inversely to thermal tuning (phase −180°). The tuning coefficient contribution caused by the plasma effect is described by the laser rate equations. The linearized rate equations can be solved if a spatially homogeneous laser model is assumed. According to Ref. [40, section 5.2] one obtains

$$k_{\mathrm{pl}} = \frac{\alpha_{\mathrm{H}}}{4\pi e}\frac{\partial G}{\partial S}, \qquad H_{\mathrm{pl}}(f) = \frac{1 + \mathrm{i}f/f_{\mathrm{g}}}{1 + \mathrm{i}f/f_{\mathrm{d}} - f^2/f_{\mathrm{r}}^2}, \tag{2.24}$$

with α_{H} the linewidth enhancement factor [41], $\partial G/\partial S$ the dependency of the normalized gain on photon number S. It models the gain dependency on light intensity, which can be caused by several physical effects [42]. The characteristic frequencies f_{r} (relaxation frequency), f_{d} (damping frequency) and f_{g} typically lie in the GHz range [40]. For frequencies $f < 100\,\mathrm{MHz}$, H_{pl} is essentially flat so in this work $H_{\mathrm{pl}} \equiv 1$ is assumed (Fig. 2.5, green curve). Note, that spatial effects like spatial hole burning in VCSELs may cause a low-frequency roll-off that is not described by Eq. (2.24) [43, 44].

iii. Laser chip-submount interaction

The additional small contribution at low frequencies is due to interaction of the laser chip and the submount. This is presented and modeled in this work for the first time. All investigated lasers were packaged in a commercial TO5 housing including a thermo-electric cooler. In this set-up the laser chip was placed on an insulating $\mathrm{Al_2O_3}$ submount which is the reason for the observed effect.

From measured data it is evident that a small process is present that accounts to 2 % to 4 % of the overall thermal tuning and has cutoff frequencies in the 10 Hz to 100 Hz range (see also Fig. 2.9). This explains the additional weak step in the tuning coefficient amplitude in Fig. 2.5a and the small peak in the tuning phase-shift in Fig. 2.5b (at $f < 200\,\mathrm{Hz}$). With FEM (finite element method) computer simulations that include the laser chip and the submount it was possible to reproduce this effect. Simulations without the submount, where the laser chip is placed on a constant temperature body did not show this effect. It can be explained as follows: when the laser current is modulated also the dissipated electric power is modulated. The heat is essentially removed through the submount and so also small temperature variations on the heat-sink of laser chip are created. This together with the heat capacity of the submount and the laser chip has a cutoff frequency in the 10 Hz to 100 Hz range. Although the exact physical description of this effect would include many parameters, it is modeled by a simple first order low-pass model with a single time constant (or cutoff frequency f_{chip}), i.e.,

$$H_{\mathrm{chip}}(f) = \frac{1}{1 + \mathrm{i}f/f_{\mathrm{chip}}}, \tag{2.25}$$

because it is a weak effect and high accuracy modeling is not required.

2.3.3. Impossibility of reconstruction of the FM phase from FM amplitude

It is well known that real and imaginary part of the frequency response of a causal filter are the Hilbert transform of each other. Practically, all physical systems are causal and thus fully described by the imaginary or real part of the frequency response only, and a measurement of either will be sufficient for full characterization. However, one may also ask if a similar relationship holds for the amplitude and phase-shift of the frequency response. This is possible if the system additionally to causality fulfills the minimum phase condition. Then the Kramers-Kronig relations hold for amplitude and phase. According to systems theory of time discrete systems the system

$$\log H_{\mathrm{FM}}(f) = \log A(f) + \mathrm{i}\phi(f) \tag{2.26}$$

is causal if and only if $H_{\mathrm{FM}}(f) = A(f)\mathrm{e}^{\mathrm{i}\phi(f)}$ is a causal and minimum phase system [45]. Thus the log amplitude response $\log A(f)$ and $\phi(f)$ are a Hilbert transform pair:

$$\phi(f) = -\frac{1}{\pi}\,\mathrm{PV}\int_{-\infty}^{\infty} \frac{\log A(\nu)}{f-\nu}\mathrm{d}\nu. \tag{2.27}$$

For proper convergence it is essential to use the Cauchy principle value integral and to integrate also over the negative part of the spectrum. Since $\log A(f)$ is symmetric for real valued systems, Eq. (2.27) is equivalent to the Kramers-Kronig relation:

$$\phi(f) = -\frac{2f}{\pi}\,\mathrm{PV}\int_{0}^{\infty} \frac{\log A(\nu)}{f^2-\nu^2}\mathrm{d}\nu. \tag{2.28}$$

From Eq. (2.27) it follows that a minimum phase system with asymptotic slopes of 0, $-1/2$, and -1 in a log-log plot of $A(f)$ has asymptotic phase-shifts of 0°, −45°, and −90°, respectively. A slope of $-n$ is $A(f) \to 1/f^n$ behavior for $f \to \infty$.

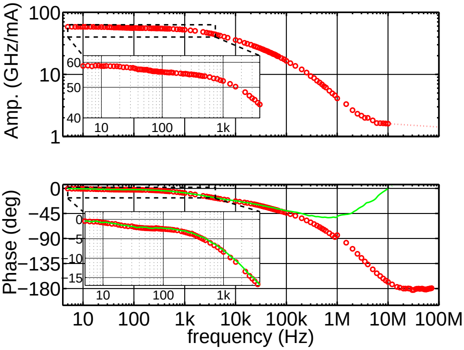

Fig. 2.7: *The measured tuning coefficient (circles, top) and tuning phase-shift (circles, bottom) for an InP-based* 2.3 µm *VCSEL and the minimum phase reconstruction from amplitude using the Hilbert transform Eq. (2.27) (solid line, bottom). At frequencies* $f > 100\,\mathrm{kHz}$*, deviations are due to the plasma effect, which destroys the minimum phase property of the tuning behavior.*

The minimum phase reconstruction for the measurement of the 2.3 µm VCSEL was computed using the method described in section B.3 and is shown in Fig. 2.7. An excellent agreement between measured phase and reconstructed phase at low frequencies is observed, which indicates that the thermal tuning component alone (which is dominating at low frequencies) is a minimum phase system. Deviations start at $f > 100\,\mathrm{kHz}$ and show that the presence of the plasma effect (which dominates at high frequencies) causes the laser tuning behavior to be a non-minimum phase system. In a minimum-phase system the observed constant tuning coefficient at several MHz should cause an associated 0° phase-shift, which is in different from the observed $-180°$ phase-shift. This can also be seen in Fig. 2.5b where the phase-shift of the intrinsic thermal component H_{thm} starts to deviate at around 100 kHz from the measurement. Remarkably, the influence of the plasma effect is stronger in the FM phase-shift because there deviations are more pronounced than in the amplitude response. The fact that the laser tuning behavior is no minimum phase system shows that both tuning phase-shift and amplitude measurements are required for proper device characterization and correct prediction of the wavelength response for arbitrary current modulation waveforms. For the other investigated VCSELs a similar behavior is obtained: the plasma-effect starts to influence the FM phase-shift at around 100 kHz.

2.3.4. Measurement and fit results

All measured devices are single-mode and continuous-wave laser devices, which were placed on a ceramic submount on top of a thermoelectric cooler (TEC) for temperature stabilization. Operation temperature was slightly above room temperature. An overview of the devices and their characteristic parameters is given in Tab. 2.2. The measurements

Data	Laser 1	Laser 2	Laser 3	Laser 4
Wavelength	763 nm	1854 nm	2365 nm	2330 nm
Substrate	GaAs	InP	InP	GaSb
Top DBR	Epitaxial	Epitaxial	Epitaxial	Dielectric
Bottom DBR	Epitaxial	Dielectric	Dielectric	Epitaxial
Aperture	Lateral Oxidation	Buried Tunnel Junction	Buried Tunnel Junction	Buried Tunnel Junction
Heat-sink	GaAs Substrate	Gold	Gold	GaSb Substrate
Reference	[46]	[47]	[35, 36]	[18, 48]
R_Q $(= R_M/0.6)$ [1]	$1.5\,\mu\mathrm{m}^4$	$2.5\,\mu\mathrm{m}^4$	$3.25\,\mu\mathrm{m}^4$	$2.5\,\mu\mathrm{m}^4$
D	$\approx 4\,\mu\mathrm{m}^2$	$\approx 2.4\,\mu\mathrm{m}^2$	$2.58\,\mu\mathrm{m}^2$	$8.18\,\mu\mathrm{m}^2$
Z_Q, Z_M	$1.5\,\mu\mathrm{m}^{3,4}$	$0.42\,\mu\mathrm{m}^{3,4}$	$0.68\,\mu\mathrm{m}^{3,4}$	$0.68\,\mu\mathrm{m}^{3,4}$

[1] Current aperture radius. Light mode radius assumed to be 60 % of aperture.
[2] Thickness of the bottom mirror and layers between mirror and active region.
[3] Penetration depth of the light mode into one mirror plus the thicknesses of additional layers between the mirror and the active region.
[4] Entries multiplied by $\sqrt{2\log 2} \approx 1.18$ for conversion of a "standard deviation" to a "HWHM (half-width as half-maximum)".

Tab. 2.2: *Investigated VCSELs and their characteristic parameters* including the least squares curve fit to the model Eq. (2.17) are shown in Fig. 2.8 with a zoom for low frequencies shown in Fig. 2.9. At the lower end of the frequency

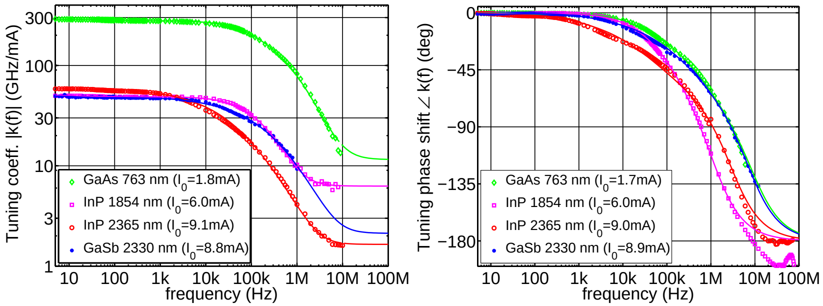

(a) Tuning coefficient amplitude

(b) Tuning phase-shift

Fig. 2.8: *The absolute value (a) and phase (b) of the tuning coefficient $k_\lambda(f)$ versus frequency for measurement (markers) and fit to theoretical model Eq. (2.17) with Eq. (2.23) (solid lines).*

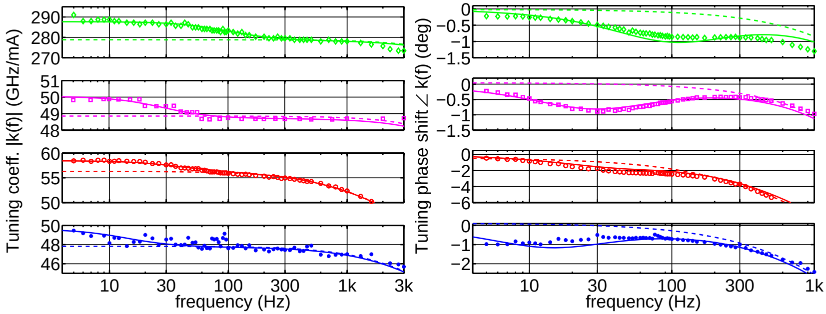

(a) Tuning coefficient amplitude

(b) Tuning phase-shift

Fig. 2.9: *Zoom of Fig. 2.8 at low frequencies, showing the absolute value (a) and phase (b) of the tuning coefficient $k_\lambda(f)$ versus frequency for measurement (markers) and fit to theoretical model (solid lines). The difference between model behavior without H_{chip} (dashed lines) and measurement indicates the effect of the laser submount interaction.*

scale (Fig. 2.9), the effect due to the interaction between submount and laser chip is clearly visible. This effect is present in all investigated VCSELs but with different cutoff frequencies in the range of 5 Hz (GaSb-based VCSEL) to 100 Hz (GaAs-based VCSEL) and different relative strength to the overall tuning coefficient, which is attributed to the different sizes and thicknesses of the VCSEL chips mounted on the submount. The determined model parameters are summarized in Tab. 2.3. The η values give the

Description		Intrinsic thermal				Submount		Plasma
	$k_\lambda(0)$ (GHz/mA)	k_thm (GHz/mA)	η_R (f_R (kHz))	η_Z (f_Z (kHz))	η_D (f_D (kHz))	k_chip (GHz/mA)	f_chip (Hz)	k_pl (GHz/mA)
GaAs 763 nm	287.6	289.9 (100.8%)	0.169 (755.6)	0.248 (752.6)	0.0492 (15.17)	9.2 (3.2%)	99.4	-11.5 (-4.0%)
InP 1854 nm	50.0	55.0 (109.9%)	0.021 (41.1)	0.008 (373.1)	0.1682 (172.9)	1.3 (2.7%)	28.0	-6.3 (-12.5%)
InP 2365 nm	58.4	57.9 (99.0%)	0.034 (38.5)	0.133 (2357)	0.0004 (0.38)	2.2 (3.8%)	38.5	-1.6 (-2.8%)
GaSb 2330 nm	49.6	49.8 (100.5%)	0.220 (262.6)	0.390 (4279)	0.0192 (1.05)	1.9 (3.8%)	13.8	-2.1 (-4.3%)

Tab. 2.3: *Best fit model parameters for the theoretical model curves shown in Fig. 2.8 and Fig. 2.9.*

normalized "effective" thermal diffusivity in the laser to reproduce the measurements together with the parameters given in Tab. 2.2. Low η_R values are caused by a low thermal diffusivity in radial direction in the active region or a larger heat source or mode diameter than assumed. Low η_Z values are caused by a low thermal diffusivity in longitudinal direction in the active region or a larger lateral heat source or mode extension than assumed. Finally, low η_D values indicate a low thermal diffusivity between the active region and the heat-sink or a larger effective distance to the heat-sink than assumed. Note that in the latter case this is **not** influenced by the chip mounting technology, because the η-parameters only describe the intrinsic thermal tuning. A high thermal resistance due to mounting would be described by the k_chip parameter. For the examined VCSEL the mounting only contributes $2-4$ % of the overall thermal resistance.

For time domain computer simulation programs a zero / pole form of the frequency response is required, whereas the zeros and poles can not be related directly to physical parameters. In the next section 2.3.5 it is shown that the poles must lie on the negative real line and the zeros that best fit the measurement also lie on the negative real line. This proves that the "N time constants" model, which is frequently used in literature for empirical description of the FM response, is also suited for simulation of VCSELs.

2.3.5. Empirical FM response model (ODE based)

For a pure computer simulation of a system containing a tunable laser the FM response must be present in a rational form[2]. A rational frequency response always corresponds to a system that is described with ordinary differential equation in the time domain. The first order lowpass (one "time constant") or the "N time constants" model are of such a rational form. Time domain simulation programs like "SPICE" or "Simulink" require models to be rational. In such a model, however, the obtained parameters (zeros and poles) can not be related to real physical quantities inside the laser device. For pure mathematical description of measured data, e.g. for computer simulation of a laser

---

[2] this means that the frequency response it is a quotient of two polynomials with real coefficients in the variable $s = 2\pi\mathrm{i}f$

system, this approach can be powerful, since with a certain number of time constants arbitrary FM responses can be fitted.

For thermal modeling, all poles p_i have to lie on the negative real line. They have to be real, because a thermal defined system does not describe oscillations at an impulse excitation. A negative real part is required for the system to be stable. The zeros also must have negative real part to describe a minimum phase system. Since the heat equation only contains the first order time derivative an asymptotic slope between 0 and -1 or $|H_{\text{thm}}(f)| \to 1/f$ for high frequencies is expected. The only meaningful selection for the numerator degree is thus one minus the denominator degree (asymptotic $1/(\mathrm{i}f)$ behavior). Hence the following model is used:

$$H_{\text{thm}}(f) = \frac{\prod_{i=1}^{N-1}(1 - 2\pi \mathrm{i}f/z_i)}{\prod_{i=1}^{N}(1 + \mathrm{i}f/f_i)}. \tag{2.29}$$

The poles are $p_i = -2\pi f_i$ and z_i the (possibly complex) zeros. If a zero is complex then the conjugate complex zero must be a zero as well, so that using complex zeros does not increase the degrees of freedom of the model (which is $2N - 1$). Note that also multiple zeros or poles can be present (i.e., zeros/poles of higher order).

In the case of single poles and real zeros the model Eq. (2.29) can be simplified to the "N time constants" model [49, 50]:

$$H_{\text{thm}}(f) = \sum_{i=1}^{N} a_i \frac{1}{1 + \mathrm{i}f/f_i}, \tag{2.30}$$

with positive values a_i and distinct characteristic frequencies f_i. For $a_i > 0$ this even always describes a minimum phase system with real zeros. For $a_i < 0$ this is not necessarily the case, but also complex zeros can be described. Note that Eq. (2.30) is not a fully general model such as Eq. (2.29), since it can not describe multiple poles. This is even so when some f_i are chosen to be equal. It can easily be seen when the partial fraction decomposition of Eq. (2.29) is computed: in case of multiple poles also terms $\frac{1}{(1+\mathrm{i}f/f_i)^{r_i}}$ with $r_i > 1$ would have to be present in Eq. (2.30). For the measurement data of the VCSELs studied in this work, the best fit with model Eq. (2.29) did not produce complex zeros or poles with multiplicity greater than one. This empirically proves that for the specific measurement data the "N time constant" model Eq. (2.30) is indeed suitable. The necessary order was between $N = 3$ or $N = 4$. It turned out, that the necessary order can be estimated from the fit itself. If N is chosen to be "too large" in the beginning, then the fit will produce a zero and a pole that are lying very close by. So their contribution in Eq. (2.29) will nearly cancel out which indicates that N can be chosen lower. The fitted zeros and poles are listed in Tab. 2.4 and the experiment with fit shown in Fig. 2.10.

2.3.6. Summary

The FM response (amplitude and phase) for different VCSELs is found to consist of three components (intrinsic thermal tuning, plasma effect and thermal tuning by laser chip-submount interaction). A physical model for the FM response is developed which shows good agreement with measurement.

The plasma effect has a significant impact to the FM response (especially the phase-

Description		Intrinsic thermal			Submount		Pl. eff.
	$k(0)$ (GHz/mA)	k_{thm} (GHz/mA)	f_i (kHz)	$-z_i/(2\pi)$ (kHz)	k_{chip} (GHz/mA)	f_{chip} (Hz)	k_{pl} (GHz/mA)
GaAs 763 nm	287.7	288.5 (100.3%)	15.86, 127.4, 856.3	18.27, 239.2	9.4 (3.3%)	103.3	-10.2 (3.6%)
InP 1854 nm	50.0	54.9 (109.9%)	22.47, 91.58, 377.7	25.54, 169.8	1.3 (2.6%)	31.5	-6.2 (12.5%)
InP 2365 nm	58.4	56.5 (96.6%)	1.85, 13.64, 107.4, 648.6	2.39, 25.36, 308.1	3.5 (6.0%)	57.5	-1.5 (2.6%)
GaSb 2330 nm	49.7	49.4 (99.2%)	0.80, 22.98, 202.0, 1077	0.83, 35.41, 449.3	1.8 (3.6%)	11.0	-1.4 (2.9%)

Tab. 2.4: *The fitted poles and zeros for empirical model Eq. (2.29).*

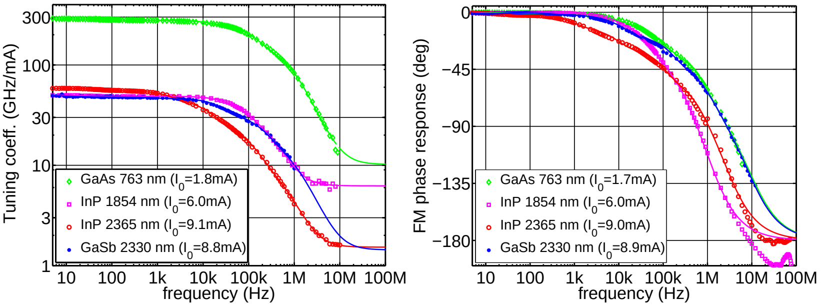

(a) Tuning coefficient amplitude

(b) Tuning phase-shift

Fig. 2.10: *The absolute value (a) and phase (b) of the tuning coefficient $k_\lambda(f)$ versus frequency for measurement (markers) and fit with the rational model Eq. (2.29) and parameters given in Tab. 2.4 (solid lines).*

shift) starting at frequencies as low as 100 kHz. A consequence is that the laser FM tuning behavior can not be modeled as a minimum phase system, i.e., the FM phase response can not be computed via Hilbert transform/Kramers-Kronig methods from only the FM amplitude response. An exception from this is if only the response at frequencies $\ll$ 100 kHz is of interest. For proper prediction of the wavelength response over a broader frequency range characterization of both the amplitude and phase-shift are essential.

A third result is that the high resolution FM phase-shift measurements reveal an unexpected peaking of the FM phase-shift at low frequencies. This is explained with interaction between the submount and the laser chip. This creates an additional low intensity tuning effect at low frequencies which contributes another 2 % to 4 % of the overall tuning coefficient.

Fourth, the intrinsic thermal tuning is modeled by a physical laser model with Gaussian shaped mode and heat source distribution. It reproduces both the slope of -1/2 in the transition region between cutoff and the start of the plasma effect in the tuning coefficient amplitude as well as the high phase-shift of $-90°$ for the thermal component. This is achieved by assuming the heat source and mode distribution with a certain thickness. This improved model allows for a good fit of measured spectra with a low number of parameters.

2.4. Combined thermal VCSEL model for emitted power and wavelength

Using the results of the previous sections now a simplified thermal VCSEL model is developed and fitted to measured data. The model is based on the following assumptions:

- The behavior of the intrinsic laser diode, without self-heating, is assumed to be frequency independent up to 10 MHz.
- The threshold current and external quantum efficiency only depend on the average junction temperature (this implies the laser behavior can be described by an average temperature).
- The contribution of the electronic tuning is negligible at DC conditions.
- The average cavity and junction temperature are assumed to be the same (If there are differences these are likely to be smaller than 5 K, as shown in section 2.2).
- The intrinsic thermal (normalized) FM response is independent on laser bias and temperature.

2.4.1. Developed model for static operation

Implementing the above assumptions and using the knowledge obtained in previous sections, the following model is derived. The equations for static behavior are:

$$\begin{aligned}
P(I, T_\mathrm{S}) &= \frac{h\nu}{e}\eta_e(T_\mathrm{jcn})(I - I_\mathrm{th}(T_\mathrm{jcn})), \quad I > I_\mathrm{th}, \quad \text{zero otherwise} && (2.31)\\
\lambda(I, T_\mathrm{S}) &= l_1 + l_2 T_\mathrm{jcn}, && (2.32)\\
P_\mathrm{diss}(I, T_\mathrm{S}) &= U(I, T_\mathrm{S})I - P(I, T_\mathrm{S}), && (2.33)\\
T_\mathrm{jcn} &= T_\mathrm{S} + R_\mathrm{thm}(T_\mathrm{jcn})P_\mathrm{diss}(I, T_\mathrm{S}), && (2.34)\\
\eta_e(T_\mathrm{jcn}) &= e_1 - e_2 T_\mathrm{jcn}, && (2.35)\\
I_\mathrm{th}(T_\mathrm{jcn}) &= \exp\left(i_1 + i_2 T_\mathrm{jcn} + i_3 T_\mathrm{jcn}^2\right), && (2.36)\\
R_\mathrm{thm}(T_\mathrm{jcn}) &= \frac{1}{2}(r_1 + r_2 T_\mathrm{jcn}) \times 1.471\,\frac{\mathrm{K\,cm}}{\mathrm{W}}\left(\frac{T_\mathrm{jcn} + 273.15}{296}\right)^{1.477}. && (2.37)
\end{aligned}$$

The e_i, l_i, i_i and r_i parameters are free parameters to be determined through the curve-fit.

i. Rationale for $P(I, T_\mathrm{S})$

The behavior of the laser output power can be understood to a substantial level, without knowing much details about laser internals[3]. In the ideal case one recombining electron generates exactly one photon. Practically, this ideal case is not achieved because of losses. These can be grouped into optical losses (i.e., the photon is absorbed after creation but before it is emitted from the cavity) and electrical losses (i.e., the recombining electron did not generate a photon). Note, that in literature it is often assumed that η_e represents optical losses and I_th electrical losses. This originates from the formulas derived by a simplified laser model, which assumes a linear dependence of gain on carrier density, constant internal temperature and no spatial dependence of all internal laser variables. It should also be noted, that both loss mechanisms can not be distinguished by observation of the external variables I and P (i.e., the "missing" number of photons). For the phenomenological model here, $\eta_e < 1$ just quantifies losses proportional to current and $I_\mathrm{th} > 0$ current independent losses. A separation into electrical losses and optical losses can not be made. A linear dependency of threshold current on injection current could not be distinguished from a lower value of η_e.

ii. Rationale for η_e and I_th

The choice for the two functions Eq. (2.35) and Eq. (2.36) for η_e and I_th is taken from the experimental observation in Fig. 2.3. They are assumed to be only dependent on internal temperature T_jcn. A current dependence of η_e or I_th would correspond to curved P-I-characteristics at constant T_jcn, which has not been observed in experiment (cf. Fig. 2.2).

iii. Rationale for R_thm

The ansatz function for the thermal resistance R_thm was chosen in analogy to the known formula for the heat resistance of a structure with a disk heat source (which was previously shown to give good results when modeling VCSELs [51, chapter 3]):

$$R_\mathrm{thm,disc} = \frac{1}{2\lambda_\mathrm{thm} D_\mathrm{disc}}, \tag{2.38}$$

with λ_thm the material thermal conductivity and D_disc the diameter of the heat source. Note, that Eq. (2.37) contains the temperature dependent thermal resistivity of InP and a linear function to model other effects. This can be a varying heat source diameter, deviations between the actual thermal conductivity and the assumed one, or deviations between the actual device behavior and the idealized disc heat source model. The model assumption Eq. (2.37) is only justified by its success in the application: During fitting of measurement data with different models, an additional current dependency or additional second order temperature dependency did not improve results. The only significant improvement was observed when changing the Eq. (2.37) from constant (i.e., $r_2 = 0$) to linear (i.e., $r_2 \neq 0$) behavior.

---

[3] Here only conventional non-cascaded interband lasers are considered. For interband cascase or quantum cascade lasers the behavior is different – due to multiple electron use.

2.4.2. Developed model for dynamic operation

For the dynamic (sinusoidal) small-signal operation the equations were chosen as follows: (for clarity the T_{jcn} dependence of η_e, I_{th} and R_{thm} is omitted. Derivatives with respect to T_{jcn} are denoted with a dash '):

$$\frac{\Delta P(I,T_{\mathrm{S}},f)}{\Delta I} = \frac{h\nu}{e}\left(\eta_e + \left(\eta_e'(I-I_{\mathrm{th}}) - \eta_e I_{\mathrm{th}}'\right)\frac{\Delta T_{\mathrm{jcn}}(I,T_{\mathrm{S}},f)}{\Delta I}\right), \quad I > I_{\mathrm{th}} \tag{2.39}$$

$$\frac{\Delta\lambda(I,T_{\mathrm{S}},f)}{\Delta I} = l_1 \frac{\Delta T_{\mathrm{jcn}}(I,T_{\mathrm{S}},f)}{\Delta I}, \tag{2.40}$$

$$\frac{\Delta T_{\mathrm{jcn}}(I,T_{\mathrm{S}},f)}{\Delta I} = \frac{R_{\mathrm{thm}}H_{\mathrm{thm}}(f)}{1-R_{\mathrm{thm}}'P_{\mathrm{diss}}(I,T_{\mathrm{S}})}\frac{\Delta P_{\mathrm{diss}}(I,T_{\mathrm{S}},f)}{\Delta I}, \tag{2.41}$$

$$\frac{\Delta P_{\mathrm{diss}}(I,T_{\mathrm{S}},f)}{\Delta I} = U(I,T_{\mathrm{S}}) + \frac{\Delta U(I,T_{\mathrm{S}},f)}{\Delta I}I. \tag{2.42}$$

These equations – except for the equation for $\Delta T_{\mathrm{jcn}}/\Delta I$ – directly follow from the static equations, when the derivative with respect to I is formed and the terms $\partial T_{\mathrm{jcn}}/\partial I$ are replaced by $\Delta T_{\mathrm{jcn}}/\Delta I$. This is equivalent to the assumption of an instantaneous response of the intrinsic laser diode.

For derivation of the expression Eq. (2.41) for $\Delta T_{\mathrm{jcn}}/\Delta I$ the Eq. (2.34) is derived by I and solved for $\partial T_{\mathrm{jcn}}/\partial I$. This then would correspond to the static temperature variation when no dynamic effects are present. To model dynamic effects, ΔT_{jcn} is assumed to be $\partial T_{\mathrm{jcn}}$ multiplied by the FM response of the intrinsic thermal tuning $H_{\mathrm{thm}}(f)$ from section 2.3.2.

2.4.3. Fitting procedure and curve-fit results

The model describes the static and dynamic small-signal measurement data of emission power P, $\Delta P/\Delta I$ and emission wavelength λ, $\Delta\lambda/\Delta I$. The laser voltage is not modeled, but measurement data for U and the impedance $\Delta U/\Delta I$ are needed.

Unfortunately, the model is in an implicit form, because the equations have to be solved for T_{jcn} due to the physical and recursive definition of R_{thm} (see Eq. (2.37)). Hence, during each iteration of the curve-fit (which varies the e_i, l_i, i_i and r_i coefficients) the equations have to be numerically solved for T_{jcn} for each data point.

i. Weighting of data groups

Since different types of data with different magnitude and sample size are fitted simultaneously, weighting has to be applied. Each data group is weighted with

$$\frac{F_{\mathrm{group}}}{N_{\mathrm{group}}\mathrm{Pk}_{\mathrm{group}}} \tag{2.43}$$

with N_{group} the number of samples in the data group, $\mathrm{Pk}_{\mathrm{group}}$ the peak to peak variation of the data in the group and F_{group} an empirically chosen weight to obtain a good fit. If F_{group} would be 1 for all groups a fair weighting is implemented, considering all data groups as equally important regardless on data magnitude and sample size.

Due to difficulties of fitting non-smooth data (i.e., laser power around the threshold) the experimental threshold current values were additionally added as data to the fit. For the i-th measured P-I-characteristic at heatsink temperature $T_{\mathrm{S},i}$ a laser threshold current $I_{\mathrm{th},i}$ is obtained. At these values the threshold current is known and is added as an additional data group for fitting, which significantly improved the fit quality.

ii. Measurement data

The same InP-based BTJ-VCSEL as in section 2.2 at 1.4 µm wavelength and 4 µm BTJ diameter is utilized for verification of the model.

Measurement data of P and U was recorded in 5 K steps from approximately 10 °C to 80 °C, at different frequency points and 401 current values from 0 mA to 13.5 mA. The data was recorded sequentially with repeated current sweeps while increasing frequency and finally variation of temperature. The measurement setup is described in appendix A.1. The DC data for U and P was measured simultaneously with the AC data. The modulation amplitude was varying with operating point (due to changes in laser impedance) but always below 15 µA. The laser was focused on the detector and the optical setup was purged with nitrogen to remove (or at least to suppress as much as possible) distortions by H_2O absorption lines. The optical light power was determined by dividing the photocurrent by the detector responsivity.

Measurement of wavelength was done in a separate measurement by identifying H_2O absorption lines in the P-I-characteristics from ambient air and comparing these with known tabulated HITRAN data [19]. In a third measurement the absolute value of the tuning coefficient was measured using an Michelson interferometer with an optical path length difference of 1.03 m. Heatsink temperature was varied from 10 °C to 80 °C in 10 K steps and laser current with 11 points between 2 mA to 11 mA. Fringe counting of the detector signal was used for determination of the absolute optical frequency variation (see section A.1.1). The modulation amplitude was chosen depending on the operating point and kept below 0.5 mA.

iii. Fit results

To minimize the complexity of the fit, only the static measurement data and dynamic measurement data at 1 kHz and $f = 10\,\mathrm{MHz}$ are fitted with the model. Therefore, the FM response is assumed to be

- $H_{\mathrm{thm}}(1\,\mathrm{kHz}) = 1$, and,
- $H_{\mathrm{thm}}(10\,\mathrm{MHz}) = 0$.

The individual weights for the data groups are shown in Tab. 2.5.

Data group	P	$\Delta P/\Delta I(1\,\mathrm{kHz})$	$\Delta P/\Delta I(10\,\mathrm{MHz})$	λ	$\Delta\lambda/\Delta I(1\,\mathrm{kHz})$	I_{th}
Weight F_{group}	10	1	1	3	5	5000

Tab. 2.5: *The fit weights for different groups of data; empirically chosen according to the desired accuracy for reproduction of the specific data.*

The fitted parameters are listed in Tab. 2.6 and the corresponding internal laser parameters are shown in Fig. 2.11. The high weight for threshold was chosen due to problems of the fit to correctly reproduce the laser threshold current with low weight. Likewise, the wavelength and power parameters were given a higher priority over the AC intensity data ($\Delta P/\Delta I$). This is the reason why the wavelength data fits better to the model than the other data (cf. Fig. 2.11); it is not because the model is inherently better suited for description of wavelength.

η_e params		I_{th} params			R_{thm} params		λ params	
$\eta_e = e_1 - e_2 T_{\mathrm{jcn}}$		$I_{\mathrm{th}} = e^{i_1 + i_2 T_{\mathrm{jcn}} + i_3 T_{\mathrm{jcn}}^2}$			(see Eq. (2.37))		$\lambda = l_1 + l_2 T_{\mathrm{jcn}}$	
e_1	$e_2 \times 10^3$	i_1	$i_2 \times 10^3$	$i_3 \times 10^3$	r_1	r_2	l_1	$l_2 \times 10^3$
0.426	2.521	−7.25	−6.111	0.200	3698	−5.218	1.38843	0.100

Tab. 2.6: *Values of the fitted parameters in Eq. (2.35), Eq. (2.36), Eq. (2.34) and Eq. (2.32). The units are I_{th} in A, T_{jcn} in °C and λ in µm.*

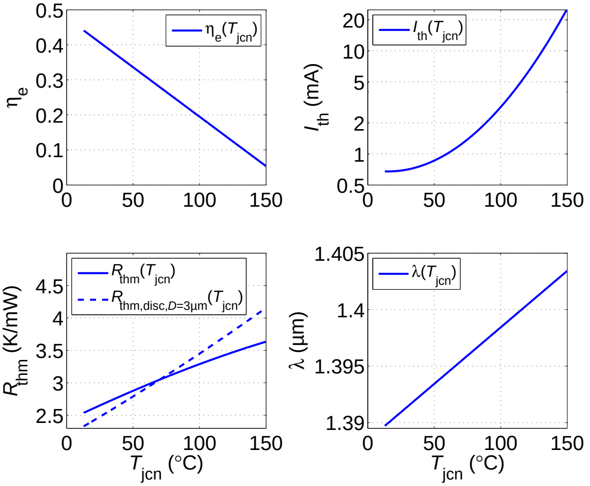

Fig. 2.11: *The extracted internal laser parameters according to the simplified thermal model. Numerical values for parameters describing the functions are listed in Tab. 2.6. In the lower left plot the thermal resistance Eq. (2.38) for a* 3 µm *diameter disc heat source in an InP crystal is shown for comparison.*

The following is observed from the fit results in Fig. 2.12:

- The temperature dependency of the laser intensity and wavelength is qualitatively and quantitatively correct.
- Measurement data is qualitatively reproduced (i.e. similar values, signs of slope and curvature are correct).
- The AC intensity (especially at 10 MHz) is not reproduced (at high currents the

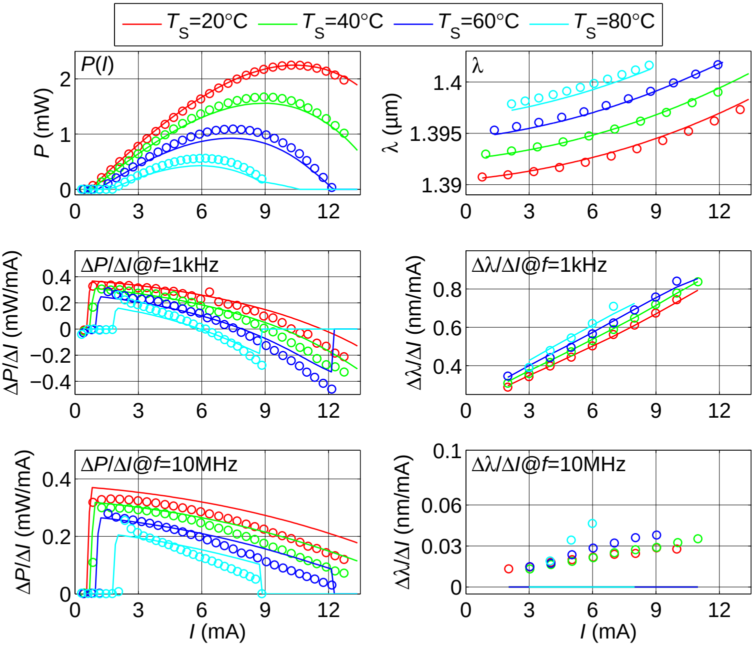

Fig. 2.12: *Comparison of measurement (circles) and model (solid lines) with best fit parameters listed in Tab. 2.6.*

error can be as high as 100 %). A simultaneous good fit of wavelength and power seems impossible, even when the weighting prioritizes power over wavelength.

- The order of the ansatz functions is appropriate: The fit quality can not be improved when increasing the order of the functions describing I_{th} and R_{thm}. A current dependence of R_{thm} does not improve results either. An increase of the order for η_e to 2 does not improve results and, depending on the starting values and fit weights, this may give physically not meaningful results, e.g. an increasing and – at high temperatures – strongly decreasing threshold current.
- The tuning coefficient at 10 MHz – caused by the plasma effect – can not be reproduced. This is expected because the model only covers thermal effects.

2.4.4. Summary and further improvements

The simplified thermal model gives good qualitative and – for wavelength and DC power data – good quantitative results. However, it can not reproduce wavelength and laser output power at high frequencies.

This is attributed to either neglection of the (small) curvature of internal power characteristic, or dynamic effects of the intrinsic laser diode at low frequencies. Both can be caused by spatial hole burning (SHB), which is known to be strong in VCSELs due to the non-uniform carrier injection in the active region [43, 44].

For an improved version of the model, one or more of the following items would be necessary:

- Better understanding of processes controlling laser carrier density:
  - Modeling of current and temperature dependency of carrier-density (to improve accuracy of the laser output power, by more accurately reproducing the AC components – also the plasma-effect could be modeled)
  - The above includes modeling of spatial hole burning, the low-frequency roll-off and a current dependent threshold current.
- Better understanding of processes controlling laser voltage and differential resistance, and the origin of the drop of η_e
  - Ideally, the laser voltage should only be temperature dependent (due to gain clamping) and differential resistance of the intrinsic diode be zero above threshold and $\propto 1/I$ below threshold. Both does not match experimental data.
  - Modeling of the temperature dependence of the DBR resistance.
  - Modeling of the temperature dependence of the blocking and non-blocking resistivity (eventually impedance) of the tunnel-junction.
  - If the above characteristics are known, the measurement of the sub-threshold impedance will yield carrier lifetimes and, by integration, the threshold carrier density. The latter could be an important characteristic parameter in an improved model.

The carrier density model can not be accomplished by the standard zero-dimensional laser rate equations because spatial hole burning (and, hence, a possible low-frequency roll-off) are caused by spatial non-uniformity effects. Finding a suitable ansatz for SHB and its frequency, current and temperature dependence is left as future work.

3. System Modeling

This chapter deals with the modeling of the complete sensor system. In the first section 3.1 a classification of sensor system components is developed. It is shown that most methods known from literature can be grouped into this scheme.

Optical cells will be treated in section 3.2 with emphasis on highly multi-mode hollow capillary fiber based cells. These will be analyzed with a mode-matching technique to understand the origin of the experimentally observed spectral background (section 3.2.3).

Two other relevant topics are the detection method "wavelength modulation spectrometry" (WMS) (section 3.3) and the method of data extraction from measured spectra (section 3.4). Important results will be the derivation of many new WMS fundamentals and the development of proper notation for the system description. This will be the basis for development, comparison and qualitative judgment of different detection methods and other implications for the sensor design which are presented in chapter 4 and section 5.2.

The chapter (particularly section 3.3.2) is partly based on the following publications

- A. Hangauer, J. Chen, *et al.*, "Modeling of the n-th harmonic spectra used in wavelength modulation spectroscopy and their properties", *Appl. Phys. B: Lasers Opt.*, vol. 90, no. 2, pp. 249–254, Feb. 2008. DOI: `10.1007/s00340-007-2902-5`, and
- J. Chen, A. Hangauer, *et al.*, "Tunable diode laser spectroscopy with optimum wavelength scanning", *Appl. Phys. B: Lasers Opt.*, vol. 100, pp. 331–339, 2010. DOI: `10.1007/s00340-010-3973-2`.

Significant extensions to the published results are presented in this chapter.

3.1. Taxonomy of relevant sensor components

Each TDLAS sensor consists of a laser as the light source, an optical cell where the light-gas interaction takes place and a detection method with the corresponding parameter extraction. The term detection method is defined here as the method of operating the laser diode and the way of recording the measured data (e.g., use of a lock-in amplifier or else). Note, that once the detection method is chosen, the data extraction method is also determined. Parameter extraction is done by using the appropriate model for the measured data (which is determined through the models of the laser, the cell including gas and the detection method) together with least squares curve-fitting to extract the desired gas parameters (see section 3.4 for detailed explanation why this is the case).

3.1.1. Laser and optical cell

There are different types of optical cells, which were found in this thesis to be groupable into four categories that specify the cells behavior (Fig. 3.1). There are cavity-based

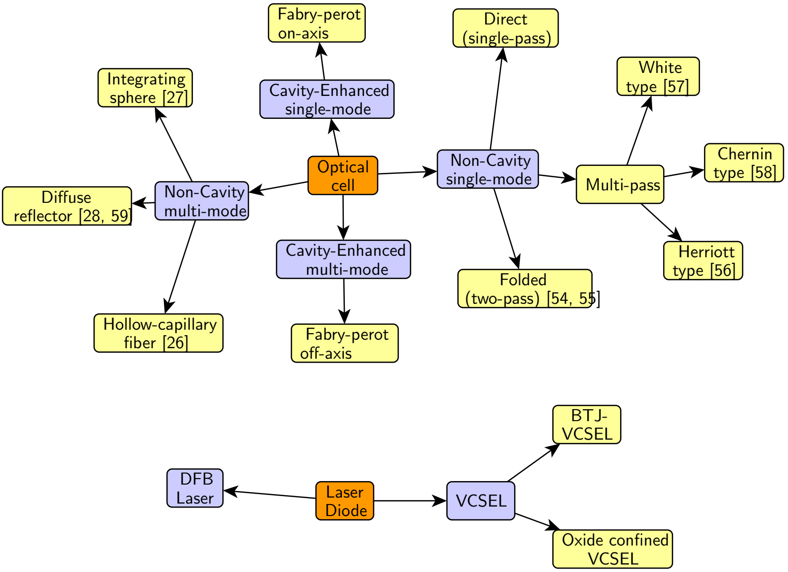

Fig. 3.1: *Taxonomy of transmissive optical cells and relevant types of lasers. The former can be grouped into four categories which determine their behavior.*

(with resonator) and non-cavity based cells. Both exist in single- and multi-mode propagation variants, and have fundamentally different design constraints.

Although from the system point of view the laser with the optical cell have to be treated as a unit, the laser type may not always have fundamental influence on the overall behavior of the laser and cell entity. Differences such as laser output power, linewidth or current tuning range are only important for specific applications. Nevertheless, the lasers behave differently, which results in different system models for the parameter extraction method (see chapter on lasers, chapter 2).

3.1.2. Detection method

Many different detection methods can be found in the literature. All were developed for specific purposes. In this thesis it was found useful to group these into two categories, the first with the laser AM (amplitude modulation) being essential and the second with laser AM as a parasitic effect (Fig. 3.2). Laser AM is essential when the laser is modulated at high frequency (0.1 GHz to 1 GHz) to create sidebands to the laser emission line (e.g., for frequency modulation spectrometry (FMS) [60], or two-tone-FMS (TTFMS) [61]). It is also essential with pulsed or step response measurements, i.e., where the laser on/off-switching is elementary for the measurement (an example is cw-cavity ring-down spectrometry).

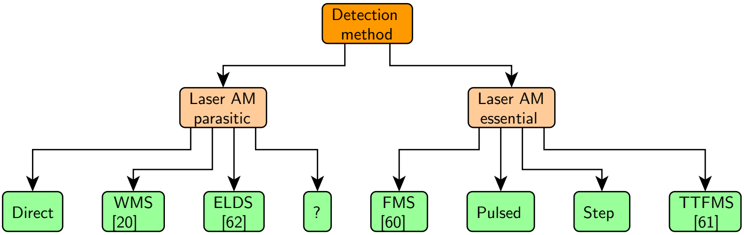

Fig. 3.2: *Taxonomy of TDLAS detection methods, i.e., how the laser is operated to probe the gas-induced behavior change of the optical cell. Methods which rely on the presence of laser AM usually require high speed operation, because the alteration of the emission spectrum must be in range of the linewidths in the system (e.g., laser-, cavity- or absorption linewidth;* MHz *to* GHz*).*

All other methods where the laser AM is a parasitic effect are solely based on the FM tuning behavior of the laser. This includes wavelength modulation spectrometry (WMS, see later section 3.3) [20], the method ELDS [62] which is a two-tone WMS, and standard direct detection.

It is important to note that the latter methods have a much lower technological demand because the required electronic components are typically operated at frequencies $\ll 1\,\mathrm{MHz}$. The other methods which rely on the laser AM, require, besides a suitable laser, a high speed detector and appropriate circuits (bandwidth $\gg 1\,\mathrm{MHz}$).

Hence, in this thesis only the methods are considered where the laser AM is a parasitic effect, or equivalently where the relevant modulation frequencies are typically in the kHz range.

The simplest detection method is direct spectrometry, which implements a straightforward approach of a spectroscopic measurement.

i. Direct spectrometry

Direct detection or direct spectroscopy is a straightforward way to measure the transmission of the optical cell. The laser current I is ramped which results in an almost linear ramp of the optical frequency $\nu(I)$. The light intensity after passing the optical cell is detected and recorded and then analyzed. Let the laser power at current I be denoted as $P(I)$, then the detector signal $S(I)$ at laser injection current I is given by

$$S(I) = P(I)\,T(\nu(I)). \tag{3.1}$$

Typically I is sampled at N discrete points I_i running from I_1 to I_N and cause the laser to cover the absorption line of interest. The gas parameters are then extracted using least squares curve-fitting (see section 3.4). Appropriate models for $P(I)$, the optical frequency $\nu(I)$ and the gas transmission $T(\nu)$ need to be known.

The method only works because $P(I)$ has a very smooth behavior, in contrast to $T(\nu(I))$ which has very sharp and narrow characteristics on it (i.e., the absorption lines). If the laser shows a behavior that is similar to the features caused by the absorption lines, a gas measurements would be impossible or possible only to a limited extent. The same is true if the gas cell adds a fringe distortion (cf. Eq. (3.7)) that has similar periodicity as the gas absorption line width. A quantitative metric which fully describes the effect of fringes on the sensor output value is developed in section 5.1.1.

3.1.3. Possible system combinations

In principle all detection methods can be used with all types of optical cells. However, not all combinations are meaningful in the sense that high performance can be obtained. Some combinations are also known under specific names in the literature. For example ICOS (integrated cavity output spectrometry) is given by the off-axis Fabry-Pérot type cell with any non-laser AM related detection method (e.g., WMS or direct detection). The NICE-OHMS method is characterized by an on-axis Fabry-Pérot cavity together with the FMS detection method.

For an overview of some commercially available sensor systems see Fig. 3.3.

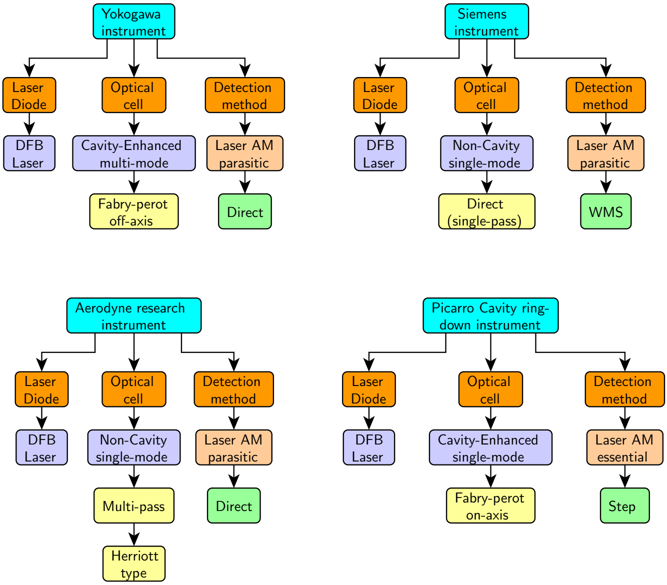

Fig. 3.3: *Overview of commercial sensor systems and their components.*

Possible, but not meaningful, combinations are, e.g., step response measurements with a single-mode non-cavity enhanced cell. Such measurements only make sense with a single-mode cavity. Furthermore, the cavity linewidth depends on the absorption coefficient of the containing gas, which is the foundation of the cavity ring-down method.

There are high requirements on the mechanical stability and manufacturing tolerance of the cavity which make the approach sensitive but expensive. Hence, in this thesis cavity-enhanced methods will not be covered.

3.2. Cell behavior

The gas cell is the component of the sensor where the light matter interaction takes place. It includes appropriate means for guiding the light and provides a spatial overlap of the light mode with the gas sample. The behavior of the (homogeneously filled) gas cell is characterized by its transmission $T(\nu)$ which relates the input and output power of light (P and P_0) passed through the cell.

$$T(\nu) = \frac{P(\nu)}{P_0(\nu)} = \mathrm{e}^{-\tau(\nu)} = \mathrm{e}^{-D(\nu)L} \tag{3.2}$$

with

T : Transmission (unit: 1),
τ : Attenuance, extinction or optical depth (unit: 1),
D : Attenuation or extinction coefficient (unit: 1/cm),
L : Optical path length (unit: cm),
ν : Optical frequency (unit: Hz).

The attenuation coefficient (and hence transmission) are typically dependent on optical frequency ν. Attenuation always refers to a light intensity decrease and can be caused by many physical effects like, absorption, scattering, diffraction and reflection.

Usually one distinguishes between optically thin and optically thick conditions:

$$\tau \ll 1: \text{ Optically thin,} \qquad \tau \gg 1: \text{ Optically thick.}$$

The significance of optically thin conditions is that the above exponential can be linearized, i.e.,

$$T(\nu) \approx 1 - D(\nu)L, \qquad \text{for optically thin conditions.} \tag{3.3}$$

3.2.1. Fundamentals: Absorption effect by the gas

The absorbance quantifies the contribution of the absorption effect to the overall attenuation. If only the absorption effect of the gas is considered, the transmission for a single optical mode (or beam) of the homogeneously filled cell is given by the Lambert-Beer law:

$$T_{\mathrm{gas}}(\nu) = \mathrm{e}^{-A(\nu)} = \mathrm{e}^{-\alpha(\nu)L}, \tag{3.4}$$

with

A : Absorbance (unit: 1),
α : Absorption coefficient (unit: 1/cm).

If absorption is the only relevant effect, attenuation and absorbance are the same. For multi-mode or multi-path propagation each mode has to be considered separately.

Usually one distinguishes between unsaturated and saturated conditions:

$$A \ll 1: \text{ Unsaturated,} \qquad\qquad A \gg 1: \text{ Saturated.}$$

The significance of unsaturated conditions is that the exponential in the Lambert-Beer law can be linearized, i.e.

$$T_{\text{gas}}(\nu) \approx 1 - \alpha(\nu)L, \qquad\qquad \text{for unsaturated conditions.} \tag{3.5}$$

For a homogeneous mixture of gases the absorption coefficient is a weighted sum of individual contributions from the pure gases. The molar absorption coefficient (i.e., the absorption coefficient of the pure gas) is denoted by α_{mol}:

$$\alpha(\nu) = C_{\text{mol},1}\, \alpha_{\text{mol},1}(\nu) + C_{\text{mol},2}\, \alpha_{\text{mol},2}(\nu) + \dots, \tag{3.6}$$

with

α_{mol} : Molar absorption coefficient (unit: 1/cm),
C_{mol} : Concentration or volume mixing ratio (unit: 1 or L/L),

and $C_{\text{mol},i}$ the concentrations or volume mixing ratio (a number between 0 and 1) for the i-th gas molecule. Common abbreviations for the unit of concentration (but not advised by the ISO 31-0 norm) are "ppm" for µL/L or "ppb" for nL/L.

At atmospheric conditions the Voigt line shape (see section B.4 for definition) is a very good approximation to the observed absorption line shape of gases. For a large number of gases line-by-line databases with molecule parameters exist, e.g., HITRAN [6], CDMS [63], JPL catalog [64] and GEISA [65]. Using this parameters, the molar absorption coefficient can be theoretically computed under different physical conditions of pressure and temperature.

3.2.2. Fundamentals: Interference effects in single-mode cells

Distortion by interference is an important limiting factor for TDLAS sensors. In this work interference with a second weakly excited mode or beam is included in the overall transmission model. If either the gas absorption or the interference is weak (i.e., $\ll 1$) the overall transmission is given by

$$T(\nu) = T_{\text{gas}}(\nu)(1 - A + A\cos(2\pi\nu L_{\text{OPD}}/c)) \tag{3.7}$$

with ν the frequency of the light, L_{OPD} the optical path length difference of the two interfering beams or modes and A the amplitude of the interference. The inverse of the optical path length difference is called free spectral range ν_{fsr} of the interference, which is its period length $\nu_{\text{fsr}} = \frac{c}{L_{\text{OPD}}}$.

The amplitude A is related to the intensity ratio r of the interfering modes or beams:

$$A = 2\frac{\sqrt{r}}{1+r} \approx 2\sqrt{r}, \qquad\qquad \text{for small } r. \tag{3.8}$$

Due to the square root relationship it is evident that for a certain maximum distortion the interfering mode suppression ratio must be very high. For example for $A = 10^{-5}$ a ratio of $1/r = 2.5 \times 10^9$ ($\equiv$ 94dB) is necessary. The formula follows from the Fabry-Pérot etalon transmission [66] with low mirror reflectivity.

3.2.3. Interference in multi-mode hollow capillary fiber based cells

In this section a theory is developed to explain the strange behavior in a hollow multi-mode waveguide and how it affects the transmission of such a cell.

Modes in lossless waveguides are orthogonal and can in principle not cause interference if the power is fully integrated over the mode area during detection. Furthermore, due to energy conservation, interference can in this case only be caused by back-reflection or scattering effects. This will be theoretically verified for the case of a multi-mode hollow fiber. The question is whether the experimentally observed interference in the order of 10^{-4} to 10^{-3} [26] can be explained from the back-reflection at the fiber end.

Therefore, the transmission of the waveguide junction depicted in Fig. 3.4 is analyzed with the mode-matching technique. Since this technique requires a discrete set of modes in both sections, the free space is approximated by a larger circular waveguide.

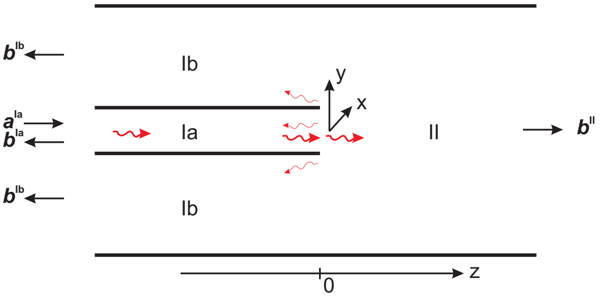

Fig. 3.4: *Modeling of the fiber ending as a waveguide junction. The fiber (circular metal waveguide Ia) is inside a larger circular hollow metal waveguide (II and Ib) modeling the free space. The aim is to compute the amplitudes of the transmitted modes* ($\boldsymbol{b}^{II}$) *and the back-scattered modes* ($\boldsymbol{b}^{Ia}$ *and* $\boldsymbol{b}^{Ib}$) *from the incoming mode amplitudes* ($\boldsymbol{a}^{Ia}$).

i. Fundamentals and choice of mode normalization

The E and H field (separated in tangential and longitudinal field components) in waveguide segment I can be written as:

$$\boldsymbol{E}_{\mathrm{t}}^{\mathrm{I}}(x,y,z) = \sum_p a_p^{\mathrm{I}} \boldsymbol{E}_{p,\mathrm{t}}^{\mathrm{I}}(x,y)\mathrm{e}^{-\mathrm{i}\beta_p^{\mathrm{I}} z} + \sum_p b_p^{\mathrm{I}} \boldsymbol{E}_{p,\mathrm{t}}^{\mathrm{I}}(x,y)\mathrm{e}^{\mathrm{i}\beta_p^{\mathrm{I}} z}, \tag{3.9}$$

$$E_{\mathrm{z}}^{\mathrm{I}}(x,y,z) = \sum_p a_p^{\mathrm{I}} E_{p,\mathrm{z}}^{\mathrm{I}}(x,y)\mathrm{e}^{-\mathrm{i}\beta_p^{\mathrm{I}} z} - \sum_p b_p^{\mathrm{I}} E_{p,\mathrm{z}}^{\mathrm{I}}(x,y)\mathrm{e}^{\mathrm{i}\beta_p^{\mathrm{I}} z}, \tag{3.10}$$

$$\boldsymbol{H}_{\mathrm{t}}^{\mathrm{I}}(x,y,z) = \sum_p a_p^{\mathrm{I}} \boldsymbol{H}_{p,\mathrm{t}}^{\mathrm{I}}(x,y)\mathrm{e}^{-\mathrm{i}\beta_p^{\mathrm{I}} z} - \sum_p b_p^{\mathrm{I}} \boldsymbol{H}_{p,\mathrm{t}}^{\mathrm{I}}(x,y)\mathrm{e}^{\mathrm{i}\beta_p^{\mathrm{I}} z}, \tag{3.11}$$

$$H_{\mathrm{z}}^{\mathrm{I}}(x,y,z) = \sum_p a_p^{\mathrm{I}} H_{p,\mathrm{z}}^{\mathrm{I}}(x,y)\mathrm{e}^{-\mathrm{i}\beta_p^{\mathrm{I}} z} + \sum_p b_p^{\mathrm{I}} H_{p,\mathrm{z}}^{\mathrm{I}}(x,y)\mathrm{e}^{\mathrm{i}\beta_p^{\mathrm{I}} z}. \tag{3.12}$$

A similar relation holds for waveguide section II, but with role of the a and b coefficients exchanged. The components $\boldsymbol{E}_p^{[i]}$ and $\boldsymbol{H}_p^{[i]}$ are distinct solutions to Maxwell's equations (with certain boundary conditions) and are called the E and H field of the p-th mode in waveguide section i. The modes are normalized so that the absolute value of the Poynting vector is one and has positive real part for guided modes, i.e.,

$$1 = \left| \iint_{z=0} (\boldsymbol{E}_p^{[i]} \times \boldsymbol{H}_p^{[i]*}) \cdot \boldsymbol{e}_z \mathrm{d}A \right|, \quad \text{and} \tag{3.13}$$

$$0 < \operatorname{sign} \operatorname{Re} \iint_{z=0} (\boldsymbol{E}_p^{[i]} \times \boldsymbol{H}_p^{[i]*}) \cdot \boldsymbol{e}_z \mathrm{d}A, \qquad \text{for } \operatorname{Re}\left\{\beta_p^{[i]}\right\} \neq 0. \tag{3.14}$$

Only using this normalization the a and b coefficients represent power waves propagating in the $+z$ and $-z$ direction respectively. The propagation constant $\beta_p^{[i]}$ is given by

$$\beta_p^{[i]} = \sqrt{(2\pi\nu/c)^2 - {\eta_p^{[i]}}^2}, \tag{3.15}$$

with $\eta_p^{[i]}$ the p-th radial wave vector, which is determined by the boundary conditions of waveguide section i. c is the speed of light and ν the light frequency. The sign of the square root must be chosen so that the imaginary part of the result is negative, or, if the imaginary part is zero, the real part is positive. For guided modes this is equivalent to Eq. (3.14) and for evanescent modes this is necessary to yield physically meaningful behavior around $z = 0$. This square root convention is different from the principle branch square root implemented in many programming languages.

For the circular waveguides the radial wave vectors are zeros of the characteristic equations. In the present work the modes in section I are interleaved from waveguide modes of subsection Ia and Ib according to the waveguide diameter ratio.

The radial wave vector is always nonzero for closed waveguides. A zero radial wave vector corresponds to a TEM mode (i.e., E_z and H_z are zero) [67, Eq. 2.3.17] and has no cutoff frequency. Such a mode can only exist in open waveguides like a parallel plate waveguide but not in the circular waveguides under consideration here [68, p. 196].

The transmittance and reflectance spectrum of the fiber end junction is given as:

$$T(\lambda) = \frac{\sum_{\operatorname{Re}\beta_q^{\mathrm{II}} \neq 0} |b_q^{\mathrm{II}}|^2}{\sum_{\operatorname{Re}\beta_p^{\mathrm{Ia}} \neq 0} |a_p^{\mathrm{Ia}}|^2}, \qquad R(\lambda) = \frac{\sum_{\operatorname{Re}\beta_p^{\mathrm{I}} \neq 0} |b_p^{\mathrm{I}}|^2}{\sum_{\operatorname{Re}\beta_p^{\mathrm{Ia}} \neq 0} |a_p^{\mathrm{Ia}}|^2}. \tag{3.16}$$

ii. The mode-matching technique

The coefficients $a_n^{[i]}$ and $b_n^{[i]}$ are to be determined with respect to the continuity of the tangential fields at the waveguide endings/junctions. The continuity of tangential E and H fields is a necessary and sufficient condition for fields, which are already solutions to Maxwell equations in two half-spaces, to be a solution at the half-spaces separating plane. From tangential continuity the other relations for normal components or the tangential B and D fields follow in all cases including junctions with different materials.

To match the E- and H- tangential fields in region I and II at $z = 0$

$$\sum_p (a_p^\mathrm{I} + b_p^\mathrm{I}) \boldsymbol{E}_{p,\mathrm{t}}^\mathrm{I} = \sum_q (a_q^\mathrm{II} + b_q^\mathrm{II}) \boldsymbol{E}_{q,\mathrm{t}}^\mathrm{II}, \quad \text{and} \quad \sum_p (a_p^\mathrm{I} - b_p^\mathrm{I}) \boldsymbol{H}_{p,\mathrm{t}}^\mathrm{I} = \sum_q (b_q^\mathrm{II} - a_q^\mathrm{II}) \boldsymbol{H}_{q,\mathrm{t}}^\mathrm{II}$$

must be fulfilled. Equality can only be achieved if all modes (i.e., infinitely many) are used in the summation. Practically only a finite subset can be used and then the equations should be solved in a least squares sense. The squared absolute error[1] between both sides is given by

$$\begin{aligned}\|\Delta \boldsymbol{E}_\mathrm{t}\|_A^2 = (\boldsymbol{a}^\mathrm{I}+\boldsymbol{b}^\mathrm{I})^H \langle \boldsymbol{E}^\mathrm{I}, \boldsymbol{E}^\mathrm{I}\rangle_A (\boldsymbol{a}^\mathrm{I}+\boldsymbol{b}^\mathrm{I}) + (\boldsymbol{a}^\mathrm{II}+\boldsymbol{b}^\mathrm{II})^H \langle \boldsymbol{E}^\mathrm{II}, \boldsymbol{E}^\mathrm{II}\rangle_A (\boldsymbol{a}^\mathrm{II}+\boldsymbol{b}^\mathrm{II}) \\ - 2\,\mathrm{Re}\left\{(\boldsymbol{a}^\mathrm{I}+\boldsymbol{b}^\mathrm{I})^H \langle \boldsymbol{E}^\mathrm{I}, \boldsymbol{E}^\mathrm{II}\rangle_A (\boldsymbol{a}^\mathrm{II}+\boldsymbol{b}^\mathrm{II})\right\}, \end{aligned} \tag{3.17}$$

$$\begin{aligned}\|\Delta \boldsymbol{H}_\mathrm{t}\|_B^2 = (\boldsymbol{a}^\mathrm{I}-\boldsymbol{b}^\mathrm{I})^H \langle \boldsymbol{H}^\mathrm{I}, \boldsymbol{H}^\mathrm{I}\rangle_B (\boldsymbol{a}^\mathrm{I}-\boldsymbol{b}^\mathrm{I}) + (\boldsymbol{b}^\mathrm{II}-\boldsymbol{a}^\mathrm{II})^H \langle \boldsymbol{H}^\mathrm{II}, \boldsymbol{H}^\mathrm{II}\rangle_B (\boldsymbol{b}^\mathrm{II}-\boldsymbol{a}^\mathrm{II}) \\ - 2\,\mathrm{Re}\left\{(\boldsymbol{a}^\mathrm{I}-\boldsymbol{b}^\mathrm{I})^H \langle \boldsymbol{H}^\mathrm{I}, \boldsymbol{H}^\mathrm{II}\rangle_B (\boldsymbol{b}^\mathrm{II}-\boldsymbol{a}^\mathrm{II})\right\} \end{aligned} \tag{3.18}$$

with $\langle \boldsymbol{E}^{[i]}, \boldsymbol{E}^{[j]}\rangle_A$ and $\langle \boldsymbol{H}^{[i]}, \boldsymbol{H}^{[j]}\rangle_B$ denoting the matrices of all scalar products between individual modes with respect to integration area A and B:

$$\left[\langle \boldsymbol{E}^{[i]}, \boldsymbol{E}^{[j]}\rangle_A\right]_{pq} = \iint_A \boldsymbol{E}_{p,\mathrm{t}}^{[i]}(x,y)^H \boldsymbol{E}_{q,\mathrm{t}}^{[j]}(x,y)\mathrm{d}x\mathrm{d}y, \tag{3.19}$$

$$\left[\langle \boldsymbol{H}^{[i]}, \boldsymbol{H}^{[j]}\rangle_B\right]_{pq} = \iint_B \boldsymbol{H}_{p,\mathrm{t}}^{[i]}(x,y)^H \boldsymbol{H}_{q,\mathrm{t}}^{[j]}(x,y)\mathrm{d}x\mathrm{d}y. \tag{3.20}$$

Since in free space the ratio of the magnitude of E and H field is the free-space wave impedance Z_w, the combined error function is chosen as

$$L(\boldsymbol{a}^\mathrm{I}, \boldsymbol{b}^\mathrm{I}, \boldsymbol{a}^\mathrm{II}, \boldsymbol{b}^\mathrm{II}) = \|\Delta \boldsymbol{E}_\mathrm{t}\|_A^2 + Z_w^2 \|\Delta \boldsymbol{H}_\mathrm{t}\|_B^2 . \tag{3.21}$$

In the mode-matching technique the $\boldsymbol{b}^{[i]}$ coefficient vectors are determined for given $\boldsymbol{a}^{[i]}$ coefficient vectors so that the error function L is minimized. Due to linearity of the problem an analytical solution exists. In the following $\boldsymbol{a}^\mathrm{II} = \boldsymbol{0}$ will be assumed, because no light is incident to waveguide II. It is well known, that the minimum of a quadratic form with Hermitian $\boldsymbol{M}$ is given by

$$\boldsymbol{M}^{-1}\boldsymbol{v} = \underset{\boldsymbol{x}}{\mathrm{argmin}}\,\mathrm{Re}\left\{\boldsymbol{x}^H \boldsymbol{M}\boldsymbol{x} - 2\boldsymbol{x}^H\boldsymbol{v}\right\}. \tag{3.22}$$

It is tedious but not difficult to show that L is of the form $L(\boldsymbol{a}^\mathrm{I}, \boldsymbol{b}^\mathrm{I}, \boldsymbol{a}^\mathrm{II}, \boldsymbol{b}^\mathrm{II}) = \mathrm{Re}\left\{\boldsymbol{x}^H \boldsymbol{M}\boldsymbol{x} - 2\boldsymbol{x}^H\boldsymbol{v}\right\} + \mathrm{const}(\boldsymbol{a}^\mathrm{I}, \boldsymbol{a}^\mathrm{II})$, with

$$\boldsymbol{M} = \begin{pmatrix} \langle \boldsymbol{E}^\mathrm{I}, \boldsymbol{E}^\mathrm{I}\rangle_A + Z_w^2 \langle \boldsymbol{H}^\mathrm{I}, \boldsymbol{H}^\mathrm{I}\rangle_B & -\langle \boldsymbol{E}^\mathrm{I}, \boldsymbol{E}^\mathrm{II}\rangle_A + Z_w^2 \langle \boldsymbol{H}^\mathrm{I}, \boldsymbol{H}^\mathrm{II}\rangle_B \\ -\langle \boldsymbol{E}^\mathrm{I}, \boldsymbol{E}^\mathrm{II}\rangle_A^H + Z_w^2 \langle \boldsymbol{H}^\mathrm{I}, \boldsymbol{H}^\mathrm{II}\rangle_B^H & \langle \boldsymbol{E}^\mathrm{II}, \boldsymbol{E}^\mathrm{II}\rangle_A + Z_w^2 \langle \boldsymbol{H}^\mathrm{II}, \boldsymbol{H}^\mathrm{II}\rangle_B \end{pmatrix}, \tag{3.23}$$

$$\boldsymbol{v} = \begin{pmatrix} -\langle \boldsymbol{E}^\mathrm{I}, \boldsymbol{E}^\mathrm{I}\rangle_A + Z_w^2 \langle \boldsymbol{H}^\mathrm{I}, \boldsymbol{H}^\mathrm{I}\rangle_B \\ \langle \boldsymbol{E}^\mathrm{I}, \boldsymbol{E}^\mathrm{II}\rangle_A^H + Z_w^2 \langle \boldsymbol{H}^\mathrm{I}, \boldsymbol{H}^\mathrm{II}\rangle_B^H \end{pmatrix} \boldsymbol{a}^\mathrm{I}, \quad \text{and} \quad \boldsymbol{x} = \begin{pmatrix} \boldsymbol{b}^\mathrm{I} \\ \boldsymbol{b}^\mathrm{II} \end{pmatrix}. \tag{3.24}$$

The mode-matching problem is, hence, solved in a least squares sense (this is true for both guided and evanescent modes) with the above symbols by

$$\boldsymbol{x} = \boldsymbol{M}^{-1}\boldsymbol{v}. \tag{3.25}$$

Note, that once the coefficient vectors $\boldsymbol{b}^\mathrm{I}$ and $\boldsymbol{b}^\mathrm{II}$ are obtained, also the matching error in both the E and H field can be computed by Eq. (3.17) and Eq. (3.18).

All one needs to know are the scalar products between all modes in waveguide section I

---

[1] Note that $\|\boldsymbol{X}-\boldsymbol{Y}\|^2 = \langle \boldsymbol{X}-\boldsymbol{Y}, \boldsymbol{X}-\boldsymbol{Y}\rangle = \langle \boldsymbol{X}, \boldsymbol{X}\rangle + \langle \boldsymbol{Y}, \boldsymbol{Y}\rangle - 2\,\mathrm{Re}\{\langle \boldsymbol{X}, \boldsymbol{Y}\rangle\}$.

and II over cross sections A and B for E and H field, respectively. For the geometry shown in Fig. 3.4 the cross sections A and B are the full cross section of I or II. If waveguide section Ib is replaced by an ideally conducting electric or magnetic wall, A and B have to be chosen accordingly. For an electric wall the tangential E field needs to be matched over the cross section II (it must be zero in Ib) and the H field over cross section Ia (it is arbitrary in Ib). For a magnetic wall the situation is reversed.

Note, that due to the large size of the matrix $\boldsymbol{M}$, Eq. (3.25) is best solved with an iterative method. Good performance was obtained using the GMRES (Generalized minimal residual) method [69]. The advantage is that the matrix $\boldsymbol{M}$ does not need to be stored in computer memory – only a routine for computation of $\boldsymbol{Mx}$ has to be supplied. This saves computer memory (only the matrices with the scalar products for E and H are stored) and exploits the diagonality of the diagonal submatrices. A 10000×10000 matrix with complex double precision numbers requires 1.5 GB of computer memory.

iii. Simulation results

Since in the mentioned experimental results [26] the lateral position of the laser had no influence on the fiber spectral background, central laser coupling is assumed in this theoretical investigation. The coupling coefficient of the laser to the fiber modes is modeled by the overlap integral of the E-field of a $\mathrm{TE}_{1,1}$ mode of a 6 µm diameter circular metallic waveguide (modeling the laser) and the E-field modes in section Ia. The coupling coefficients which were obtained are shown in Fig. 3.7. As a consequence only modes with $\nu = 1$ (ν denotes here the order of the Bessel function) need to be considered and only one polarization direction. On the contrary, TE and TM modes couple between section I and II and have to be included in the ansatz.

The simulated transmission and reflection spectrum of a lossless fiber with length $l = 20$ cm is shown in Fig. 3.5. The fiber diameter is 100 µm and the diameter of

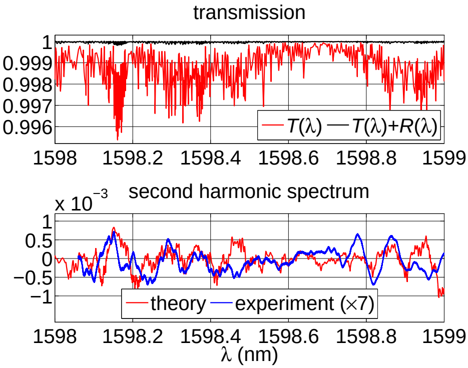

Fig. 3.5: *The simulated transmission, reflectance (top) and second harmonic spectrum (bottom) of the fiber end. The backscattering at the fiber end recreates the pseudo random structure of the experimentally observed multi-mode pattern (blue).*

waveguides Ib and II is 300 µm. The simulation indeed reproduces the experimentally observed spectral background with a similar order of magnitude of $\sigma(H_2) = 2.3 \times 10^{-4}$. The experimental result shown in Fig. 3.5 (from Ref. [26]) was scaled by factor of 7 because the fiber used in experiment was larger by this factor.

iv. Necessary number of modes and limitations of the technique

The convergence plot (i.e., the E and H field matching error versus number of modes in section I and II) for the previous geometry is shown in Fig. 3.6. The mode-matching

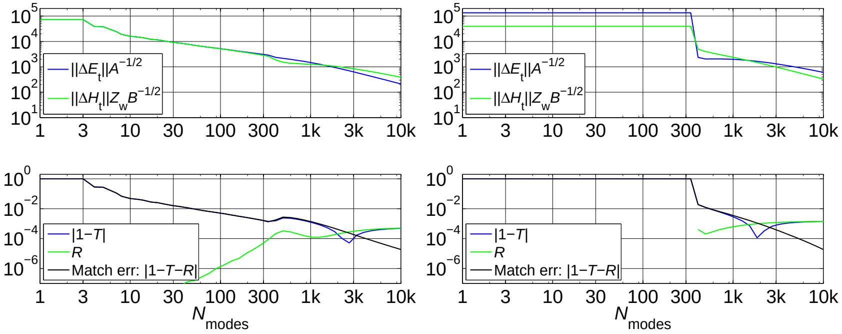

(a) $TE_{1,1}$ exitation (b) $TE_{1,60}$ exitation

Fig. 3.6: *The convergence plot showing error in E and H field versus number of modes in the matching. To obtain stable reflected R and transmitted power T, 20 times more modes (~ 7500) than guided modes (374) are needed. Parameters: λ: 1.6 µm, guided modes: 124 (Ia), 249 (Ib), 374 (II), total modes: 3334 (Ia), 6666 (Ib), 10000 (II).*

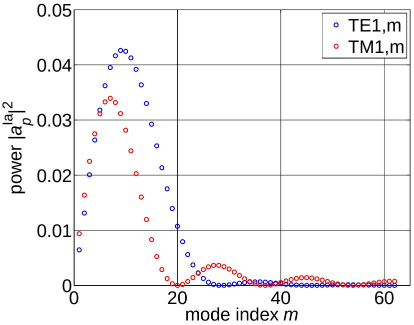

Fig. 3.7: *The distribution of power coupled to the hollow fiber (waveguide Ia)*

converges, and a sufficient accuracy of reflected and transmitted power is obtained for $N_{\text{modes}} = 7500$, which was selected in the previous simulation. This is 20 times more than guided modes in waveguide II. Practically, the number of modes is limited to about 10000 with the present method, due to computer memory limitations. This inhibits the simulation of larger structures with either larger fiber or larger outside area II for better approximation of the free space.

3.3. Wavelength modulation spectrometry

For technical reasons a special method called wavelength modulation spectrometry (WMS) [20] is frequently used to realize the TDLAS measurement. It uses a slow wavelength ramp superimposed with a small sinusoidal wavelength modulation with a phase sensitive detection (lock-in amplifier) for the demodulation of the received detector signal (see Fig. 3.8). Due to this modulation and demodulation with rates typically in the kHz range, different signals are obtained - instead of the transmission signal - which contain the relevant information. In literature WMS is often regarded as a method for effective noise suppression and for partially removing the influence of the laser power variation during the frequency scan.

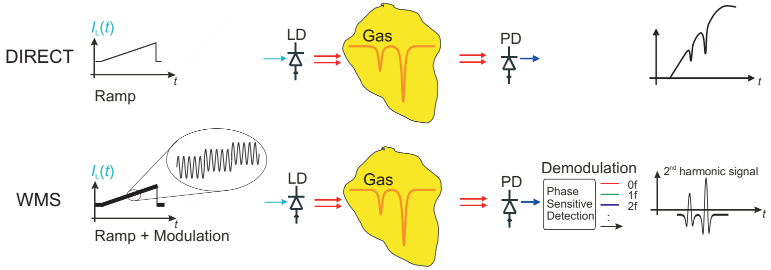

Fig. 3.8: *Comparison between direct spectroscopy (top) and wavelength modulation spectroscopy (WMS) (bottom). WMS realizes a superimposed sinusoidal modulation and a demodulation which results in detection signals with derivative like shapes (harmonic signal/spectrum instead of transmission signal or spectrum*

To achieve the goal of devising new detection methods in the WMS framework it is necessary to have a theoretical description that gives a more clear insight in the generation of signals as the more or less complicated measurement process provides. Therefore the existing theoretical description for WMS [70] was extended and simplified in this thesis by using a more compact description. The idea was to derive general results that may be useful for application or development of new methods. Essentially the system was analyzed in a mathematical style where as many properties as possible of the WMS system/harmonic spectra are derived hoping to create a more complete and detailed understanding of the process of signal generation which in the end should lead to improved methods.

The investigation will start by a presentation of the definition and behavior of a WMS system and what is established in the literature or what is generally known. The subsequent analysis with modeling will yield a new filter based model which leads to new ideas for the system design. The following questions will be answered:

- Does WMS have an ability of effective fringe reduction?
- Can fundamental improvements be expected by non-sinusoidal waveforms?
- Are there fundamental advantages of WMS over direct detection?
- What are implementation possibilities of multi-harmonic detection?
- How to efficiently compute harmonic spectra?
- Differences of WMS using DFB lasers and VCSELs?

Related questions on differences between WMS and direct detection are treated in the section section 5.1.

3.3.1. Fundamentals: Known properties of WMS

In this section WMS is defined and its known properties presented. For details on the origin of the chosen definitions, choice of nomenclature, comparison with literature and assumptions see section A.2.

i. Definition

Let ν denote the frequency of the central laser emission which implements the slow (discrete) laser emission frequency sweep with ν_a the frequency modulation amplitude and f_m the modulation or repetition frequency (typically in the kHz range). The n-th harmonic output of the lock-in amplifier of the relative light power variation after passing through the sample with transmission $T(\nu)$ is called the harmonic coefficient H_n. Mathematically, the Fourier series decomposition

$$H_n(\nu;\nu_\mathrm{a}) = \frac{\epsilon_n}{2\pi}\int_{-\pi}^{\pi} T(\nu+\nu_\mathrm{a}\cos{(z)})\cos{(nz)}\,\mathrm{d}z \tag{3.26}$$

is computed.

$T(\nu)$: Transmission spectrum (unit: 1),
$H_n(\nu;\nu_a)$: Harmonic (transmission) spectrum (unit: 1),
ν_a : Frequency modulation amplitude (unit: Hz),
n : WMS detection order (unit: 1).

When the harmonic coefficients are plotted against the slow sweep frequency ν the **harmonic spectra** $H_n(\nu)$ are obtained (for an example see Fig. 3.9). The term **harmonic coefficient** is used when the dependence on the detection order n (at constant ν) is to be emphasized. In this work the term **harmonic signal** (symbol S_n) refers to measured quantities in an experimental setup (i.e., output of the lock-in amplifier) whereas harmonic spectra represent the theoretically expected physical quantities. Both are the same in an idealized system with differences for non-ideal systems (see section 3.3.4 for treatment of these differences). The appropriate units for harmonic spectra and signals are 1 versus frequency ν or wavelength λ and time t or laser current I respectively. Arbitrary or meaningless units like voltage or A/D converter digits as the y-unit as frequently seen in the literature are avoided in this work.

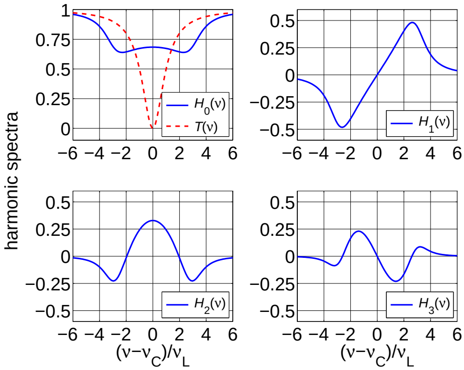

Fig. 3.9: *The first four harmonic spectra (i.e., $H_n(\nu)$ with $n = 0, \dots, 3$) (blue, solid) for a Lorentzian absorption line (red, dashed) computed with theory from Ref. [71]. The wavelength modulation amplitude is ν_a, the absorption line center position is ν_C and the half-width $\nu_L = \nu_a/3$.*

ii. Similarity of harmonic spectra and transmission derivatives

WMS is sometimes called derivative spectroscopy. The first harmonic is for small modulation amplitudes approximately[2] the derivative of the transmission at ν times the wavelength modulation amplitude ν_a, i.e., $H_1(\nu) \approx \nu_\mathrm{a} T'(\nu)$. Similar relationships hold between higher harmonics and the higher derivatives.

iii. Linearity and shift invariance

Due to the inherent linearity of the signal processing, there is an ideally linear relationship between the transmission spectrum and the corresponding harmonic spectra[3]. It is linear in the sense that scaling and summation of the transmission also results in scaling and summation of the corresponding harmonic spectra. The linearity of the relationship essentially means that for unsaturated absorption lines the individual lines simply add in the harmonic spectra. This is a well known fact and it is one of the reasons why WMS can be applied for spectroscopic purposes at all.

It is also the reason why the convolution model exists, which is developed in the next section (see section 3.3.2).

iv. Offset and slope removal

As mentioned before, the concentration or peak absorption strength scales the harmonic spectrum, whereas for orders greater than zero additionally the large offset is removed.

---

[2] This approximation can not be made for accurate modeling because the optimum/real-world modulation amplitudes are large compared to the absorption line width.

[3] This is also valid for saturated lines/thick optical samples, i.e., where the exponential in the Lambert-Beer law can no longer be linearized. This is because the harmonic spectra are defined in terms of transmission and not absorbance or absorption coefficient.

This offset removal property of WMS is usually considered as one of its advantages, because detection of a small signal on a large offset is not needed. This general behavior is also subject to this investigation and it should be understood in a more mathematical rigorous fashion. Especially, what actually is removed from arbitrary transmission functions for higher detection orders $n > 1$ is investigated (see section 3.3.3).

v. Expression for unsaturated Lorentzian lines (Arndt's formula)

Arndt derived an analytical expression for the harmonic spectrum of an unsaturated Lorentzian line [71]. This line shape is an important approximation of the Voigt line shape, valid in the mid and near infrared at atmospheric pressure:

$$T(\nu) = 1 - a_{\mathrm{mol}} \frac{\nu_{\mathrm{L}}^2}{\nu_{\mathrm{L}}^2 + (\nu - \nu_{\mathrm{C}})^2} \tag{3.28}$$

$$\Rightarrow H_n(\nu) = \delta_n - a_{\mathrm{mol}} A_n\left((\nu - \nu_{\mathrm{C}})/\nu_{\mathrm{L}}, \nu_{\mathrm{a}}/\nu_{\mathrm{L}}\right), \tag{3.29}$$

with Arndt's formula [71]

$$A_n(x, m) = \frac{\epsilon_n}{m} \operatorname{Re}\left\{ \frac{\mathrm{i}^n \left(\sqrt{q^2+1} - q\right)^n}{\sqrt{q^2+1}} \right\}, \qquad q = \frac{1 - \mathrm{i}x}{m}. \tag{3.30}$$

vi. Series expansion

In the literature the harmonic spectra are often expressed in terms of the transmission derivatives [72]:

$$H_n(\nu; \nu_{\mathrm{a}}) = \sum_{k=0}^{\infty} \frac{\epsilon_n (\nu_{\mathrm{a}}/2)^{n+2k}}{(n+k)!k!} T^{(n+2k)}(\nu). \tag{3.31}$$

The drawback of this expression is that it is not convergent in all cases. For the Lorentz profile with ν_{a} larger than the Lorentz half-width ν_{L} the series is divergent [73] and for ν_{a} close to ν_{L} the series converges very slowly, making it even for the convergent cases impractical. The reason for the convergence problems is that the underlying Taylor approximation of the transmission function is not good. Nevertheless this often presented in the literature [72, 74–76] despite the fact that it can not be used to compute the harmonic spectra for the relevant case of atmospheric sensing. This formula is the inverse of the expression Eq. (3.42) which gives transmission derivatives as infinite sum of the harmonic spectra.

vii. Complex change with absorption line width

If the width of a line in the transmission changes (e.g., due to a pressure, temperature or concentration dependent self-broadening effects), a complex alteration of the shape of the harmonic spectrum of this single line is observed. Both width and amplitude change. The shape depends on the modulation index, i.e., the ratio of line width and frequency modulation amplitude. The width of the harmonic spectrum is also typically much larger than the width of the absorption line, since the "broadening" is dominated by the frequency modulation amplitude which is usually a factor of 2 to 3 larger than the absorption line half-width (cf. Fig. 3.9).

3.3.2. Model of harmonic spectra (ideal physical)

In this section a model for the ideal behavior of wavelength modulation spectrometry is developed. Giving the same results as existing models it provides new viewpoints helpful for understanding. This will lead to new insights into signal generation, derivation of new properties which lead to further improvement of detection methods.

Because of the linear shift invariance property of WMS it is possible to model this relationship with a convolution expression. This is due to the fact that all linear shift invariant operators can be expressed as a convolution expression (For explanation see section B.6). This WMS description compatible with filter theory was published partly within the frame of this thesis in Applied Physics B [52] and the TDLS conference [77]. Significant extensions to the published article are included here, e.g., decomposition of the convolution into differentiation and subsequent smoothing.

Starting with the Fourier integral Eq. (3.26) it is not difficult to derive the convolution expression. Substituting $\eta = -\nu_{\mathrm{a}} \cos(z)$ it becomes

$$H_n(\nu) = \int_{-\infty}^{\infty} T(\nu - \eta)\, K_{\mathrm{wms}}(\eta) \mathrm{d}\eta = (T * K_{\mathrm{wms}})(\nu) \tag{3.32}$$

with the kernel

$$K_{\mathrm{wms}}(\eta) = \begin{cases} \frac{\epsilon_n \, \mathrm{T}_n(-\eta/\nu_{\mathrm{a}})}{\pi\sqrt{\nu_{\mathrm{a}}^2 - \eta^2}} & |\eta| < \nu_{\mathrm{a}} \\ 0 & \text{otherwise} \end{cases} . \tag{3.33}$$

Here $\mathrm{T}_n(x) = \cos(n \arccos(x))$ is the Chebyshev polynomial of degree n [78, chapter 22]. A similar formula was obtained by R. Arndt [71], but not recognized as a convolution or filter expression. The convolution kernel K_{wms} depends on the modulation amplitude ν_{a} and the order n of the frequency component selected by the lock-in amplifier. By applying integration by parts n times, this can be written in the following second, alternative form:

$$H_n(\nu) = \frac{\epsilon_n}{2^n n!} \int_{-\infty}^{\infty} \frac{\mathrm{d}^n T(\nu - \eta)}{\mathrm{d}(\nu/\nu_{\mathrm{a}})^n} K_{\mathrm{wms}}^{\mathrm{der}}(\eta) \mathrm{d}\eta \tag{3.34}$$

with

$$K_{\mathrm{wms}}^{\mathrm{der}}(\eta) = \begin{cases} \frac{4^n n!^2 (\nu_{\mathrm{a}}^2 - \eta^2)^n}{\pi (2n)! \nu_{\mathrm{a}}^{2n} \sqrt{\nu_{\mathrm{a}}^2 - \eta^2}} & |\eta| \le \nu_{\mathrm{a}} \\ 0 & \text{otherwise} \end{cases} . \tag{3.35}$$

See derivation C.1. This is also a convolution expression, but containing the n-th derivative instead of the transmission itself. The n-th derivative is formed with respect to the normalized wavelength coordinate ν/ν_a. This normalized derivative is related to the normal derivative by simple scaling with ν_{a}^n, i.e., $\frac{\mathrm{d}^n T(\nu)}{\mathrm{d}(\nu/\nu_{\mathrm{a}})^n} = \nu_{\mathrm{a}}^n T^{(n)}(\nu)$. This

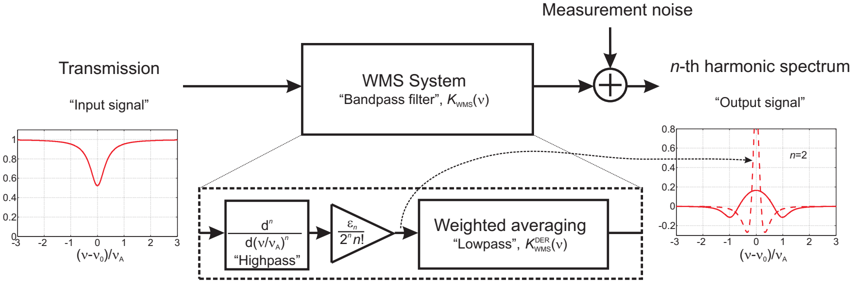

Fig. 3.10: *Interpretation of the WMS harmonic spectra as a bandpass filtering of the transmission (Filtering is carried out with respect to ν). It is a combination of a n-th differentiation (highpass) and subsequent smoothing (lowpass). This general model provides an intuitive view on how the harmonic spectra are connected to the transmission despite their more or less complicated process of generation.*

seems natural because the output of the WMS system can not depend on the special unit of ν. Note that the pre-factor is chosen in a way that $K^{\text{der}}_{\text{wms}}(\eta)$ is area normalized, i.e., $\int_{-\infty}^{\infty} K^{\text{der}}_{\text{wms}}(\eta)\text{d}\eta = 1$, and, hence, $K^{\text{der}}_{\text{wms}}$ represents a true unit-gain lowpass[4].

Eq. (3.32) and Eq. (3.34) allow for a new system theoretic viewpoint for WMS measurement systems: the transmission function is regarded as the input of the WMS system and the output is the n-th harmonic spectrum (for an illustration see Fig. 3.10). The signal or spectrum generation in WMS can be seen in two equivalent ways

- **The transmission function is convolved or filtered with a fixed function**. This filtering can be interpreted as a bandpass filtering (except for $n = 0$ where it is a lowpass) which removes both the coarse structure and the fine details.
- **The transmission function is first differentiated n times, damped and then smoothed**. This filtering or smoothing after differentiation is a low-pass filtering which removes the fine details. The coarse structure like offset, slope and so on is removed by the n-th differentiation.

The convolution is done in the frequency domain and hence the convolution kernel K_{wms} is the "instrument function" of WMS based spectrometers. The convolution can be interpreted as a filter if the frequency variable ν is linearly swept through with time with a tunable laser. Then the variable ν is replaced with time t and ordinary time signals are obtained which are filtered by the WMS filter. Note that this filter model is only valid for the analytic signal, the measurement noise is not passed through this filter it has to be added at the model output.

The second expression Eq. (3.34) explains why the harmonic spectra have a similar structure to the n-th derivatives and share similar properties. The n-th order detection removes all components from the original transmission as n-th order differentiation would do. So second harmonic detection is insensitive to offset and linear slopes in the transmission. Any change of offset and (additive) linear components in the transmission

---

[4] It is a lowpass because the convolution kernel is non-negative and not oscillating. It is also clear from the Fourier transform of the kernel (see Eq. (3.36))

does not affect the second harmonic spectrum.

When applying the Fourier transform (see section B.3) to both sides of the expression Eq. (3.32) and Eq. (3.34), the convolution turns into a multiplication and the frequency response of the WMS filter and the smoothing lowpass for the n-th derivative of the transmission is obtained

$$\widehat{H}_n(k) = \widehat{T}(k) \cdot \underbrace{\epsilon_n \mathrm{i}^n \, \mathrm{J}_n\left(2\pi\nu_{\mathrm{a}}k\right)}_{\widehat{K}_{\mathrm{wms}}(k)} = \nu_{\mathrm{a}}^n \widehat{T^{(n)}}(k) \cdot \frac{\epsilon_n}{2^n n!} \cdot \underbrace{\frac{n! \, \mathrm{J}_n\left(2\pi\nu_{\mathrm{a}}k\right)}{(\pi\nu_{\mathrm{a}}k)^n}}_{\widehat{K}^{\mathrm{der}}_{\mathrm{wms}}(k)}, \tag{3.36}$$

with the Bessel function of the first kind $\mathrm{J}_n\left(x\right)$ (Chapter 9 in Ref. [78]). Note that for $n > 0$ we have $\widehat{K}_{\mathrm{wms}}(0) = 0$ and $|\widehat{K}_{\mathrm{wms}}(k)| \sim 1/\sqrt{k}$ for $k \to \infty$, which proves that the first expression is a bandpass filter. The second filter kernel for the n-th derivative is $\widehat{K}^{\mathrm{der}}_{\mathrm{wms}}(0) = 1$ and $|\widehat{K}^{\mathrm{der}}_{\mathrm{wms}}(k)| \sim 1/k^{n+1/2}$ for $k \to \infty$ which shows that this is a lowpass filter.

3.3.3. Derived properties of the harmonic spectra

Because of the convolution structure of the harmonic spectra many of the properties of the kernel apply to the harmonic spectra as well. The following general properties could be derived. In case there is a possible application of this property in a sensor this is also indicated. Almost all properties are derived in this thesis for the first time.

i. Zero mean value

Harmonic spectra have the general property of zero mean value

$$\int_{-\infty}^{\infty} H_n(\nu)\mathrm{d}\nu = 0, \text{ for } n > 0. \tag{3.37}$$

See derivation C.2. It explains the observed fact that the area of the negative part of the second harmonic spectrum exactly equals the area of the positive part. Furthermore, it states that this is true for all harmonic spectra of any nonzero order and also holds for arbitrary absorption line shapes. So this is a very general result. Even a more general result can be derived showing that higher order harmonic spectra are also orthogonal to higher order polynomials (next paragraph).

ii. First $n-1$ moments vanish (orthogonality to polynomials of degree $< n$)

Mathematically this means that the n-th harmonic spectrum is orthogonal to all polynomials of degree lower than n:

$$\int_{-\infty}^{\infty} \nu^i H_n(\nu)\mathrm{d}\nu = 0, \text{ for } 0 \leq i < n. \tag{3.38}$$

See derivation C.3. This is an important property for curve-fitting because then a polynomial baseline can be included in the spectral model without increasing the noise on the fitted parameters (due to this orthogonality). Furthermore, it is very easy to estimate a polynomial baseline from measured spectra. A scalar product of experimental data with such a polynomial will directly give the coefficients of the baseline in the measurement. This fact, that baseline estimation and subtraction is possible without curve fitting, is the basis for the in-line wavelength stabilization method developed in section 4.1.

iii. Recursion formula

It is possible to express the n+1-th harmonic spectrum in terms of the n and n-1-th harmonic spectrum:

$$H_{n+1}(\nu) = -\frac{2n\epsilon_{n+1}}{\epsilon_n \nu_\mathrm{a}} \int_{-\infty}^{\nu} H_n(\nu)\mathrm{d}\nu + \frac{\epsilon_{n+1}}{\epsilon_{n-1}} H_{n-1}(\nu). \tag{3.39}$$

See derivation C.4. It shows that there is redundancy in the harmonic spectra and specification of two consecutive spectra contains in principle all information the higher harmonics carry.

iv. First reconstruction formula

The zeroth-harmonic spectrum can be corrected with the higher harmonic spectra to yield the original transmission spectrum:

$$T(\nu) = H_0(\nu) - H_2(\nu) + H_4(\nu) + \ldots + (-1)^n H_{2n}(\nu) + \ldots \tag{3.40}$$

See derivation C.5. The zeroth harmonic spectrum $H_0(\nu)$ is basically the smoothed transmission function (cf. Fig. 3.9). It is distinct from the transmission function due to the additional wavelength modulation.

The practical use of the formula requires accurate measurement of the zeroth harmonic spectrum. So employing this formula in a sensor for reconstruction of $T(\nu)$ is not meaningful because the transmission could be directly measured with the same system and accuracy by just switching off the modulation. So this reconstruction would have no general advantage over direct spectroscopy. It could be useful when a simultaneous measurement of the direct spectrum and the harmonic spectra is desired for some reason. Then the measurement is just performed as for direct spectroscopy but with the additional wavelength modulation and higher harmonic detection. The modulation will "distort" the measurement of the transmission (in fact the zeroth harmonic spectrum is obtained) but this can be corrected with the help of the higher harmonic spectra which may also serve a different purpose.

However, using this formula in a sensor may be impractical because the noise increases during evaluation of the sum. For a detailed explanation see the third reconstruction formula which contains this formula as special case.

v. Second reconstruction formula

The harmonic coefficients are the coefficients of the Chebyshev expansion of the transmission function. So these coefficients can be used to reconstruct the transmission:

$$T(\nu) = \sum_{n=0}^{\infty} H_n(\eta)\, \mathrm{T}_n\left((\nu - \eta)/\nu_\mathrm{a}\right), \qquad |\nu - \eta| \le \nu_\mathrm{a}. \tag{3.41}$$

See derivation C.6. Application of this formula allows for development of a multi-harmonic detection scheme, which is presented in section 4.2. Since the harmonic spectra are approximately equal to the derivatives, this series is formally similar to the Taylor expansion (see section A.2.6 for details).

vi. Third reconstruction formula (for transmission derivatives)

The n-th harmonic spectrum can be corrected with the higher harmonic spectra to yield the original n-th derivative of the transmission:

$$\nu_{\mathrm{a}}^{n} T^{(n)}(\nu) = 2^{n} n! \sum_{k=0}^{\infty} (-1)^{k} \frac{n+2k}{2(n+k)} \binom{n+k}{k} H_{n+2k}(\nu). \tag{3.42}$$

See derivation C.7. This formula contains the first reconstruction formula Eq. (3.40) as a special case $(n = 0)^5$. The first coefficient is just the expression for the asymptotic behavior (see Eq. (3.48)) for low modulation amplitude.

For example for first and second derivative we have

$$\nu_{\mathrm{a}} T'(\nu) = H_1(\nu) - 3H_3(\nu) + 5H_5(\nu) - 7H_7(\nu) + 9H_9(\nu) - \ldots, \tag{3.43}$$

$$\nu_{\mathrm{a}}^{2} T''(\nu) = 4H_2(\nu) - 16H_4(\nu) + 36H_6(\nu) - 64H_8(\nu) + 100H_{10}(\nu) - \ldots \tag{3.44}$$

This result for the first harmonic $n = 1$ has been found before [73, 79]. The formula is not convergent in all cases – it can only be applied if the harmonic spectra are decreasing rapidly enough. Even if it is convergent the noise is strongly amplified due to increasing weight factors. In fact the signal to noise ratio will become zero if the series is not truncated. This is easily understood with help of the convolution model. The information, that is removed by the lowpass filtering after the n-th differentiation can only be recovered at the cost of infinite noise amplification. Note that the noise on the harmonic spectra of different orders n is uncorrelated and of same magnitude as the noise of a direct transmission measurement (at same repetition frequency as WMS modulation frequency).

This formula is the inverse of the expression Eq. (3.31) which gives harmonic spectra as infinite sum of the transmission derivatives.

vii. Peak value of harmonic spectrum

The absolute peak value of the harmonic spectrum is limited by the absolute peak value of the transmission:

$$\max_{\nu} |H_n(\nu)| \leq \max_{\nu} |T(\nu)| \times \begin{cases} 1 & n = 0 \\ \frac{4}{\pi} & n > 0 \end{cases}, \tag{3.45}$$

$$\max_{\nu} |H_n(\nu)| \leq \max_{\nu} |T^{(n)}(\nu) \nu_{\mathrm{a}}^{n}| \cdot \frac{\epsilon_n}{2^n n!}. \tag{3.46}$$

See derivation C.8. This is a very important result because it explains several effects. First it explains that the structure or variation of the harmonic spectra can not be larger than the variation or structure on the transmission function times 1 or $1.27 \approx 4/\pi$.

---

[5] For $k + n = 0$ the fraction $\frac{n+2k}{2(n+k)}$ has to be replaced by 1

Due to the linearity, Eq. (3.45) also holds for differences of transmission and harmonic spectra. So if there is some error or variation or noise on the transmission T then the corresponding error or variation or noise[6] on the harmonic spectrum, is always 1 or $1.27 \approx 4/\pi$ times smaller. This is even independent on the harmonic detection order n and the modulation amplitude ν_a. The formula gives a prediction of absolute accuracy for harmonic spectra computed from transmission spectra superimposed with measurement error or other unwanted artifacts. This is somewhat counterintuitive because generally this computation is considered impossible or impractical because the differentiating nature of WMS is expected to strongly amplify the noise. However, Eq. (3.45) shows that this viewpoint must be incorrect. The reason for this is that the n-th differentiation is followed by a lowpass filtering with attenuation which compensates the amplitude increase due to differentiation (cf. Fig. 3.10).

Furthermore, Eq. (3.45) explains how well to approximate the transmission function for numerical computation of synthetic harmonic spectra. A method for this is developed in section 3.3.5.

viii. Invariance of sinusoidal interference

An additive sinusoidal component on the transmission will display itself also as a sinusoid on the harmonic spectrum with same periodicity:

$$\begin{aligned} T(\nu) &= 1 + A\cos\left(2\pi\nu L_{\mathrm{OPD}}/c + \phi\right) \\ \Rightarrow H_n(\nu) &= \delta_n + \epsilon_n A\, \mathrm{J}_n\left(2\pi\nu_{\mathrm{a}} L_{\mathrm{OPD}}/c\right) \cos\Big(2\pi\nu L_{\mathrm{OPD}}/c + n\frac{\pi}{2} + \phi\Big), \end{aligned} \tag{3.47}$$

with L_{OPD} being the optical path length difference between the two beams causing the interference. $c/L_{\mathrm{OPD}} = \nu_{\mathrm{fsr}}$ is the period length ("free spectral range") of the interference. The symbols A and ϕ represent some arbitrary amplitude and phase-shift. A similar, slightly more general but more complex formula is found in Ref. [70]. This property (sinusoids stay sinusoids) is not obvious from the complicated measurement process but generally true in an exact sense, for all modulation amplitudes and detection orders. In fact it is a consequence of the linearity and shift invariance of the relationship relating harmonic spectra and transmission.

ix. Asymptotic behavior

In the limiting case of small modulation amplitude the harmonic spectrum becomes proportional to the n-th derivative of the transmission function:

$$H_n(\nu;\nu_{\mathrm{a}}) \to \frac{\epsilon_n \nu_{\mathrm{a}}^n}{2^n n!} T^{(n)}(\nu), \qquad \text{for } \nu_{\mathrm{a}} \to 0. \tag{3.48}$$

This is also known from the literature [72]. Most interestingly, Eq. (3.46) tells that the absolute peak value of the left hand side is always smaller than the absolute peak value of the right hand side. Only in the limiting case both sides become equal. This again can be understood by the WMS model of lowpass filtering after the n-th differentiation. The peak values of the n-th derivative is attenuated, because the lowpass filtering/smoothing

---

[6] The noise is meant to be part of the transmission and not measurement noise, e.g., interferometric noise

can not amplify any signal independent on its shape. Equality is only achieved for $\nu_a \to 0$ because the lowpass then approaches infinite bandwidth.

x. Independence from the frequency coordinate

Both integral equation relationships Eq. (3.32) and Eq. (3.34) can be simplified if the integration variable η is replaced with $x = \eta/\nu_\mathrm{a}$: the integral borders will change to -1 and 1 and the convolution kernel will become independent on ν_a. The relationship between transmission or its n-th derivative and the harmonic spectrum in normalized wavelength coordinates is universal. This is especially useful since the n-th differentiation has to be carried out in this normalized coordinates anyway. Let be $\widetilde{T}(x) = T(\nu_a x)$ and $\widetilde{H}_n(x) = H_n(\nu_a x)$ then

$$\widetilde{H}_n(x) = \int_{-1}^{1} \widetilde{T}(x-y)\,\frac{\epsilon_n\,\mathrm{T}_n\,(-y)}{\pi\sqrt{1-y^2}}\mathrm{d}y, \tag{3.49}$$

$$\widetilde{H}_n(x) = \int_{-1}^{1} \widetilde{T}^{(n)}(x-y)\,\frac{\epsilon_n 2^n n!(1-y^2)^n}{\pi(2n)!\sqrt{1-y^2}}\mathrm{d}y, \tag{3.50}$$

i.e., expressions independent on the modulation amplitude ν_a are obtained.

3.3.4. Model of harmonic signals (measurement system, non-ideal)

The modeling of the harmonic spectra presented in the last sections is based on an ideal laser which does not change its output intensity during tuning. For real devices this is not the case and nonlinear behavior with respect to current I is observed. This causes overtones in the light intensity modulation resulting in a non-ideal measurement. Hence the measured harmonic signals are different to the ideal harmonic spectra. Modeling of harmonic signals is scope of this section.

For second harmonic detection using VCSELs a small negative offset ($\sim -10^{-4}$) is observed on measured signals. Using DFB lasers additionally to the negative offset also a distortion making the measured signals unsymmetrical may exist.

Neglecting dynamic effects, harmonic signals for a laser with (possibly nonlinear) P-I-characteristic can be modeled if the transmission is just multiplied by this laser P-I-characteristic and the result is converted to an harmonic spectrum (belonging to this hypothetical transmission). Recall, that the second harmonic spectrum is formed by second differentiation and subsequent filtering, so the negative bending of the laser P-I-characteristic will show as an small negative offset on the harmonic signal. The asymmetry of the resulting signal is caused by the “mixing terms” which occur during differentiation of a product. In this section it will be shown that a similar relationship holds for the general case (including dynamic effects).

Practically, the spectral models necessary for VCSELs based sensors are typically more simplified in contrast to those necessary for sensors based on DFB lasers. While for VCSELs inclusion of a baseline is sufficient [28, 54, 55], DFB laser-based sensors often utilize an exact but more complex model (e.g. that of Kluczynski [70]). This model has more unknown parameters, which must be either known or estimated in the fit which either increases sensor complexity or decreases the fit performance.

The following questions will be answered:

- What is the proper model for (non-ideal) harmonic signals?
- How to model normalization using the zero-th harmonic signal?
- Where do differences between DFB lasers and VCSELs originate from?

In Fig. 3.11 a schematic of a real WMS system is presented. Aim of this section is to relate the measured signals to the harmonic spectra. For WMS applications the laser current is modulated sinusoidally at frequency f_m around a bias current I:

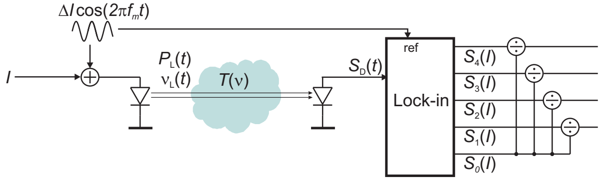

Fig. 3.11: *The spectrometry system including laser, medium, detector and lock-in amplifier including the used symbols. The tunable laser, modulated around bias current I, generates light of intensity $P_L(t)$ and optical frequency $\nu(t)$, which is passed through a medium with transmission $T(\nu)$. The received signal intensity $S_D(t)$ is decomposed into harmonic signals $S_n(I)$ with a lock-in amplifier and subsequent power normalization.*

$$I_\mathrm{L}(t) = I + I_\mathrm{a}\cos(2\pi f_\mathrm{m} t), \tag{3.51}$$

which results in an instantaneous laser emission frequency $\nu_\mathrm{L}(t)$ and instantaneous intensity $P_\mathrm{L}(t)$ given by

$$\nu_\mathrm{L}(t) = \nu + \nu_a\cos(2\pi f_\mathrm{m} t - \phi), \tag{3.52}$$

$$P_\mathrm{L}(t) = P_0 + |P_1|\cos(2\pi f_\mathrm{m} t - \angle(P_1)) + |P_2|\cos(4\pi f_\mathrm{m} t - \angle(P_2)) + \dots. \tag{3.53}$$

Here $\nu = \nu(I)$ is the central emission frequency of the laser in steady state when a DC current I is applied and it is assumed that the wavelength modulation can be regarded as "small", i.e., no higher order harmonics are generated. $\nu_a = \nu_\mathrm{a}(I, \Delta I, f_\mathrm{m})$ is the frequency modulation amplitude and $\phi = \phi(I, f_\mathrm{m})$ the tuning phase-shift. The coefficients $P_n = P_n(I, \Delta I, f_\mathrm{m})$ are complex coefficients and denote the amplitude and phase of the higher order harmonics of the intensity modulation caused by the non-linearity of the laser device. The P_n are related to the time signal $P_\mathrm{L}(t)$ by Fourier series decomposition:

$$P_n(I) = \frac{\epsilon_n}{2\pi}\int_{-\pi}^{\pi} P_\mathrm{L}(z/(2\pi f_\mathrm{m}))\mathrm{e}^{-\mathrm{i}nz}\mathrm{d}z. \tag{3.54}$$

These coefficients are the harmonic signals obtained with a standard wavelength modulation spectrometry setup when no gas or analyte is present. In Fig. 3.12 a measurement of P_0, P_1 and P_2 (the latter two normalized to P_0) for a 2.0 µm VCSEL at a typical modulation amplitude[7] is shown.

---

[7] Note that the P_n coefficients strongly depend on modulation amplitude. With an approximation neglecting dynamic effects we have $P_n \sim I_\mathrm{a}^n$. More precisely it is $P_n(I) \approx \frac{\epsilon_n I_\mathrm{a}^n}{2^n n!} P^{(n)}(I)$, which is analogously to the asymptotic expression for the harmonic spectra Eq. (3.48).

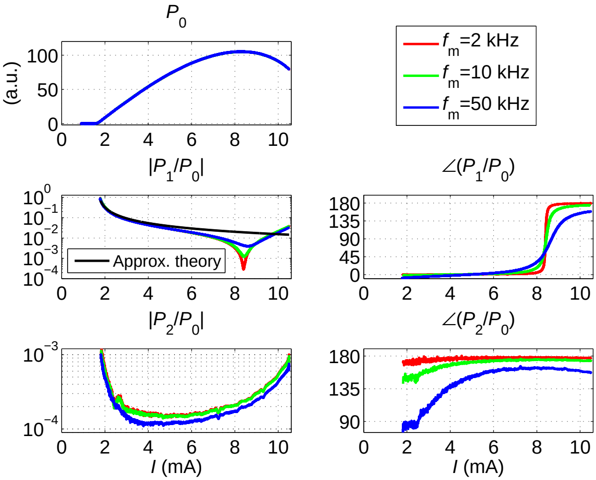

Fig. 3.12: *The amplitude and phase of the complex* $P_n(I)$ *coefficients for a* 2.0 µm *VCSEL.* $P_3(I)$ *was below the measurement accuracy of* 1×10^{-6}. *The current modulation amplitude* I_a *is around* 130 µA. *The black curve corresponds to theory for the simplified laser model without self-heating, Eq. (3.73).*

According to the setup shown in Fig. 3.11, the light passes through a medium with a transmission function $T(\nu)$ and is detected with a photo-detector. If noise and nonlinear distortion of the detection process are neglected the detected intensity is given by

$$S_{\mathrm{D}}(t) = P_{\mathrm{L}}(t)T(\nu_{\mathrm{L}}(t)). \tag{3.55}$$

The lock-in amplifier decomposes the detector signal into the (complex) harmonic coefficients S_n, which form the harmonic signal if plotted against I:

$$S_n(I) = \frac{\epsilon_n}{2\pi}\int_{-\pi}^{\pi} S_{\mathrm{D}}(z/(2\pi f_{\mathrm{m}}))\mathrm{e}^{-\mathrm{i}nz}\mathrm{d}z. \tag{3.56}$$

Using the convolution theorem for the Fourier series, the laser IM coefficients P_n and harmonic spectra H_n can express the harmonic signals S_n:

$$S_n(I) = \frac{\epsilon_n}{2}\sum_{m=0}^{\infty} H_m(\nu(I);\nu_a(I))\left(\frac{P_{n+m}(I)\mathrm{e}^{\mathrm{i}m\phi(I)}}{\epsilon_{n+m}} + \frac{P_{n-m}(I)\mathrm{e}^{-\mathrm{i}m\phi(I)}}{\epsilon_{n-m}}\right). \tag{3.57}$$

See derivation C.9. To enable a compact notation, a negative index to the P coefficients has to be replaced by the conjugate complex, i.e., $P_{-i}(I) = P_i^*(I)$.

Now two general approximations can be made to simplify Eq. (3.57). The first approximation is based on the general observation that above laser threshold $|P_i(I)| \gg |P_{i+2}(I)|$, i.e., the amplitudes of the overtones of the laser modulation are rapidly decreasing. Thus the term with smaller absolute value in each summand in Eq. (3.57) can be neglected. Furthermore, Eq. (3.57) for the DC component $S_0(I)$ is dominated by the first summand, giving the final expression for the WMS harmonic signals:

$$S_n(I) \approx \sum_{m=0}^{\infty} \frac{\epsilon_n \mathrm{e}^{-\mathrm{i}m\phi(I)}}{\epsilon_m \epsilon_{n-m}} H_m(\nu(I); \nu_\mathrm{a}(I))\, P_{n-m}(I), \tag{3.58}$$

$$S_0(I) \approx H_0(\nu(I); \nu_\mathrm{a}(I))\, P_0(I). \tag{3.59}$$

For the ideal system (with $P_0 = \mathrm{const}$, $P_n = 0$ for $n > 0$) the harmonic spectra are proportional to the harmonic signals which is in agreement with their definition:

$$S_n(I) = P_0\, H_n(\nu(I); \nu_\mathrm{a}(I)) \qquad \text{for ideal system.} \tag{3.60}$$

Since at least the laser emission power P_0 is unknown, a power normalization is needed for TDLS. The following methods are distinguished:

- Balanced detection (“best method”). The detector signal is normalized with the instantaneous laser power before the decomposition with the lock-in amplifier is employed. This suppresses laser noise and artifacts due to laser amplitude modulation very efficiently (in this case the model derived in this section is unnecessary) . This method is required for ultra sensitive and precise measurements, first demonstrated by Carlisle [80]. Note that the ratiometric detection is best implemented by a compact analog circuit that allows for noise cancellation down to twice the shot noise limit [81, 82].

  Advantages: Compensates laser intensity variation and laser excess noise. No calibration. Measurement signals are ideally proportional to harmonic spectra.

  Disadvantages: Additional photodetector needed, special design constraints (detectors physically close, need matched devices). Stray light compensation required.

- $1f$ normalization (“traditional, limited”): The first harmonic component at the absorption line center is used for normalization. This method is mostly applied to second harmonic center point detection, or with narrow scanning range, because it assumes a constant or linearly varying laser intensity during scanning. Besides its simplicity another advantage is insensitivity to stray light. It requires knowledge of a laser parameter (that is $P_0(I)/P_1(I)$) which can not be determined in-situ and may change when the laser ages. This parameter depends on modulation amplitude ΔI, bias point I, modulation frequency f_m and laser temperature.

  Advantages: Simple method. Insensitive to stray light.

  Disadvantages: Narrow spectral scans only. Laser calibration constant required.

- Zeroth harmonic or DC normalization (“new, no limitations”): The detector DC signal $S_0(I)$ is used for power normalization, i.e., $S_n(I)/S_0(I)$ is formed. Compared to $1f$ normalization no calibration factors are required. No assumption on the laser intensity variation is made, hence the method is suitable for wide spectral scans where the nonlinearity of $P_0(I)$ is non-negligible. Influence of stray light can be compensated by using an on-off modulation after each scan. The relevant signal model that is also correct for high absorbance is developed below.

  Advantages: Simple method. Arbitrary laser power variation (wide scans). No calibration constants.

  Disadvantages: Stray light compensation required.

If the absorbance is in the range of 1 % to 10 % or even higher, a significant influence from this normalization with $S_0(I)$ instead of $P_0(I)$ is expected. In the following the model for DC scan (zeroth harmonic) normalization is given which is also valid for the high absorbance regime. Introducing the normalization, Eq. (3.58) with Eq. (3.59) reduces for $n > 0$ to

$$\underbrace{\frac{S_n}{S_0}\mathrm{e}^{\mathrm{i}n\phi}}_{\text{measured}} \approx \underbrace{\frac{H_n}{H_0}}_{\text{desired}} + \underbrace{\frac{P_n}{P_0}\mathrm{e}^{\mathrm{i}n\phi}}_{\text{baseline}} + \underbrace{\frac{1}{2}\sum_{\substack{m=1\\ n\neq m}}^{\infty} \frac{H_m}{H_0}\frac{P_{n-m}}{P_0}\mathrm{e}^{\mathrm{i}(n-m)\phi}}_{\text{other distortion}}, \tag{3.61}$$

where the notation of the I or ν dependency of all quantities (including ν_a and ϕ) has been suppressed for clarity. The interpretation of Eq. (3.61) is straightforward: In case of an ideal laser, i.e. $P_n(I) = 0$ except for $P_0(I) = \text{const} > 0$, obviously the normalized harmonic spectrum $H_n(\nu(I))/H_0(\nu(I))$ is obtained.

For a non-ideal laser and no absorber present in the optical path, i.e., $H_n = 0$, except for $H_0 = 1$, the “laser background” $P_n(I)/P_0(I)$ is measured. If both are present, the sum of the normalized harmonic spectrum and the “laser background” is obtained, as well as mixing products which further distort the measurement. The “mixing products” cause the asymmetry of the measured spectra.

For the VCSEL from the example in Fig. 3.12 the mixing products become negligible and the spectral model for second harmonic detection only needs to include a baseline, which is due to the low relative intensity modulation:

$$\frac{S_2}{S_0}\mathrm{e}^{\mathrm{i}2\phi} \approx \underbrace{\frac{H_2}{H_0}}_{\frac{a_\mathrm{mol}}{3}} + \underbrace{\frac{P_2}{P_0}\mathrm{e}^{\mathrm{i}2\phi}}_{10^{-4}} + \frac{1}{2}\left(\underbrace{\frac{H_1}{H_0}}_{\frac{a_\mathrm{mol}}{2}} \underbrace{\frac{P_1}{P_0}\mathrm{e}^{\mathrm{i}\phi}}_{10^{-2}} + \underbrace{\frac{H_3}{H_0}}_{\frac{a_\mathrm{mol}}{4}} \underbrace{\frac{P_1^*}{P_0}\mathrm{e}^{-\mathrm{i}\phi}}_{10^{-2}} + \underbrace{\frac{H_4}{H_0}}_{\frac{a_\mathrm{mol}}{7}} \underbrace{\frac{P_2^*}{P_0}\mathrm{e}^{-\mathrm{i}2\phi}}_{10^{-4}} + \dots \right) \tag{3.62}$$

$$\approx \frac{H_2}{H_0} + \frac{P_2}{P_0}\mathrm{e}^{\mathrm{i}2\phi}. \tag{3.63}$$

The laser background is based on data shown in Fig. 3.12 for the VCSEL at 2 µm operated at a bias current around 7 mA, with a modulation amplitude setting for detection in ambient air. It is evident that for this VCSEL the mixing terms can be neglected because these only contribute only about 1% to the overall signal, independent on the value of the absorbance a_mol. For the mixing terms to be negligible, the laser has to be operated as close as possible to roll-over. A discussion on differences between VCSELs and DFBs and lasers on different material system in context of this requirement is in section 3.3.6.ii.

3.3.5. Fast and accurate computation of harmonic spectra

A practical problem is the computation of harmonic spectra from the transmission. The task is the evaluation of the Fourier integral Eq. (3.26), which is stated again for convenience of the reader:

$$H_n(\nu; \nu_\mathrm{a}) = \frac{\epsilon_n}{2\pi}\int_{-\pi}^{\pi} T(\nu + \nu_\mathrm{a}\cos(z))\cos(nz)\,\mathrm{d}z. \tag{3.64}$$

Although numerical integration can be employed, it is computationally intense and in the literature a wide range of other approaches has been considered. These approaches are all limited to special cases. The question is: Can the convolution model provide a better computation method? It should be universal (i.e., for arbitrary $T(\nu)$), fast (faster than numerical integration) and accurate (in the sense that the maximum error is guaranteed to be smaller than a certain prescribed bound). Such a method is outlined after a brief presentation of other approaches known from the literature.

Existing approaches: analytical formulas, numerical integration or approximation

- **Analytical formulas**: For unsaturated Lorentzian absorption lines, closed-form analytical formulas exist for harmonic spectra [71, 73, 83], which simplify signal processing in these cases where they can be applied [20, 28, 54, 55, 84]. Harmonic spectra for the dispersion Lorentzian line shape (Hilbert transform of Lorentzian spectrum) is also known in closed form [85]. Lines in the mid-infrared at atmospheric pressure have a Lorentzian shape to a very good approximation.

  Disadvantages: Not applicable to saturated or Voigt shaped lines.

  Advantages: Fast and exact computation.

- **Numerical integration**: If analytical formulas for the specific line shape are unavailable it is a common method to use numerical integration of the Fourier integral [20, 73, 74, 86–91]. Whereas in Ref. [90] a FFT approximation is used, i.e., the uniform discretization of the integral (with respect to z) and its evaluation as a simple sum. Also numerical Gauss-Chebyshev integration of the convolution expression for harmonic spectra Eq. (3.32) is used [92, 93]. Note that in the literature it was not observed that these two approaches are mathematically equivalent[8].

  Disadvantages: Computational expensive, many evaluations of $T(\nu)$ are needed.

  Advantages: Accurate (error can be made smaller than any prescribed bound).

- **Approximation by truncated infinite series:** For arbitrary line shapes infinite series expansions are available (see Eq. (3.31)), but these do not converge for all practically important cases as mentioned before [73]. See section B.4 for a summary of the necessary n-th derivatives of common line profiles. Nevertheless it is often presented in the literature (cf. section 3.3.1.vi). For the Gaussian and saturated Lorentzian line profiles infinite series expansions are available for even harmonics at line center [94] or for unsaturated Gaussian lines [95, 96].

  Disadvantages: Possibly slow or no convergence for important lines hapes. Derivatives of T needed, hence impossible to apply for measured data.

  Advantages: Simple algorithm.

- **Other approximation:** Approximation by derivatives of the profiles is also used [97, 98], but limited to low modulation amplitudes. Other approaches are based

---

[8] There the convolution integral is discretized according to the Gauss-Chebyshev rule, which can be applied for integrals with a $1/\sqrt{1-x^2}$ weighting term as it is present in Eq. (3.49). The nodes where the integrand (without weighting function) has to be evaluated is given by the Chebyshev nodes. Then the integrand evaluated at these nodes is summed up with certain weighting factors which are also determined by the Gauss-Chebyshev rule. If this is simplified the same expression as uniform discretization of the Fourier integral expression is obtained. Hence these two approaches are equivalent.

on approximation of the harmonic spectra of a Voigt profile by a sum of Lorentz profiles for which an analytical expression is used [99, 100]. A similar approach is used in Ref. [101].

Disadvantages: Limited range of validity. Error can not be controlled.

Advantages: Simple algorithm

- **Frequency domain** The Fourier transform of the n-th harmonic spectrum is given by multiplication of the Fourier transform of the transmission with the Bessel function of order n (Eq. (3.36)). This simple structure allows for a fast computation of the n-th harmonic spectra in the Fourier domain. Evans et. al [102, 103] used a similar method to compute the first harmonic spectra (i.e., $n = 1$), whereas from Eq. (3.36) the general case can be derived, which allows for computation of harmonics of all orders. This has also been found by other authors [104]. The Fourier transform of the transmission in Eq. (3.36) is either computed with the help of the FFT algorithm, or in case of unsaturated Voigt lines, directly with known analytical formulas (which are briefly summarized in section B.4).

  Disadvantages: Uniform sampling and constant modulation amplitude per scan only. Error depends on choice of sampling points and is unknown a-priori.

  Advantages: All points of a spectral scan are computed simultaneously.

New method (derived in this work): The new method is based on approximation of the transmission by a piecewise polynomial from which the harmonic spectrum can be computed exactly. Spline interpolation or approximation of arbitrary degree is one possible method to obtain such a piecewise polynomial approximation. Hence, this is a very general approach. Due to the error bound Eq. (3.45) this is feasible and the computation error is very easy to control. The error bound states that the error on the harmonic spectrum is maximally $\pi/4$ times as large as the error on the transmission. Hence the problem of controlling the computation accuracy is shifted to approximation of the transmission by a suitable class of functions (piecewise polynomials in this case), which is an relatively easy task. Furthermore the method is also suitable for computation of harmonic spectra from measured transmission functions, where the maximum error on the harmonic spectrum is typically also known (e.g., measurement noise or spectral accuracy). If for example harmonic spectra with an absolute accuracy of 10^{-6} are desired, the transmission must be measured or approximated by piecewise polynomials with absolute accuracy of $\frac{\pi}{4}10^{-6} = 0.79 \times 10^{-6}$ prior to transformation to a harmonic spectrum.

The exact analytical expression for the harmonic spectrum of a piecewise polynomial transmission of arbitrary degree will be derived in the following. This includes the special case of linear, constant and arbitrary degree spline interpolation/approximation. Neither equidistant sampling on the ν values is needed nor a constant modulation amplitude ν_a. The points ν_k where the spectrum is to be computed and the modulation amplitude ν_a can be chosen freely without affecting the computation accuracy. The spline approximation of the transmission only needs to be determined once with a certain prescribed accuracy. Then harmonic spectra of arbitrary degree and with arbitrary modulation amplitude can be obtained with the desired maximum error.

The piecewise polynomial interpolation or approximation of degree k can be expressed as:

$$T(\nu) = \sum_{j=1}^{N} p_j(\nu - \nu_{j-1})\chi_{[\nu_{j-1},\nu_j)}(\nu). \tag{3.65}$$

The ν_j, $j = 0, \dots, N$ denote the breaks of the piecewise approximation, i.e., the subdivision in N sub-intervals that cover the interval $[\nu_0, \nu_N]$. The p_j symbol specifies a polynomial of degree k and χ is the characteristic function

$$\chi_{[\nu_{j-1},\nu_j)}(\nu) = \begin{cases} 1 & \nu_{j-1} \le \nu < \nu_j \\ 0 & \text{otherwise} \end{cases} . \tag{3.66}$$

The harmonic spectrum belonging to Eq. (3.65), i.e.,

$$H_n(\nu;\nu_a) = \frac{\epsilon_n}{2\pi}\int_{-\pi}^{\pi} T(\nu + \nu_\mathrm{a}\cos(z))\cos(nz)\,\mathrm{d}z \tag{3.67}$$

is analytically given by the following expression:

$$= \sum_{j=1}^{N} Q_n\left(\frac{\nu - \nu_{j-1}}{\nu_\mathrm{a}}, \boldsymbol{d}_j(\nu)\right) - Q_n\left(\frac{\nu - \nu_j}{\nu_\mathrm{a}}, \boldsymbol{d}_j(\nu)\right), \tag{3.68}$$

with the fixed function $Q_n(w, \boldsymbol{d})$:

$$Q_n(w, \boldsymbol{d}) = \frac{\epsilon_n}{\pi}\left(\sqrt{1 - w_\mathrm{C}^2}\sum_{i=0}^{n+k-1}(\boldsymbol{S}_n\boldsymbol{d})_i\,\mathrm{T}_i(-w_\mathrm{C}) + \boldsymbol{r}_n^T\boldsymbol{d}\arcsin w_\mathrm{C}\right). \tag{3.69}$$

Furthermore, the vector $\boldsymbol{d}_j(\nu)$ of the first k derivatives of polynomial segment j and w_C the number w clamped to the interval $[-1, 1]$ are defined as:

$$\boldsymbol{d}_j(\nu) = \begin{pmatrix} p_j(\nu - \nu_{j-1}) \\ p_j'(\nu - \nu_{j-1})\frac{\nu_\mathrm{a}}{2} \\ \vdots \\ p_j^{(k)}(\nu - \nu_{j-1})\frac{\nu_\mathrm{a}^k}{2^k k!} \end{pmatrix}, \qquad w_\mathrm{C} = \begin{cases} 1 & w > 1 \\ w & -1 \le w \le 1 \\ -1 & w < -1 \end{cases} . \tag{3.70}$$

See derivation C.10. The symbol $(\boldsymbol{S}_n\boldsymbol{d})_i$ denotes the $i-$th component of the result vector from the matrix vector product $\boldsymbol{S}_n\boldsymbol{d}$. The constant $(n+k) \times (k+1)$ matrix $\boldsymbol{S}_n$ and constant $(k+1)$ element vector $\boldsymbol{r}_n$ are given by:

$$(\boldsymbol{S}_n)_{ij} = \sum_{\substack{m=-j,-j+2,\\ \dots,j-2,j\\ m\neq -n}} \begin{cases} \frac{\epsilon_i}{|n+m|}\binom{j}{(m+j)/2} & i < |n+m|, |n+m| - i \text{ odd} \\ 0 & \text{otherwise} \end{cases}, \tag{3.71}$$

$$(\boldsymbol{r}_n)_j = \begin{cases} \binom{j}{(j-n)/2} & j \ge n, j - n \text{ even} \\ 0 & \text{otherwise} \end{cases}, \tag{3.72}$$

with $i = 0, \dots, n+k-1$ and $j = 0, \dots, k$.

The coefficient for the arcsin term is zero if $n > k$, which simplifies computation in this case. Then only a square root and a polynomial of degree $n+k$ has to be evaluated. Fortunately, the coefficients of the polynomial are given in the Chebyshev form, which allows for a fast and numerically stable evaluation with the Clenshaw algorithm (see section B.1). The coefficients for the Chebyshev sum are given by the vector matrix product $\boldsymbol{S}_n \boldsymbol{d}_j$. The matrix has constant elements (see below for $\boldsymbol{S}_1$ and $\boldsymbol{S}_2$) and the vector $\boldsymbol{d}_j$ just contains the derivatives of the j-th polynomial segment. This requires simultaneous evaluation of a polynomial and its normalized derivatives (i.e., $p^{(i)}(x)/i!$) which can be efficiently implemented without need for explicit differentiation [105].

The sum in Eq. (3.68) only needs to run over indices j where $\nu_{j-1} \leq \nu + \nu_a$ and $\nu_j \geq \nu - \nu_a$[9], because the two Q_n summands become equal in the other cases.

The whole process is even more simplified and possibly numerically stabilized if the transmission is given in normalized coordinates $\widetilde{T}(x) = T(\nu_a x)$ and the computation carried out with respect to x and the corresponding modulation amplitude x_a set to 1 (see section 3.3.3 on the independence of the harmonic spectrum on the unit of the frequency axis). This has the advantage that the numbers during computation of the vector $\boldsymbol{d}_j$ are not excessively small or large which improves numerical stability.

The $\boldsymbol{S}_n$ matrix and $\boldsymbol{r}_n$ vector for first and second harmonic detection $n = 1, 2$ and polynomial degrees up to $k = 7$ read:

$$\boldsymbol{S}_1 = \begin{pmatrix} 1 & 0 & \frac{10}{3} & 0 & \frac{178}{15} & 0 & \frac{1524}{35} & 0 & \frac{51218}{315} \\ 0 & 1 & 0 & \frac{9}{2} & 0 & \frac{55}{3} & 0 & \frac{875}{12} & 0 \\ 0 & 0 & \frac{2}{3} & 0 & \frac{56}{15} & 0 & \frac{598}{35} & 0 & \frac{23056}{315} \\ 0 & 0 & 0 & \frac{1}{2} & 0 & \frac{10}{3} & 0 & \frac{203}{12} & 0 \\ 0 & 0 & 0 & 0 & \frac{2}{5} & 0 & \frac{108}{35} & 0 & \frac{5416}{315} \\ 0 & 0 & 0 & 0 & 0 & \frac{1}{3} & 0 & \frac{35}{12} & 0 \\ 0 & 0 & 0 & 0 & 0 & 0 & \frac{2}{7} & 0 & \frac{176}{63} \\ 0 & 0 & 0 & 0 & 0 & 0 & 0 & \frac{1}{4} & 0 \\ 0 & 0 & 0 & 0 & 0 & 0 & 0 & 0 & \frac{2}{9} \end{pmatrix}, \qquad \boldsymbol{r}_1 = \begin{pmatrix} 0 \\ 1 \\ 0 \\ 3 \\ 0 \\ 10 \\ 0 \\ 35 \\ 0 \end{pmatrix},$$

$$\boldsymbol{S}_2 = \begin{pmatrix} 0 & \frac{4}{3} & 0 & \frac{26}{5} & 0 & \frac{416}{21} & 0 & \frac{3398}{45} & 0 \\ 1 & 0 & \frac{5}{2} & 0 & \frac{28}{3} & 0 & \frac{145}{4} & 0 & \frac{2128}{15} \\ 0 & \frac{2}{3} & 0 & \frac{12}{5} & 0 & \frac{202}{21} & 0 & \frac{1756}{45} & 0 \\ 0 & 0 & \frac{1}{2} & 0 & \frac{7}{3} & 0 & \frac{41}{4} & 0 & \frac{658}{15} \\ 0 & 0 & 0 & \frac{2}{5} & 0 & \frac{16}{7} & 0 & \frac{496}{45} & 0 \\ 0 & 0 & 0 & 0 & \frac{1}{3} & 0 & \frac{9}{4} & 0 & \frac{178}{15} \\ 0 & 0 & 0 & 0 & 0 & \frac{2}{7} & 0 & \frac{20}{9} & 0 \\ 0 & 0 & 0 & 0 & 0 & 0 & \frac{1}{4} & 0 & \frac{11}{5} \\ 0 & 0 & 0 & 0 & 0 & 0 & 0 & \frac{2}{9} & 0 \\ 0 & 0 & 0 & 0 & 0 & 0 & 0 & 0 & \frac{1}{5} \end{pmatrix}, \qquad \boldsymbol{r}_2 = \begin{pmatrix} 0 \\ 0 \\ 1 \\ 0 \\ 4 \\ 0 \\ 15 \\ 0 \\ 56 \end{pmatrix}.$$

For lower degrees as $k = 8$ the matrix/vector is simply truncated by the corresponding number of rows and column, because the entries do not depend on the maximum degree k of the piecewise polynomials.

---

[9] This is just the intervals $[\nu_{j-1}, \nu_j]$ which intersect with the interval $[\nu - \nu_a, \nu + \nu_a]$. It is obvious that the harmonic spectrum at ν can only depend on the behavior of the transmission in the interval $[\nu - \nu_a, \nu + \nu_a]$ because the modulation around ν only covers these frequencies.

3.3.6. Discussion and implications for system improvement

The convolution or filter model of WMS has a lot of implications which allow for re-interpretation of many of the advantages WMS is claimed to have over direct spectroscopy. Some of these are summarized in this section and discussed in view of this new model.

It has been found that the signal to fringe ratio of harmonic spectra can be optimized by using either non-sinusoidal modulation waveforms[10] [106], by employing higher harmonic detection ($n > 2$) [107–109] or adjustment of the modulation amplitude [110]. Additionally, increased sensitivity to density fluctuations [111, 112] or improved resolvability of overlapping lines [113] of higher order detection compared to second harmonic detection was found.

While these findings are not questioned, there can be no – or if at all only a slight – benefit in terms of more stable or more accurate sensing compared with direct spectroscopy or second harmonic detection. This is because it is possible to achieve the same effect as indicated in the literature by subsequent filtering of the transmission or second harmonic spectrum. With subsequent filtering, even more flexibility in filter design is available and there is no known reason why the inherent WMS filtering should be optimum for the specific distortions contained in measured TDLAS spectra.

This view in agreement with the observation that lower order spectra contain more information than the higher order spectra[11]. The alleged stronger or reduced sensitivity of the higher harmonic spectra to some variables is just because of the special behavior of the intrinsic filtering of WMS. For example interference fringes can be suppressed if a zero of the frequency response of the WMS filter is exactly at the inverse of the free spectral range of the interference. Different modulation waveforms have different zeros in the frequency response and hence different signal to fringe ratio may result explaining the results by Iguchi [106]. The same can be achieved by adjusting the modulation amplitude, which allows to shift a zero to any position and hence cancel arbitrary sinusoidal components (cf. results in Ref. [110]). As mentioned before, the same can be achieved by subsequent filtering of spectra (e.g., notch filtering), or better, curve-fitting with an appropriate spectral model and/or appropriate noise covariance matrix.

The previous results in literature hence do not show fundamental advantages of WMS, the same or even better results can be achieved by additional spectral filtering or proper curve-fitting.

A quantitative comparison of different spectroscopic methods will become possible with the metrics developed in section 5.1.1 with further results presented in section 5.1.3.

i. Discussion of methods for fringe reduction

In a similar manner the argument can be extended to a non WMS frame, with the general question which methods at all allow for effective fringe reduction and which

---

[10] For this non-sinusoidal WMS also a convolution or filter type model exists, because this WMS also has the linear shift invariance property. The specific filtering is of course different for each waveform.

[11] This viewpoint is supported by the recursion formula for harmonic spectra Eq. (3.39), which shows that the information content of harmonic spectra is decreasing with detection order, in the sense that the higher order spectra can be computed from the lower order spectra, but not vice versa.

not. As shown before, fringe reduction using special properties of WMS is not better than simple filtering because WMS is actually just special filtering with an adjustable free parameter. Other methods include the use of pulsed measurements [114] or second modulation, dithering or special averaging [106, 115–117].

In literature it is stated that post processing for fringe reduction can only be applied when the fringe and the desired spectral components are separated in the frequency domain [118]. While this is clearly true, it has been unnoticed that this is the limitation in the general case. All mentioned methods (WMS, pulsed measurements, double modulation, dithering) essentially implement a filtering/convolution because they also have the linear-shift invariance dependence of the detected signals on the transmission. Hence, all benefits these methods provide, can be achieved by digital filtering as well, with better or at least equal performance.

Efficient methods for fringe suppression separate the fringe and gas absorption signal in the frequency domain or spatial domain with multiple detectors [119]. The first can be done by either modulation of the fringe component while the gas absorption does not change or by change of the gas absorption and the fringe being unchanged. The first is either employed by piezo modulation of the resonator length [114] or general mechanical vibration [26] which distributes the fringe distortion in the frequency domain making it more easily filterable. The second is the employment of the Zeeman or Stark effect with which the gas absorption lines are tuned and the fringe interference remains unaffected. This effectively shifts the fringe signal to zero frequency, where it is also easily filtered. These consideration was the rationale for development of a method based on the Zeeman effect in section 4.3.

ii. Difference of wavelength modulation spectroscopy realized with VCSELs or edge-emitters

Obviously the approximation from Eq. (3.62) to Eq. (3.63) can only be made because the relative intensity variation (more precisely the first harmonic P_1/P_0) is very low for VCSELs. The question is why in sensors this relative power modulation is different for DFB lasers and VCSELs. The answer is the different bias point current relative to threshold and laser roll-over. For low relative power modulation the laser should be operated as high as possible above threshold close to or at the thermal roll-over, so that the mixing terms in the spectral model become negligible[12]. Due to their higher power these operation conditions may not be desired or possible to reach with DFB lasers, which have in this case a disadvantage over VCSELs. There are no fundamental differences between DFBs and VCSELs, but between laser wavelengths: GaAs based lasers have much lower relative modulation amplitudes than higher wavelength lasers (see Tab. 3.1).

Detailed explanation: If for both laser types self-heating is neglected this normalized first harmonic is inversely proportional to current, i.e.,

$$\frac{P_1(I)}{P_0(I)} = \frac{\eta_e \Delta I}{\eta_e (I - I_{\mathrm{th}})} = \frac{\Delta I / I_{\mathrm{th}}}{I/I_{\mathrm{th}} - 1}. \tag{3.73}$$

---

[12] Strictly speaking this may just be true for ambient conditions, because the relative magnitudes depends on the modulation amplitude ν_{a}. If this is significantly larger than typical, the mixing products may not be neglected even at roll-over, because P_1/P_0 may always be too large.

This value is influenced by the following

- The normalized modulation amplitude $\Delta I/I_{\mathrm{th}}$. The value of ΔI depends on the laser tuning coefficient (at the modulation frequency) because the frequency modulation amplitude ν_{a} is predetermined (given by width of the gas line). This value is the same for VCSELs and DFBs but different at different wavelength.
- The normalized bias point I/I_{th}. For DFBs this can be as low as $I/I_{\mathrm{th}} = 1.5$ [120]. According to Tab. 3.1 maximum values are in the range 2 to 4 depending on the wavelength, while VCSELs have values of 3.3 to 6.5. These may be even exceeded because operation at roll-over or beyond is possible for VCSELs since these do not suffer from catastrophic optical damage.
- Deviation from the simplified laser model. Self-heating effects cause the the formula to typically over-estimate P_1 close to roll-over (cf. experiment in Fig. 3.12).

λ	VCSEL		DFB		Ref.
	$\Delta I/I_{\mathrm{th}}$	$I_{\max}/I_{\mathrm{th}}$	$\Delta I/I_{\mathrm{th}}$	$I_{\max}/I_{\mathrm{th}}$	
763 nm	$\frac{20\,\mu\mathrm{A}}{0.6\,\mathrm{mA}} \approx 0.033$	$\frac{2\,\mathrm{mA}}{0.6\,\mathrm{mA}} \approx 3.3$	$\frac{0.6\,\mathrm{mA}}{15\,\mathrm{mA}} = 0.04$	$\frac{30\,\mathrm{mA}}{15\,\mathrm{mA}} = 2$	[121, 122]
2 µm	$\frac{266\,\mu\mathrm{A}}{1.6\,\mathrm{mA}} \approx 0.17$	$\frac{10.5\,\mathrm{mA}}{1.6\,\mathrm{mA}} \approx 6.6$	$\frac{4\,\mathrm{mA}}{25\,\mathrm{mA}} = 0.16$	$\frac{100\,\mathrm{mA}}{25\,\mathrm{mA}} = 4$	[123]

Tab. 3.1: *Comparison of laser parameters that influence the relative power modulation P_1/P_0 for DFBs and VCSELs (see simplified model Eq. (3.73)).*

3.4. Parameter extraction from measured data

The aim of this section is to provide the basic tools with which signal processing methods can be analyzed to improve the overall sensing performance. Signal processing is understood here as the process of extraction of target data values from measured spectra. It depends on, but is distinct to the detection method which defines how the measured spectra/signals are related to the optical transmission.

First, certain definitions and a notation needs to be developed. In section 3.4.1 the extraction of parameters using least squares curve-fitting is described and section 3.4.2 a filter model of the fits behavior for perturbations is presented.

Single scan The sensor can be regarded as a black-box that performs a measurement on the optical transmission $T(\nu)$ of the cell including the gas. A single scan probes the transmission and outputs a value which represents the gas concentration $\widehat{C}_{\mathrm{mol}}$ or gas number density value $\widehat{n}_{\mathrm{mol}}$. For better comparison of sensors in this thesis the output values are normalized to the gas peak absorbance $\widehat{a}_{\mathrm{mol}}$. This was chosen for the sensor output values to become independent of optical path length L and absorption line strength:

$$\widehat{C}_{\mathrm{mol}} = \frac{1}{\alpha_{\mathrm{pk}} L} \widehat{a}_{\mathrm{mol}}, \qquad \widehat{n}_{\mathrm{mol}} = \frac{1}{\sigma_{\mathrm{pk}} L} \widehat{a}_{\mathrm{mol}}. \tag{3.74}$$

$\widehat{a}_{\mathrm{mol}}$: Sensor output value in terms of peak absorbance (unit: 1),
$\widehat{C}_{\mathrm{mol}}$: Sensor output value in terms of concentration (unit: 1 or L/L),
$\widehat{n}_{\mathrm{mol}}$: Sensor output value in terms of number density (unit: $1/\mathrm{cm}^3$),
α_{pk} : Target gas peak absorption coefficient (unit: 1/cm),
σ_{pk} : Target gas peak absorption cross section (unit: cm^2),
L : Gas cell optical path length (unit: cm).

This sensing process consists of the spectral measurement and subsequent signal processing for data extraction. This is written in this thesis in the abstract notation:

$$\widehat{a}_{\mathrm{mol}} = \mathrm{SENS}\{T(\nu)\} = \mathrm{EXTRACT}\left\{\mathrm{DETECT}\{T(\nu)\}\right\}. \tag{3.75}$$

The optical transmission $T(\nu)$ depends on physical gas parameters like C_{mol}, pressure p, temperature T and optical path length L. Due to measurement noise, the sensor output values are only estimates (denoted with a hat accent) differing from the true physical values (denoted without hat accent). Any sensor can be written in this way even if the sensor output values are directly concentration values or number densities. Then Eq. (3.74) serves as a definition for $\widehat{a}_{\mathrm{mol}}$. The gas absorbance values are the relevant quantity to compare the signal processing performance because they are independent on the gas absorption line strength and optical path length.

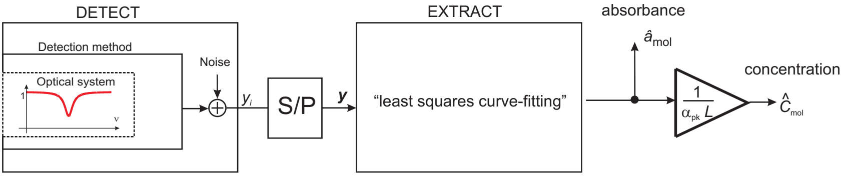

Fig. 3.13: *Sensor schematic for a single scan. The detection method generates the measurement signals from the optical transmission function. Samples y_i (measurements at different optical frequencies) are grouped to a scan vector and processed using curve-fitting to obtain the absorbance of the target gas.*

During each measurement cycle the detection method generates a single scan consisting of N samples (usually at different optical frequencies) which are grouped into the scan vector $\boldsymbol{y} = (y_1, \ldots, y_N)$:

$$\boldsymbol{y} = \mathrm{DETECT}\{T(\nu)\}. \tag{3.76}$$

y_i : Sample i of the spectral scan (unit: 1),
$\boldsymbol{y}$: Vector of all samples of the spectral scan (elements: y_i, size: N) (unit: 1),
N : Number of samples per scan (unit: 1).

This vector depends on the transmission function (dependency defined by the detection method) and the non-ideality of the sensor hardware (e.g., laser wavelength or intensity variation during tuning). For direct spectrometry and wavelength modulation spectrometry the measurement could be modeled by

$$\begin{aligned} y_i &= P_i\, T(\nu_i) + \epsilon_i, && \text{for “direct spectrometry”},\\ y_i &= P_i\, (T * K_{\mathrm{wms}})(\nu_i) + \epsilon_i, && \text{for “wavelength modulation spectrometry”}, \end{aligned}$$

with ν_i being the frequency points where the transmission is sampled, P_i the corresponding laser emission power, ϵ_i random variables representing measurement noise and K_{wms} the WMS filter kernel from Eq. (3.33).

The parameter extraction then obtains the wanted information from the measurement:

$$\widehat{a}_{\mathrm{mol}} = \mathrm{EXTRACT}\{\boldsymbol{y}\}. \tag{3.77}$$

Usually this is implemented by employing least squares curve-fitting with an appropriate model (denoted by $\boldsymbol{f}(\ldots)$)

$$\widehat{a}_{\mathrm{mol}} = \underset{a_{\mathrm{mol}},\theta_2,\ldots}{\operatorname{argmin}} \; |\boldsymbol{y} - \boldsymbol{f}(a_{\mathrm{mol}}, \theta_2, \ldots)|^2 \,. \tag{3.78}$$

The θ_j are nuisance parameters, i.e., unknown parameters that are not of interest but have to be determined in the curve-fitting because the measurement signal data depends on it. The signal model reflects the designers assumptions and knowledge on the measured signals and how it is assumed that they change with the wanted quantity. It depends on the detection method and also contains the assumptions about the random measurement distortion, i.e., the noise influence and the noise statistics.

For all data processing strategies (also other than curve-fitting) there exists a signal model. Also for heuristic data extraction there must be such a signal model, even if it is neither explicitly needed nor explicitly formulated during algorithm design. For example second harmonic center detection has the implicit signal model that the laser emission frequency is the same as the line center, modulation index (i.e., modulation amplitude divided by line-width) stays constant, attenuation is equal to absorbance (implies that there are no fringes) and there is no spectral baseline. The noise is uncorrelated to the analytic signal, additive and of zero mean. If the sensor system deviates from these assumptions systematic errors in the extracted values are likely to occur. These problems could then display as drift or instability over longer times. Quantification of such problems is possible with the Allan plot (see section B.5).

Repeated scans During sensor operation the scans take time $\Delta t = 1/R$ and are repeated with the rate R (unit: Hz). See Fig. 3.14 for an illustration of the signals and the corresponding timing. Hence a stream of values

$$\boldsymbol{y}(k) = \mathrm{DETECT}\{T(\nu; t = t_0 + k/R); \Delta t = 1/R\}, \tag{3.79}$$

$$\widehat{a}_{\mathrm{mol}}(k) = \mathrm{EXTRACT}\{\boldsymbol{y}(k)\}, \tag{3.80}$$

each corresponding to the physical situation at time instants $t = t_0 + k/R$, is obtained. It is convenient to concatenate the measurement vectors (with N samples each) to a stream of scalar values with rate RN

$$y(l) = y_i(k), \qquad i + kN = l. \tag{3.81}$$

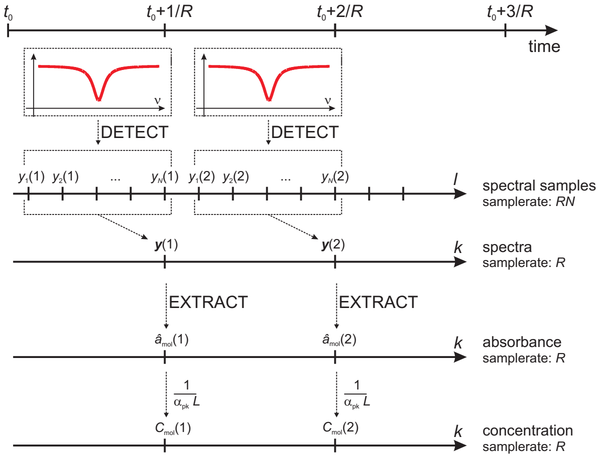

Fig. 3.14: *Depiction of sensor signals and their timing.*

3.4.1. Fundamentals: Signal model and least squares curve-fitting

The aim of this section is to develop an appropriate description of the parameter extraction by curve-fitting. The following variables (extra to the in Eq. (3.76)) are used:

I_i : Independent variable belonging to the i-th sample (unit: n/a),
θ_i : Unknown model parameter i (unit: n/a),
$\boldsymbol{\theta}$: Vector of unknown model parameters (unit: n/a),
$f(I, \boldsymbol{\theta})$: Analytic signal model (unit: 1),
ϵ_i : Random variable representing noise on i-th sample (unit: 1),
$\boldsymbol{\epsilon}$: Vector of random variables representing measurement noise (unit: 1),
$\boldsymbol{W}$: Matrix with covariance structure of the noise (unit: 1),
S_{yy} : Noise spectral density on y (unit: 1/Hz)

i. The signal model

The measured scan consist of N points which are denoted as y_i and the P unknown parameters are grouped in the vector $\boldsymbol{\theta} = (a_{\text{mol}}, \theta_2, \ldots, \theta_P)^T$. The noise is described by the random variable ϵ_i and the model for the analytic signal by $f(I, \boldsymbol{\theta})$:

$$y_i = f(I_i, \boldsymbol{\theta}) + \epsilon_i, \qquad \text{Cov}\{\epsilon_i, \epsilon_j\} = \sigma^2 w_{ij},\ i, j = 1, \ldots, N \tag{3.82}$$

or in vector notation

$$\boldsymbol{y} = f(\boldsymbol{I}, \boldsymbol{\theta}) + \boldsymbol{\epsilon}, \qquad \text{Var}\{\boldsymbol{\epsilon}\} = \sigma^2 \boldsymbol{W}. \tag{3.83}$$

The values of the independent variable I_i are strictly speaking not important – they are just added for convenience because the TDLAS signal models can be compactly written using this form. If the laser is tuned by current, then these I_i could represent the laser current of the spectral sample y_i in an appropriate unit (e.g., mA or DA converter digits). Writing $\boldsymbol{f}(\boldsymbol{\theta}) = \begin{pmatrix} f(I_1, \boldsymbol{\theta}) & \dots & f(I_N, \boldsymbol{\theta}) \end{pmatrix}^T$ instead of $f(\boldsymbol{I}, \boldsymbol{\theta})$ is equally valid. The signal model can be empirical (e.g., by using recorded spectra from a reference channel [124]) or adaptive (i.e., change during sensor operation) [124, 125].

Noise correlation properties and the noise spectral density The matrix $\boldsymbol{W}$ (elements w_{nm}) with the noise covariance structure and noise variance $\sigma^2(y)$ are completely determined from the (single sided) noise spectral density on the spectrum $S_{yy}(f)$:

$$w_{nm} = 2 \int_0^{1/2} \frac{S_{yy}(\Omega R N)}{\overline{S}_{yy}} \cos\left(2\pi\Omega(n-m)\right) \mathrm{d}\Omega, \quad \overline{S}_{yy} = 2 \int_0^{1/2} S_{yy}(\Omega R N) \mathrm{d}\Omega. \tag{3.84}$$

See derivation C.11. The total noise variance is given by $\sigma^2(y) = RN/2\,\overline{S}_{yy}$. In case of white noise ($S_{yy}(f) = \overline{S}_{yy}$) this reduces to $\boldsymbol{W} = \boldsymbol{I}$. Note that RN is the sampling rate with which the spectrum is discretized and the integrations are carried out between zero and positive Nyquist frequency. These only conver the positive frequency part because the engineering convention of a one-sided spectral density is assumed.

Example signal model For example, the signal model for a gas sensor employing WMS second harmonic detection could be given by the following substitutions:

I_i	laser current for the i-th spectral sample
$y_i = S_2(I_i)/S_0(I_i)$	normalized detector signal
$\boldsymbol{\theta} = (a_{\text{mol}}, \text{ofs}, \text{slope})^T$	unknown gas and linear baseline parameters
$f(\boldsymbol{I}, \boldsymbol{\theta})$	model Eq. (3.61)
$\epsilon_i \overset{\text{i.i.d}}{\sim} \mathcal{N}(0, \sigma^2)$, $\boldsymbol{W} = \boldsymbol{I}$	normally distributed, independent (white) noise
$N = 64$	Number of points per spectrum

The following parameters are not part of the signal model but are stated for completeness:

$R = 1 \dots 10\,\text{Hz}$,	Measurement rate
$\overline{S}_{yy} = 10^{-14} \dots 10^{-12}\,\text{Hz}^{-1}$,	Noise spectral density.

ii. Least squares fit parameter extraction

Because the measurement data are superimposed with random noise, Eq. (3.83) can not be solved for $\boldsymbol{\theta}$ (even if $\boldsymbol{f}$ can be solved for $\boldsymbol{\theta}$) so the extraction is impossible in an exact way. The best one could expect is to obtain an estimate $\widehat{\boldsymbol{\theta}}$ as close as possible to the "true" parameters $\boldsymbol{\theta}$.

A very important estimation method is the (generalized) least squares estimation in which case the estimate $\widehat{\boldsymbol{\theta}} = \widehat{\boldsymbol{\theta}}(\boldsymbol{y})$ is obtained by

$$\widehat{\boldsymbol{\theta}}(\boldsymbol{y}) = \underset{\boldsymbol{\theta}}{\operatorname{argmin}} \left\{ (\boldsymbol{y} - \boldsymbol{f}(\boldsymbol{\theta}))^H \boldsymbol{W}^{-1} (\boldsymbol{y} - \boldsymbol{f}(\boldsymbol{\theta})) \right\}. \tag{3.85}$$

This method is frequently employed and is known as curve-fitting or nonlinear regression. In case of a linear model the least squares estimate has a closed form expression [126]

$$\widehat{\boldsymbol{\theta}}(\boldsymbol{y}) = (\boldsymbol{F}^H \boldsymbol{W}^{-1} \boldsymbol{F})^{+} \boldsymbol{F}^H \boldsymbol{W}^{-1} \boldsymbol{y}, \qquad \text{for } \boldsymbol{f}(\boldsymbol{\theta}) = \boldsymbol{F}\boldsymbol{\theta}, \tag{3.86}$$

with $\boldsymbol{F}$ the observation matrix for the linear model. The symbol $^+$ specifies the Moore-Penrose pseudoinverse matrix (for definition and properties see section B.2). In the TDLAS literature often the simplified formula with $\boldsymbol{W} = \boldsymbol{I}$ and the regular inverse instead of the pseudoinverse is given. The form here has the advantage that it is also valid if components to nuisance parameters are linearly dependent [126].

For a nonlinear model the least squares estimate has to be determined by iterative algorithms such as the Levenberg-Marquardt algorithm. Computation of the least squares estimate is a standard procedure [127] and will not be covered in this thesis.

iii. Error propagation of the least squares estimate

The sensitivity of the fitted parameters to certain small perturbations on the measured spectrum $\Delta\boldsymbol{y}$ is needed, i.e.,

$$\Delta\widehat{\boldsymbol{\theta}} = \widehat{\boldsymbol{\theta}}(\boldsymbol{y} + \Delta\boldsymbol{y}) - \widehat{\boldsymbol{\theta}}(\boldsymbol{y}). \tag{3.87}$$

Using first order perturbation theory one can derive from Eq. (3.85):

$$\Delta\widehat{\boldsymbol{\theta}} \approx (\boldsymbol{F}(\boldsymbol{\theta})^H \boldsymbol{W}^{-1} \boldsymbol{F}(\boldsymbol{\theta}))^{+} \boldsymbol{F}(\boldsymbol{\theta})^H \boldsymbol{W}^{-1} \Delta\boldsymbol{y}. \tag{3.88}$$

See derivation C.12. This is formally the same equation as for the linear fit Eq. (3.86), so for small changes the nonlinear fit behaves the same as the linear fit. The observation matrix $\boldsymbol{F}$ of the linear model has just to be replaced by the Jacobian matrix of the nonlinear model: $\boldsymbol{F}(\boldsymbol{\theta}) = (\nabla \boldsymbol{f}(\boldsymbol{\theta})^T)^T$. For the linear model the Jacobian matrix is equal to the observation matrix $\boldsymbol{F}$ and, hence, usage of the same symbol is justified.

The result is easily understood. The nonlinear fit behaves differently at different "operation conditions", i.e., at different parameter estimates $\widehat{\boldsymbol{\theta}}$, around of which the fluctuation $\Delta\widehat{\boldsymbol{\theta}}$ occurs. The noise on the fitted parameters depends on these operation conditions.

3.4.2. Digital filter model for the curve-fit

The result of the previous sections allows to interpret the (linear or nonlinear) least squares curve-fit as a filter with following decimation. It relates small perturbations on the spectrum ($\Delta\boldsymbol{y}$ or $\Delta y(l)$) to differences on the fitted parameters ($\Delta\widehat{\boldsymbol{\theta}}$). In section 5.1.1.iii it will be shown experimentally that this perturbation description allows for correct modeling of the noise behavior of TDLAS sensors. The current operating point is denoted as $\boldsymbol{y}$ and $\boldsymbol{\theta}$. The dependence on $\boldsymbol{\theta}$ is suppressed in the following small signal analysis because the operation point $\boldsymbol{\theta}$ is fixed.

From Eq. (3.88) a small perturbation Δy on the spectrum causes a perturbation of the gas absorbance of

$$\Delta\widehat{a}_{\mathrm{mol}}(k) = \sum_{m=0}^{N-1} h(m)\Delta y(kN - m) = (h * \Delta y)(kN), \tag{3.89}$$

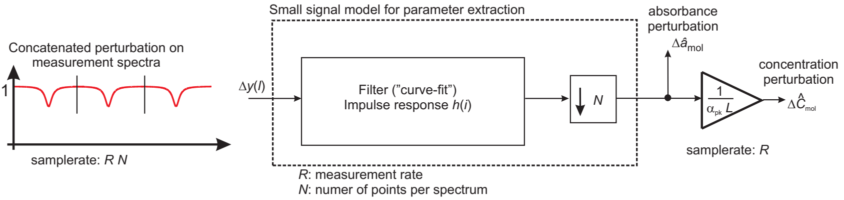

Fig. 3.15: *The filter model for the curve-fit. The change on the measurement samples* $\Delta y(l)$ *(each* N *belonging to a separate spectrum) are the input of the curve-fitting routine and the output is change of the peak absorbance* $\Delta\widehat{a}_{mol}$*. For the linear case this model is exact and for the non-linear case it depends on the current sensor operation point and holds for perturbations.*

with $h(l) = h(l, \boldsymbol{\theta})$ the reverse of the first row of the matrix in Eq. (3.88):

$$h(l) = ((\boldsymbol{F}^H \boldsymbol{W}^{-1} \boldsymbol{F})^{+} \boldsymbol{F}^H \boldsymbol{W}^{-1})_{1,N-l+1}, \qquad l = 0, \ldots, N-1. \tag{3.90}$$

This $h(l)$ is the impulse response of the filter describing the small signal behavior of the fit. Eq. (3.89) is a convolution or filtering of the stream of spectral samples $\Delta y(k)$ and a subsequent N-fold decimation (i.e., selection of every N-th sample, giving one output sample per input scan). This is depicted in Fig. 3.15.

Independence of h from certain linear parameters Due to the non-linearity of the fit the filter generally depends on the current operation point $\boldsymbol{\theta}$, i.e., the parameters around which the linearization is carried out. Because the number of parameters (3 to 10) is high, a theoretical judgment or performance optimization can be a complicated task. Fortunately, the filter response is independent on parameters θ_i which enter the signal model linearly and from which the first row of the Jacobian is independent, i.e.,

$$\frac{\partial \boldsymbol{F}}{\partial \theta_i} = \boldsymbol{F}\boldsymbol{D}, \text{ with } \boldsymbol{D} \text{ diagonal matrix, } D_{11} = 0 \qquad \Rightarrow \qquad \frac{\partial h(l)}{\partial \theta_i} = 0. \tag{3.91}$$

See derivation C.13. This is for example the case for the gas absorbance at unsaturated optical conditions ($\theta_i = \theta_1 = a_{\mathrm{mol}}$) and additive baseline parameters like offset or slope (with θ_i as a baseline parameter). The behavior of the sensor then only has to be quantified with the remaining model parameters being varied. Linear parameters which enter the model in the way as in Eq. (3.91) can be set to arbitrary values, because the fits small signal behavior does not depend on the average values of linear parameters.

Range of validity of the small perturbation approximation It is clear, that the model must be valid for small relative changes on the parameters $\Delta\boldsymbol{\theta}$, but it gives no information on how large this range may be. In section 3.4.3 it will be explained that this region of validity corresponds to the region where the curve-fitting is also the optimum method.

3.4.3. Optimality of curve-fitting

It is not clear a-priori if least squares fitting (minimization of the difference between measurement and model) also corresponds to a minimum distance between estimated parameters $\widehat{\boldsymbol{\theta}}$ and their true values $\boldsymbol{\theta}$.

This can be answered for the class of unbiased estimators. This means that the expected value of the parameter estimation is equal to the true parameter value ($\mathrm{E}\,\widehat{\boldsymbol{\theta}} = \boldsymbol{\theta}$).

There is no unbiased estimator that has a lower variance than the of least squares curve-fitting with Gaussian noise. In this case the minimum squared errors on the measured spectrum directly translate to a minimum variance on the extracted parameters. For linear models this is valid for Gaussian noise with arbitrary amplitude and for nonlinear models for the limit of "small" Gaussian noise.

The detailed explanation is:

- For a linear model with white or non-white (i.e., correlated) noise the (generalized) linear least squares estimator (as presented in the last section) has the lowest variance of all linear unbiased estimators ("BLUE" property) [128]. In the limit of "low noise" or normally distributed errors of arbitrary amplitude the estimator is optimum among all (possibly nonlinear) estimators because then it achieves the Cramér-Rao lower bound ("asymptotically efficient" and "efficient" property) [126].
- In case of a non-linear model with (possibly correlated) noise the generalized nonlinear least squares estimator is optimum for "low noise" and normally distributed errors ("asymptotically efficient" and "asymptotically unbiased"). For a large number of measurement points, or equivalently, vanishing noise at fixed number of measurement points, the non-linear curve-fit behaves the same as if it was linearized and in this case has same properties [127].

The "efficient" property means that the Cramér-Rao lower bound for the variance is attained. In that case there is no other unbiased estimator with a lower variance.

The above low noise assumption for optimality is usually fulfilled in a sensing application because the relative noise on the sensor output values is low. The experimental proof that the non-linear fit attains, for typical sensor operation conditions, the Cramér-Rao lower bound is shown in section 5.1.1.iii.

4. Newly developed methods

This chapter deals with the development of new methods for diode laser spectroscopy sensors to overcome limitations of existing methods. This is based on the understanding obtained in chapter 3 on modeling of wavelength modulation spectroscopy (WMS) and the hollow fiber based cell.

The first covers identification of the wavelength scale from measured spectra (section 4.1). It has been applied in the CO sensor [54, 129] (section 5.4) and the CO_2/H_2O sensor [55] (section 5.3). This method allows for a much more compact realization of sensors because the usual separate reference cell can be replace by a in-line reference cell.

The second method is multi-harmonic detection for WMS systems (section 4.2). Two multi-harmonic detection methods for WMS systems are presented and compared: simultaneous curve-fitting of multiple harmonic spectra and reconstruction of the transmission from harmonic coefficients. The latter is a method based on the WMS modeling results in section 3.3.

The third topic is Zeeman modulation spectrometry inside a multi-mode hollow capillary waveguide (section 4.3) for improved suppression of the fiber spectral background. The fiber background was analyzed in section 3.2.3 and in section 3.3.6 it was concluded that broad band fringes can not be effectively suppressed by signal processing. Compared to wavelength modulation spectrometry the advantage of Zeeman modulation spectrometry is insensitivity to interference by multi-mode propagation in the fiber and absorption by other non-paramagnetic gases, which should enhance both sensor stability and sensitivity. Experimental and theoretical results are presented, showing the feasibility of the approach.

The chapter is partly based on the following publications:

- A. Hangauer *et al.*, “Laser wavelength stabilization using gases with complex spectral fingerprint”, in *International Conference on Field Laser Applications in Industry and Research*, Garmisch-Partenkirchen, Germany, 2009, p. 44,
- A. Hangauer *et al.*, “Multi-harmonic detection in wavelength modulation spectroscopy systems”, *Appl. Phys. B: Lasers Opt.*, 2012. DOI: `10.1007/s00340-012-5049-y`,
- A. Hangauer *et al.*, “Feasibility study of Zeeman modulation spectrometry with a hollow capillary fiber based gas cell”, *Opt. Lett.*, vol. 37, no. 7, pp. 1265–1267, Apr. 2012. DOI: `10.1364/OL.37.001265`.

4.1. Laser wavelength stabilization

Motivation and limitation of existing methods For tunable laser spectroscopy applications precise knowledge of the laser emission wavelength during spectral measurement is necessary. A common method is to apply line-locking where the laser wavelength is stabilized using laser current or laser heat-sink temperature adjustments to match a specific absorption line [133] (see Fig. 4.1a). But with this method both the linear and nonlinear tuning coefficients of the laser remain unknown, which are, however, required in the spectral model for curve fitting. Also the absolute width of absorption lines (HWHM) can not be determined without further assumptions on the laser behavior. In cases where this is critical, reference etalons are usually used [134]. However, etalons alone do not allow for determination of the absolute wavelength, only the wavelength shift during a spectral scan can be determined. Furthermore, the reference etalon method and – for trace gas applications – the line locking method require the use of beam splitters and a second photodetector, because if a cuvette with the target gas or an etalon would be placed in the main absorption path, reliable and sensitive gas detection would no longer possible.

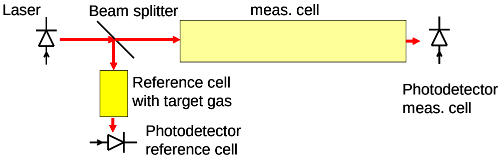

(a) Conventional reference cell with separate cuvette

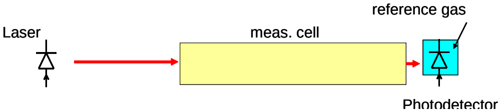

(b) Integrated reference cell (new)

Fig. 4.1: *Reference cell designs.*

Proposed new method These disadvantages can be overcome when a cuvette with a second absorbing gas is placed in the main absorption path and the absorption lines of the second gas serve as wavelength markers (see Fig. 4.1b). This allows for determination of the absolute wavelength scale, including wavelength offset, linear and nonlinear tuning coefficients of the laser. Due to their wide current tunability, VCSELs are predestined for this application. The signal processing for identification of the wavelength scale from a broad second harmonic spectrum (several nm) is briefly outlined here for CO detection at 2.3 µm with CH_4 as reference gas. The basic blocks of a WMS sensor system are shown in Fig. 4.2. The lock-in amplifier is operated at twice the modulation frequency and outputs the (peak) amplitude of the second harmonic component of the detector signal. In case of an analog lock-in realization the amplified and zero shifted data is digitized and buffered to form groups of separate spectral scans. In a digital realization the A/D conversion takes place after amplification of the detector current but the basic functions are the same as shown in Fig. 4.2.

1. After initial (rough) estimation of the spectral baseline the spectrum is normalized with respect to the incident laser power. This is done by division by the zeroth harmonic, which is a good approximation to the incident laser power when the absorbance is small.

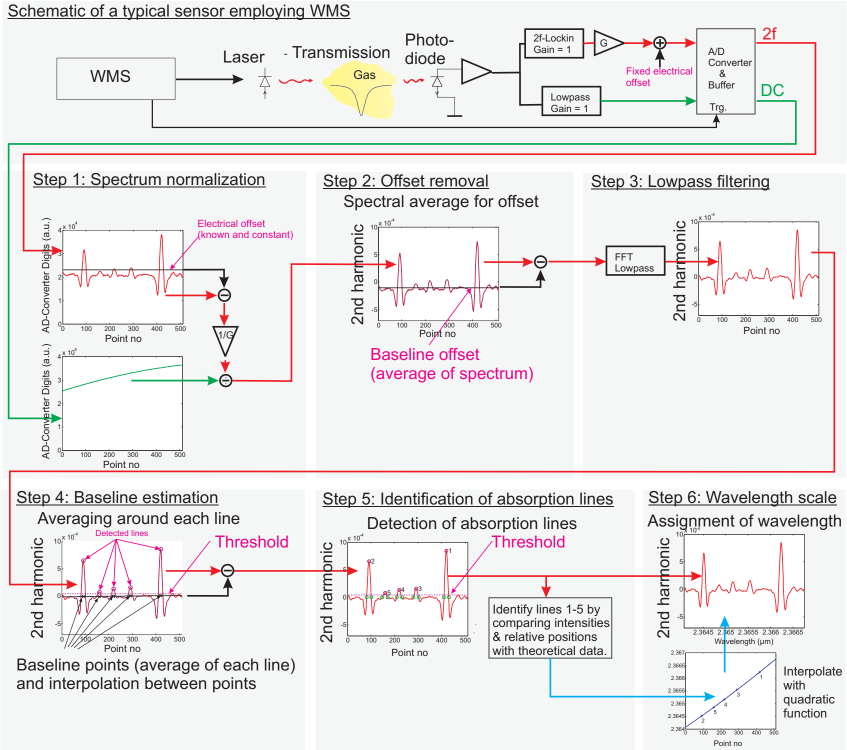

Fig. 4.2: *Wavelength identification scheme.*

2. By computing the average of all spectral points the baseline offset is estimated. It is caused by the laser RAM (residual amplitude modulation), i.e. the “curvature” of the PI characteristic. Theoretically, harmonic spectra have a mean value of zero.
3. DFT filtering. After transforming the data with the discrete Fourier transform (DFT) the frequency components above a certain frequency are set to zero and the data is transformed back. This effectively removes high-periodicity interference and noise, which would hinder detection of the absorption lines in step 4 and 5).
4. With a fixed threshold, absorption lines are detected. Since the y-unit of the harmonic spectrum directly relates to absorbance, this threshold is independent of laser power and absolute optical transmission value and is proportional to the peak absorbance caused by the known minimum concentration of the gases. Symmetric averaging around each line is used to determine the local baseline offset (red marked area). This uses the fact that the second harmonic spectrum always has a mean value of zero regardless of the physical line shape (see section 3.3.3.i). Then the linear or quadratic spectral baseline is interpolated and subtracted.

This refines the baseline estimation in step 2. This is necessary because the offset caused by laser RAM typically increases with current.

5. Due to the updated baseline, detection of the spectral peaks using a threshold is carried out again. The relative position and relative strength of the peaks is then compared with theoretical data from the HITRAN database [19] and the detected peaks are assigned to HITRAN lines.
6. A second order polynomial fit with the theoretical wavelength data and positions of the maxima is done to interpolate the full wavelength scale. Finally the second harmonic spectrum is obtained. The determined relationship between laser current and wavelength (the laser current for each spectral sample must be known) is stored and used for subsequent curve-fitting.

   Practically, the presented method is used periodically (every few seconds) to recalibrate the wavelength scale, whereas the actual concentration measurement is done with narrow spectral scans that only cover the absorption line of the gas of interest [135].

This method is universal and can also at be used at other wavelengths, e.g., for CO_2 and H_2O detection at 2.004 µm which is implemented in the sensor presented in section 5.3.

4.2. Multi-harmonic detection

In a WMS system the harmonic spectra have to be analyzed instead of the absorption spectrum itself. This can be done either by curve-fitting to an appropriate spectral model or by heuristic evaluation of the spectrum at a single frequency point. The single point evaluation is only suitable for spectral models with a single parameter. Nevertheless it is employed as detection of the maximum value of the second harmonic in a frequent number of applications due to its simple signal processing. There the sensor parameters which are not determined by the spectral evaluation are assuming to have specific values or are determined in a one-time calibration. For more realistic spectral models that include e.g., a variable spectral baseline or laser emission frequency change this is not suitable and a such drifts could not be compensated with single point detection, which is the reason for employing curve-fitting instead [136].

There are (theoretically) infinitely many harmonic spectra or harmonic components which all could be used to extract the desired information. For single-harmonic detection the signal energy that arrives at the photodetector is not fully utilized, whereas theoretically complete utilization of the signal energy should enable an improved sensing [70, sec 10.4]. Furthermore, there is no or only very little additional effort to detect the higher harmonic components if a digital lock-in technique is utilized. Therefore **multi-harmonic detection** should therefore be a simple way to increase sensitivity or versatility of the WMS technique. However, it is not a standard approach in the literature. Note, that this multi-harmonic detection assumes a sufficiently wideband detection, which standard photodetetors always provide. Systems with an inherent resonant/narrowband detection method like photoacoustic spectroscopy [137] may not benefit from multi-harmonic detection. Optical systems based on cavities (e.g., ICOS) have limited bandwidth since the light buildup and decay in the optical cavity is not arbitrarily fast. This sets limits on the maximum number of harmonics that can be detected and/or the maximum modulation frequency.

Two different multi-harmonic detection methods have to be distinguished:

- the simultaneous curve-fitting of harmonic spectra, or
- evaluation of a plurality of harmonic components at a single spectral frequency.

The harmonics at a single frequency ν_0 contain all information about the shape of the absorption line (see Fig. A.7), so in principle these should allow for extraction of all extractable parameters and not only for the peak absorbance with single-harmonic detection. Multi-harmonic detection at a single frequency was first proposed in Ref. [138], with an empirical approach by relating the ratios of the n-th harmonic components to the absorption line parameters, like half-width, center wavelength or peak absorbance. Drawback of the method is that it requires an empirical calibration. This will be improved here to an exact method where the full absorption line profile can be recovered. This method is exact and therefore allows for curve-fitting to an arbitrary spectral model which is used for direct spectroscopy. Both methods are also suitable for saturated lines, i.e., thick optical sample conditions where the linearization of the Lambert-Beer law does not hold anymore. These methods will be presented, analyzed and finally compared.

In the sections below the following questions will be answered:

- How to implement multi-harmonic detection?
- How many harmonics are needed?
- Performance compared to single-harmonic detection?
- Performance compared to direct spectroscopy?

4.2.1. Method 1: reconstruction of the transmission

A reconstruction method that combines the harmonics at a single frequency ν_0 (i.e., no spectral scanning) can be derived as follows.

i. Theoretical background

In section 3.3.3.v a reconstruction formula for the transmission function from harmonic coefficients was derived:

$$T(\nu) = \sum_{n=0}^{\infty} H_n(\nu_0)\,\mathrm{T}_n\left((\nu-\nu_0)/\nu_\mathrm{a}\right), \tag{4.1}$$

with $\mathrm{T}_n(x) = \cos(n \arccos(x))$ the n-th Chebyshev polynomial. This reconstruction formula will serve as multi-harmonic detection scheme. Practically the right hand side of Eq. (4.1) is evaluated with a finite number of measured harmonic coefficients $S_n(I_0)/S_0(I_0)$ in place of $H_n(\nu_0)$[1]. The central laser emission frequency ν_0 should be – but is not required to be – close to the absorption line center. Because of the additional offsets on the lower order terms in $S_n(I_0)/S_0(I_0)$ due to the laser power variation (cf. Eq. (3.61)), Eq. (4.1) predicts that the obtained reconstructed data must be the same as the measurement signal obtained with direct spectroscopy. The signal model for the

---

[1] Actually, $\mathrm{Re}\left\{S_n(I_0)/S_0(I_0)\mathrm{e}^{\mathrm{i}n\phi}\right\}$ is used with ϕ being a small corrective FM phase-shift.

reconstruction method, hence, has to include, in the same way as direct spectrometry, the proper baseline due to variation of the laser intensity.

Because the substitution made to derive Eq. (4.1) is only valid for $|\nu - \nu_0| \leq \nu_\mathrm{a}$ this determines the range in which the reconstruction can be done. This is also clear from a physical point of view: since the sinusoidal frequency modulation only covers the range $\nu_0 - \nu_\mathrm{a}$ to $\nu_0 + \nu_\mathrm{a}$, actually no measurement is performed outside this spectral interval and it can not be expected to obtain information that is not measured. Practically, the method can be seen as an implementation of direct spectrometry with sinusoidal frequency scanning instead of linear scanning.

ii. Signal model for curve-fitting reconstructed transmission data

Since the laser center frequency ν_0 and frequency modulation amplitude ν_a are generally unknown it is convenient to use the normalized emission frequency coordinate $x = (\nu - \nu_0)/\nu_\mathrm{a}$ for evaluation of right hand side of Eq. (4.1). Therefore, the spectral model does not need to be changed: all determined frequency parameters like Gaussian or Lorentzian absorption line half-width or line position will be obtained in this normalized units (relative to scanning range, multiples of ν_a centered around ν_0). Only if these obtained parameters are to be compared with an absolute frequency, the quantities ν_a and ν_0 need to be determined with a frequency calibration scheme (e.g., with a reference etalon or using the method described in section 4.1). If only a single Lorentzian line and a linear laser power characteristic is considered the model has the following form:

$$\sum_{n=0}^{N} S_n(\nu_0) T_n(x) = \exp\left(\frac{-a_\mathrm{mol} x_\gamma^2}{x_\gamma^2 + (x - x_\mathrm{C})^2}\right)(y_\mathrm{o} + y_\mathrm{s} x) + \epsilon. \tag{4.2}$$

The five unknown fit parameters are line position x_C, line half-width x_γ both in normalized frequency coordinates ($x = (\nu - \nu_0)/\nu_\mathrm{a}$), peak absorbance a_mol and y_o and y_s modeling the y-offset and y-slope due to laser amplitude modulation, respectively. The normalized frequency variable x lies between -1 to 1 and ϵ is a random variable that represents the noise on the reconstructed spectrum. The numerically stable evaluation of the sum of the left hand side of Eq. (4.2) is preferably done using the Clenshaw algorithm (see section B.1) and then the least squares curve-fit to the given model is carried out (for both see Fig. 4.3 bottom). For the reconstruction and subsequent fit, the variable x was discretized with 64 equidistant values from -1 to 1. The actual number of points is irrelevant if it is high enough so that the reconstructed spectrum is adequately sampled.

iii. Required number of harmonics

Due to the increasing oscillatory behavior it is clear that each term in Eq. (4.1) adds more detail to the result with a magnitude corresponding to the amplitude of the harmonic coefficient. This is because the values of the Chebyshev polynomials all lie in the range of -1 to 1. Since the harmonic coefficients typically show an exponential decay with increasing order n, the sum in Eq. (4.1) can be truncated when the desired accuracy is reached. The first few Chebyshev polynomials are shown in Fig. 4.4. The minimum number N of harmonics depends on the system noise level. Due to the uncorrelated noise on the harmonic spectra, the error by including the harmonic in the

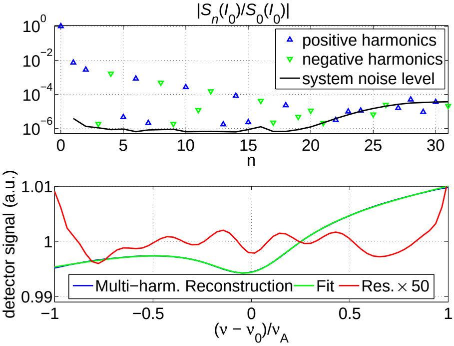

Fig. 4.3: *The upper plot shows the measured harmonic coefficients* S_n/S_0 *of the experiment (different symbols for positive and negative values) and the corresponding noise level (black). The bottom plot shows the corresponding reconstructed transmission (using* $n = 0, \ldots, 20$ *with Eq. (4.2)) (blue) and the corresponding Lorentz fit (green) with residual (red).*

reconstruction is higher than the error by its omission if the noise amplitude in the harmonic is higher than the signal amplitude. The reconstruction thus should include all harmonics with a signal to noise ratio higher than one. Using a typical modulation amplitude $\nu_\mathrm{a} = 3\gamma$ (γ: half-width at half-maximum of the absorption line) and system noise level of 1×10^{-5} to 1×10^{-6} a full reconstruction can be obtained with $N = 20$ to $N = 25$ harmonics, when the peak absorbance is around 1 %. This can be seen in Fig. 4.3 (top) where the signal level of the harmonics drops below the noise level at approximately $n = 20$. Note, that using more harmonics than necessary should not affect the overall precision of the parameters the curve-fits extracts. This is because the contribution of the higher harmonics to the reconstructed transmission is of increasing detail (this is a property of the Chebyshev polynomials, cf. Fig. 4.4) so that the curve-fit will filter the additional high frequency noise on the reconstructed transmission.

4.2.2. Method 2: curve-fitting multiple spectra

As mentioned earlier, simultaneous curve fitting of multiple harmonic spectra is the other alternative to multi-harmonic detection.

i. Signal model for curve-fitting

Since different harmonics all originate from a measurement of the same physical system (gas transmission, laser and detector) a curve-fit with a shared set of parameters to all harmonics has to be carried out. This is different to the approach in Ref. [139] where several higher harmonics have been curve-fitted, but separately with individual parameter sets and subsequent averaging. Note that this approach can not be expected to have the highest precision, because a least squares curve fit is the optimum method for estimation of parameters from noisy data. This holds exactly for linear models and

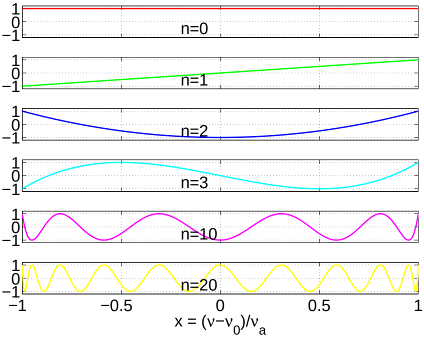

Fig. 4.4: *The Chebyshev polynomials $T_0(x)$ to $T_3(x)$, $T_{10}(x)$ and $T_{20}(x)$.*

is asymptotically true (for low noise) for nonlinear models (cf. section 3.4.3).

The signal model used for fitting the unsaturated O_2 absorption line around 763 nm is the following:

$$\begin{aligned} S_1(I_i)/S_0(I_i) &= -a_{\mathrm{mol}} \cdot A_1\left((x_i - x_C)/x_\gamma, x_{\mathrm{a}}/x_\gamma\right) + y_{\mathrm{o},1} + \epsilon_1, \\ S_2(I_i)/S_0(I_i) &= -a_{\mathrm{mol}} \cdot A_2\left((x_i - x_C)/x_\gamma, x_{\mathrm{a}}/x_\gamma\right) + y_{\mathrm{o},2} + \epsilon_2, \\ S_3(I_i)/S_0(I_i) &= -a_{\mathrm{mol}} \cdot A_3\left((x_i - x_C)/x_\gamma, x_{\mathrm{a}}/x_\gamma\right) + \epsilon_3, \\ &\vdots \end{aligned} \tag{4.3}$$

The $S_n(\nu_i)/S_0(I_i)$ represent the normalized measured harmonic signals at laser injection current I_i and optical frequency ν_i with $i = 1, \ldots, N$ points per scan (cf. section 3.3.4). The actual frequency points ν_i are unknown but assumed to be linearly increasing. The variable $x = \frac{\nu-(\nu_N+\nu_1)/2}{(\nu_N-\nu_1)/2}$ is defined as the normalized frequency scale. It runs from -1 to 1 and covers exactly one spectral scan. If the slow laser tuning is carried out linearly the N spectral samplings correspond to the points $x_i = \frac{2(i-1)}{N-1} - 1$. The line center x_{C} is the index of the absorption line center, x_γ the line half-width and x_{a} the frequency modulation amplitude all in this relative units. $y_{\mathrm{o},1}$ and $y_{\mathrm{o},2}$ model the laser AM caused offset on the first and second harmonic spectrum. The laser AM effects are modeled in the same way as for single harmonic detection. For the case of a VCSEL the simple approximation by offsets is sufficient (as the experiment shows – see also Eq. (3.63) and the discussion in section 3.3.6.ii).

The parameter a_{mol} is the desired peak absorbance value and $A_n(x, m)$ the formula by Arndt Eq. (3.30), which is the harmonic spectrum of a peak normalized unsaturated Lorentzian function. The ϵ_n are random variables representing the measurement noise. The parameters describing the relationship between index x and ν (i.e., offset and proportionality factor) can not be determined from the fit when only a single absorption line with unknown line width is scanned.

With the curve-fit the six parameters a_{mol}, x_{C}, x_γ, x_{a}, $y_{\mathrm{o},1}$ and $y_{\mathrm{o},2}$ are determined. Although the frequency parameters x_{C}, x_γ and x_{a} are in non-standard units, the model is formally the same as for absolute units. Ratios are independent of the unit i.e.,

$$\frac{\nu-\nu_\mathrm{C}}{\gamma}=\frac{x-x_\mathrm{C}}{x_\gamma}, \qquad \text{and,} \qquad \frac{\nu-\nu_\mathrm{C}}{\nu_\mathrm{a}}=\frac{x-x_\mathrm{C}}{x_\mathrm{a}}. \tag{4.4}$$

Hence $(\nu-\nu_\mathrm{C})/\nu_\mathrm{a}$ can be chosen as plot x-axis. In Fig. 4.5 the simultaneous fit of the first four harmonic spectra is shown.

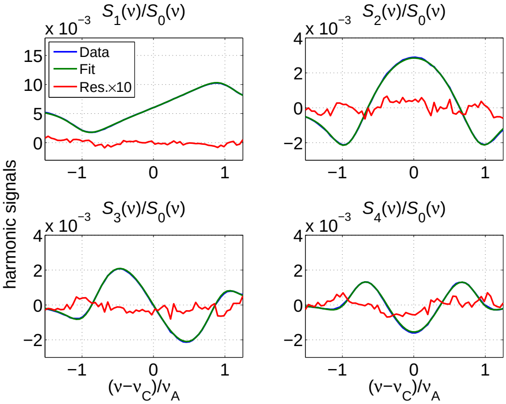

Fig. 4.5: *Measurement (blue) and simultaneous curve-fit of the first four harmonic spectra (green) and the magnified residual (red).*

ii. Required number of harmonics

Since the amplitude of the harmonic spectra decreases with increasing order it is expected that there is an optimum number of harmonics for simultaneous curve-fitting. Using more harmonics than this optimum value will not further improve the noise on the extracted parameters.

It turned out experimentally that fitting of the first four harmonic spectra is optimum in the sense that using more does not give any further improvement (Fig. 4.6). This optimum number is independent of the system noise level and peak absorbance value, as the relative improvement becomes negligible. It will however depend on the modulation index ν_a/γ because for higher modulation indices the signal energy is shifted to higher orders of the harmonic spectra. The same is true when a thick optical sample (i.e., absorbance > 0.1) is measured.

4.2.3. Experimental results and comparison of methods

i. Experimental setup and system noise analysis

For experimental verification both methods were tested using an O_2 absorption line probed with a 763 nm VCSEL. A 20 cm double pass gas cell exposed to laboratory air

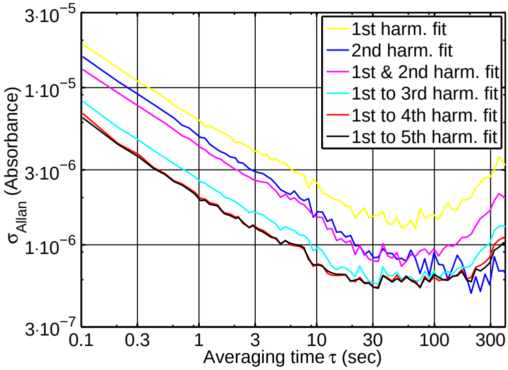

Fig. 4.6: *The Allan plots for multi-harmonic detection with a variable number of spectra that are simultaneously fitted. The measurement data is the same for all curves. Fitting more than four harmonic spectra gives a saturation behavior, whereas including the third harmonic gives the highest improvement.*

was utilized with neither temperature nor pressure stabilization. The peak absorbance of the line is around 9×10^{-3}. A custom build electronics for laser and detector control as well as data processing served as platform to record the harmonic spectra or harmonic coefficients. For simplicity the curve fitting was done off-line on a PC. The modulation frequency was set to 3 kHz and the sinusoidal laser modulation amplitude set close to three times the absorption line width, so that the typical modulation index m of around 3 is realized.

Regarding the ideality of the realization of the electronics, the noise on the harmonic spectra or harmonic coefficients is a factor 1.2 to 2 higher than the noise that would be expected from the intrinsic noise by the laser diode (Fig. 4.7 bottom). This is a technical issue attributed to strong receiver noise above 55 kHz (Fig. 4.7 top) and the frequency response of the applied filtering during detection of the harmonics. It indicates that in a better realization of the electronics the absolute noise performance could be a factor of 1.2 to 2.0 lower with the same laser. Comparison of the methods is however not affected.

ii. Comparison of multi- and single-harmonic detection

In Fig. 4.8 the Allan plot of the two multi-harmonic detection methods, the corresponding single harmonic detection and the extrapolated direct detection is shown. For the latter formula Eq. (5.1), i.e.

$$\sigma(\widehat{a}_{\text{mol}})_{\text{DS}} = G\sqrt{\overline{S}_{yy}\, R/2} \tag{4.5}$$

is used, with a spectral noise density of $\overline{S}_{yy}^{1/2} = 1.7{\times}3.5 \times 10^{-7}\,/\sqrt{\text{Hz}}$ and $\tau = 1/R$. This is the receiver noise density at 3 kHz times a non-ideality factor 1.7. The appropriate observation factor G for the spectral model (single Lorentzian line and linear laser

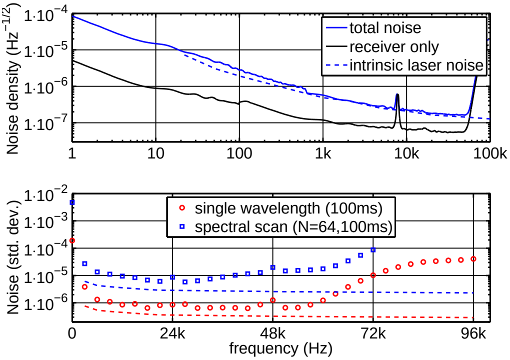

Fig. 4.7: *Top: The total noise spectral density* $S_{yy}^{1/2}(f)$ *of the measurement system (blue) and the contribution of receiver (black) and intrinsic laser intensity noise (blue dashed). Bottom: the noise level (standard deviation) on the harmonics for spectral scanning (blue) and single point detection (red). The dashed lines indicate the calculated noise level from intrinsic laser noise.*

power characteristic) is $G = 3.37$ (cf. Tab. 5.1).

These results are also summarized in Tab. 4.1 together with relevant system parameters. The column "scanning range" specifies the range of the slow frequency sweep of ν and hence is zero for the single spectral frequency detection.

Description	n	$\nu_N - \nu_1$ $(\times \nu_\gamma)$	ν_a $(\times \nu_\gamma)$	Evaluation	σ_Allan @ $\tau = 1\,\mathrm{s}$ $(\times 10^{-6})$
1st harm. fit	1	8.9	3.2	Fit to Eq. (4.3)	6.1
2nd harm. fit	2	8.9	3.2	Fit to Eq. (4.3)	4.8
1st & 2nd harm. fit	$1, 2$	8.9	3.2	Fit to Eq. (4.3)	4.2
2nd harm. center detection	2	0	3.3	multiply with factor	2.6
1st to 3rd harm. fit	$1, 2, 3$	8.9	3.2	Fit to Eq. (4.3)	2.5
1st to 4th harm. fit	$1, 2, 3, 4$	8.9	3.2	Fit to Eq. (4.3)	2.0
1st to 5th harm. fit	$1, 2, 3, 4, 5$	8.9	3.2	Fit to Eq. (4.3)	1.9
Multi harm. reconstruction & fit	$0, \ldots, 20$	0	3.3	Fit to Eq. (4.2)	1.6

Tab. 4.1: *Overview and comparison of wavelength modulation spectroscopy detection methods. All measurements were done with the identical experimental setup and identical settings.*

iii. Comparing both multi-harmonic detection methods

It can be seen that the reconstruction method has a slightly better noise performance than multi-harmonic curve-fitting but is more sensitive to drift as the relatively worse

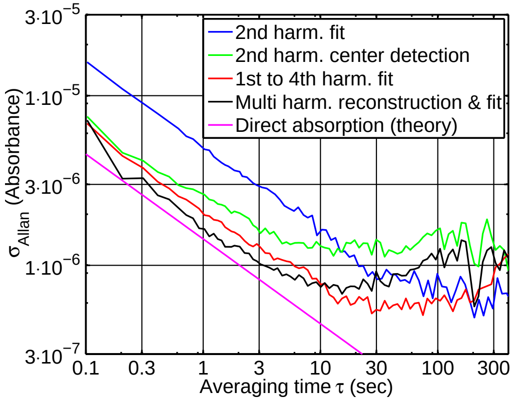

Fig. 4.8: *Comparison between single-harmonic detection (single-point and spectral fitting) and the corresponding multi-harmonic detection (single-point reconstruction and simultaneous spectral fitting). The multi-harmonic detection methods lie close to what direct absorption spectroscopy could theoretically achieve (white noise only, no drifts).*

minimum of the Allan deviation shows. The behavior with respect to noise and drift performance of the reconstruction method is however better than for second harmonic single point detection. Although second-harmonic curve fitting shows a slightly better performance in terms of drift sensitivity than multi-harmonic detection this is probably not a generic property of multi-harmonic curve-fitting, because it is seemingly caused by the more drift affected contribution of the first harmonic in the multi-harmonic detection. This can be seen in Fig. 4.6 where the minimum of the Allan plot for second harmonic detection is better compared to first-harmonic detection.

iv. Comparing single and multi-harmonic detection

If only white noise performance is considered (the region of the Allan plot with low averaging times where the slope is -1/2) both multi-harmonic detection methods give a factor of approximately 3 performance increase (2.7 for simultaneous curve-fitting) compared to second harmonic curve-fitting.

The improvement is less compared to single harmonic center point detection, which however is an unfair comparison because the number of determined parameters are different. For spectral scanning the noise on the harmonic spectra is higher than for single harmonic center point detection because a higher bandwidth around each harmonic frequency is required. Theoretically a $\sqrt{N}$ fold increase of the noise standard deviation is expected (N: number of scanned spectral points). This is partly compensated by the filtering effect of the curve-fit, however, because the curve fit has to extract other parameters than absorbance, the noise improvement is a certain factor less than $\sqrt{N}$. The reason is not due to the curve-fit itself, but is fundamental. The information content about peak absorbance is less in a scanned spectrum than for the single spectral frequency detection (see section 5.1.3.v). That is why second harmonic peak detection has a better white noise performance than second harmonic curve fitting (cf. Fig. 4.8). The ability to determine more than one parameter and to obtain better stability or calibration-free operation are payed off by a poorer white noise performance. This is also indicated in Fig. 4.8 where the minimum of the Allan deviation is much higher for the single harmonic center detection than for second harmonic curve fitting, despite a better white noise performance. This is attributed to the higher sensitivity to fringes and laser wavelength instability, which are better compensated by the curve-fit.

v. Comparing multi-harmonic detection and ideal direct spectroscopy

Both multi-harmonic detection methods show white-noise performances in the order which could be achieved by direct absorption spectroscopy (white noise limited) with the sensor electronics (pink curve in Fig. 4.8). Theoretically, multi-harmonic WMS and direct spectroscopy should achieve both the same precision, because both the overall frequency scanning range and the relative distribution of time the laser spends on different spectral frequency regions during one scan are (approximately) the same (see section 5.1.3.v). The slightly lower white noise performance of the multi-harmonic curve-fit may result from the missing 0-th harmonic spectrum in the fit. It can be excluded because the necessary weighting to equalize noise amplitude among all harmonic spectra (cf. Fig. 4.7) would damp the zeroth-harmonic very much so that the benefit of its inclusion is negligible.

4.2.4. Summary

It is experimentally shown that multi-harmonic detection gives a noise improvement of approximately factor of three compared to single harmonic curve-fitting. The overall performance is close to the theoretical performance of direct spectroscopy with its typically factor of three larger amplitude under same conditions. For simultaneous curve-fitting the inclusion of the first to fourth harmonic spectrum is sufficient to achieve optimum performance. For the reconstruction of the transmission method all harmonics above the noise level have to be included, which was 20 in this case. For systems with spectral scanning the simultaneous curve fitting approach is probably more promising due to its lower drift sensitivity and the lower number of required harmonics.

Finally, it is concluded that multi-harmonic detection can be regarded as a technical implementation method of direct spectroscopy with the advantage that no requirement on bandwidth of the laser tuning behavior is necessary.

4.3. In-fiber Zeeman spectrometry

Zeeman Modulation Spectrometry (ZMS) also called zero-field Laser Magnetic Resonance (LMR) is a spectroscopic detection method for paramagnetic gases, i.e., gases that show a Zeeman splitting of absorption lines if a magnetic field is applied (e.g., NO, NO_2, O_2, OH). In this technique the gas absorption line center wavelength is modulated by the magnetic field instead of the emission wavelength of a tunable laser [134, 140]. Even though this method is old – invented when room temperature tunable lasers were not available in the mid infrared – it has two advantages. First, it is insensitive against other non-paramagnetic gases (e.g., H_2O vapor) [141], i.e., presence of these gases does not cause a ZMS signal and second, it is also insensitive to fringes generated by multi-path propagation inside the gas cell that typically limit the detection sensitivity in TDLAS (tunable diode laser absorption spectrometry) sensors. Hence, a superior sensor stability – in the sense of low baseline drift – is expected for Zeeman modulation spectrometry, as observed in the technically similar Faraday rotation spectrometry (FRS) [142, 143].

4.3.1. Zeeman modulation spectrometry

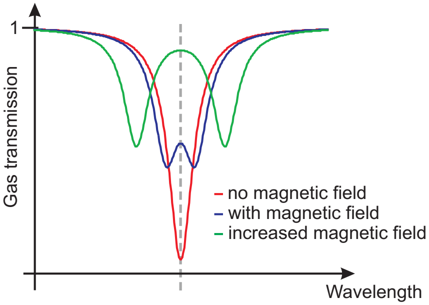

Fig. 4.9: *Illustration how the Zeeman effect changes the transmission of a paramagnetic gas in the presence of a magnetic field. The absorption line splitting (here special case of splitting into two components, i.e., a $J = 0 \to J = 1$ transition) is because the magnetic field removes the degeneracy of one energy state involved in the transition.*

In the presence of a magnetic field in direction of light propagation the absorption line will split into two or more separate lines with a spectral separation proportional to the magnetic field strength (linear Zeeman effect, see Fig. 4.9). A comparison between the set-ups for ZMS and wavelength modulation spectrometry (WMS) is shown in Fig. 4.10. Compared to LMR [144] where the static offset of the magnetic field is tuned to generate the LMR spectrum, Zeeman modulation (or zero field LMR) uses a tunable laser to scan the spectrum and only a magnetic field modulation without static offset. The modulation together with a lock-in amplifier based detection is employed to solve certain technical difficulties (e.g., suppression of $1/f$ noise). As a consequence, a derivative like detection is realized where harmonic spectra in place of ordinary transmission spectra are obtained.

The even order harmonic spectra for ZMS and WMS (e.g. second harmonic) are the same if the Zeeman splitting is into two separate lines. However, ZMS does not generate odd order harmonic spectra (e.g., the first harmonic). This can be understood if the individual split Zeeman components are considered separately. Each component alone would generate the same spectrum as WMS because it makes no difference whether the absorption line is moving sinusoidally or the laser emission wavelength. The WMS modulation amplitude corresponds to the amplitude of the Zeeman shift. For even

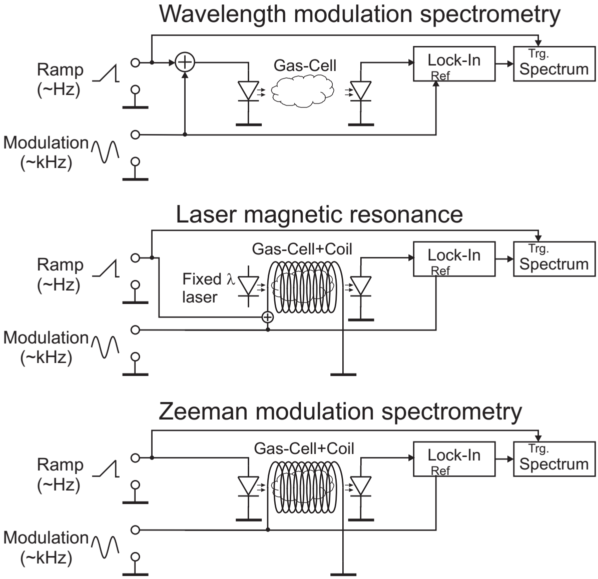

Fig. 4.10: *Schematic setup of wavelength and Zeeman modulation systems as well as Laser magnetic resonance. The slow current ramp is used to scan the spectrum by laser tuning for WMS and ZMS. The faster modulation of wavelength or the magnetic field and corresponding demodulation with the lock-in amplifier realizes a derivative-like spectrum. For LMR the spectral x-axis is the DC magnetic field strength instead of wavelength.*

order harmonic spectra the sign of the modulation amplitude (for ZMS this is whether the line is shifting to higher or lower wavelength for a positive magnetic field) has no influence on the spectral shape and odd order harmonics appear inverted around the y-axis. Hence, in total, for odd orders the individual components cancel out and for even orders a superposition of WMS harmonic spectra of (possibly) different modulation index is observed.

The modulation amplitude that gives maximum signal for a single Doppler broadened line is 2.11 times the line half width [95]. The Doppler linewidth for lines in the O_2 A-band is around 420 MHz for room temperature. Assuming an average splitting coefficient of 7 MHz/mT a magnetic field strength amplitude of 126 mT is needed for optimum detection. A lower modulation amplitude results in an (approximately) linear decrease in amplitude. The situation improves in the mid-infrared where for optimum NO detection only 18 mT is needed due to the reduced Doppler linewidth of 62 MHz.

With an simple calculation (see below) it can be shown that the power consumption for a given magnetic field strength is inherently linked to the physical dimensions of the coil. It is important to have a small inner coil diameter (where the gas-cell is contained) and short coil length, which is in conflict with long optical path length.

4.3.2. In-fiber sensing

To enable long optical path length under low power consumption, a hollow capillary fiber (HCF) is applied as gas cell. Recently, these HCFs were investigated as an alternative to multi-pass cells [26]. They provide long optical path lengths (m range) at simultaneously extremely low volume (mL range). The drawback is the spectral background, given by optical interference due to the highly multi-mode character of the fiber. Although the spectral background could be greatly reduced by applying mechanical vibration [26], it still limits the sensitivity in wavelength modulation systems. For Zeeman modulation, the spectral background of the cell is inherently removed, because the AC signals (second harmonic of modulation frequency in this case) are only generated by the Zeeman modulation of the gas absorption line. Unfortunately FRS can not be applied here, since the HCF is not polarization maintaining and a detection of a rotation in polarization angle seems impossible.

Since the HCF can be wound up and needs only very little volume it can easily be placed in a toroidal air coil with small inner hole diameter. This keeps both the coil length (toroid circumference) and as well as its inner diameter small, which is required for low electrical power consumption (see calculation below). The experimental setup and the used HCF are shown in Fig. 4.11 and Fig. 4.12, respectively.

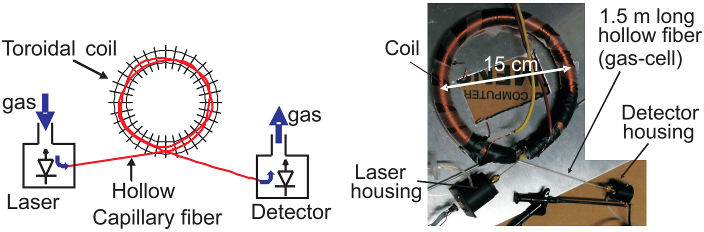

(a) Gas cell schematic (b) Photograph

Fig. 4.11: *(a) Schematic and (b) photograph of the gas cell for Zeeman spectroscopy with the hollow capillary fiber based gas cell.*

4.3.3. Design considerations and fundamental limits

To the knowledge of the author no study has been done on the necessary power consumption and its fundamental limits, neither for LMR, ZMS or FRS. This is however of great importance for possible sensor applications.

i. Minimum power consumption

When designing the coil the relevant parameters are number of windings n, wire diameter d_w and dimensions of the coil like diameter of the toroid D, diameter of the windings d_s and diameter of the hole where the fiber is inside d_i (see Fig. 4.12).

The total volume of the copper wire forming the coil can be expressed in two ways:

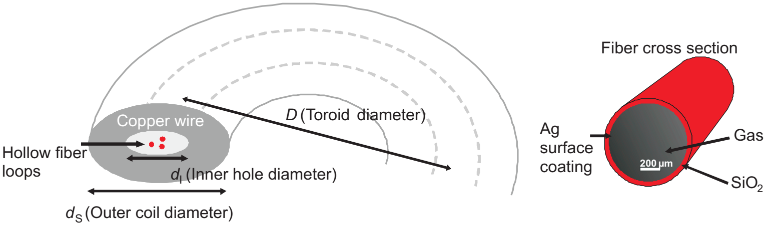

Fig. 4.12: *The design parameters specifying the coil dimensions. The individual winding layers of the coil are located in the dark gray area labeled "copper wire". The HCF cross section is shown on the right.*

first, by the volume of the toroid and, second, by the length of the wire times the cross section of the wire, which gives

$$F\frac{\pi^2}{4}(d_s^2 - d_i^2)D = \frac{\pi^2}{8}n(d_s + d_i)d_w^2. \tag{4.6}$$

Here F is the filling factor, which depends on the type of winding. Its maximum value is obtained for the orthocyclic or hexagonal style winding and is in this case $F = \frac{\pi}{2\sqrt{3}} \approx 0.91$ [145]. The ohmic resistance of the coil R and the magnetic field strength amplitude B inside the coil for electric current amplitude I are given by:

$$R = \rho_{\mathrm{Cu}}\frac{2n(d_s + d_i)}{d_w^2}, \qquad B = \mu_0\frac{nI}{\pi D}, \tag{4.7}$$

with $\rho_{\mathrm{Cu}} = 1.68 \times 10^{-8}\,\Omega\,\mathrm{m}$ the resistivity of copper and $\mu_0 = 4\pi \times 10^{-7}\,\mathrm{T\,m/A}$ the vacuum permeability. The dissipated power $P = RI^2/2$ can be expressed in terms of B by using Eq. (4.7) and eliminating d_w using Eq. (4.6):

$$P = \rho_{\mathrm{Cu}}\frac{\pi^2 B^2 D}{2\mu_0^2 F}\frac{d_s + d_i}{d_s - d_i} \approx 525\,\frac{\mathrm{W}}{\mathrm{T^2\,cm}}\frac{B^2 D}{F}\frac{d_s + d_i}{d_s - d_i}. \tag{4.8}$$

peak field B	toroid diameter D	d_i/d_s	power P
18 mT (NO)	15 cm*	0	2.8 W
18 mT (NO)		1/3*	5.6 W
18 mT (NO)		9/10	53.3 W
126 mT (O$_2$)		0	137 W
126 mT (O$_2$)		1/3*	274 W
126 mT (O$_2$)		9/10	2.69 kW

Tab. 4.2: *Necessary power for relevant coil geometries (* for present setup) and sinusoidal magnetic fields optimum for detection of NO (@5.3 µm) and O$_2$ (@763 nm), respectively.*

Note, that the number of windings, the diameter of the wire or the strength of the electrical current have no influence on power consumption. If the hole diameter d_i is large compared to the winding diameter d_s the required power P can increase dramatically, as well as if the filling factor F is worse than optimum. In fact, the power consumption goes to infinity if $d_i/d_s \to 1$, i.e., the coil winding layers are very thin compared to the inner hole diameter (see Tab. 4.2). This is a fundamental problem for setups where a multi- or single-pass cell is placed inside the coil (corresponds closer to the 9/10 case in Tab. 4.2). On the other hand, when making the winding thicker or the hole smaller ($d_i/d_s \to 0$) the electrical power requirement still has a lower limit. Values of $d_i/d_s < 1/3$ are already within a factor of two close to the optimum. Hence, $d_i/d_s = 1/3$ has been chosen for the present setup because it gives a good compromise between low power consumption and compactness. The toroid diameter D is limited by the minimum bending radius of the hollow core fiber and is in the range of 12 cm to 15 cm. Only the use of superconductors as wire material can improve the minimum required power, in which case it goes to zero for all cases.

ii. Ring current in Ag coating

Another important question is whether the conductive Ag coating inside the fiber has a negative effect. First, the induced current due to modulated magnetic field will cause heating and second may weaken the magnetic field inside the fiber. By computing the induced voltage and the resistance of the coating, the dissipated power in the silver coating P_{Ag} for a fiber with length l, inner fiber hole diameter d and coating thickness h_{Ag} can be expressed as $P_{\mathrm{Ag}} = \pi^3/(8\rho_{\mathrm{Ag}})B^2 f_{\mathrm{m}}^2 d^3 h_{\mathrm{Ag}} l$, with $\rho_{\mathrm{Ag}} = 1.59 \times 10^{-8}\,\Omega\,\mathrm{m}$ being the resistivity of silver. For a fiber with diameter $d = 750\,\mu\mathrm{m}$ and assuming typical values for $h_{\mathrm{Ag}} = 200\,\mathrm{nm}$ [146], $B = 100\,\mathrm{mT}$ and a modulation frequency $f_{\mathrm{m}} = 1\,\mathrm{kHz}$ a value of $P_{\mathrm{Ag}}/l = 206\,\mu\mathrm{W/m}$ is obtained. Hence, heating can be neglected. Equivalently, the magnetic field generated from the loop current in the coating is $B_{\mathrm{Ag}} = \mu_0\pi/(2\rho_{\mathrm{Ag}}) f_{\mathrm{m}} B d h_{\mathrm{Ag}}$. Using the same values as before $B_{\mathrm{Ag}}/B = 1.68 \times 10^{-5}$ is obtained, i.e., the magnetic field inside the HCF is not significantly weakened.

4.3.4. Experimental results

Using the setup shown in Fig. 4.11 WMS and ZMS spectra of ambient air (O_2 mixing ratio 21 %) at reduced pressure of 300 mbar (limited by experimental conditions) are recorded (Fig. 4.13). The second harmonic spectra are measured, which are the second harmonic intensities divided by the DC intensities and have the unit of 1. The values are directly proportional to absorbance (cf. section 3.3.1). The 763 nm vertical-cavity surface-emitting laser has a power around 300 µW and the HCF is 1.5 m in length with two loops (or 1.05 m of the HCF) placed inside the coil. The received photocurrent is 40 nA corresponding to a total loss of 41 dB. This is due to the missing coating in the HCF which is a technical, not a fundamental limitation because (commercially available) HCFs with proper coating for the visible spectral region have very low loss (few dB/m) [147]. The modulation frequency of $f_{\mathrm{m}} = 333\,\mathrm{Hz}$ was chosen to be non-harmonically related to the 50 Hz line frequency. The coil with inductance 2.9 mH and resistance 3.2 Ω was operated with a modulation current of $I = 6.1\,\mathrm{A}$ and generates a magnetic field amplitude of $B = 50\,\mathrm{mT}$.

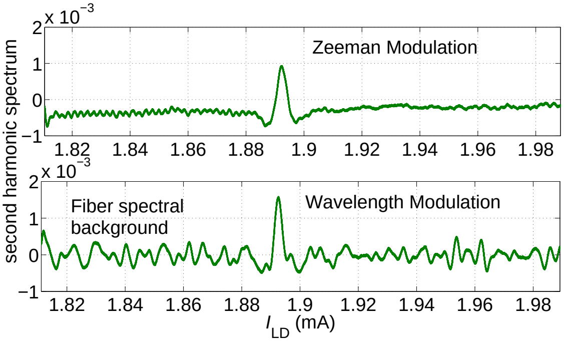

Fig. 4.13: *Second harmonic spectra obtained by Zeeman modulation (top) and traditional wavelength modulation (bottom) at an O_2 transition around* 763.73 nm*. The wavelength modulation spectrum shows the fiber spectral background in the order* 5×10^{-4} *which is not present in the Zeeman spectrum.*

i. Expected Zeeman splitting

To compute the Zeeman shift for the individual components for the given transition one can proceed as follows. The Zeeman shift (displacement of each component from the line position without magnetic field) $\Delta\nu$ (unit: wavenumber) for a $(J'', N'', m''_J) \rightarrow (J', N', m'_J)$ transition is [134]:

$$\Delta\nu = B\frac{e}{4\pi m_e c}(m'_J g_{J'} - m''_J g_{J''}). \tag{4.9}$$

The O_2 molecule is approximately a Hund case *b* molecule, where each state has a g_J factor of [148]:

$$g_J = 1.001\frac{J(J+1) - N(N+1) + S(S+1)}{2J(J+1)}. \tag{4.10}$$

The symbols m_e and e denote the electron mass and elementary charge respectively and c the speed of light. The magnetic quantum number m_J assumes integral values from $-J, \ldots, J$ whereas only transitions with $\Delta m_J = \pm 1$ are allowed. Transitions with $\Delta m_J = +1$ are only active to left circularly polarized light and $\Delta m_J = -1$ only for right circularly polarized light [148]. For linearly or unpolarized light they both are active to equal parts. The quantum number S is 1 for O_2. The laser probes the $(J'' = 8, N'' = 9) \rightarrow (J' = 8, N' = 8)$ transition of O_2 at $\nu = 13\,093.66\,\mathrm{cm}^{-1}$ (763.73 nm) which then splits into 32 Zeeman components. For this transition we have $g_{J'} = -0.111$ and $g_{J''} = 0.014$. The splitting coefficients $\Delta\nu/B$ range from −13.8 MHz/mT to 13.8 MHz/mT depending on the quantum numbers $m_{J'}$ and $m_{J''}$.

ii. Discussion of results

In Fig. 4.13 the fiber spectral background with a peak to peak amplitude of 5×10^{-4} is easily observed for traditional wavelength modulation spectrometry. As expected, the background vanishes in the Zeeman modulated spectrum, because there only the modulation of the absorption line contributes to the optical spectrum. However, due to high the coil current (several A) and the high photocurrent amplification factor (2×10^7 V/A) a certain (time variable) electromagnetic interference (EMI) on the second harmonic is observed. This is considered as the cause of the baseline and the small high frequency noise on the Zeeman spectrum Fig. 4.13. This background depends on the magnetic field amplitude and strongly rises if the coil current is increased, which is typical for such a non-linear distortion. Nevertheless, the spectral background is reduced by a factor of four despite the existence of EMI. It is expected that it can be reduced further using a high transmittance fiber or using less magnetic field.

The modulation index (modulation amplitude divided by line half-width) for both WMS and ZMS is estimated to be around 0.7 by comparing the experimental signal amplitude with a simulated result. The consumed power is approximately 60 W whereas the lower limit Eq. (4.8) predicts 43 W. The difference is attributed to a non-optimum filling factor F and the measurement inaccuracy of the magnetic field strength.

4.3.5. Summary

In conclusion, it is demonstrated that ZMS with a HCF is feasible. Theoretical investigations showed that power consumption is much less than for ZMS with multi- or single-pass cells because of the much smaller diameter of the coil. Future work has to quantify the sensitivity limit for the gas detection and reduction of the EMI. Theoretically, the sensitivity is only limited by the laser and detector noise but not the spectral background of the cell. For quantification a fiber with dielectric coating will enhance the fiber transmission and consequently the electrical distortion on the photocurrent will be reduced. Furthermore, detection of NO in the mid-infrared is more appealing than oxygen detection in the visible, because the electrical power consumption is much less due to the reduced Doppler linewidth and, hence, a much lower magnetic fields are needed.

5. Application of results and sensors

In this chapter the previously obtained knowledge will be applied to sensors.

First, two metrics to evaluate sensor performance will be derived (section 5.1.1), and extensively utilized to compare detection methods (section 5.1). This, together with results from chapter 3, will lead to conclusions regarding sensor realization which will be summarized as design guidelines in section 5.2.

Finally, two sensors, which were realized in this thesis and are partly based on this design guidelines, are presented. The first is an air-quality sensor for simultaneous detection of CO_2 and H_2O and the second a CO sensor based fire detector. The practical suitability of the sensors is demonstrated. They are analyzed with respect to the performance metrics (sensitivity to noise, fringes and cross-sensitivity to other gases). The fire detector is tested under realistic conditions described by the European standard EN54.

The chapter is partly based on the following publications:

- A. Hangauer *et al.*, "Compact VCSEL-based CO_2 and H_2O sensor with inherent wavelength calibration for safety and air-quality applications", in *Conference on Lasers and Electro Optics (CLEO)*, San Jose, USA, May 2010, JThB3,
- A. Hangauer *et al.*, "Wavelength modulation spectroscopy with a widely tunable InP-based 2.3 μm vertical-cavity surface-emitting laser", *Opt. Lett.*, vol. 33, no. 14, pp. 1566–1568, 2008. DOI: `10.1364/OL.33.001566`, and
- A. Hangauer *et al.*, "Fire detection with a compact, 2.3 μm VCSEL-based carbon monoxide sensor", in *Conference on Lasers and Electro Optics (CLEO)*, Baltimore, USA, Jun. 2009, CTuA3.

For public recognition and received awards in context of these sensors see the appendix on page 181.

5.1. Comparison of detection methods

The aim of this section is to find out what signal processing methods can be used to improve the overall sensing performance. Signal processing is understood here as the process of extraction of desired data values from measured spectra. It depends on, but is distinct to, the detection method which defines how the measured spectra/signals are related to the optical transmission.

To fulfill this aim one has to first define which metrics are relevant for performance comparison. In this thesis it will be the noise on the sensor output values and the sensitivity of the sensor output values to sinusoidal fringes (see section 5.1.1).

The following questions will be answered from fundamental theoretical considerations:

- Under what conditions is curve-fitting the optimum data extraction method? (this has been answered in section 3.4.3)

- How to describe the data extraction/signal processing performance? (see section 5.1.1)
- Benefit of pre-processing of spectra? (see section 5.1.3.i)
- What are the optimum conditions for well performing data extraction?
  - What is the optimum spectral range to be scanned around the absorption line(s)? (see section 5.1.3.ii)
  - Optimum WMS modulation amplitude ν_a? (see section 5.1.3.iii)
  - Benefits of measuring nuisance parameters (e.g., gas temperature or gas pressure) instead of estimating with the curve-fit?
  - How to shape the sensor's response to fringes (see section 5.1.3.vi)
- Which detection method is better, wavelength modulation spectrometry or direct detection? (section 5.1.3.iii)
- How compare wavelength modulation or direct detection to the best detection method? (see section 5.1.3.iv)
- Which property determines the theoretical performance limit of a detection method? (see section 5.1.3.v)

5.1.1. Metrics for sensor performance: theory and experiment

The existence of measurement noise (random) and additive distortion (deterministic) on the measured spectra imposes fundamental limits on the accuracy and precision the unknown parameters can be determined with. Applying the results of section 3.4 it was possible for the first time to derive two metrics that theoretically describe the sensor response to both types of noise. This allows for a comparison of different detection/signal processing methods without influences from non-ideal sensor realizations. Furthermore, comparison of a particular sensor realization with the theoretically expected performance becomes possible. This gives limits on the maximum possible improvement from enhancing the signal processing.

i. Random noise ("Observation factor")

In the literature often only the noise on the recorded spectra is reported, although the noise on the sensor output values is of ultimate relevance (see section 5.1.2.i for an explanation). Additionally, there is not even a standard metric for comparison of the noise on measured spectra because there is no consensus what is the relevant bandwidth to normalize with [150] (see section 5.1.2).

In the frame of this thesis all these problems are solved by deriving expressions for the noise on the sensor output values. To quantify the influence of the fit it is proposed to introduce a number called "observation factor", which is independent on measurement rate R (unit Hz) and noise spectral density S_{yy} of spectra (unit: 1/Hz)[1].

The definition of the observation factor was proven to be an appropriate definition to assess the performance of the data extraction – within the frame of this thesis several publications were made together with J. Chen in Applied Physics B [53, 54] and the

---

[1] This is the variance of relative intensity noise in a one hertz bandwidth.

FLAIR conference [151]. This work here will go far beyond the published results and extend the theory to the general case of nonlinear signal models.

Definition: The **observation factor** G is the ratio between the noise amplitude on the gas peak absorbance values $\sigma(\widehat{a}_{\mathrm{mol}})$ (these are a result of the data extraction/signal processing) and the root of the (one-sided) density of noise on the measured spectrum $\overline{S}_{yy}$ times sensor bandwidth $R/2$:

$$G = \frac{\sigma(\widehat{a}_{\mathrm{mol}})}{\sqrt{R\,\overline{S}_{yy}/2}}. \tag{5.1}$$

The factor of 2 appears because of the use of the one-sided definition of the noise spectral density. If the sensor resolution is only available in terms of concentration ($\sigma(\widehat{C}_{\mathrm{mol}})$) or number density ($\sigma(\widehat{n}_{\mathrm{mol}})$) these values can be converted using Eq. (3.74).

The observation factor is independent of the noise amplitude and detection bandwidths, optical path length and absorption line strength. It measures how well the desired information is extractable from the measured spectrum. Performance degradation due to the estimation of nuisance parameters, overlapping spectral lines from other gases and the specific detection method (e.g., WMS) is quantified by it. The observation factor depends on the sensor operation conditions which include for nonlinear models the active operating point of nonlinear parameters.

For each spectral model the observation factor has a lower limit. This is the minimum obtained by variation of the spectral sampling points. For the case of a linear model this optimum spectral sampling theory has been published before in frame of this thesis together with J. Chen [53]. The observation factor can not be lower than 1. This value is attained for direct spectroscopy with center point detection and the gas absorbance being the only unknown parameter.

Analytic expression: A closed form expression for the observation factor is easily obtained, using the filter model of the nonlinear curve-fit derived in section 3.4.2. Recall, that for small perturbations the data extraction can be written as a linear filter with impulse response h and subsequent downsampling (Eq. (3.89)):

$$\Delta\widehat{a}_{\mathrm{mol}}(k) = (h * \Delta y)(kN). \tag{5.2}$$

This will now be used for examination of the fit's response to noise. The noise on the spectrum has variance $\sigma^2(y) = R\,N\,\overline{S}_{yy}/2$ and covariance matrix $\boldsymbol{W}$ (Eq. (3.84)). When computing the variance of Eq. (5.2) the sum has to be expanded and the covariance terms substituted by $\operatorname{cov}\{y(kN-n), y(kN-m)\} = w_{nm}\sigma^2(y)$. In compact notation

$$\sigma^2(\widehat{a}_{\mathrm{mol}}) = \boldsymbol{h}^H\boldsymbol{W}\boldsymbol{h}\;R\,N\,\overline{S}_{yy}/2, \qquad \text{(hence: } G = \sqrt{\boldsymbol{h}^H\boldsymbol{W}\boldsymbol{h}\,N}\text{)} \tag{5.3}$$

is obtained. The expression for G is generally valid for a all linear or linearized signal processing methods.

In the case of least squares curve-fitting this can be simplified (see Eq. (3.90) for h):

$$G = \sqrt{N(\boldsymbol{F}^H\boldsymbol{W}^{-1}\boldsymbol{F})^+_{11}}, \tag{5.4}$$

with $(\boldsymbol{X})^+_{11}$ denoting the top-left element of the pseudoinverse matrix of $\boldsymbol{X}$ (see section B.2). The matrices $\boldsymbol{F} = \boldsymbol{F}(\boldsymbol{\theta})$ are the observation matrix from the linear model or the Jacobian of the nonlinear model and $\boldsymbol{W}$ the optional matrix specifying the correlation structure of the measurement noise.

Dependency on parameters: For the case of a nonlinear model the observation factor depends on the values of the nonlinear parameters in $\boldsymbol{\theta}$, i.e., generally

$$G = G(\boldsymbol{\theta}).$$

It is, however, independent from certain linear parameters such as absorbance or additive baseline parameters (cf. section 3.4.2).

In any case, the observation factor depends on the signal model, possible "non fitted" parameters and conditions the signal model is influenced by. Such a parameter may be for example gas pressure or absorption line-width. If gas pressure is determined by the fit, the observation factor will typically be higher than if gas pressure is measured, because there are more unknown parameters which decreases noise performance.

The observation factor is, hence, the right tool to examine and optimize sensor performance. Comparing the above cases, the observation factor gives the cost or benefit of measuring the pressure in terms of the increase or decrease of sensor noise. Furthermore, it can be used to determine the optimum pressure (for which the observation factor is minimum) in both cases of pressure measurement and fitting.

Relevant sensor parameters, that can be optimized (regardless if these are fitted or not), are: spectral scanning width, WMS modulation amplitude, gas pressure and the spectral region itself (where e.g., interfering gases may absorb as well).

Note, that the quantification of sensor performance in terms of noise alone is not sufficient, because the influence of interference fringes is an equally important issue. Therefore the second metric for sinusoidal (deterministic) distortion is derived.

ii. Deterministic distortion ("Fringe response")

A systematic investigation of the sensor response to interferometric distortion has not been done in the literature so far. Let $T(\nu)$ be the optical transmission of the cell including the gas. According to the nomenclature in section 3.4 the sensor performs measurements on T (which each take time $1/R$) and outputs for each measurement a single value $\widehat{a}_{\mathrm{mol}}$, which is the peak absorbance from the gas of interest:

$$\widehat{a}_{\mathrm{mol}} = \mathrm{SENS}\{T(\nu)\}. \tag{5.5}$$

If the transmission is distorted by a small sinusoid, the sensor output value $\widehat{a}_{\mathrm{mol}}$ will generally also be distorted.

Definition: The **fringe response** $F(L_{\mathrm{OPD}})$ is defined as the maximum distortion on the output value divided by the amplitude of the sinusoidal distortion:

$$F(L_{\mathrm{OPD}}) = \frac{1}{A} \max_{\phi \in [0,2\pi]} \left| \mathrm{SENS}\{T(\nu)(1 + A \sin(2\pi\nu L_{\mathrm{OPD}}/c + \phi))\} - \mathrm{SENS}\{T(\nu)\} \right|.$$

See Fig. 5.1 for an illustration.

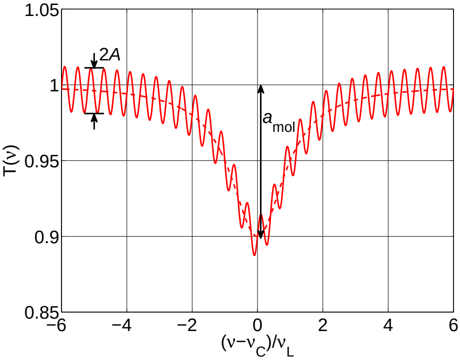

Fig. 5.1: *Explanation of the symbols* A *and* a_{mol} *used in the definition of the fringe response. The fringe response describes the maximum fit error due to the presence of the fringe* ($F(L_{OPD}) = \max \Delta\widehat{a}_{mol}/A$)*.* L_{OPD} *is the optical path length between the two light beams causing the interference.*

For example, if the fringe response has a value of 0.1 at a certain optical path length difference L_{OPD} ($F(L_{\mathrm{OPD}}) = 0.1$) a sinusoidal interference with amplitude $A = 10^{-3}$ on the optical transmission will generate an maximum error of the gas absorbance $\Delta\widehat{a}_{\mathrm{mol}}$ of 10^{-4}. This value relates to a concentration error by Eq. (3.74).

Analytic expression: For WMS with normalization by the zeroth harmonic, a fringe with optical path length difference L_{OPD} and small amplitude A will appear as the following distortion on the measured spectrum

$$\Delta y_i(L_{\mathrm{OPD}}) = \frac{A\epsilon_n \mathrm{i}^n \,\mathrm{J}_n\left(2\pi\nu_{\mathrm{a},i}L_{\mathrm{OPD}}\right)\mathrm{e}^{\mathrm{i}2\pi\nu_i L_{\mathrm{OPD}}}}{1 + A\,\mathrm{J}_0\left(2\pi\nu_{\mathrm{a},i}L_{\mathrm{OPD}}\right)\mathrm{e}^{\mathrm{i}2\pi\nu_i L_{\mathrm{OPD}}}} \tag{5.6}$$

$$= A\epsilon_n \mathrm{i}^n \,\mathrm{J}_n\left(2\pi\nu_{\mathrm{a},i}L_{\mathrm{OPD}}\right)\mathrm{e}^{\mathrm{i}2\pi\nu_i L_{\mathrm{OPD}}} + \mathcal{O}(A^2), \qquad \text{for } A \to 0, \tag{5.7}$$

with $n > 0$ the harmonic detection order, $\nu_{\mathrm{a},i}$ and ν_i the modulation amplitude and center wavenumber corresponding to the i-th spectral sampling (see Eq. (3.36)). For direct spectroscopy or WMS with detection order $n = 0$

$$\Delta y_i(L_{\mathrm{OPD}}) = AH_0(\nu)\,\mathrm{J}_0\left(2\pi\nu_{\mathrm{a},i}L_{\mathrm{OPD}}\right)\mathrm{e}^{\mathrm{i}2\pi\nu_i L_{\mathrm{OPD}}} + \mathcal{O}(A^2) \tag{5.8}$$

is the proper choice[2]. Applying the filter model equation Eq. (3.89) the result for small distortion ($A \to 0$) is obtained (h is given by Eq. (3.90)):

$$F(L_{\mathrm{OPD}}) = \frac{1}{A}\left|\sum_{i=1}^{N} h(N-i)\Delta y_i(L_{\mathrm{OPD}})\right|, \tag{5.9}$$

which is independent from A. The dependency of the fringe response on sensor operation conditions is qualitatively the same as for the observation factor (see above).

---

[2] Direct spectroscopy is contained as special case with $\nu_a = 0$ and $H_0(\nu) = T(\nu)$

iii. Experimental verification for random noise

For experimental verification of the claim that the noise behavior of the nonlinear curve-fitting in TDLAS context is predicted by its linearization, the following experiment was carried out. Using a 763 nm VCSEL a oxygen absorption line was probed using a standard WMS setup. The normalized second harmonic of the detector signal $y_i = S_2(I_i)/S_0(I_i)$ was fitted with the following model ("single Lorentzian line"):

$$y_i = f_i(\boldsymbol{\theta}) + \epsilon_i \tag{5.10}$$

$$f_i(\boldsymbol{\theta}) = -a_{\mathrm{mol}} \cdot A_2\left((I_i - I_{\mathrm{C}})/I_\gamma, I_{\mathrm{a}}/I_\gamma\right) + y_{o,2} \tag{5.11}$$

$$\boldsymbol{\theta} = (a_{\mathrm{mol}}, I_{\mathrm{C}}, I_\gamma, I_{\mathrm{a}}, y_{o,2})^T \tag{5.12}$$

with ϵ_i representing white noise ($\boldsymbol{W} = \boldsymbol{I}$) on the spectrum with $N = 40$ points. The parameter a_{mol} is the desired peak absorbance value and $A_n(x, m)$ the formula by Arndt Eq. (3.30) which is the ideal shape of the harmonic spectrum for a peak normalized Lorentzian line. The laser injection current values I_i were known and I_{C}, I_γ and I_{a} are the unknown line center, line halfwidth and modulation amplitude with the same units as the I_i. Including an unknown spectral offset $y_{o,2}$ (equivalent to assumption of a quadratic laser power characteristic) the fit has to determine five unknown parameters which are grouped into the parameter vector $\boldsymbol{\theta}$.

There are two nonlinear parameters which determine the performance of the fit significantly: 1) the modulation index $m = I_{\mathrm{a}}/I_\gamma$ and 2) the normalized spectral scanning width $(I_N - I_1)/I_\gamma$. For selected values of both parameters the results are shown in

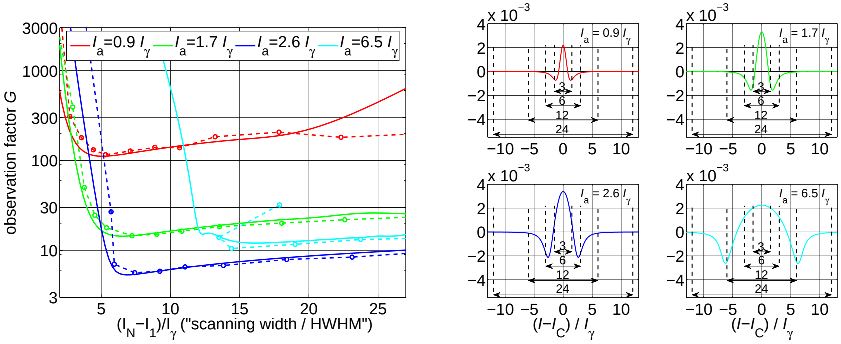

(a) Observation factor for different scanning width (x-axis) and modulation amplitudes (trace). Both theory (solid) and experiment (dashed).

(b) Theoretical reference spectra corresponding to the traces in the left plot, several scanning widths are indicated by arrows.

Fig. 5.2: *Experiment (dashed) and theory (solid) for the observation factor. Both match well in regions where the absorption line is scanned over a sufficiently wide range. In this region the theory for the observation factor is correct and the nonlinear curve-fitting achieves the absolute minimum variance predicted by the Cramér-Rao bound (cf. section 3.4.3).*

Fig. 5.2. The observation factor G was experimentally determined by

$$G_{\mathrm{exp}}(\widehat{I}_{\mathrm{a}}, \widehat{I}_{\gamma}) = \frac{\sigma(\widehat{a}_{\mathrm{mol}})}{\sqrt{R S_{yy}/2}}, \tag{5.13}$$

with $R = 10\,\mathrm{Hz}$ and a noise spectral density of $S_{yy} = 4.75 \times 10^{-12}/\mathrm{Hz}$. The latter was determined in a calibration measurement with spectral scanning turned off and recording data over a long time, which also confirmed that the noise is Gaussian (see Fig. 5.3). Hence, the two conditions (besides the low noise assumption) for the optimality of the least squares curve-fitting are fulfilled.

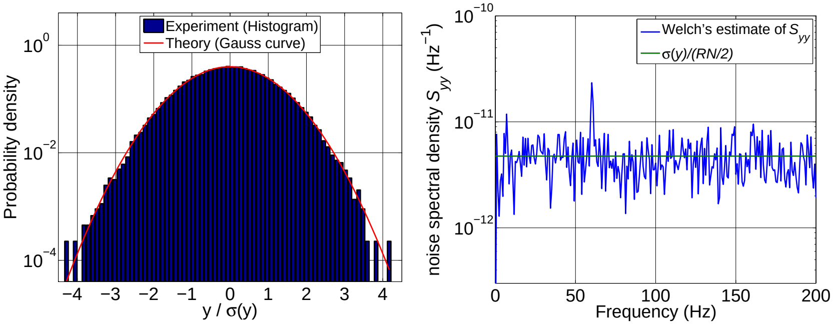

(a) The estimation of the probability density of the noise on the spectrum and comparison with a Gaussian curve.

(b) The noise spectral density estimation using Welch's method and the formula for white noise.

Fig. 5.3: *Probability density and correlation properties of the measurement noise of the particular sensor hardware.*

Several measurements with different sensor settings were done which resulted in different values for the modulation amplitude $\widehat{I}_{\mathrm{a}}$ and scanning width (represented by $1/\widehat{I}_{\gamma}$).

The theoretical observation factor curve is computed using Eq. (5.3):

$$G_{\mathrm{theo}}(I_{\mathrm{a}}, I_{\gamma}) = \sqrt{N(\boldsymbol{F}(\boldsymbol{\theta})^{H}\boldsymbol{F}(\boldsymbol{\theta}))^{+}_{11}}, \tag{5.14}$$

with $N = 40$ points and $\boldsymbol{F}(\boldsymbol{\theta}) = (\nabla \boldsymbol{f}(\boldsymbol{\theta})^{T})^{T}$ the Jacobian of the model Eq. (5.11) and $\boldsymbol{\theta} = (a_{\mathrm{mol}}, I_{\mathrm{C}}, I_{\gamma}, I_{\mathrm{a}}, y_{o,2})^{T}$ the vector of unknown parameters. The peak absorbance for the line was in the range of $a_{\mathrm{mol}} = 10^{-2}$ and the baseline offset $y_{o,2} = 10^{-2}$. But note, that, as explained before, the observation factor does not depend on these linear parameters, and, hence, the actual values are not important. Evaluation using the formula always gives the same result regardless of the value of these linear parameters.

Limit of the validity of the small perturbation approximation: Although the above is correct for the theoretically computed observation factor, the region where the linearization is valid is determined by the linear parameters. This is because the condition of "low noise" is to be understood in a relative sense. Hence, if the absorbance a_{mol} (which is a linear parameter, from which the observation factor is independent) approaches zero, the noise can no longer be considered to be low and the behavior of nonlinear curve-fitting is no longer predictable using its linearization. This is obvious for the extreme case $a_\mathrm{mol} = 0$ because then the measurement signal only consists of the baseline overlapped with noise, and, hence, the unknown parameters, like line half-width I_γ and modulation amplitude I_a can not be extracted by the fit. In fact, the estimates for these parameters will be completely random and do not contain any information about their true values. This causes the peak absorbance estimate to be completely random because the ratio of amplitude on the measurement signal and peak absorbance depends (approximately linearly) on the modulation amplitude I_a. Hence, in this case, the noise on the absorbance will be much higher than that predicted by the observation factor (which is independent from the value of $a_\mathrm{mol} > 0$, and noise on the absorbance should be the same for all positive values of a_mol). But this is not a contradiction to the derived theory, because the noise on the spectrum is simply too high for the small signal approximation to be valid. This explains why the “low noise” condition is to be understood in a relative fashion. Practically, the cases of “high noise” are avoided because the nonlinear curve-fitting does not work well in this domain as the example showed. This demonstrates that the assumptions in the theory of the observation factor and fringe response are suitable in the practical TDLAS sensor context.

5.1.2. Conversion of noise on the spectrum to concentration noise

In the literature several metrics for quantification of noise on the spectrum exist. However, the noise amplitude on the spectrum $\sigma(y)$ is not a relevant metric (see below section 5.1.2.i) because no method is known so far to theoretically relate these values to noise on the concentration values. The solution is provided in this thesis by means of the observation factor G.

In the literature two important measures for the noise density on the spectrum can be found (for definitions see below section 5.1.2.ii):

- **Minimum detectable absorbance per point**: $\mathrm{MDA_{pp}}$ (unit: $\mathrm{Hz}^{-1/2}$).
- **Noise equivalent absorbance sensitivity**: NEAS (unit: $\mathrm{Hz}^{-1/2}\mathrm{cm}^{-1}$).

These numbers are converted to concentration values in the following way:

$$\sigma(\widehat{C}_\mathrm{mol}) = \frac{\sqrt{R/2\,\overline{S}_{yy}}}{\alpha_\mathrm{pk} L}\,G = \frac{\sqrt{R/2}\,\sigma(y)}{\sqrt{N}\alpha_\mathrm{pk} L}\,G = \frac{\sqrt{R/2}\,\mathrm{MDA_{pp}}}{\alpha_\mathrm{pk} L}\,G = \frac{\sqrt{R/2}\,\mathrm{NEAS}}{\alpha_\mathrm{pk}}\,G. \tag{5.15}$$

The relevant quantities nicely enter in this formula. The (average) noise spectral density $\overline{S}_{yy}$ or $\mathrm{MDA_{pp}}$ (together with L) or NEAS are quality measures of the sensor hardware (without gas) and independent from detection bandwidths, sensor measurement rate R or detection method. The target gas peak absorption coefficient α_pk is depending only on the gas type and the spectral region in which the measurement takes place. The effect of the curve-fitting is solely described by the observation factor G. It is independent from the number of spectral points N (at least if the spectrum is sampled adequately dense), any noise amplitude and time resolution. If the noise is non-white the observation factor includes the correlation properties of the noise ($\boldsymbol{W}$ matrix in Eq. (5.3)). The factor is independent from the amplitude of the theoretical gas spectrum, it only depends on the spectral shape and the unknown signal model parameters. The former includes cases with overlapping spectral lines from the same or different gases, change of the spectral range and influence of the WMS modulation amplitude.

The interpretation of Eq. (5.15) is straightforward. The value $\mathrm{MDA}_{\mathrm{pp}}$ is the root of the noise density and has unit of “absorbance per square root of hertz” ($\mathrm{Hz}^{-1/2}$). This value is converted to an absorbance resolution by multiplication of the root of sensor bandwidth ($R/2$) and the unitless observation factor G which quantifies the performance of the data extraction.

The unit of NEAS is “absorption coefficient per square root of hertz” ($\mathrm{cm}^{-1}\mathrm{Hz}^{-1/2}$). Dividing it by the peak absorption coefficient of the target gas and multiplication with root of the sensor bandwidth gives a unit of mixing ratio. Multiplication by the observation factor then yields the sensor resolution including data extraction.

Note, that the factor of 1/2 as in $R/2$ is because the quantities representing spectral densities (i.e., $\mathrm{MDA}_{\mathrm{pp}}$, NEAS and S_{yy}) are taken in the usual one-sided convention of noise spectral densities.

i. Limited relevance of signal to noise ratio on spectra

In the literature often the signal to noise ratio on the spectra is investigated or compared [124, 139, 152–160]. While this measure is relevant for inter-comparisons within the same system with similar parameters it is not meaningful between different systems. This is because the noise amplitude may vary strongly without influencing the noise on the extracted parameters (i.e., the sensor resolution). It is obvious, that the sensor resolution can not depend on the number of points of the spectrum. On the other hand it is clear that the noise behavior of the curve-fit will improve if the number of points of the spectrum is increased (assuming equal noise amplitude on each point). How can this seemingly contradiction be resolved? The answer is that the noise variance on each spectral point increases when the number of points is higher. This is because the time to scan the spectrum is fixed ($1/R$) and an increase of the number of points corresponds to a higher sampling rate. Hence the sampling bandwidth rises and accordingly the noise variance. The relevant noise metric is, hence, the noise spectral density and not the noise variance. In case of white noise, the proper bandwidth normalization is then division of the noise variance on the spectrum by the sampling bandwidth $RN/2$ [3]. This is in agreement with the conclusions in Ref. [150].

ii. Collection of relationships describing noise on the spectrum

In the literature many different quantities to specify the noise amplitude on the measured spectra exist [150]. Using the definitions:

$S_{yy}(f)$	Noise spectral density on spectrum (unit: 1/Hz),
N	Number of points per spectrum (unit: 1),
$R = 1/T_{\mathrm{scan}}$	Measurement rate/inverse scanning time (unit: Hz),

---

[3] Here the single-sided noise spectral density convention is used. For the double-sided convention, division by RN (without factor 2) has to be used.

different noise measures exist in the literature (taken from Ref. [150]):

$\sigma(y) = \sqrt{R/2N\,\overline{S}_{yy}}$	Noise standard deviation on the spectrum (unit: 1),
$\mathrm{MDA}_{\mathrm{ps}} = \sigma(y)/\sqrt{R/2}$	Minimum detectable absorbance per scan (u.: $\mathrm{Hz}^{-1/2}$),
$\mathrm{MDA}_{\mathrm{pp}} = \sigma(y)/\sqrt{RN/2}$	Minimum detectable absorbance per point (u.: $\mathrm{Hz}^{-1/2}$),
$\mathrm{NEAS} = \mathrm{MDA}_{\mathrm{pp}}/L$	Noise equivalent absorbance sensitivity (u: $\mathrm{Hz}^{-1/2}\mathrm{cm}^{-1}$).

Especially the definition of “minimum detectable absorbance” is not consistent in literature because two different normalization methods exist. The $\mathrm{MDA}_{\mathrm{pp}}$ is equal to the square root of the average noise spectral density $\overline{S}_{yy}^{1/2}$ and is a proper metric for comparison. The $\mathrm{MDA}_{\mathrm{ps}}$ is not a useful definition, because it depends on the number of spectral points at equal sensor performance or equal sensor hardware.

5.1.3. Discussion and implications for signal processing improvement

In the following section specific questions regarding signal processing will be answered using the tools developed in the last sections. Because many results are specific to a signal model or sensor hardware model the following typical conditions are assumed:

A single Lorentzian line at SATP (HWHM typically $\nu_\gamma = 2\,\mathrm{GHz}$) and a quadratically modeled laser emission power during scanning are assumed. Unknown parameters are line width, line position and line depth (which is the targeted peak absorbance). The three polynomial coefficients of the laser characteristic are also unknown. For WMS the modulation amplitude is also determined during the fit. For n-th harmonic detection (with $n = 0, \ldots, 2$) the quadratic P-I characteristic translates into a baseline of degree $2 - n$ with accordingly less parameters.

i. Benefit of pre-processing of spectra and or a biased estimation

It is a well established fact from the literature that the signal to noise ratio of the measured spectrum can be significantly improved by filtering [156, 160].

However, it was shown in the previous section that for the class of unbiased estimation the least squares curve-fitting is the optimum parameter extraction method under conditions TDLS sensors are typically operated at. Spectral filtering prior to curve-fitting may enhance the signal to noise ratio but will not improve the overall performance of the curve-fit unless the parameter estimation becomes biased. The condition under which the least squares curve-fitting is the optimum unbiased extraction method is presence of (not necessarily white) Gaussian noise of low amplitude, i.e., low relative variation of the estimated parameters.

As a consequence, spectral pre-processing may only make sense if the conditions for the curve-fitting to be optimal are violated, or if the unbiasedness requirement is given up. Note, that in case of a linear model, linear filtering (e.g., lowpass-, bandpass-, Wiener- or matched- filtering) can only improve the performance at the cost of introducing a sensor bias, regardless of the noise amplitude and noise distribution (because of the BLUE property of the linear fit, cf. section 3.4.3).

This viewpoint is in agreement with the wavelet-denoising approach (which is a nonlinear filtering technique) as demonstrated in Ref [160] which provided a factor of 2 improvement of SNR in the spectra but only around 22 % noise improvement on concentration values[4]. The reason for the small observed improvement may be attributed to a non-ideality of the sensor hardware with non-Gaussian noise or an introduction of an estimation bias. Even if there was no bias observed, the sensor may still introduce a bias that is lower than the noise (and, hence, a bias was not observed). The bias might become evident if averaging is applied to reduce the noise. For the work in Ref [160] this remains unclear. However, this discussion leads to an important question:

Is "biasedness" a disadvantage? Introduction of a sensor bias is not necessarily a disadvantage, provided the introduced bias is smaller than the simultaneous reduction in noise. How much bias can be "afforded" depends on the absolute noise amplitude.

Note, that if the mean square error instead of noise amplitude is the performance criterion (i.e., "accuracy" instead of "precision"), introduction of a sensor bias may lower the absolute error, because the noise attenuation may be higher than the introduced bias. The mean square error $\mathrm{MSE}\{\widehat{\theta}_i\}$ is related to estimation bias $\mathrm{E}\{\widehat{\theta}_i - \theta_i\}$ and estimation variance $\sigma^2(\widehat{\theta}_i)$ by

$$\mathrm{MSE}\{\widehat{\theta}_i\} = \mathrm{E}\{(\widehat{\theta}_i - \theta_i)^2\} = \sigma^2(\widehat{\theta}_i) + \mathrm{E}\{\widehat{\theta}_i - \theta_i\}^2. \tag{5.16}$$

Obviously, only for the class of unbiased estimators a minimum variance also corresponds to minimum error on the estimated parameters. It may theoretically be possible to find estimators which have lower mean square error than the best unbiased estimator. But these estimators are not uniformly better, i.e. over the full parameter range, but only for specific parameters. This may, however, not be suitable for gas sensors.

ii. Influence of the wavelength scanning range

It has been observed before (in section 5.1.1.iii about experimental verification of the theory) that the wavelength scanning range has a great influence on the performance of the sensor. If the scanning range is too small, the noise will be very high and the target parameter can not be well extracted from the measured signal (information is missing). In the other case, if the scanning range is too large, measurement time is wasted during measurement of the baseline which does not contain information about the target parameter and noise will be high as well.

Hence, in a sensor the scanning range should be chosen appropriately for optimum noise performance (corresponding to minima of the observation factor in Fig. 5.2).

iii. Which detection method is intrinsically better: Wavelength modulation spectrometry (WMS) or direct spectrometry (DS)?

Although the second harmonic spectrum has the linear components removed, its amplitude is only about one third of the peak value of the direct spectrum. It is an old question why WMS often achieves superior sensitivities compared to DS[5].

---

[4] The relative noise on concentration values was around 1 %, so the variations can be considered small and the theory here is applicable.

[5] This might not be explained by only the fact, that it is more difficult (but not impossible) to operate DS in domains with same noise spectral density as WMS.

Question: What is better: wavelength modulation or direct spectrometry?

Answer: Theoretically, WMS and DS have approximately equal performance (WMS slightly better) if the laser power characteristic is modeled by a polynomial with degree same as WMS detection order. If the WMS detection order is greater than this polynomial order, WMS performance will be worse and slightly better otherwise. The intrinsic n-th differentiation of WMS only removes information, which the DS fit can not use anyway because of the unknown n-th order multiplicative baseline. Furthermore, WMS has a better natural suppression of fringes with high frequency or high OPD, due to the intrinsic lowpass filtering of WMS.

Detailed Explanation: Since the measurement noise on the direct spectrum and the harmonic spectra have the same amplitude, provided the sensor hardware is properly realized, one might expect that second harmonic detection will give worse results (due to the factor of three lower signal amplitude). However, as stressed in the last sections the signal to noise ratio on the spectra is irrelevant for the overall sensor performance. The correct formulation of the question should be, is there any difference in the observation factor for both detection methods? This takes into account the different amplitudes and includes the performance of the parameter extraction. Additionally, the sensitivity to fringes should be examined as well. Assuming the Lorentzian single line model with variable order laser P-I-characteristic (section 5.1.3) the observation factors (see Tab. 5.1) and fringe response (see Fig. 5.4) for both methods can be computed. Due to the intrinsic filtering property of WMS, the direct spectrum certainly contains more information and it could be expected that the fit to the latter has a better performance, expressed as a lower observation factor. However, this is not always the case, as Tab. 5.4 shows, and, apparently, the intrinsic WMS filtering only removes irrelevant information. This is because of the multiplicative baseline the direct spectroscopy fit has to determine. This essentially renders useless all lower order components of the analytic signal in the transmission. Hence, WMS, which removes these components by the intrinsic differentiation, does not have worse performance. For an explanation why WMS even has a slightly better performance than direct spectroscopy see section 5.1.3.v.

Method	P-I Char. n_{PI}	Det. order n	Scan range $(I_N - I_1)_{\mathrm{opt}}$ $(\times I_\gamma)$	Mod. amp. $I_{a,\mathrm{opt}}$ $(\times I_\gamma)$	Obs. factor G (lower values better)
DS	1	-	6.88	-	3.37
WMS	1	0	6.88	0	3.37
WMS	1	1	4.02	1.63	2.68
WMS	1	2	0.43	2.20	4.37
DS	2	-	14.21	-	4.93
WMS	2	1	9.26	1.73	4.31
WMS	2	2	6.98	2.95	4.80
WMS	2	3	4.57	3.52	5.57

Tab. 5.1: *Noise performance (observation factor) for direct detection and wavelength modulation spectrometry for different orders n_{PI} of the laser P-I-characteristic. The scanning range and modulation amplitude are optimally chosen.*

Note, that the low values of the fringe response for short OPDs (Fig. 5.4) are caused by the fitting of the quadratic baseline of DS and the differentiation property of WMS.

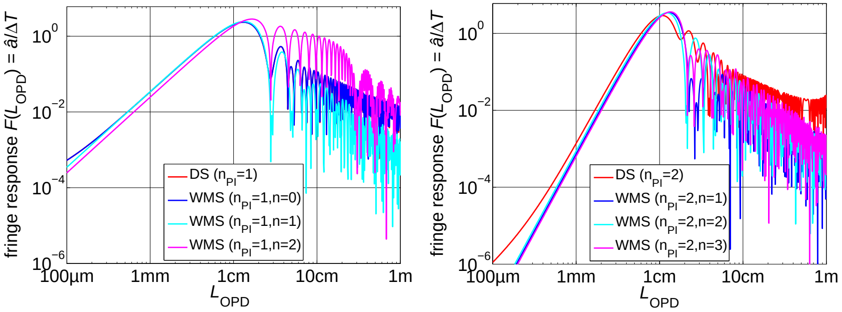

(a) Linear laser *P*-*I*-characteristic (b) Quadratic laser *P*-*I*-characteristic

Fig. 5.4: *The fringe responses for WMS and direct spectroscopy based sensor for a single Lorentzian line model with different laser P-I-characteristic models.*

Fringes of very low periodicity will appear as a slope or bending on the scanned spectrum and are indistinguishable from a modified laser *P*-*I*-characteristic. Hence, the fit of the multiplicative baseline (for DS) or the intrinsic differentiation will yield same performance with fringes from low OPD. This explains the differences in fringe response for low OPDs for linear and quadratic laser power characteristic and the (approximately) equal response of DS and WMS under same conditions. This is in agreement with the experimental results in Ref [161], where no significant difference between WMS and DS was found[6].

The high frequency fringe filtering (high OPDs) for WMS is better due to the intrinsic lowpass filtering after the n-th differentiation.

The relatively worse fringe response of WMS with $n = 2, n_{\mathrm{PI}} = 1$ has no fundamental reason, but is due to the low scanning range (cf. Tab. 5.1). The scanning range is significantly lower than for the other methods because the spectrum has no baseline and the optimum range is just a small region around the center peak.

iv. Comparison of different detection methods (optimum sampling, single- and multi-harmonic WMS and DS)

In the last section (single harmonic detection) WMS and DS performance was compared and it turned out, that WMS has equal or slightly better performance than DS if the detection order n is not larger than the order of the laser power characteristic n_{PI} . This is despite the fact, that single harmonic WMS only utilizes a part of the detected signal power.

In this section the reason for the (slight) differences are analyzed and a comparison of WMS and DS to the absolutely best detection method is done. For this the optimum sampling theory which was originally co-developed in this thesis for linear models [53]

---

[6] Unfortunately, the authors do not specify all relevant details of the signal processing. The order of the baseline for DS is unknown. Furthermore, a two step fitting process is made with an unclear theoretical performance compared to the optimum case. Hence, this experimental results only show that direct detection is not worse than WMS.

is applied to the non-linear model. The obtained wavelength sampling method has best noise performance of all detection methods, i.e., achieves, by definition, the lowest possible observation factor for the particular model under consideration.

In Tab. 5.2 the theoretically computed performance measures for four different detection methods are shown. The corresponding signal model, scanning range, measurement signal and fringe response are shown in detail in Fig. 5.5. The best noise performance has (by definition) optimum sampling, which achieves an observation factor as low as $G = 2.99$. Direct spectrometry achieves under optimum conditions only $G = 4.93$ which is 1.64 times worse. However, due to the discreteness of the optimum spectral sampling, its response to fringes is orders of magnitude worse compared to the other methods which employ (quasi) continuous sampling. It turns out, that multi-harmonic detection theoretically can provide both a near optimum noise performance and very good natural suppression of fringes. Hence, multi-harmonic detection is a promising method and investigated in detail in section 4.2.

	Parameter		Noise	Response to fringe with L_{OPD}				
Method	$(I_N - I_1)_{\text{opt}}$ ($\times I_\gamma$)	$I_{a,\text{opt}}$ ($\times I_\gamma$)	G	100 µm ($\times 10^{-7}$)	1 mm ($\times 10^{-4}$)	1 cm ($\times 1$)	10 cm ($\times 10^{-2}$)	1 m ($\times 10^{-3}$)
OPT	−(discr.)	–	2.99	480	100	2.7	250	2500
mWMS	9.95	2.72	3.24	1.4	14	2.7	2	1.2
sWMS	7.00	2.96	4.80	1	89	2.9	4	2
DS	14.38	–	4.93	12	14	2.8	8	30

Tab. 5.2: *Characteristic parameters of different detection methods (Optimum sampling, multi-harmonic WMS, second harmonic WMS, and direct detection). The scanning range and WMS modulation amplitude were chosen for minimum noise. The methods have different noise behavior and different natural sensitivity to fringes.*

v. Overall sensor performance

Question: Why direct spectrometry (DS) theoretically has a 50 % worse noise performance compared to multi-harmonic wavelength modulation spectrometry even under idealized, equal and (for each method) optimum conditions?

Answer: The distribution of the emitted laser wavelengths (or injection currents) is more fortunate for multi-harmonic WMS than for DS. Effectively more time is spent around the absorption line (see Fig. 5.7).

Explanation: In the last sections it was shown, that wavelength modulation spectrometry (WMS) and direct spectrometry (DS) have different observation factors, even if the operation conditions like wavelength scanning range and modulation amplitude were optimally chosen (see Tab. 5.2). The overall performance of any TDLAS method only depends on the system model, the total spectral frequency coverage during one scan (”‘which wavelengths/frequencies”’) and the relative distribution of time the laser spends on different frequencies regions during the scan (”‘how long?”’). The system model is independent from the specific detection method, it essentially describes the behavior of the black-box containing optical system with laser and detector (for illustration see Fig. 5.6). This system has just an electrical input (laser control) and electrical output

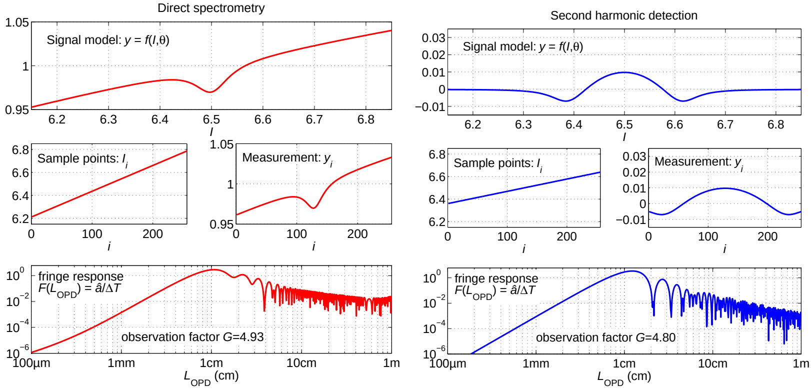

(a) Direct spectrometry with scanning range optimally chosen for minimum observation factor.

(b) WMS second harmonic detection with scanning range optimally chosen for minimum observation factor

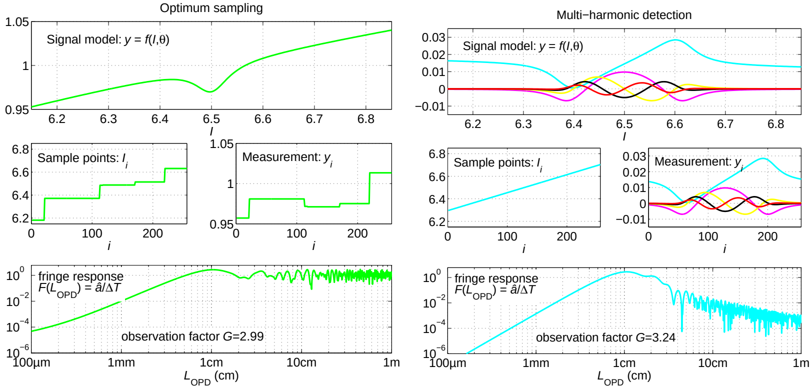

(c) Optimum sampling. This achieves the minimum observation factor for the given spectral model.

(d) WMS multi-harmonic detection with scanning range optimally chosen for minimum observation factor

Fig. 5.5: *Comparison of different detection methods. The behavior of the hardware as black-box* $y = f(I, \boldsymbol{\theta})$*, the sampled values* I_i*, the corresponding measurement signal* $y_i = f(I_i, \boldsymbol{\theta})$ *and the resulting fringe response* $F(L_{OPD})$ *with observation factor* G *are shown.*

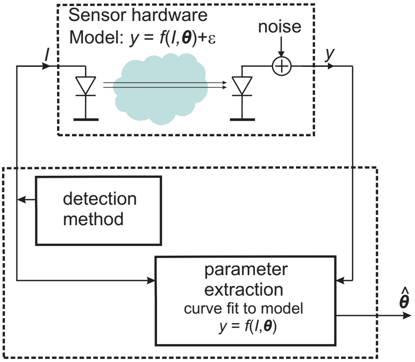

Fig. 5.6: *The abstract sensor model. The measurement hardware is described by the model function* $f(I,\boldsymbol{\theta})$ *with unknown parameter vector* $\boldsymbol{\theta}$*. The detection method selects specific I values for one scan and the data extraction estimates the unknown parameter vector* $\boldsymbol{\theta}$ *using curve-fitting with the known model. The key understanding is that sensor performance (noise on the* $\widehat{\boldsymbol{\theta}}$*) is solely determined by the distribution of I values during one scan.*

(detector current or preamplifier output).

How the parameter extraction is exactly implemented does not matter if it is assumed to be optimally operating. Hence, whether there is a decomposition of signals with a lock-in amplifier before fitting of all harmonics or a direct curve-fitting of the detector signal makes no difference[7].

In case "‘important"’ regions of the transmission (i.e., those which are more sensitive to changes by parameters one is interested in) are measured over longer time fractions, than other "‘unimportant"’ frequency regions, a better quality of extraction of wanted parameters can be expected. The same is true vice versa, if less important regions of the transmission are sampled over relatively long fractions of time the extraction will be of less quality. This may be for example illustrated in a very simplified model, where a single absorption line is scanned and the peak absorbance and baseline offset is unknown. If the measurement of the baseline consumes far more time than measurement of the absorption line peak performance will be non optimum. This is because the peak absorbance is the difference between both values and measurement of them should be done with same precision, i.e., the same amount of time should be spent for both points.

Hence, differences for WMS and DS must be explainable by the time distribution of the emission wavelength (or laser current) during one scan. This distribution can be simulated and is depicted in Fig. 5.7. DS realizes an uniform coverage and WMS spends relatively more time around the absorption line because the modulation covers of the inner wavelength points more often. Also shown in the figure is the optimum spectral sampling. There the wavelength points are chosen optimally for lowest possible observation factor. Although the current values are free during optimization, a discrete sampling is obtained. For linear signal models this has been co-developed with J. Chen

---

[7] This is because the optimality property of the fit is not changed by linear transforms such as Fourier decomposition of the data before fitting.

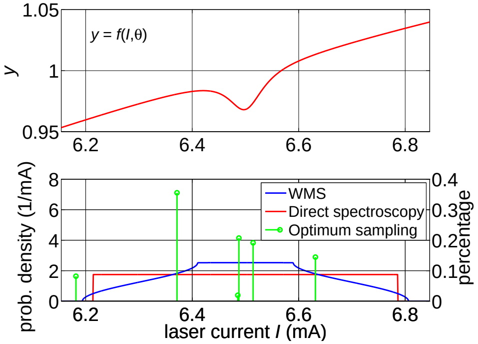

Fig. 5.7: *The frequency coverage during one spectral scan by several methods. If all information at the detector is used for data extraction, this coverage function solely determines the noise performance.*

and was published in Applied Physics B [53] and the TDLS conference [162].

Although the performance difference between (multi-harmonic) WMS and optimum sampling is not great ($G = 2.99$ versus $G = 3.24$) the wavelength coverage is very different. This shows that a close to optimum noise performance can also be achieved with continuous scanning. This has better performance in terms of fringes than the discrete jump-scanning (cf. Fig. 5.5).

vi. Shaping the fringe response

In the last section only the white noise performance was optimized (i.e., minimum observation factor) and the fringe response was obtained as a result.

Note, that the fringe response depends on the spectrum scanning range and on gas pressure or more precisely absorption linewidth. For optimum observation factor there is an optimum scanning range. However, for a good fringe suppression it is typically better to have a wide scanning range. For an example of bad fringe response because of low scanning range see the purple curve in the left plot of Fig. 5.4 (the scanning width is noted in Tab. 5.1). For the influence of a pressure change see section 5.8 (The curve belongs to direct detection with second order laser characteristic, parameters as given in Tab. 5.1 and curve shown in right plot of Fig. 5.4). The optimum scanning width of the spectrum scales with reduction of linewidth. If the scanning width would not be shrinked together with the linewidth, a better fringe response but worse observation factor would be obtained.

It would be beneficial if the fit would implement an optimum trade-off between noise performance and low fringe response (at least at prescribed OPDs, e.g., multiples of the cell length). An old method of fringe suppression is inclusion of a sinusoid with known frequency in the curve-fit model. This does not work very well, because the sinusoidal distortion on the spectrum is not as narrowband as assumed by the model. In fact, the fringe distortion is random and possesses a certain bandwidth or distribution around a certain base periodicity even during a single spectral scan.

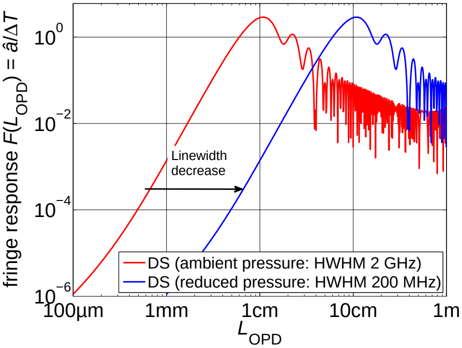

Fig. 5.8: *The x-axis of the fringe response is scaled when the linewidth of the absorption line is changed (or, equivalently, the x-axis of the spectrum is scaled). Hence, pressure reduction improves behavior at low OPD but worsens behavior at high OPD.*

This problem can be solved if the white noise together with the fringe are treated in the same way. In this case the noise spectral density consists of a white noise component (this is the noise by electronic components) and a narrowband distortion (which models the fringe). The specification of the relative strength then allows for the fit to implement fringe suppression optimally. This information enters the fit using the covariance structure matrix $\boldsymbol{W}$ which is computed from the noise spectral density with Eq. (3.84)

An example is shown in Fig. 5.9. There a fringe corresponding to an optical path length difference of 10 cm with a bandwidth corresponding to ±0.3 cm was assumed. As can be seen in the figure, specification of the proper covariance matrix causes fringes

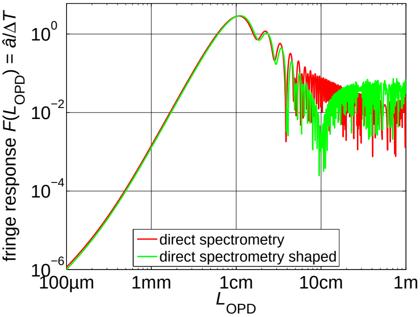

Fig. 5.9: *The fringe response of the sensor using standard curve-fitting (red) and curve-fitting with the modified covariance matrix to include the presence of fringes (green) at optical path length differences of around* 10 cm.

with specified periodicity to be suppressed by an additional order of magnitude. The observation factor rises only slightly (from $G_{\text{shaped}} = 4.96$ versus $G_{\text{non-shaped}} = 4.93$). This is because the fringe response was already very low at $L_{\text{OPD}} = 10\,\text{cm}$. The (non-shaped) fringe response is also a measure of the distribution of signal energy. In regions with high fringe response (i.e., where the parameter extraction is very sensitive to sinusoidal distortion) much information is present about the wanted parameter. This is because the fit selects the information from the spectrum based on the assumption that all frequency components are distorted by the same amount of noise (this is the white noise assumption, reflected by the choice $\boldsymbol{W} = \boldsymbol{I}$). With a nontrivial a noise covariance matrix ($\boldsymbol{W} \neq \boldsymbol{I}$) the fit weights components with different periodicity accordingly. This then shapes the fringe response. However, the observation factor will rise because the fit may not be able to use the important components. Especially, if those components, which correspond to $L_{\text{OPD}} \approx 1\,\text{cm}$, are heavily distorted, the observation factor will be very high. Consequently, efficient fringe response shaping is only possible if the fringe response is already low, or, equivalently, if the signal does not overlap with the fringe in the frequency domain. This is in agreement with section 3.3.6.i where it is argued, that for an efficient fringe suppression using signal processing, fringe and analytic spectrum have to be separated in the Fourier domain.

5.2. Obtained design guidelines

From the theoretical conclusions in the last sections, the optimum sensor should implement multi-harmonic WMS with curve-fitting and an optical cell avoiding critical distances that may cause interference. For information on what distances are critical for the specific method see, e.g., Fig. 5.4. In case interference can not be avoided, methods for physical separation of fringe and analytic signal should be used, e.g. Zeeman spectrometry or vibration of the cell. The sensor electronics should be designed to generate white noise only, pre-filtering of spectra is not necessary. In case of a residual interference/fringe structure on the spectrum or possibly non-white noise, the proper noise covariance matrix should be specified in the fit.

Alternatively to multi-harmonic WMS, direct detection or single-harmonic WMS can be used, wheras in the latter case the detection order should not be greater than the order of the modeled laser P-I characteristic.

Detailed explanation

Optical cell Although TDLAS is called absorption spectrometry, physically a transmission measurement is performed. Even through ideal normalization with laser power and the optical path length, only the attenuation coefficient is obtained (see section 3.2 for definitions of terms). However, for a qualitative gas measurement the absorption coefficient is needed. For attenuation and absorption to be the same, one has either to exclude absorption, scattering, reflection, refraction effects from the list of possible effects influencing attenuation, or to separate these effects by other means. Since many of these unwanted effects are broad-band only interference created from multi-path propagation is a relevant distortion for laser spectroscopic gas sensing.

Use of special detection methods for fringe reduction is not advised, because there is no advantage over digital filtering (see section 3.3.6.i), or, equivalantly, inclusion of the finge distortion in the model's noise spectral density. Direct detection and (single or multi-harmonic) WMS have approximately the same natural fringe response whereas WMS performs slightly better at high OPDs because of its intrinsic filtering (see Fig. 5.4 in section 5.1.3.iii). Fringes should either be avoided by avoiding critical distances during cell design (for qualitative comparison see Fig. 5.4 in section 5.1.3.vi) or by using special physical means like mirror vibration or Zeeman modulation. Single mode optical cells should have lengths of 10 cm or more for atmospheric pressure operation. In any case, the fringe response can be shaped by specification of a proper noise covariance matrix (see Fig. 5.9 in section 5.1.3.vi), but at cost of reducing the white noise performance. The latter automatically performs fringe suppression in optimum relation to the other (white) measurement noise. Reduced pressure should be avoided with compact optical cells because then the OPDs which cause maximum distortion are close to the cell length (see Fig. 5.8 in section 5.1.3.vi).

Data processing Data processing should be done by (single step) least squares curve-fitting because it gives the minimum variance on the extracted parameters under general assumptions (Gaussian distributed noise with low relative amplitude, see section 3.4.3). Hence, pre-filtering of spectra can only be beneficial if these assumptions are violated, which is, however, not the case for typical TDLAS sensors (see section 5.1.1.iii). Filtering of special components can be implemented by specifying the covariance matrix of the noise on the spectrum (see section 5.1.3.vi). Processing of the data by a lock-in amplifier prior to curve-fitting instead of direct curve-fitting of the detector signal does not give worse performance, because lock-in detection is a linear transformation that does not affect the optimality of the curve-fit (at least if all harmonics are utilized). For single-harmonic detection this is not true because only part of the information is passed to the curve-fit.

Detection method The best detection method, examined and developed in this work, is multi-harmonic WMS but, however, all methods including single- and multiharmonic detection WMS and direct detection are within a factor of two close to the absolute optimum (see section 5.1.3.iv). Due to the better wavelength distribution during one scan, even single-harmonic WMS is, in certain cases, slightly better than direct detection in terms of noise, even though the signal energy at the detector is not fully utilized. For single-harmonic detection WMS the detection order should not be higher than the order of the polynomial of the laser P-I characteristic (see section 5.1.3.iii). Because of the sinusoidal modulation, the compensation of a non-ideal laser FM response is easier for WMS than compared to DS.

5.3. Sensor for air quality (Gases: CO_2 and H_2O)

Carbon-Dioxide (CO_2) is an important gas for environmental, industrial and medical applications. The background level of CO_2 present in outside air (~400 µL/L) is very small compared to the amounts of CO_2 that are exhaled by humans or animals (up to 40 000 µL/L). In closed rooms the CO_2 concentration rises strongly when one or more persons are present, which happens more often during wintertime. CO_2 sensors allow for an optimized air conditioning, and the energy savings can lead to an important cost reduction for automatically ventilated buildings. CO_2 monitoring for automotive applications serves the same purpose [163]; with the possible further application of detection of dangerous CO_2 levels, which may occur when the future refrigerant for automotive air-conditioning systems R744 (CO_2) leaks into the cabin of the car. Although CO_2 itself is not poisonous, high ambient CO_2 concentrations (vol% range) inhibit the CO_2-O_2 gas exchange in the lung, and, can cause a life threatening situation, even if still enough O_2 is present. Besides leaking of large amounts of CO_2 in industrial or environments with volcano activity, high CO_2 levels may occur in any closed compartments where biological fermentation takes place that steadily generates CO_2 which may accumulate on the ground (e.g., in silos, cellars for wine making and caves). Therefore, CO_2 sensors for these applications are strongly required and have to fulfill several requirements like long-term stability, reliability and fail-safe operation.

These requirements are difficult to meet with the most prominent/conventional industrial solution for CO_2 detection: NDIR spectrometry (Non-dispersive infrared spectrometry). It uses a broadband lightsource (glow lamp, LED) a filter and a detector to detect the light attenuation from CO_2 in its fundamental absorption band at 4.3 µm wavelength [163, 164]. Also electro-chemical sensors [165] and experimental chemical sensing techniques for CO_2 exist. However, all electrochemical or NDIR-spectrometry based sensors do not have the ability of self-monitoring and have to be replaced or tested from time to time if reliable operation is needed.

In contrast to this, laser spectroscopy based sensors do not suffer from these drawbacks (see section 1.3.3). Widespread use of these sensors is limited by the price of the laser diode. Promising, more cost efficient solutions are based on vertical-cavity surface-emitting lasers (VCSELs) that have several advantages over DFB edge-emitters in mass production like on-wafer testability. Existing laser based sensors for CO_2 are either complex instruments for isotopic ratio measurements operating in the MIR at 4.3 µm [166], based on fibers and multipass cells at 1.5 µm [74] or at 2.0 µm with several cm optical path length but using DFB lasers and conventional line-locking [167].

In addition to the advantages TDLAS inherently provides, a simultaneous gas measurements can be performed with no increase of sensor complexity. In this work measurement of two gases (CO_2 and H_2O) will be demonstrated by fitting overlapping spectral lines. Additional measurement of H_2O is important for air-quality applications because, among other factors, the “sick building syndrome” [168] is caused by deficient ventilation or malfunctioning air-condition and linked to high humidity concentrations.

5.3.1. Sensor design

Besides their low-cost potential, VCSELs have other significant advantages compared to DFB lasers, like low power consumption and wide current tunability (cf. section 2). In this sensor a 2 µm VCSEL is utilized, which is able to scan at least several nm via current tuning covering several CO_2 and H_2O lines (Fig. 5.12a). Because CO_2 and H_2O have ambient concentrations of at least 400 µL/L and 10 000 µL/L respectively, absorption lines always exist in the scanned spectrum of ambient air. This allows for application of the wavelength stabilization method developed in section 4.1, which itself is based on the knowledge gained during analysis of the WMS method. The absorption features are detected and assigned to theoretical line data with an algorithm that works under all concentration ratios of H_2O and CO_2, provided the CO_2 concentration stays above its ambient level of 400 µL/L. By comparison of experimental line positions with theoretical data the wavelength scale for the scanned spectrum is obtained. Compared to ordinary line locking, where only the wavelength offset is adjusted, the linear and quadratic tuning coefficient are determined without having a reference etalon. This, including the multi-line curve fitting, is realized for the first time in the present sensor.

i. Spectral model and data processing

Using the wavelength scale information a non-linear fit is avoided (gas pressure and temperature are known). As a consequence, it is possible to employ an efficient linear curve fitting routine which allows for a measurement rate of $R = 10\,\mathrm{Hz}$ with a 20 MHz clock frequency, 16 bit micro-controller. The employed linear fitting is given by formula Eq. (3.86) with $\boldsymbol{W} = \boldsymbol{I}$ to reflect the white noise assumption and $\boldsymbol{F}$ is the 64×4 observation matrix:

$$F_{i1} = H_2(\nu(I_i); I_a\nu'(I_i))\big|_{\mathrm{Abs(CO2)=1,Abs(H2O)=0}}, \qquad \text{“CO}_2\text{ spectrum”} \tag{5.17}$$

$$F_{i2} = H_2(\nu(I_i); I_a\nu'(I_i))\big|_{\mathrm{Abs(CO2)=0,Abs(H2O)=1}}, \qquad \text{“H}_2\text{O spectrum”} \tag{5.18}$$

$$F_{i3} = 1, \qquad \text{“Offset”} \tag{5.19}$$

$$F_{i4} = i/N - 1/2, \qquad \text{“Slope”}. \tag{5.20}$$

The values I_i are the known laser current values of the spectral sample and $\nu(I_i)$ is the wavenumber of the spectral sample. The current to wavenumber tuning behavior $\nu(I)$ is known and repeatedly re-updated with the mentioned wavelength stabilization method. The current modulation amplitude I_a is known and the wavelength modulation amplitude determined from the static tuning coefficient expression Eq. (2.12). The harmonic spectra are computed with peak absorbance of the CO_2 and H_2O line scaled to 1 or 0, respectively. The first two unknown parameters θ_1 and θ_2 are the peak absorbance of the two gas lines and related to the concentrations by Eq. (3.74). For the utilized lines around 2.003 µm the peak absorption coefficients of the two lines are [6]:

$$\alpha_{\mathrm{CO2}} = 0.1334\,\frac{1}{\mathrm{cm}}, \qquad \alpha_{\mathrm{H2O}} = 5.184 \times 10^{-3}\,\frac{1}{\mathrm{cm}}. \tag{5.21}$$

To theoretically quantify the white noise performance of the sensor, the observation factor of the model is computed according to the theory developed in section 5.1.1:

$$G_{\mathrm{H2O}} = 7.0, \qquad G_{\mathrm{CO2}} = 6.8. \tag{5.22}$$

These values are slightly higher than for typical single line models (~ 5) because the two gas lines are overlapping. Although the fit will separate both spectral components in an ideal way (in the sense that there is no cross-sensitivity) provided the reference spectra are ideally exact, this is at the cost of a worse noise performance. Essentially, it is because of the non-orthogonality of these two lines. However, the cost of resolving these overlapping lines is less than a factor of two compared to individual single gas measurements. Using the observation factor, the theoretically expected sensor resolution in absolute units can be obtained. First, this will be done for absorbance (for comparison between sensor realizations) and, second, the concentration (for judging the sensor performance for the application): Assuming a noise spectral density on the recorded spectra of $\overline{S}_{yy} = 2 \times 10^{-6}/\mathrm{Hz}$ [8] a one hertz time resolution ($R = 1\,\mathrm{Hz}$), an absorbance

---

[8] Corresponds to a laser with relative intensity noise of RIN = −120 dB

resolution and concentration resolution of

$$\sigma(\widehat{a}_{\mathrm{H2O}}) = 7 \times 10^{-6}, \qquad \sigma(\widehat{a}_{\mathrm{CO2}}) = 6.8 \times 10^{-6}, \tag{5.23}$$

$$\sigma(\widehat{C}_{\mathrm{H2O}}) = 68\,\frac{\mu\mathrm{L}}{\mathrm{L}}, \qquad \sigma(\widehat{C}_{\mathrm{CO2}}) = 2.6\,\frac{\mu\mathrm{L}}{\mathrm{L}}, \tag{5.24}$$

is obtained (cf. Eq. (3.74) and Eq. (5.1)).

ii. Optical cell design

Applying the theory developed in section 5.1.1 the sensitivity of the sensor to interference on the transmission can be quantified by simulation (see Fig. 5.10). These includes all effects such as the differentiating property of WMS and the filtering of the curve fit. This gives indication which optical path length between reflectors in the optical setup have to be avoided and how strong the multi-path propagation must be attenuated by the optical design to not distort the measurement. For a maximum concentration error corresponding to an absorbance of 7×10^{-6} (which is theoretical white noise limit Eq. (5.23)) the interference from detector window-chip reflections and the full cell length reflections must have amplitudes below 0.01 and 8×10^{-4}, respectively. Interference corresponding to distances between reflecting surfaces of 1 cm generate a more than two to three orders of magnitude higher error on the concentration values and hence must be avoided in the optical setup. Note, that the peaks at $L_{\mathrm{OPD}} = 60\,\mathrm{cm}$ in Fig. 5.10 are caused by "aliasing" due to the spectral sampling with $N = 64$ points.

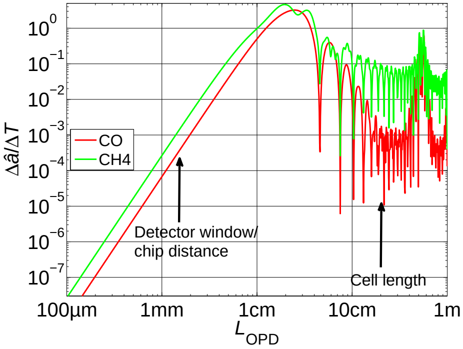

Fig. 5.10: *Simulated fringe response of the sensor. For a maximum distortion of concentration values corresponding to* 7×10^{-6} *absorbance, the interference amplitude on the transmission must be below* 0.01 $(= 7 \times 10^{-6}/7 \times 10^{-4})$ *and* 8×10^{-4} $(= 7 \times 10^{-6}/9 \times 10^{-3})$ *for the reflections inside the detector housing and the whole cell, respectively.*

In Fig. 5.11 the folded optical cell design ($L = 20\,\mathrm{cm}$) is shown. Physical distances corresponding to the high sensitivity OPD region in Fig. 5.10 are avoided.

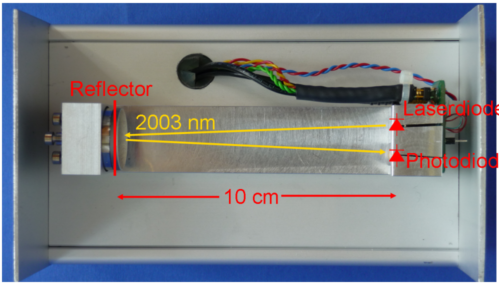

Fig. 5.11: *Schematic of the sensor optics. The optical path length is* 2 × 10 cm. *The* 2.0 µm *VCSEL and the InGaAs photodiode are mounted side by side.*

5.3.2. Experimental results

The linear curve-fit with computed reference spectra is done in 200 ms intervals ($R = 5\,\mathrm{Hz}$) ("narrow wavelength scans", Fig. 5.12b) where the CO_2 and H_2O concentrations are determined. Every few seconds a wide spectral scan is done to recalibrate the wavelength scale (Fig. 5.12a). Recorded spectra (non-averaged) are shown in Fig. 5.12a and Fig. 5.12b respectively. The sensor was tested during a day inside a household; with averaging time set to 30 s (Fig. 5.13). Although relative humidity stays almost constant during a day, the CO_2 concentration varies strongly. Between 13h and 15h and after 22h no persons were in the room so a decay of CO_2 is observed. With presence of one or more persons a steady concentration increase is observed (despite the very high volume of the room of $> 300\,\mathrm{m}^3$), whereas positive or negative peaks correspond most likely to open windows or persons standing near to the sensor.

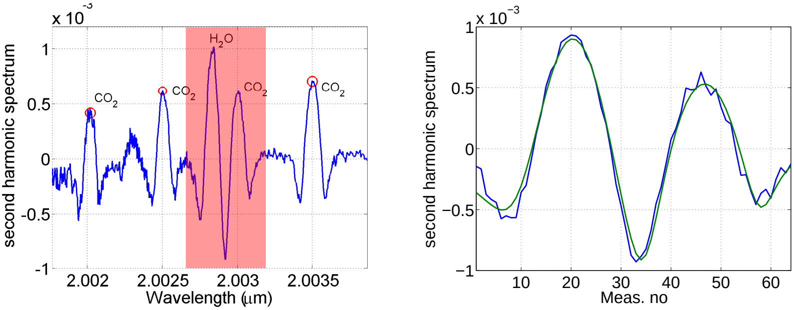

(a) The wide spectral scan for wavelength identification. At least three CO_2 absorption lines (red circles) serve as wavelength markers to determine the linear and quadratic coefficients of the wavelength scale. The red box marks the range of the narrow scan

(b) The narrow spectral scan (blue) and corresponding linear curve fit (green) with computed spectra from theoretical absorption line data. It consists of overlapping H_2O (right, 2.0028 µm) and CO_2 (left, 2.003 µm) absorption lines

Fig. 5.12: *Wide and narrow spectral scan*

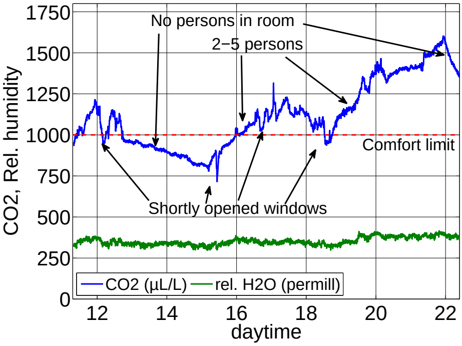

Fig. 5.13: *Measured CO_2 concentrations (blue) and relative humidity (green) during a day inside a household. The averaging time was set to* 30 s.

5.3.3. Summary

A compact TDLS-based CO_2 and H_2O sensor was realized. It is based on a single 2.0 µm VCSEL and employs a 20 cm double-pass cell. The sensor employs a repetitive inherent wavelength calibration every few seconds using broad wavelength scans covering at least four CO_2 absorption lines that serve as wavelength markers. This is possible because of the large current tuning range provided by VCSELs. Besides compensation of wavelength drift due to laser aging, knowledge of the full wavelength scale – not only wavelength offset – enables the use of an efficient linear curve fitting routine that is particularly suited for micro-controllers with only low computation power. Compared to other CO_2 sensors, a laser based sensor can be designed for self-monitored, fail-safe and calibration-free operation. This is particularly important for safety applications where long-term stability and reliability needs to be guaranteed.

5.4. Gas sensor based fire detection (Gas: CO)

For industrial and safety applications, e.g., exhaust-gas monitoring, fire detection and workplace monitoring, reliable and long term stable sensors are required. Spectroscopic gas sensors usually have the lowest possible cross-sensitivity to other gases due to the spectroscopic measurement. TDLAS has the further advantage that sensors allow for self-monitoring to enable fail-save operation.

Carbon monoxide (CO) is a toxic gas and affects human health whenever it is present in ambient air in high concentrations. The threshold limit value for carbon monoxide by the American Conference of Governmental Industrial Hygienists is 25 µL/L [169]. Carbon monoxide can be generated by fires in large amounts and CO poisoning is the most frequent cause of unintentional death at home in the USA with a death toll of about 500 persons per year [170]. Usually fire detection is done by employing temperature sensors or smoke detectors which sense particles by either a scattering or ionization effect. Although these detectors can be very sensitive, and are the most frequently used fire detectors, they have several disadvantages. The false alarm rate can be very high (up to 50 % of all alarms, or in some areas up to 99 % according to Ref. [171]), due to unwanted cross-sensitivities to other gases and all kinds of particles that are not necessarily generated by fires, e.g., water vapor, hairspray, insects or general dust.

A relatively new approach to fire detection is the use of gas sensors to detect prominent combustion gases like carbon monoxide (CO), nitrogen oxides (NO, NO_2) or carbon dioxide (CO_2). In the literature, fire detection using hybrid suspended gate field effect transistors [172], TDLAS-based photoacoustic sensors [137] with simultaneous detection of traces of NH_3, C_2H_2 and HCN for spacecraft applications [173], as well as sensors based on near-infrared ($\lambda = 1.5\,\mu m$) TDLAS detection of CO and CO_2 [74, 171, 174] are reported. Smoldering fires usually generate high fluxes of CO, while fires with visible/open flames generate less, but still significant, amounts of CO and also certain levels of nitrogen oxides. CO_2 is present in ambient air ($\sim 380\,\mu L/L$ in outside air) and is generated in large amounts by human beings and animals ($\sim 40\,mL/L$ in exhalation), so a CO_2-only based gas sensor fire detector would suffer from an increased false alarm rate or reduced fire detection sensitivity. Furthermore, the levels of nitrogen oxides generated by fires are often significantly lower than the concentration level of the generated carbon-monoxide.

5.4.1. Sensor design

The sensor used for the experiments and the measurement principle was co-developed within this thesis and has been published in Applied Physics B [54, 175]. The optical cell (Fig. 5.14) realizes an absorption path length of 10 cm, which is enough to achieve a sensor resolution in the lower µL/L range. Compactness ($\sim$ 7 cm) is further improved by using a folded optical geometry and the novel feature of a reference gas filled in the photodetector housing, so that additional optical components, e.g., separate reference cell, second detector, beam splitter are spared. Conventionally, a separate reference cell containing the target gas is used for stabilization of the laser emission wavelength to the center of the target absorption line [74, 171, 174]. Using the inline wavelength stabilization method developed within this thesis (see section 4.1) this additional complexity is avoided. Adjacent absorption lines of methane (CH_4), which is filled inside the photodetector housing, are used for wavelength identification. This

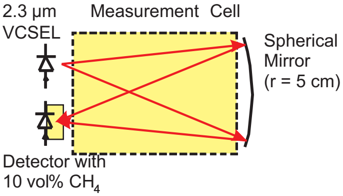

Fig. 5.14: *The compact optical cell with overall dimensions of* $\sim$ 7 cm. *The folded geometry provides an absorption path length of* 10 cm *between laser and photodetector. The photodetector housing is filled with* CH_4*, which is used for wavelength stabilization and makes a separate reference cell unnecessary.*

allows for determination of both the absolute emission wavelength as well as the linear and quadratic tuning coefficient of the laser. Note, that this technique takes advantage of wide current tunable lasers like VCSELs [35, 36, 48] so that both the CO and CH_4 absorption lines at 2.365 µm can be included in a single scan.

The WMS modulation frequency is $f_m = 6\,\mathrm{kHz}$ with a spectral scan repetition rate of $R = 10\,\mathrm{Hz}$. The wavelength modulation amplitude is set to a value of approximately three times the half-width of the CO line at ambient conditions, because this is the optimum setting as the spectral baseline is also fitted. Each spectrum is curve-fitted and a concentration value is obtained, whereas the concentration values are averaged afterwards. For the following fire-detection experiments, the averaging time of the sensor was set to 60 s to minimize the sensor noise on the concentration values at an acceptable time resolution for fire detection.

The concentration values are determined by a linear least squares curve-fit to synthetic reference spectra. These reference spectra are based on the line parameters from the HITRAN database [19] and the Lorentzian linshape model [71].

For the CO and CH_4 lines in the range of the narrow scan 2.365 15 µm to 2.3658 µm the peak absorption coefficients of the two spectra are [6]:

$$\alpha_{\mathrm{CO}} = 0.3569\,\frac{1}{\mathrm{cm}}, \qquad \alpha_{\mathrm{CH4}} = 0.076\,92\,\frac{1}{\mathrm{cm}}. \tag{5.25}$$

To theoretically quantify the white noise performance of the sensor the observation factor of the model is computed according to the theory developed in section 5.1.1:

$$G_{\mathrm{CO}} = 7.9, \qquad G_{\mathrm{CH}_4} = 13.1. \tag{5.26}$$

Assuming a noise spectral density on the recorded spectra of $\overline{S}_{yy} = 10^{-6}/\mathrm{Hz}$ (laser relative intensity noise was measured to be RIN $= -120$ dB), a one hertz ($R = 1\,\mathrm{Hz}$) time resolution, an absorbance resolution and concentration resolution of

$$\Delta\widehat{a}_{\mathrm{CO}} = 5.6 \times 10^{-6}, \qquad \Delta\widehat{a}_{\mathrm{CH4}} = 0.93 \times 10^{-5}, \tag{5.27}$$

$$\Delta\widehat{C}_{\mathrm{CO}} = 1.56\,\frac{\mathrm{\mu L}}{\mathrm{L}}, \qquad \Delta\widehat{C}_{\mathrm{CH4}} = 12.0\,\frac{\mathrm{\mu L}}{\mathrm{L}}, \tag{5.28}$$

is theoretically predicted (Eq. (3.74) and Eq. (5.1)). This value is a factor of 2 worse than the experimentally obtained CO resolution of 3 µL/L and attributed to the imperfect electronics hardware realization.

5.4.2. Experimental setup for fire detection

The fire detection experiments were carried out under the regulations of the European standard EN54 for fire detection (part 7 for smoke detectors [176] and part 15 and 26 (draft) for gassensors [177, 178]). The room dimensions in which fires are created is 6 m × 10 m × 3.8 m, whereas the sensor gas inlet is mounted at the ceiling on a 3 m radius circle around the test fire in the center of the room (see Fig. 5.15). The fire test is ended when the transmission of the air in the room falls below a certain threshold, i.e., a certain level of smoke is present. This is then followed by a purge of the room with fresh outside air. To verify the measured CO concentrations, a commercial CO reference analyzer (HORIBA model PG-250) was used in parallel during this experiment. The

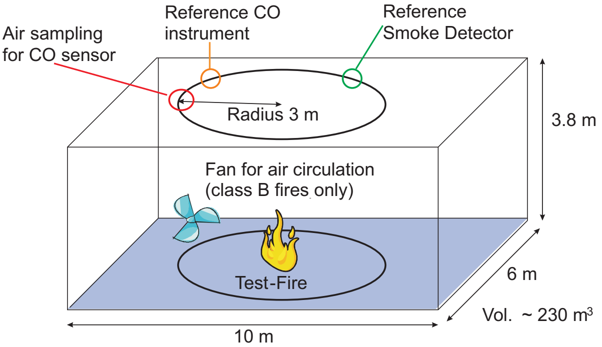

Fig. 5.15: *Experimental setup. The gas inlet for the laser based CO sensor at the ceiling in 3 m distance of the test fire. A commercial reference CO analyzer was also employed but the gas inlet is at a different position on the 3 m circle. For class B fires additional air circulation is employed in the room to enable better distribution of the combustion gases. The fire is ended and the room purged with fresh air when the transmission of the air in the room falls below a certain threshold (determined with the reference smoke detector).*

measurements of the reference instrument have been corrected for the different gas sampling delay time of about 1 min.

There are several fire types named TF1-TF6, optionally with suffix B or C denoting the size of the fire. These types simulate different fire incidents, such as burning of different substances (e.g. wood, ethanol, n-heptane) under different conditions (e.g., smoldering fires or fires with open flames) (see Tab. 5.3). Clearly, class B fires generate much less gases and are, hence, more difficult to detect. According to EN54, for single point sampling detectors class C fires (large), with no additional air circulation in the room, are relevant, so in this experiment all class C fire tests were carried out without

Name	Type of fire	CO_2	CO	NO_2	T
TF1	open wood fire	+++	+++	++	++
TF2-B	pyrolysis, wood	−	+	−	−
TF2-C	pyrolysis, wood	−	++	−	−
TF3-B	pyrolysis, wick	−	+++	−	+
TF3-C	pyrolysis, wick	++	+++	++	+
TF5-C	n-heptane	+++	++	++	++
TF6	ethanol	+++	+	++	++

Tab. 5.3: *Overview of test fires used in this experiment and expected generation of gases and heat during this type of fire. − means that no measurable concentration is generated and the number of pluses indicate the relative amount of gas/temperature generated among the test fires. TF2 consists of several small pieces of beechwood (two for class B and twelve for class C) on a hotplate and TF3 comprises of several glowing cotton wicks (28 for class B and 99 for class C) both arranged in a special manner as described in EN54 [176].*

additional air circulation. The smaller class B fires had additional air circulation to ensure better distribution of the combustion gases inside the room during the fire. The fire test starts either with ignition of the fire (TF1,TF5,TF6), power-on of the hotplate (TF2) or the inflammation of the cotton wicks (TF3). TF2-B consists of two and TF2-C of twelve beechwood pieces and TF3-B and TF3-C consist of 28 respectively 99 pieces of dry cotton wick of 80 cm length.

5.4.3. Experimental results and evaluation of cross-sensitivity

i. Fires with high level of CO generation (TF1,TF2-C,TF3-C)

Due to the high volume of the room, the CO concentration stays below 120 µL/L for the wood fire and the pyrolysis (TF2-C and TF3-C), as shown in Fig. 5.16a. The latter is a very incomplete burning with no flame and very high CO generation. The pyrolysis probably generates more CO than the wood fire with an open flame (TF1), but due to missing air circulation it does not distribute very well, which may explain the lower measured CO concentration. The steep falling of the CO concentration is caused by the purge of the room which ends the fire. High deviations between the sensor and the reference instrument are observed for class C fires. This is attributed to the missing air circulation of the room and different mounting positions of both sensor gas inlets. During the design of the experiment such an observed strong inhomogeneity of the gas distribution was not expected. In future experiments sampling at the same or closely located positions should be carried out. These large deviations were not observed for the smaller class B fires (Fig. 5.16b), which had additional air circulation in the room and thus much better homogeneity in gas distribution than the larger fires discussed previously. Even if a detection threshold as high as the Threshold Limit Value of 25 µL/L is employed, all fires would have been detected in the required time, i.e., before the reference smoke detectors signal the end of the fire test.

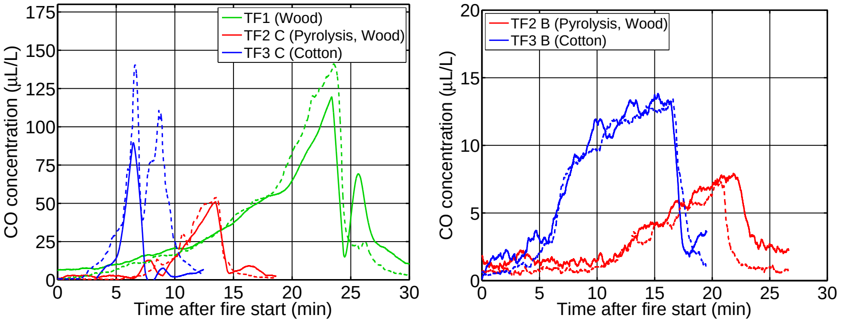

(a) Large (class C) fires

(b) Small (class B) fires

Fig. 5.16: *Measured CO concentrations with laser based sensor (solid) and the reference analyzer (dashed). The deviations are attributed to different measurement positions and the missing air circulation in the test room.*

ii. Fires with low CO generation (TF2-B,TF3-B,TF5,TF6)

In case of fires with open flames like n-heptane or ethanol (EtOH) (Fig. 5.17) much less CO is generated. The ethanol fire is also typically the most difficult one to detect using smoke detectors because of virtually no particle generation. In this case the reference analyzer also only measured 3 µL/L CO, compared to 6 µL/L of this sensor. This may be due to different air sampling points, the sensor baseline or both. The sensor baseline is nonzero due to inaccurate sensor reference spectra, which causes a varying background CO concentration between 0 µL/L to 5 µL/L. Reliability could further be improved by combining the gas sensor with a temperature sensor, to also detect the significant amount of heat ($\Delta T > 10\,\mathrm{K}$) generated by open fires. Note, that the measurement cell can be made robust against this heating. This was demonstrated by application of the sensor in an exhaust gas pipe of a gas furnace [54].

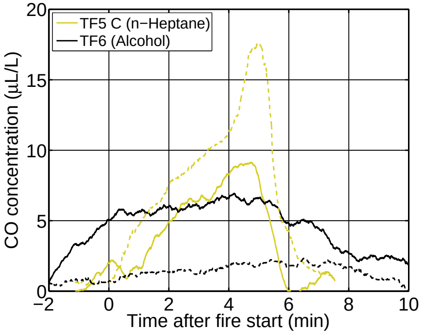

Fig. 5.17: *Measured CO concentrations with laser based sensor (solid) and the reference analyzer (dashed). The fires cease very quickly and generate very low concentrations of CO because of the nearly complete burning with open flames.*

iii. Evaluation of cross-sensitivity

Solid-state based carbon-monoxide sensors usually have cross-sensitivities to many reducing gases. This also applies to electro-chemical instruments used in chemical analysis. Particle detectors have cross-sensitivities to all kinds of particles like hairspray, water-vapor or dust, whereas TDLS-based sensors generally have excellent selectivity. Nevertheless, the accuracy of TDLS-based sensors can be affected in three ways:

- A loss in absolute light transmission results in an increase of sensor noise. This happens if broad-band absorber, e.g., dirt or some absorbing gas phase molecule with a broad absorption spectrum is present. At 2.3 µm this is the case for many hydrocarbons like butane, heptane, etc.
- Presence of molecules that have a structured transmission function in the wavelength range of interest. This can only be the case for molecules with a low number of atoms. Molecules with high number of atoms usually have a very smooth and broad-band absorption spectrum and thus do not contribute to the

second harmonic spectrum, which is approximately the second derivative of the transmission. At 2.3 µm possible interferers are H_2O, NH_3, C_2H_6 and other hydrocarbons [19, 179].

- Sensitivity to interference on the transmission ("fringes"). This is depending on the chemical composition of the gas sample and the cause for drift and deterministic measurement errors.

The sensor has no cross-sensitivity to H_2O. Simulations have shown, that even with 100 % absolute water vapor concentration (which is even impossible to reach at temperatures below 100 °C), the spectral interference due to absorption by water vapor is below the sensor resolution of 3 µL/L ($\sim 10^{-5}$ in terms of absorbance). However, sensor noise may increase when the absolute transmission due to condensed water vapor is low. Since the absorption strength of NH_3 is an order of magnitude lower than CO and the spectral overlap to CO is also low, it was not considered to be relevant for inclusion in the sensor spectrum model. If NH_3 might be present in air at higher µL/L concentrations this has to be reconsidered (cf. Tab. 5.4 for the exact cross sensitivities). In this case the wavelength stabilization method has to be modified to cope with the possible presence of NH_3 absorption lines in the wide scan. Since NH_3 is a flammable gas it is not expected to be generated by fires with open flames in high concentrations. It may be created by pyrolysis of protein containing organic substances, e.g., meat and is also contained in cigarette smoke due to the additive carbamide. Note that cellulose which is the main constituent of wood and cotton does not contain nitrogen and thus even pyrolysis of this can not generate NH_3.

	ΔC_{H_2O}	ΔC_{NH_3}
$\Delta\widehat{C}_{CO}$	-2×10^{-8}	9.2×10^{-5}
$\Delta\widehat{C}_{CH_4}$	-6.7×10^{-6}	-2.9×10^{-2}

Tab. 5.4: *Theoretically calculated cross sensitivities of the sensor to spectrally interfering gases, according to the theory developed in section 5.1.1. For example presence of* 100 µL/L *NH_3 would cause a false response of* 9.2 nL/L *CO and* −2.9 µL/L *CH_4 respectively.*

In Fig. 5.18 the measured sensor response to general aerosols[9] and hairspray is shown. Tests were carried out by spraying in front of the gas inlet of the sensor (but not directed to) (legend "room") and by directly spraying into the gas inlet (legend "direct"). Both hairspray and aerosols (which classical fire detectors most likely would generate a false alarm for) contain a high concentrations of hydrocarbons which are expected to absorb in the wavelength region around 2.3 µm. It can be seen, that during spectrum scanning a rather high amount of light is broad-band absorbed (see Fig. 5.19a), summing to an absorbance of 3.6 % to 7 %. However, due to the differentiating nature of second harmonic detection this broad-band absorption is almost invisible in the measured second harmonic spectrum Fig. 5.19b. Only a small fine structure in the order of 10^{-4} of the broad-band absorber is present around 2.365 µm to 2.3655 µm, which, however, creates the slight false CO concentration signal observed in Fig. 5.18. This problem can be solved by identifying the substance that exactly causes the fine structured spectrum and include it as an additional component in the spectral model. Note, that the cross

---

[9] Aerosol mixture for testing of smoke detectors was used. The exact contents are unknwon.

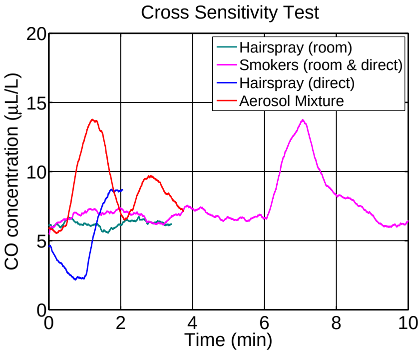

Fig. 5.18: *Tests under conditions suspected to create cross-sensitivities, either by releasing the substance in the room in front of the sensor (room) or directly into the sensor gas inlet (direct). Four smokers are standing below the sensor, whereas at* 6 min *a cigarette is hold directly in front of the sensor gas inlet. The constant offset of* 5 µL/L *is either due to an incompletely purged room or the sensor baseline of few* µL/L.

sensitivity to hairspray and aerosols is not caused by the particles but most likely the solvent these are contained in. To evaluate the overall sensor sensitivity to interference fringes the theory from section 5.1.1 is employed for simulation of the fringe response (see Fig. 5.20). Although the white noise performance for the CH_4 detection is not much worse than that for CO detection (cf. the observation factor in Eq. (5.26)) the sensitivity to fringes caused by reflections in the full cell length is worse by two orders of magnitude. This is due to the similarity of the irregular CH_4 spectrum with sinusoids of the specific periodicity. This is due to the increased overlap of fringe and analytic spectrum in the Fourier domain. Hence the sensor in its present form is not suitable for stable CH_4 detection. The sensitivity of the CO detection on fringes is even an order of magnitude better as for the air quality sensor (cf. Fig. 5.10) and is not limiting the detection.

5.4.4. Summary

In this section a compact laser spectroscopy based carbon-monoxide sensor is tested for fire detection under conditions described by the European standard EN54. It turns out that, using an averaging time of 60 s, all class C fires can be reliably detected. The sensor is thus well suited as a point-sampling fire detector. Although TDLS-based sensors typically have the lowest possible cross-sensitivities to other gases among all sensing principles, a cross-sensitivity analysis with critical substances (hydrocarbons) was performed using the theoretical results. Furthermore, it has been shown experimentally that direct application of hairspray or aerosols into the sensor gas inlet gives false CO concentrations of only a few µL/L. This is a very low value, and can be further reduced by identifying the relevant substance and the inclusion of its spectrum in the sensor spectral model used for curve-fitting. Using theoretical results from section 5.1.1 the sensitivity to fringes was simulated. While the suppression of fringes is very good for

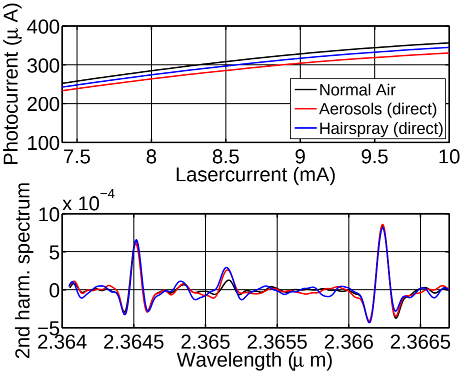

Fig. 5.19: *Single non-averaged spectral scans under conditions shown in Fig. 5.18. The absolute decrease in photocurrent indicates an absolute broad-band absorbance of* 7.4 % *for aerosols and* 3.6 % *for hairspray (top). The fine structure changes in the spectrum (especially in range* 2.365 µm *to* 2.3655 µm*) that cause the false absorption signal are also clearly visible, but orders of magnitudes lower in the* 10^{-4} *range (bottom).*

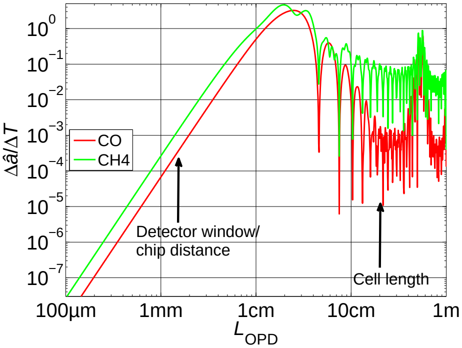

Fig. 5.20: *The sensor sensitivity to interference fringes caused by interference of two beams with different path length difference. Attenuation of possibly existing fringes is for CO between 1000 and 10000 while it is significantly worse for* CH_4 *due to its irregularly shaped spectrum.*

the CO detection the sensitivity is two orders of magnitude worse for the CH_4 detection which explains the experimentally observed high drift of sensor output values.

The smaller class B fires or the ethanol fire have also been detected successfully, but may require a higher sensing sensitivity for very reliable detection. This can be achieved by a) lowering the sensor baseline by improving the spectral model, b) increasing of the sensor optical path length to enlarge the gas absorbance or c) to combine the sensor with other sensing principles like temperature measurement or a smoke (particle) detection.

The VCSEL-based sensor operated at 2.3 µm is very compact because it does neither need a separate reference cell nor multi-pass cells and still achieves reliable and sensitive CO detection.

6. Summary of results and outlook

The dissertation explores new laser spectroscopic methods for gas sensing to increase the precision in compact sensor platforms, especially with, but not limited to, utilization of digital sensor hardware.

One idea is to utilize multi-harmonic spectral detection. It is shown both theoretically and experimentally that multi-harmonic detection provides higher precision over conventional single harmonic detection by a factor of three with same sensor complexity (see section 4.2).

The second achievement is in-fiber Zeeman spectrometry, for which a patent was filed. It uniquely combines a fringe insensitive (high signal to noise ratio) detection method with a compact sensor platform. This approach is experimentally demonstrated for O_2 detection, achieving an increase of signal to noise ratio by a factor of four with potential for further improvement (section 4.3).

Another major topic is device and system modeling with the aim of creating computer simulations of tunable diode laser spectroscopy sensors to improve and verify detection schemes prior to building a sensor. An entire model for TDLAS sensors is developed for the first time. Metrics qualifying sensor response to noise and fringes have been developed (section 5.1.1) whose application provided design guidelines (section 5.2) and significant insights for comparison of methods and answered long standing questions (see details on the next page). The defined fringe response shows that ultra-short optical cells ($\ll 1\,\mathrm{cm}$) are feasible because the fringe suppression is generally very good for interference caused from distances $\ll 1\,\mathrm{cm}$ (section 5.1.3.vi).

For the first time the spectral background of hollow capillary based cells could be explained. The analysis of the back-scattering at the fiber end, based on the mode-matching technique, recreated both the magnitude and the pseudo-random character of the spectral background (section 3.2.3).

It is very challenging to accurately model the laser diode, especially in the lower frequency range ($< 100\,\mathrm{MHz}$), including thermal tuning and intensity modulation behavior. This has not been done in the literature so far, because these effects become negligible for high-speed telecommunication applications where those lasers have been primarily used. Therefore, a general theory was developed including its comparison with experimental results for vertical-cavity surface-emitting lasers (VCSELs) of different types and wavelengths. The model reasonably describes the effects of the laser parameters and thus yields valuable information not only for improved understanding of the VCSELs, but also for device improvements and sensor layouts (section 2).

Also for the first time wavelength modulation spectroscopy can be modeled with an analytical model based on system-theory (section 3.3.2 to section 3.3.4), which is a significant contribution to the field. It allows for development of more efficient and faster computation methods (section 3.3.5), and is the basis for the two developed multi-harmonic detection schemes (section 4.2).

During the course of the work, several sensor prototypes were developed and co-developed for different applications and gases. The CO_2 sensor (section 5.3) was shown in the "Science Express" train in Germany and the CO sensor (section 5.4) was awarded with the German Kaiser-Friedrich Research Award and received a nomination to the AMA SENSOR Innovation Award. An O_2 sensor was recognized with the Best-Paper-Award (first place) at the Eurosensors conference. All sensors were tested under realistic conditions which shows the practical applicability of the sensors (chapter 5).

During this thesis 17 journal articles (6 as first author, 9 as second author) and 38 conference publications (18 as first author, 15 as second author) were published. Additionally 12 invention disclosures could be filed, of which 7 became patent applications.

Specific results regarding VCSEL modeling in chapter 2 are:

- The FM tuning behavior is determined by three processes: intrinsic thermal tuning (dominant up to few MHz), the plasma effect (above few MHz) and the thermal tuning by the chip-submount interaction (up to few 100 Hz). At DC conditions the intrinsic thermal effect dominates – the plasma effect and the chip-submount interaction contribute a few percent (see section 2.3.1 and section 2.3.2).
- The intrinsic thermal component of the FM response (including amplitude and phase) can be well described using a four parameter PDE-based thermal model. After cutoff frequency the intrinsic thermal tuning has a square root behavior which gradually changes to an inverse proportional characteristic at high frequencies (necessary to recreate the FM phase-shift) (see section 2.3.2.i). The finite thickness of the light mode and heat source is responsible for this gradual change.
- The FM tuning behavior does not show the minimum-phase property, and, hence, separate measurements of FM amplitude and FM phase response are necessary.
- The laser thermal behavior for intensity and wavelength can be well described by a simplified model (section 2.4). Threshold current, quantum efficiency and effective thermal resistance of the intrinsic laser diode is well described by simple empirical functions, only depending on internal temperature.

Specific results obtained from theoretical investigation regarding system modeling and the parameter extraction from spectra in chapter 3 are:

- WMS can be regarded as n-th differentiation with subsequent lowpass filtering (see section 3.3.2). WMS has no intrinsic advantage of fringe suppression or resolution of overlapping lines. The same effect is achieved by curve-fitting with correct signal model (see section 3.3.6.i and section 3.3.6.vi).
- The best detection method in terms of noise suppression is optimum sampling (measurement of selected wavelength points with certain duration), followed by multi-harmonic WMS, and single harmonic WMS (traditional) or direct spectrometry. However, the optimum sampling method has inferior response to interference fringes (section 5.1.3.iv) and thus multi-harmonic WMS is recommended (see section 5.1.3.iv and section 5.1.3.v).
- Single harmonic WMS and direct detection achieve (approximately) the same performance if the detection order is the same as the order of the laser PI characteristic. In this case the intrinsic differentiation only removes information the curve-fit for direct spectroscopy could not utilize anyway (see section 5.1.3.iii).
- Curve-fitting is the optimum parameter extraction method for most TDLAS

sensors (see section 3.4.3). Heuristic data extraction methods can not achieve better performance than curve-fitting. Spectral filtering prior to curve-fitting can not significantly improve performance (see section 5.1.3.i).

Outlook

Future work could include refinement of the laser model in terms of laser voltage and differential resistance of VCSELs. A refined model, or improved knowledge on laser behavior may also have benefits for sensor design, if, e.g., laser voltage is used as an additional information on laser emission wavelength. Also non-thermal effects like spatial hole burning may affect the laser behavior in the low frequency regime, which would need to be quantified and appropriately described.

In the field of sensing the fiber based optical cell could be improved by implementing different fiber ends to minimize back-scattering. This could either be done by implementing tapers or an angled fiber ending. A reduction of the spectral background by such a simple means, would be an important advance in the field of compact gas sensors. It would be important to apply the Zeeman spectrometry with hollow fibers to NO detection in the mid-infrared.

An interesting application is sensor networks for identification of sources and sinks of various gases. This can be either green house gases in the frame of a city or air quality related gases in a large office building. If these spatially resolved data is coupled with information on air transport, e.g., by weather data or information of air conditioning, sources and sinks could be quantified. This would allow for optimized air conditioning as well as spatial localization of fires sources. For this technology an improved hollow fiber design with low spectral background would also provide an enormous benefit.

A. Laser and system model

A.1. Laser characterization and modeling

The presented characterization methods have been published in:

- A. Hangauer *et al.*, "Analysis of dynamic tuning effects in vertical-cavity surface-emitting lasers", in *Proceedings of the Fifth Joint Symposium on Opto- & Micro-electronic Devices and Circuits (SODC)*, Beijing, China, 2009, pp. 28–31,
- A. Hangauer *et al.*, "Accurate measurement of the wavelength modulation phase shift of tunable vertical cavity surface-emitting lasers (vcsels)", in *Programme and Abstracts, Conference on Semiconductor and Integrated Optoelectronics*, 2008, p. 38, and,
- A. Hangauer, J. Chen, and M.-C. Amann, "Vertical-cavity surface-emitting laser light-current characteristic at constant internal temperature", *IEEE Photon. Technol. Lett.*, vol. 23, no. 18, pp. 1295–1297, Sep. 2011. DOI: `10.1109/LPT.2011.2160389`.

A.1.1. FM amplitude response

The measurements of the FM amplitude response were done using a Michelson Interferometer (setup schematic see Fig. A.1). The transmission of a Michelson interferometer is sinusoidal, i.e.,

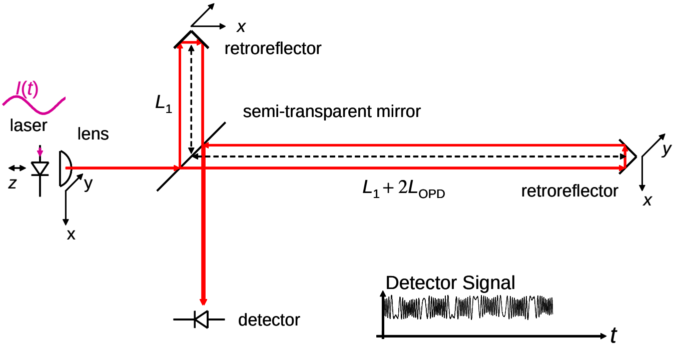

Fig. A.1: *Schemtic setup for laser FM amplitude response measurement using a* $L_{OPD} = 1\,\mathrm{m}$ *long Michelson interferometer*

$$T(\nu) = 2a(1-a)(1-\cos(2\pi\nu L_{\mathrm{OPD}}/c)) \tag{A.1}$$

with L_{OPD} the optical path length difference of the two beams and a the splitting ratio of the beam splitter (e.g., $a = 0.5$ for 50:50 splitting). Note, that the arriving beams at the photodetector always have equal strength regardless of the splitting ratio of the beam splitter. Hence, always full constructive and destructive interference is obtained

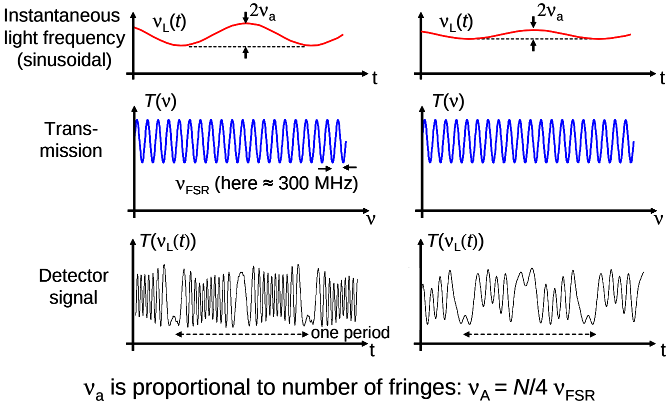

Fig. A.2: *The signals obtained with the Michelson interferometer and the relation to the FM modulation amplitude* ν_a*.*

if the two beams are in parallel and spatially fully overlapping on the detector surface (this case is described by Eq. (A.1)). If there is no full spatial overlap, or the two beams are not in parallel, an additional DC offset on the detector signal is obtained and the amplitude of the fringe is reduced accordingly.

The signal generation during the FM response measurement is depicted in Fig. A.2. The signals shown in the figure are measurements and represent two cases with different wavelength modulation amplitude ν_{a}. The modulation amplitude ν_{a} (unit: Hz) is obtained by counting the fringes N_{fringe}during one modulation period and dividing by the free spectral range ν_{fsr} (unit: Hz) of the interferometer, with

$$\nu_{\mathrm{a}} = \frac{N_{\mathrm{fringe}}}{4}\nu_{\mathrm{fsr}}, \qquad \nu_{\mathrm{fsr}} = \frac{c}{L_{\mathrm{OPD}}}. \tag{A.2}$$

The factor of four is because fringes are generated twice during rising and falling slope of the sinusoidal wavelength modulation and ν_{a} is defined as an amplitude and not peak to peak variation.

A.1.2. FM phase response

In this thesis the measurements of the phase response (i.e., the time delay between current and wavelength response) were done using gas absorption lines as markers in the recorded detector signal. The experimental setup is the same as a standard TDLAS setup (see Fig. A.3). With an increasing FM phase-shift the absorption lines, which appear in the detector signal, will shift to higher time values (see Fig. A.4). The center between the two absorption peaks (which are created in the rising and falling slope

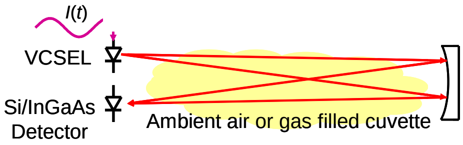

O_2:	763 nm
CH_4:	1670 nm
H_2O:	1854 nm
CO_2:	2004 nm
CH_4 (CO):	2300 nm

Fig. A.3: *The experimental setup for the FM phase-shift measurement*

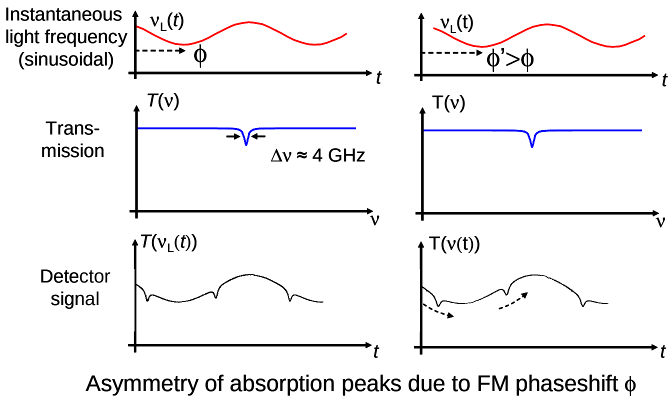

Fig. A.4: *The signals obtained with the gas absorption line method and the relation to the FM phase-shift ϕ.*

of the sinusoidal wavelength modulation) is the position of the first minimum of the wavelength modulation (indicated by the arrow in the top row diagram in Fig. A.4). The phase shift was extracted by finding the symmetry center between the two peaks. For this the IM envelope was removed by either fitting a sine wave and then dividing, or, by normalization with a second measurement without gas.

A.1.3. IM response

The IM response measurement was done using the setup shown in Fig. A.5. The cathode of the laser is connected to the $50\,\Omega$ terminated reference input (for measuring ΔI) and the photodiode is connected to the $50\,\Omega$ terminated test input (for measuring ΔP). This configuration directly measures the slope $S(I, T_{\mathrm{S}}) = \Delta P/\Delta I$, while simultaneously the $P(I, T_{\mathrm{S}})$ curves are determined as the DC components of the reference and test signals.

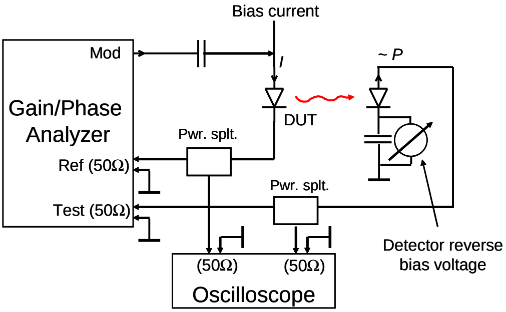

Fig. A.5: *Schematic of the setup for measurement of the laser IM response. The AC and DC components of the injected laser current I and optical output power P are measured simultaneously by the Gain/Phase Analyzer and an Oscilloscope.*

A.1.4. Internal laser temperature

In this section the two continuous wave measurement methods and measurement results for P-I-characteristics at constant junction $P(I, T_{\mathrm{jcn}})$ and cavity temperature $P(I, T_{\mathrm{cav}})$ are presented and demonstrated on a standard InP-based buried tunnel junction (BTJ) VCSEL [47] emitting at 1390 nm. In principle the ordinary measurement data $P(I, T_{\mathrm{S}})$ (output power P at current I and heat-sink temperature T_{S}) is used to extract this information. To compensate for self-heating, the heat-sink temperature T_{S} has to decrease if the injection current I is increased.

In literature internal temperature is determined by comparing continuous wave laser characteristics (output power P, laser voltage U or emission wavelength λ) with pulsed measurements [182] or from an estimation of laser thermal resistance [183]. A pulsed measurement requires a broad-band measurement setup which is not available for all wavelengths and also has other disadvantages. The laser thermal resistance is an effective value and typically changes with bias current I and internal temperature due to variations of the heat source distribution and thermal material properties. For precise determination of the internal temperature this variation has to be taken into account.

For finding the P-I-characteristic at constant T_{jcn} or T_{cav}, trajectories in the (I, T_{S}) plane have to be found, where the corresponding internal temperature is constant. For a graphical illustration of this please refer to the obtained results in Fig. 2.1. The absolute temperature value is determined by extrapolation of the trajectories to $I = 0$ (because there $T_{\mathrm{jcn}} = T_{\mathrm{cav}} = T_{\mathrm{S}}$).

i. Method 1: $T_{\mathrm{cav}} = \mathrm{const}$

The emission wavelength is dominantly determined by the intrinsic thermal tuning, i.e., the average cavity temperature (see section 2.3). For an illustration see Fig. A.6 (left). Trajectories

$$(I, T_{\mathrm{S}}), \qquad \text{where } \lambda(I, T_{\mathrm{S}}) = \mathrm{const}, \tag{A.3}$$

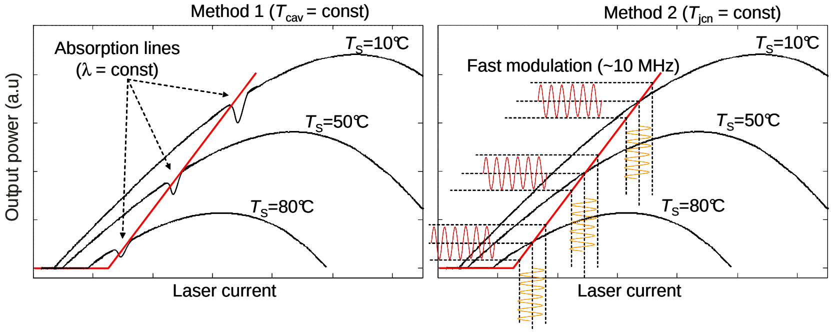

Fig. A.6: *Schematical explanation of method 1), where $\lambda = const$, known from gas absorption lines, corresponds to $T_{cav} = const$ and method 2), where a high speed modulation is used to obtain the slope S of the P-I-characteristic at $T_{jcn} = const$. The reconstruction of the P-I characteristic at constant internal temperature is shown in red.*

are thus trajectories of constant cavity temperature (see e.g. Fig. 2.1a in the results section). Here $\lambda(I, T_\mathrm{S})$ was determined by identifying the absorption lines in the measured P-I-characteristics and comparing the positions with known wavelengths from the spectral database HITRAN [19].

ii. Method 2: $T_\mathrm{jcn} = \mathrm{const}$

By applying a small-signal modulation with a frequency well above the thermal cutoff frequency and and below the relaxation frequency (here $f = 10\,\mathrm{MHz}$, see section 2.3) the slope of the P-I-characteristic at constant junction temperature $\Delta P/\Delta I = S(I, T_\mathrm{S})$ is determined. Knowing the slope $S(I, T_\mathrm{S})$ and the laser output power $P(I, T_\mathrm{S})$, the full internal P-I-characteristic can be reconstructed. For an illustration see Fig. A.6 (right). The relation $\Delta P/\Delta I|_{f=10\,\mathrm{MHz}} = S$ is easily proved, when Eq. (2.14) is differentiated by I and the $\partial T_\mathrm{jcn}/\partial I$ terms are set to zero (i.e., there is no self-heating by the fast small-signal modulation). Note, that the P-I slope S is a shorthand notation for $S = h\nu/e\,\eta_\mathrm{e}$. Mathematically, the trajectory of constant junction temperature is found by iteratively solving

$$P(I + \Delta I, T_\mathrm{S} + \Delta T_\mathrm{S}) = S(I, T_\mathrm{S})\Delta I + P(I, T_\mathrm{S}) \tag{A.4}$$

for ΔT_S with an arbitrary but fixed current step $\Delta I < 0$. There ΔT_S is the value the heat-sink temperature needs to be increased by when the injection current rises by ΔI to maintain constant junction temperature. The complete trajectory is found by repeatedly solving Eq. (A.4): First a starting point (I, T_S) with the maximum desired current I and $\Delta I < 0$ is selected and second Eq. (A.4) numerically solved for ΔT_S. The procedure is repeated with the new starting point $(I + \Delta I, T_\mathrm{S} + \Delta T_\mathrm{S})$ until the point wanders below threshold. See Fig. 2.1b in the results section for the determined trajectories and the “lasing domain” surrounded by thick black lines labeled “threshold” and “laser turn-off”.

A.1.5. General model for the intrinsic thermal tuning

To compute the intrinsic thermal contribution to the laser's FM impulse response, the heat equation has to be solved with appropriate boundary conditions and a temporal impulse excitation, i.e.,

$$c\rho \frac{\partial T}{\partial t} - \nabla \cdot (\mathbf{K} \nabla T) = Q\delta(t) \tag{A.5}$$

where $c\rho$ is the specific heat capacity times density (unit: $\mathrm{J/(m^3K)}$), $\mathbf{K}$ the thermal conductivity (unit: W/(m K)) matrix and $Q = Q(x, y, z)$ the spatial heat source term (unit: $\mathrm{J/m^3}$). Eq. (A.5) is in a general form where all parameters may depend on space variables x, y, z. A constant, but non-isotropic, thermal conductivity is assumed to account for the non homogeneous conductivity of the layered semiconductor material:

$$\mathbf{K} = \begin{pmatrix} K_R & 0 & 0 \\ 0 & K_R & 0 \\ 0 & 0 & K_Z \end{pmatrix}. \tag{A.6}$$

Boundary conditions of constant temperature like $T(x, y, -D) = 0$ can be enforced by using the method of images. There the equation without boundary condition is solved with the source term $Q(x, y, z) - Q(x, y, z - 2D)$ instead of Q alone [184].

The solution of Eq. (A.5) with Eq. (A.6) for spatially constant $c\rho$ and spatial impulse heat source $Q(x, y, z) = \delta(x)\delta(y)\delta(z)$ is given by [184, section 10.2]

$$T_P(x, y, z, t) = \frac{1}{\rho c} G_{\sqrt{2\kappa_R t}}(x) G_{\sqrt{2\kappa_R t}}(y) G_{\sqrt{2\kappa_Z t}}(z), \qquad t \geq 0, \tag{A.7}$$

with the Gaussian function

$$G_\sigma(x) = \frac{1}{\sqrt{2\pi}\sigma} \exp\left(-\frac{x^2}{2\sigma^2}\right), \tag{A.8}$$

and $\kappa = K/\rho c$ the thermal diffusivity (unit: $\mathrm{m^2/s}$). The general solution of Eq. (A.5) for arbitrary heat source Q is then given by the spatial convolution[1] of T_P with Q, i.e.,

$$T(x, y, z, t) = (T_P(\cdot, t) * Q)(x, y, z). \tag{A.9}$$

The model for the laser's FM response thus requires knowledge on the spatial heat source distribution $Q(x, y, z)$ and the light mode profile $M(x, y, z)$. The average temperature with respect to the light mode profile $\overline{T}_g(t)$ determines the wavelength of the laser, so that the FM impulse response is up to a constant factor compactly written as

$$\overline{T}_g(t) = (T * \widetilde{M})(0, 0, 0), \tag{A.10}$$

with $\widetilde{M}(x, y, z) = M(-x, -y, -z)$ the mirrored mode profile. Summarizing, the FM impulse response is given in the general case by the convolution expression

$$\overline{T}_g(t) = (T_P(\cdot, t) * Q * \widetilde{M})(0, 0, 0). \tag{A.11}$$

Eq. (A.11) leads to an important observation: Since the convolution is an associative and commutative operation, the FM response stays the same when the convolution of the mirrored mode profile $\widetilde{M}$ and heat source Q is invariant. This is for example the

---

[1] Defined as $(T_P(\cdot, t) * Q)(x, y, z) = \iiint T_P(x - x', y - y', z - z', t)Q(x', y', z')\mathrm{d}x'\mathrm{d}y'\mathrm{d}z'$

case when both are Gaussian functions and the mean square of the standard deviations is kept constant (i.e., $\widetilde{M} * Q = \text{const}(x, y, z)$). Or more generally speaking, since the convolution operation tends to broaden functions, the device behavior is the same if the light mode is very concentrated but the heat generation very distributed or vice versa. It is the combined width/height (in a mean square sense) of the heat source and light mode distribution that determines the dynamic thermal tuning behavior.

A.2. Definition of the harmonic spectrum

A.2.1. Names: harmonic spectrum, -signal and -coefficient

In the literature the naming convention for the signals or spectra which occur in WMS is not standardized. Many authors call these quantities just harmonic coefficients, nf signals or specify no name at all. Furthermore, these "signals" are often plotted in arbitrary (or meaningless) units both for the x or y axis. So the first question here is what is the best name or description for the "WMS signals" and what units or scaling should be used to describe these, not only for graphical depiction but in general.

Usually the term "signal" is associated with a function of time (or even space) but not of wavelength or frequency. In this case the term "spectrum" is more appropriate. So one should distinguish between harmonic signals (or nf signals) and harmonic spectra (or nf spectra). Also the term n-th harmonic signal/spectrum is preferred over nf signal/spectrum. The name harmonic spectrum/signal is better suited than harmonic coefficients since in most experiments and graphical printings the independent variable is the mean frequency ν, laser current I or even time t. The term harmonic coefficient is used when the dependence on the detection order n (at constant ν or I) is to be emphasized. In this work the term harmonic signal refers to measured quantities in an experimental setup (i.e., output of the lock-in amplifier) whereas harmonic spectra represent the theoretically expected physical quantities (as e.g., the gas transmission function).

A.2.2. Units

Since in TDLAS transmission measurements are performed, the appropriate units for harmonic spectra are 1 versus frequency or wavelength. So the y unit of both the spectra and signals should be normalized, i.e., the output values of the lock-in amplifier divided by the gain of the lock-in amplifier and the received laser light intensity. In this way units of voltage, photocurrent or even A/D converter digits, as frequently seen in the literature, are avoided. These are not of importance when the optical transmission spectrum is of interest and not the measurement system itself. This has the advantage that the values directly relate to absorption strength, which is a property of the analyte and not a property of the measurement system. The x-unit for harmonic spectra should be wavelength, wavenumber or optical frequency. For harmonic signals the unit may be time t or, even better, laser current I.

A.2.3. Symbol

The symbol H_n for the harmonic spectra is adopted from Ref. [20, 86], whereas the authors do not specify a name for it. Other authors use (introduced by Kluczynski et al.) $\overline{\chi}_n^{\text{even}}$ to specify the harmonic coefficients of the peak normalized line shape function $\phi(\nu)$. In case of an unsaturated line with peak absorbance $\alpha_{\mathrm{C}} L$ these are related by

$$T(\nu) = \exp\left(-\phi(\nu)\alpha_0\right) \approx 1 - \phi(\nu)\alpha_{\mathrm{C}} L, \tag{A.12}$$

$$H_n(\nu, \nu_a) = -\alpha_{\mathrm{C}} L \overline{\chi}_n^{\text{even}}(\nu, \nu_{\mathrm{a}}). \tag{A.13}$$

A.2.4. Definition in terms of transmission or absorption coefficient?

Note that, some authors [20, 70] define the harmonic spectrum (or what corresponds to it) in terms of absorption coefficient or absorbance and some others [86] in terms of the transmission. For small absorbance values (i.e., unsaturated conditions) all definitions are more or less equivalent (just by multiplication with the optical path length). Although the absorption coefficient is the desired quantity, physically a transmission measurement is performed. So in analogy to direct spectrometry where also the transmission (and not absorption coefficient) is measured, the “WMS signals” are quantities that directly relate to the transmission. Hence, it is believed that the proper definition for harmonic spectra is in terms of the transmission. This also avoids problems of the theory being only easily applicable for small absorbance values. Correction algorithms that compensate for “artifacts” [88, 185] due to saturated sample conditions are not needed. The problem of saturated optical conditions is then handled by the parameter extraction or signal processing, which then just relies on proper computation of harmonic spectra for all conditions. These issues are no more or less fundamental as for direct spectrometry and are to be handled in a similar way.

Alternatively, one could introduce different symbols for slightly different definitions of the harmonic spectrum and differentiate these by including a prefix in the name as e.g., harmonic transmission spectrum, harmonic absorption spectrum or harmonic reflection spectrum and so on. However the x and y units of these spectra should be the same as their non-harmonic counterparts, i.e., 1 for transmission and reflection and 1/cm for absorption coefficient plotted versus wavelength λ or frequency ν.

A.2.5. Mathematical definition

In the following paragraph the appropriate mathematical definition of the harmonic (transmission) spectrum is presented. The harmonic spectrum is the measurement spectrum an idealized WMS system would generate. This system is classified by the following assumptions:

1. The laser linewidth is zero.
2. The modulation frequency f_{m} does not affect the laser spectrum, i.e., f_{m} is smaller than the laser and absorption linewidth[2] (Otherwise Frequency Modulation

---

[2] Formally this requires that the necessary length of the short time Fourier transformation to achieve a frequency resolution in the order of the linewidth of the laser is much shorter than variations of the FM modulation. The linewidth is typically in the MHz range (STFT times in µs regime)

Spectroscopy (FMS) [60, 186] is obtained).

3. The laser intensity is constant during wavelength tuning.
4. The responsivity of the photodetector is not wavelength dependent.
5. The pre-amplifier and gain stages in the measurement system are not frequency selective and have a unit gain.

Let ν denote the wavenumber or frequency of the central laser emission which implements the slow (discrete) laser emission frequency sweep. The sweep is discrete so ν can be assumed constant during at least one sinusoidal modulation period. In this idealized system the instantaneous laser emission frequency $\nu_\mathrm{L}(t)$ is given by

$$\nu_\mathrm{L}(t) = \nu + \nu_\mathrm{a} \cos\left(2\pi f_\mathrm{m} t\right), \tag{A.14}$$

with ν_a the frequency modulation amplitude and f_m the modulation or repetition frequency (typically in the kHz range). The n-th harmonic output of the lock-in amplifier of the relative light power variation $T(\nu_\mathrm{L}(t))$ after passing through the sample with transmission $T(\nu)$ is the called the harmonic coefficient $H_n = H_n(\nu; \nu_\mathrm{a})$ (Fig. A.7). Mathematically, the Fourier series decomposition

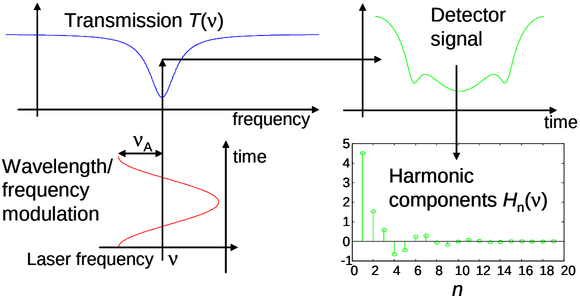

Fig. A.7: *Generation of the harmonic components in wavelength modulation spectroscopy. ν is the emission frequency of the slow sweep (not illustrated here) and ν_a the frequency modulation amplitude.*

$$T(\nu + \nu_\mathrm{a} \cos\left(2\pi f_\mathrm{m} t\right)) = \sum_{n=0}^{\infty} H_n(\nu; \nu_\mathrm{a}) \cos\left(2\pi n f_\mathrm{m} t\right) \tag{A.15}$$

is computed. If the left hand side ("the detector signal") is given, the H_n are uniquely determined. Solving for $H_n(\nu; \nu_\mathrm{a})$ yields

$$H_n(\nu; \nu_\mathrm{a}) = \frac{\epsilon_n}{2\pi} \int_{-\pi}^{\pi} T(\nu + \nu_\mathrm{a} \cos(z)) \cos(nz)\, \mathrm{d}z. \tag{A.16}$$

If these harmonic coefficients are plotted against the slow sweep frequency ν the harmonic spectra $H_n(\nu)$ are obtained (Fig. 3.9). The definition of the harmonic spectra does not include system parameters except for modulation amplitude.

---

and the modulation in the kHz range, which shows that this is valid for typical WMS.

A.2.6. Comparison of reconstruction formula and Taylor series

An interesting analogy between the Taylor series and harmonic spectra becomes evident from the reconstruction formula Eq. (3.41). If all derivatives of the transmission $T(\nu)$ at a certain point ν_0 are ideally known, then $T(\nu)$ can be reconstructed in a certain range around ν_0. This is a consequence of Taylor's theorem:

$$T(\nu) = \sum_{n=0}^{\infty} \frac{\mathrm{d}^n T(\nu_0)}{\mathrm{d}\nu^n} \frac{(\nu - \nu_0)^n}{n!}. \tag{A.17}$$

If the asymptotic expression for harmonic spectra

$$H_n(\nu; \nu_\mathrm{a}) \to \frac{\epsilon_n (\nu_\mathrm{a}/2)^n}{n!} \frac{\mathrm{d}^n T(\nu)}{\mathrm{d}\nu^n} \qquad \text{for } \nu_\mathrm{a} \to 0 \tag{A.18}$$

with $\epsilon_0 = 1$ and $\epsilon_n = 2$, for $n \neq 0$ is inserted, it is obtained:

$$T(\nu) \approx \sum_{n=0}^{\infty} H_n(\nu_0; \nu_\mathrm{a}) \frac{2^n}{\epsilon_n} \left(\frac{\nu - \nu_0}{\nu_\mathrm{a}} \right)^n. \tag{A.19}$$

However this would only be valid for low values of ν_a where the signal to noise ratio is non-optimum. On the other hand the formula derived for the multi-harmonic detection scheme Eq. (4.1) has no such limitation, but has a very similar structure. For convenience of the reader Eq. (4.1) is stated again:

$$T(\nu) = \sum_{n=0}^{\infty} H_n(\nu_0; \nu_\mathrm{a}) T_n \left(\frac{\nu - \nu_0}{\nu_\mathrm{a}} \right). \tag{A.20}$$

The weighting functions in Eq. (A.19) in are 1, x, $2x^2$, $4x^3$, $8x^4$, $\ldots$, whereas in the exact case the Chebyshev polynomials are given by 1, x, $2x^2 - 1$, $4x^3 - 3x$, $8x^4 - 8x^2 + 1$, $\ldots$ with $x = (\nu - \nu_0)/\nu_\mathrm{a}$ as shorthand notation. By comparison one sees that the approximate formula Eq. (A.19) only contains the leading coefficients of the Chebyshev polynomials in the the exact formula Eq. (4.1).

B. Mathematical methods

B.1. Clenshaw algorithm

The Clenshaw algorithm [187, section 3.11] is a method for stable numerical evaluation of a sum of Chebyshev polynomials, i.e.,

$$y = y(x) = \sum_{n=0}^{N} a_n \, \mathrm{T}_n \left(x\right). \tag{B.1}$$

Using the recursion property of the Chebyshev polynomials

$$\mathrm{T}_{n+1} \left(x\right) = 2n \, \mathrm{T}_n \left(x\right) - \mathrm{T}_{n-1} \left(x\right), \tag{B.2}$$

one can devise the following recurrence for Eq. (B.1) ("Clenshaw algorithm"):

$$b_n = 2xb_{n+1} - b_{n+2} + a_n, \qquad b_{N+1} = b_{N+2} = 0, \tag{B.3}$$

$$y = xb_1 - b_2 + a_1. \tag{B.4}$$

This method is more stable than direct evaluation of the sum because evaluation of polynomials of possibly high degree (i.e., N) is problematic because possibly numerically inexact.

B.2. Moore-Penrose pseudoinverse

The Moore-Penrose pseudoinverse [188] matrix $\boldsymbol{A}^+$ of a real or complex matrix $\boldsymbol{A}$ is uniquely defined through the following properties:

$$\boldsymbol{A}\boldsymbol{A}^+\boldsymbol{A} = \boldsymbol{A}, \qquad \boldsymbol{A}^+\boldsymbol{A}\boldsymbol{A}^+ = \boldsymbol{A}^+,$$

$$(\boldsymbol{A}^+\boldsymbol{A})^H = \boldsymbol{A}^+\boldsymbol{A}, \qquad (\boldsymbol{A}\boldsymbol{A}^+)^H = \boldsymbol{A}\boldsymbol{A}^+.$$

The dimensions of $\boldsymbol{A}^+$ are hence the same as those of the transpose or adjoint of $\boldsymbol{A}$.

For non-singular matrices the pseuoinverse is equal to the regular inverse $\boldsymbol{A}^{-1}$. The pseudoinverse also exists for singular and non-square matrices and is, hence, also described as a generalized inverse.

For matrices with full column rank the pseudoinverse is given by

$$\boldsymbol{A}^+ = (\boldsymbol{A}^H\boldsymbol{A})^{-1}\boldsymbol{A}^H, \tag{B.5}$$

and is in this case the (unique) left inverse to $\boldsymbol{A}$:

$$\boldsymbol{A}^+\boldsymbol{A} = \boldsymbol{I}. \tag{B.6}$$

For matrices with full row rank the pseudoinverse is given by

$$\boldsymbol{A}^{+} = \boldsymbol{A}^{H}(\boldsymbol{A}\boldsymbol{A}^{H})^{-1}, \tag{B.7}$$

and is in this case the (unique) right inverse to $\boldsymbol{A}$:

$$\boldsymbol{A}\boldsymbol{A}^{+} = \boldsymbol{I}. \tag{B.8}$$

Besides the property of being the unique left and right inverse to a matrix (if they exist) the other important property is the solution of equation systems in the least squares sense. If

$$\boldsymbol{y} = \boldsymbol{A}\boldsymbol{x} \tag{B.9}$$

is not solvable because it is overdetermined, then the value $\widetilde{\boldsymbol{x}} = \boldsymbol{A}^{+}\boldsymbol{y}$ gives the least squares solution, i.e.,

$$||\boldsymbol{y} - \boldsymbol{A}\widetilde{\boldsymbol{x}}||^2 \leq ||\boldsymbol{y} - \boldsymbol{A}\boldsymbol{x}||^2, \qquad \text{for all } \boldsymbol{x}. \tag{B.10}$$

In any case (even if $\boldsymbol{A}$ has neither full row or column rank) $\boldsymbol{A}^{+}$ can be expressed using the singular value decomposition (SVD) of $\boldsymbol{A}$:

$$\boldsymbol{A} = \boldsymbol{U}\boldsymbol{S}\boldsymbol{V}^{H} \qquad \text{SVD of } \boldsymbol{A} \tag{B.11}$$

$$\Rightarrow \boldsymbol{A}^{+} = \boldsymbol{V}\boldsymbol{S}^{+}\boldsymbol{U}^{H}, \tag{B.12}$$

with

$$(\boldsymbol{S}^{+})_{ij} = \begin{cases} \sigma_i^{-1} & i = j, \sigma_i > 0 \\ 0 & \text{otherwise} \end{cases}, \qquad \sigma_i = (\boldsymbol{S})_{ii}. \tag{B.13}$$

Due to the availability of numerically stable algorithms for the computation of the SVD this is a robust method for calculating the pseusoinverse. More information on the Moore-Penrose pseudoinverse including derivations and proofs can be found in the literature [188].

B.3. Efficient computation of the Fourier and Hilbert transform

It is a very common problem to compute continuous Fourier transforms (FT) from measured or theoretical data in a computer. A common approximation is the use of the FFT algorithm which implements the discrete Fourier transform (DFT). The DFT is not the same as the FT, because it assumes periodicity in both the time and frequency domain. These assumptions, however, may not resemble the reality for the data that is to be transformed even it is only known in a finite time range. A common workaround is the use of the DFT with zero padding in the time domain to decrease the influence of the time domain periodicity assumption. Nevertheless, the periodicity assumption in the frequency domain corresponds to Dirac delta shaped samples in the time domain. However, linear or any other interpolation would be a more appropriate assumption for almost all measurement data. Furthermore, the samples in both time and frequency domain have to be equidistant and, hence, the DFT approximation becomes extremely inefficient where data spanning several orders of magnitude is to be transformed. Transforms with arbitrary or logarithmically spacing are preferred.

Numerical integration of the Fourier integral which exactly describes the continuous Fourier transform for continuous and infinitely long data would solve all these problems, but is numerically very inefficient because of the highly oscillatory integrand. All these problems are solved by the following method.

Similar arguments hold for the Hilbert transform, which is even a more complicated matter because of the singularity in the integrand. Nevertheless, the presented method for the Fourier transform can be applied for the Hilbert transfrorm as well.

The Fourier transform $\widehat{f}(f)$ and Hilbert transform $\widetilde{f}(t)$ of a function $f(t)$ are defined by

$$\widehat{f}(f) = \int_{-\infty}^{\infty} f(t)\mathrm{e}^{-2\pi \mathrm{i} f t}\mathrm{d}t, \tag{B.14}$$

$$\widetilde{f}(t) = \frac{1}{\pi}\,\mathrm{PV}\int_{-\infty}^{\infty} \frac{f(\tau)}{t-\tau}\mathrm{d}\tau. \tag{B.15}$$

If the function $f(t)$ is only available at N discrete points t_i, i.e.,

$$f_i = f(t_i), \qquad i = 1, \ldots, N \tag{B.16}$$

an interpolation with appropriate assumptions on the behavior of f outside the interval has to be made for calculation of the FT.

Without interpolation the Fourier and Hilbert transform of f could not be computed in an exact mathematical sense according to Eq. (B.14) because the behavior of f between the points t_i and outside of t_1 and t_N is of course unknown. Hence, certain assumptions about the behavior of f between the points have to be made to approximate $\widehat{f}(f)$. The linear interpolation of f_i is given by

$$f^1(t) = \sum_{i=1}^{N} f_i B_i(t), \tag{B.17}$$

with $B_i(t)$ the “hat function” on the interval $[t_{i-1}, t_{i+1}]^1$:

$$B_i(t) = \begin{cases} \frac{t-t_{i-1}}{t_i-t_{i-1}} & t_{i-1} \le t < t_i \\ \frac{t-t_{i+1}}{t_i-t_{i+1}} & t_i \le t < t_{i+1} \\ 0 & \text{otherwise} \end{cases}, \tag{B.18}$$

with $t_0 = t_1$ and $t_{N+1} = t_N$. This is obviously the linear interpoland because if Eq. (B.17) is evaluated at $t = t_i$, only one summand is nonzero and $f^1(t_i) = f_i$ is obtained. In between the t_i, $f^1(t)$ is continuous and linear (because B_i is continuous and linear between the t_i).

The continuous Fourier and Hilbert transform of Eq. (B.17) are readily given as

$$\widehat{f^1}(f) = \sum_{i=1}^{N} f_i \widehat{B}_i(f), \qquad \widetilde{f^1}(f) = \sum_{i=1}^{N} f_i \widetilde{B}_i(f), \tag{B.19}$$

whereas only the Fourier and Hilbert transform of the hat function are needed. For the

---

[1] Also known as the (non-uniform) first order B-spline.

former it is given by

$$\widehat{B}_i(f) = \begin{cases} \frac{1}{(2\pi f)^2}\left(\frac{e^{-2\pi i f t_i} - e^{-2\pi i f t_{i-1}}}{t_i - t_{i-1}} - \frac{e^{-2\pi i f t_{i+1}} - e^{-2\pi i f t_i}}{t_{i+1} - t_i}\right) & f \neq 0 \\ \frac{t_{i+1} - t_{i-1}}{2} & f = 0 \end{cases}. \tag{B.20}$$

At the measurement interval edges (where the neighboring t_i values coincide) the above difference quotients have to be replaced by the derivative, i.e.,

$$\frac{e^{-2\pi i f t_i} - e^{-2\pi i f t_{i\pm 1}}}{t_i - t_{i\pm 1}} \to -2\pi i f e^{-2\pi i f t_i}, \qquad \text{for } t_i \to t_{i\pm 1}. \tag{B.21}$$

The Hilbert transform of the hat function is given by

$$\widetilde{B}_i(t) = \frac{1}{\pi} \cdot \begin{cases} 1 + \frac{\mathrm{xlnxy}(t - t_{i+1}, t - t_i)}{t_{i+1} - t_i} & t_{i-1} = t_i \\ -1 + \frac{\mathrm{xlnxy}(t - t_{i-1}, t - t_i)}{t_i - t_{i-1}} & t_{i+1} = t_i \\ \frac{\mathrm{xlnx}(t - t_{i-1})}{t_i - t_{i-1}} - \frac{\mathrm{xlnx}(t - t_i)(t_{i+1} - t_{i-1})}{(t_{i+1} - t_i)(t_i - t_{i-1})} + \frac{\mathrm{xlnx}(t - t_{i+1})}{t_{i+1} - t_i} & \text{else} \\ \frac{\mathrm{xlnxy}(t - t_{i-1}, t - t_i)}{t_i - t_{i-1}} + \frac{\mathrm{xlnxy}(t - t_{i+1}, t - t_i)}{t_{i+1} - t_i} & \text{else, } |t| \text{ large} \end{cases}, \tag{B.22}$$

with

$$\mathrm{xlnxy}(x, y) = \begin{cases} x \ln |x/y| & x, y \neq 0 \\ 0 & x = 0, y \neq 0 \\ \infty & y = 0 \end{cases}, \qquad \mathrm{xlnx}(x) = \begin{cases} x \ln |x| & x \neq 0 \\ 0 & x = 0 \end{cases}. \tag{B.23}$$

Note, that the last two entries in the case Eq. (B.22) are mathematically equivalent. However, the latter expression is preferred for large t outside of the interval $[t_{i-1}, t_{i+1}]$ because numerical problems are expected for expression 3 when t is outside of $[t_{i-1}, t_{i+1}]$ and problems are expected for expression 4 when t is close to t_i.

Note, that the function f is assumed to be zero outside of the interval $[t_1, t_N]$ and thus the linear interpolate may have steps at the end of the interval. This generally causes certain contributions to the Fourier and Hilbert transform but these may not be realistic if the real function f has a different behavior than being zero outside of the interval. This can be alleviated when the two additional points t_0 and t_{N+1} are chosen to be outside of the interval. This has the effect that at the edges of the interval the function has a more smooth behavior towards zero and does not realize a step. The actual choice of these additional "outside of interval points" requires of course knowledge on the origin of the data.

B.4. Line shape functions, their n-th derivatives, Fourier and Hilbert transform

Lorentz The area normalized Lorentz line shape $\phi_{\mathrm{L}}(\nu)$ with half-width at half maximum (HWHM) γ_{L} is given by

$$\phi_{\mathrm{L}}(\nu) = \frac{\gamma_{\mathrm{L}}}{\pi\left(\gamma_{\mathrm{L}}^2 + \nu^2\right)}. \tag{B.24}$$

The n-th derivative with respect to ν is given by

$$\phi_{\mathrm{L}}^{(n)}(\nu) = \phi_{\mathrm{L}}(\nu) \frac{n!}{(\gamma_{\mathrm{L}}^2 + \nu^2)^{n/2}} \, \mathrm{U}_n \left(-\nu / \sqrt{\gamma_{\mathrm{L}}^2 + \nu^2} \right) , \tag{B.25}$$

with U_n the Chebyshev polynomial of the second kind [78, chapter 22]. Eq. (B.25) directly follows from the generating function for U_n [78, chapter 22.9].

The Fourier and Hilbert transform of the Lorentz line shape are given by

$$\widehat{\phi}_{\mathrm{L}}(k) = \exp\left(-2\pi\gamma_{\mathrm{L}}|k|\right) , \qquad \widetilde{\phi}_{\mathrm{L}}(\nu) = \frac{\nu}{\pi(\gamma_{\mathrm{L}}^2 + \nu^2)} . \tag{B.26}$$

Gaussian The area normalized Gaussian line shape $\phi_{\mathrm{G}}(\nu)$ with HWHM γ_{G} is given by

$$\phi_{\mathrm{G}}(\nu) = \frac{\sqrt{\log 2}}{\sqrt{\pi}\gamma_{\mathrm{G}}} \exp\left(-\frac{\nu^2}{\gamma_{\mathrm{G}}^2} \log 2 \right) . \tag{B.27}$$

The n-th derivative with respect to ν is given by

$$\phi_{\mathrm{G}}^{(n)}(\nu) = \phi_{\mathrm{G}}(\nu) \frac{(\log 2)^{n/2}}{\gamma_{\mathrm{G}}^n} \, \mathrm{H}_n \left(-\nu / \gamma_{\mathrm{G}} \sqrt{\log 2} \right) , \tag{B.28}$$

with H_n the Hermite polynomial [78, chapter 22]. Eq. (B.28) directly follows from the generating function for H_n [78, chapter 22.9].

The Fourier and Hilbert transform of the Gauss line shape are given by

$$\widehat{\phi}_{\mathrm{G}}(k) = \exp\left(-(\pi k \gamma_{\mathrm{G}})^2 / \log 2 \right) , \tag{B.29}$$

$$\widetilde{\phi}_{\mathrm{G}}(\nu) = \frac{\sqrt{\log 2}}{\sqrt{\pi}\gamma_{\mathrm{G}}} \, \mathrm{Im} \left\{ w \left(\frac{\nu \sqrt{\log 2}}{\gamma_{\mathrm{G}}} \right) \right\} , \tag{B.30}$$

with $w(z)$ the Faddeeva w function (see below).

Voigt The area normalized Voigt line shape $\phi_{\mathrm{V}}(\nu)$ with Gaussian HWHM γ_{G} and Lorentzian HWHM γ_{L} is given by

$$\phi_{\mathrm{V}}(\nu) = (\phi_{\mathrm{L}} * \phi_{\mathrm{G}})(\nu) = \frac{\sqrt{\log 2}}{\sqrt{\pi}\gamma_{\mathrm{G}}} \, \mathrm{Re} \left\{ w \left(\frac{(\nu + \mathrm{i}\gamma_{\mathrm{L}}) \sqrt{\log 2}}{\gamma_{\mathrm{G}}} \right) \right\} , \tag{B.31}$$

with the Faddeeva w function

$$w(z) = \mathrm{e}^{-z^2} \left(1 + \frac{2\mathrm{i}}{\sqrt{\pi}} \int_{-\infty}^{z} \mathrm{e}^{t^2} \, \mathrm{d}t \right) = \mathrm{e}^{-z^2} \, \mathrm{erfc}\left(-\mathrm{i}z\right) . \tag{B.32}$$

The $w(z)$ function can be computed using ACM Algorithm 680 [189] which implements the method developed in Ref. [190] that gives for the relevant upper half-plane a 14 digits relative accuracy.

The n-th derivative with respect to ν is given by

$$\phi_{\mathrm{V}}^{(n)}(\nu) = \frac{\sqrt{\log 2}^{\,n+1}}{\sqrt{\pi}\gamma_{\mathrm{G}}^{n+1}} \, \mathrm{Re} \left\{ w^{(n)} \left(\frac{(\nu + \mathrm{i}\gamma_{\mathrm{L}}) \sqrt{\log 2}}{\gamma_{\mathrm{G}}} \right) \right\} , \tag{B.33}$$

$$w^{(n)}(z) = w(z)\,\mathrm{H}_n\left(-z\right) - \frac{2}{\sqrt{\pi}} \sum_{k=0}^{n-1} \binom{n}{k+1} (-\mathrm{i})^{k+1}\,\mathrm{H}_k\left(\mathrm{i}z\right)\mathrm{H}_{n-k-1}\left(-z\right). \tag{B.34}$$

The Fourier and Hilbert transform of the Voigt line shape are given by

$$\widehat{\phi}_\mathrm{V}(k) = \widehat{\phi}_\mathrm{L}(k)\widehat{\phi}_\mathrm{G}(k) = \exp\left(-(\pi k\gamma_\mathrm{G})^2/\log 2 - 2\pi\gamma_\mathrm{L}|k|\right), \tag{B.35}$$

$$\widetilde{\phi}_\mathrm{V}(\nu) = \frac{\sqrt{\log 2}}{\sqrt{\pi}\gamma_\mathrm{G}}\,\mathrm{Im}\left\{w\left(\frac{(\nu+\mathrm{i}\gamma_\mathrm{L})\sqrt{\log 2}}{\gamma_\mathrm{G}}\right)\right\}. \tag{B.36}$$

B.5. Allan variance plot

The Allan variance or Allan deviation plot is an intuitive graphical tool for analysis of noise types a time series consists of. Different slopes in the (log-log) Allan plot correspond to noise with different exponents of a power-law frequency dependence. Hence white noise and $1/f$ noise and their relative strength can be distinguished. It was introduced to examine the frequency stability of oscillators and to quantify noise types other than the (often only assumed) white noise [191]. Werle et al. introduced the Allan variance plots to investigate the stability of TDLS sensors, which has become since then a standard tool to evaluate the performance of TDLS sensors. Its main purpose is to identify causes that limit sensor stability (which might appear as $1/f$ or $1/f^2$ noise) and to find the maximum time where a calibration or background measurement should be repeated [192] (commonly referred to as the “optimum averaging time”). To make an “Allan plot” for a sensor, the sensor has to be operated with the physical quantity kept constant which it is supposed to measure. If concentration is to be measured, the gas concentration has to be constant. Then the sensor output values are recorded over as long as possible time spans and the samples then analyzed with the Allan variance to identify the different types of noise sources. A deterministic linear slope on the time series data will show the same behavior as $1/f^2$ noise in the Allan plot, and, hence, these two effects are indistinguishable [192].

The N data samples are denoted as $y_i = y(t_i)$ with uniform sample times $t_i = t_0 + iT_s$ with $i = 0, \dots, N-1$, and T_s being the data sample time. After averaging over data blocks of time length $\tau = LT_s$ (with L a positive integer number) new data samples $\overline{y}(j)$ are obtained representing the averaged and decimated (i.e., downsampled) data

$$\overline{y}(j) = \frac{1}{L}\sum_{i=0}^{L-1} y(t_{jL+i}), \qquad j = 0, \dots, M-1, \tag{B.37}$$

and $M = \lfloor N/L \rfloor$ the number of averaged samples. The Allan variance $\sigma_\mathrm{A}^2(\tau)$ is then half of the quadratic deviation of two neighboring samples

$$\sigma_\mathrm{A}^2(\tau) = \frac{1}{2(M-1)}\sum_{j=1}^{M-1}\left(\overline{y}(j) - \overline{y}(j-1)\right)^2. \tag{B.38}$$

The term $\sigma_\mathrm{A}(\tau)$ (without square) is called Allan deviation. Usually the Allan deviation is plotted because it has the same unit as the original time series data. Practically it is plotted versus averaging time τ, which however must be an integer multiple of T_s and less than half of the time length of the original data. Obviously, if the data only consists of white noise around a constant mean value also the averaged time series $\overline{y}(j)$ consists of white noise around the same mean but with $\sqrt{L}$ times less standard deviation. Consequently, also the variation between two neighboring samples becomes smaller by the same amount. Hence for white noise a $\sigma_\mathrm{A}(\tau) \sim 1/\sqrt{\tau}$ behavior is expected. Moreover, in the white noise one gets for the expected value of the Allan variance $\mathrm{E}\left\{\sigma_\mathrm{A}^2(\tau)\right\} = \frac{1}{2(M-1)}\sum_{j=1}^{M-1}(\sigma^2(\overline{y}(j)) + \sigma^2(\overline{y}(j-1))) = \sigma^2(\overline{y})$, i.e., the Allan variance of white noise is the same as the variance of the averaged data. For white noise the normal variance and the Allan variance are the same. This is not the case for other noise types.

For noise with (one-sided) noise spectral density $S_{yy}(f)$ an Allan variance of [193]

$$\sigma_\mathrm{A}^2(\tau) = \frac{2}{\pi\tau}\int_0^\infty S_{yy}\left(\frac{u}{\pi\tau}\right)\frac{\sin^4(u)}{u^2}\mathrm{d}u \tag{B.39}$$

is obtained. This shows that if two uncorrelated random processes are added together also their Allan variances add together (because for uncorrelated random processes the spectral densities add). Values at high τ reveal information about $S_{yy}(f)$ around $f = 0$. Also qualitative information about the type of the noise can be read from the slope of the Allan plot. It can be shown [191], that for noise spectral densities

$$S_{yy}(f) = \begin{cases} f^{-\alpha} & f_l \le f \le f_u \\ 0 & \text{otherwise} \end{cases} \tag{B.40}$$

with $-1 < \alpha < 3$ we get

$$\sigma_\mathrm{A}^2(\tau) \sim \tau^{\alpha-1}, \qquad \text{for } \frac{1}{2\pi f_u} \ll \tau \ll \frac{1}{2\pi f_l}. \tag{B.41}$$

For $\tau \ll \frac{1}{2\pi f_u}$ or $\tau \gg \frac{1}{2\pi f_l}$ the Allan variance becomes zero for the spectral density in Eq. (B.40). Eq. (B.41) means that if the spectral density follows a power law, this is reflected in the asymptotic slope of the (log-log) Allan plot. The slope then corresponds to the exponent of the power law minus one. Again this explains that white noise ($\alpha = 0$) appears with a slope of -1 on the Allan variance plot (or slope $-1/2$, or $\sim 1/\sqrt{\tau}$ in the Allan deviation as explained before). If the lower frequency f_l is zero then the exponent determines the asymptotic slope of the Allan plot (for $\tau \to \infty$). Practically, the Allan plot will consist of several regions with different slope. This then corresponds to different noise contributions with different exponent. The time where the transition from one to another takes place is depending on the relative strength of the noise sources. This can be seen in the example in Fig. B.1. Up to $\tau = 400\,\mathrm{s}$ a nearly white noise behavior is observed. For averaging times between $400\,\mathrm{s}$ to $5000\,\mathrm{s}$ a slope corresponding to $1/f$ noise is observed. Although the $1/f$ noise is present at all averaging times it only becomes dominant at this point because the white noise is attenuated by averaging while the $1/f$ noise is almost not attenuated. Hence, the transition is observed at a specific averaging time.

In Fig. B.1 also the conventional standard deviation is shown in red. As mentioned before, in the white noise regions (i.e., where the slope is $-1/2$) the Allan and conventional deviation are essentially the same. It also becomes evident that the Allan variance is better suited for analysis of different noise types because it gives a more pronounced response to different noise types than is visible in the conventional deviation.

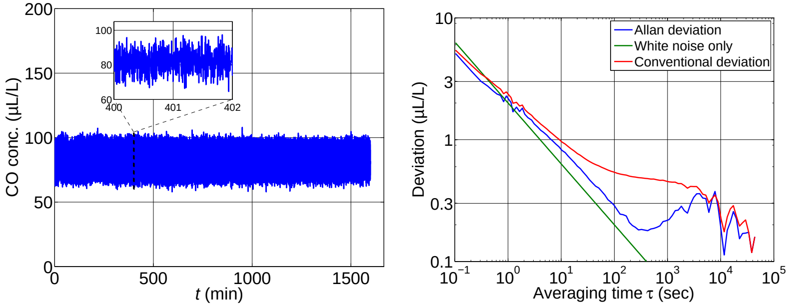

(a) One day long time series recorded with the VCSEL-based CO sensor [54] measuring a gas sample with constant physical conditions (i.e., pressure, temperature and concentration).

(b) The Allan deviation ("Allan plot") corresponding to the left time series (blue). For comparison the conventional standard deviation (red) and the expected behavior for white noise only is shown as well (green).

Fig. B.1: *An example for an Allan plot including the corresponding time data.*

B.6. Linear systems

B.6.1. Definition and representation by integral equations

A linear system is characterized by the superposition principle and homogeneity. Let $x_1 = x_1(t)$ and $x_2 = x_2(t)$ be two arbitrary input signals then a system $\mathcal{H}$ is called linear if it fulfills

$$\mathcal{H}\{\alpha x_1 + \beta x_2\}(t) = \alpha\mathcal{H}\{x_1\}(t) + \beta\mathcal{H}\{x_2\}(t) \tag{B.42}$$

for arbitrary constants α and β. If the system is additionally bounded it can always be described with an integral equation [194, Chapter 3.3], i.e.,

$$\mathcal{H}\{x\}(t) = \int_{-\infty}^{\infty} h(t,\tau)x(\tau)\mathrm{d}\tau \tag{B.43}$$

with $h(t,\tau)$ the impulse response of such system. This integral equation is to be understood in a distributional sense, i.e., it is only correct if h is allowed to be a distribution. The representability of all bounded linear systems by this type of integral equation is known as "Schwartz kernel theorem".

The impulse response is defined as the limit of the response to a rectangular function with unit area when the width approaches zero (cf. Ref. [194, Chapter 3.3]), i.e.,

$$h(t,\tau) = \lim_{d\to 0} \mathcal{H}\{\delta_d(\cdot - \tau)\}(t), \qquad \text{with } \delta_d(t) = \begin{cases} 1/d & |t| < d/2 \\ 0 & \text{otherwise} \end{cases}. \tag{B.44}$$

If a linear system is additionally time-invariant or shift-invariant, i.e.,

$$\mathcal{H}\{x(\cdot - \tau)\}(t) = \mathcal{H}\{x\}(t - \tau) \tag{B.45}$$

the behavior of the system does not depend on the absolute value of time. The response is always the same whenever the excitation (input) is applied. Hence the name time-invariant. In this case the integral equation is changed to a convolution expression, because it must be $h(t,\tau) = h(t-\tau)$:

$$\mathcal{H}\{x\}(t) = \int_{-\infty}^{\infty} h(t-\tau)x(\tau)\mathrm{d}\tau. \tag{B.46}$$

This equation describes any bounded, linear and shift-invariant system, which is a very general mathematical result. Again the impulse response h is a distribution.

As a consequence, one has the important property for bounded, linear and shift-invariant systems that a sinusoidal input always generates a sinusoidal output with the same frequency. This is easily seen when $x(t) = \mathrm{e}^{\mathrm{i}2\pi f t}$ is inserted into Eq. (B.46):

$$\mathcal{H}\{\mathrm{e}^{\mathrm{i}2\pi f\cdot}\}(t) = \widehat{h}(f)\,\mathrm{e}^{\mathrm{i}2\pi f t}, \qquad \text{with } \widehat{h}(f) = \int_{-\infty}^{\infty} h(\tau)\mathrm{e}^{-\mathrm{i}2\pi f\tau}\mathrm{d}\tau. \tag{B.47}$$

One can further see, that the appearance of the Fourier transform $\widehat{h}(f)$ of the impulse response is a natural consequence. This is actually the justification for the wide use of the Fourier transform in science and engineering. This so called “frequency response” $\widehat{h}(f)$ of the system can be split into amplitude response $A(f)$ and phase response $\phi(f)$ (with $\widehat{h}(f) = A(f)\mathrm{e}^{-\mathrm{i}\phi(f)}$) because of

$$\mathcal{H}\{\mathrm{e}^{\mathrm{i}2\pi f\cdot}\}(t) = A(f)\,\mathrm{e}^{\mathrm{i}2\pi f t - \mathrm{i}\phi(f)}. \tag{B.48}$$

Note, that the frequency response completely describes the behavior of a bounded linear shift invariant system, due to the one-to-one mapping of the Fourier transform. Hence a bounded, linear and shift-invariant system is fully characterized by its response to sinusoids of different frequency. This is a result with very great practical importance. It explains how a system – considered as a black box – is fully described, based only on a few general and easy to test properties (i.e., linearity and shift- or time-invariance).

B.6.2. Relation to ordinary differential equations

A linear and time-invariant ordinary differential equation (ODE) is of the form

$$a_0 y(t) = b_0 x(t) + b_1 x'(t) + b_2 x''(t) + \ldots - a_1 y'(t) - a_2 y''(t) - \ldots \tag{B.49}$$

Time invariance implies that the coefficients a_i and b_i are time independent and linearity implies that they are independent from x and y. Note, that not all linear and time-invariant systems are described by this form, only those which are ODEs. The Fourier transform is given by

$$\widehat{y}(f) = \widehat{x}(f)\,\underbrace{\frac{a_0 + (2\pi\mathrm{i}f)a_1 + (2\pi\mathrm{i}f)^2 a_2 + \ldots}{b_0 + (2\pi\mathrm{i}f)b_1 + (2\pi\mathrm{i}f)^2 b_2 + \ldots}}_{\widehat{h}(f)}, \tag{B.50}$$

which can be used to solve the ODE. The Fourier transform of the impulse response $\widehat{h}(f)$ is the frequency response and is a rational polynomial in $2\pi\mathrm{i}f$. This shows that linear ODE systems are not covering all linear time-invariant systems, because their frequency response is always a rational polynomial which is not necessarily the case for arbitrary linear time invariant systems.

B.6.3. Asymptotic behavior

As a consequence of the rational frequency response, ODE based linear systems are limited to specific asymptotic behaviors:

$$|\widehat{h}(f)| \to f^n, \qquad \text{for } f \to \infty, \tag{B.51}$$

with n an integer number (because it is the ratio of two polynomials in f). This number is just the difference of numerator and denominator polynomial degree. Hence, it is impossible to obtain asymptotic fractional exponent behavior, e.g., $1/\sqrt{f}$ with linear ODE based systems.

This shows the difficulty to explain the behavior of systems which do not show such an behavior by ODEs, as e.g., the laser tuning behavior (cf. section 2.3.2) or $1/f$ noise. To recreate both, a system with asymptotic $1/\sqrt{f}$ behavior would be needed. Of course it is possible to approximate any behavior within a certain finite frequency range if the ODE degree is made large.

Despite this possibility of purely mathematical approximation, it is important to know that other (non-ODE) physical models may be inherently better suited for problems with fractional asymptotic slopes of the frequency response. In the following it will be shown that second order partial differential equations, such as the heat equation, can indeed reproduce a asymptotic behavior of fractional exponent.

Most interestingly, two analytic PDE-based models in literature for the intrinsic thermal tuning behavior for VCSELs and DFBs [34, 195] predict a square root law behavior for high frequencies i.e. $H_{\mathrm{thm}}(f) \to 1/\sqrt{\mathrm{i}f}$ for $f \to \infty$.

Here reasoning is given, that the heat equation gives a square root law behavior if the heat source and mode distribution have one dimension less compared to the mathematical space in which the heat equation is solved. This is for example the case if the heat source and mode have a plane shape in a 3D space or have a line shape in a 2D space. So a plane heat source and light mode in three dimensional space or a line source in two dimensional space give a square root behavior. If either the plane heat source or light mode distribution has a nonzero thickness, a transition from square root behavior to $1/(\mathrm{i}f)$ behavior will occur at a certain frequency, depending on the tickness. This can be seen as follows:

Assuming a $T = 0$ boundary condition at $(x, y, z) \to \infty$ and using Gaussian source and mode terms (Eq. (2.19) and Eq. (2.20)), Eq. (A.11) for the thermal impulse response reads:

$$\overline{T}_g(t) \sim \frac{1}{\sqrt{t-\tau_Z}(t-\tau_R)}, \quad t \geq 0, \quad \tau_Z = \frac{2\kappa_{\mathrm{Z}}}{Z_Q^2 + Z_M^2}, \quad \tau_R = \frac{2\kappa_{\mathrm{R}}}{R_Q^2 + R_M^2}. \tag{B.52}$$

Unfortunately, the Fourier transform of this is not analytically solvable. Nevertheless, the asymptotic behavior of the Fourier transform can be studied if the $1/(t - \tau_R)$ term is neglected. When the thickness of the heat source is practically much less than the width (i.e., $\tau_Z < \tau_R$), the asymptotic behavior of the Fourier transform is determined by the square root term only (corresponds to behavior of $\overline{T}_g(t)$ around the origin).

The Fourier transform of a square root impulse gives a square root behavior:

$$g(t) = \frac{1}{\sqrt{t}}, \quad t \geq 0 \qquad \Rightarrow \qquad \widehat{g}(f) = \frac{1}{\sqrt{2\mathrm{i}f}}. \tag{B.53}$$

If, however, the square root impulse is shifted by $\tau_Z > 0$, i.e., a thickness of the heat source is introduced and, hence, the singularity removed, different behavior is obtained:

$$g(t) = \frac{1}{\sqrt{t+\tau_Z}}, \quad t \geq 0 \qquad \Rightarrow \qquad \widehat{g}(f) = \frac{e^{2\pi \mathrm{i} f \tau_Z}\,\mathrm{erfc}\left(\sqrt{2\pi \mathrm{i} f \tau_Z}\right)}{\sqrt{2\mathrm{i}f}}. \tag{B.54}$$

This now has a $1/(\mathrm{i}f)$ behavior for high frequencies, but still follows square root behavior over a large frequency range (cf. Fig. B.2). Since the behavior at high frequencies of the Fourier transform is determined by the function behavior around $t = 0$, the singularity at $t = 0$ of $1/\sqrt{t}$ seems to be essential for causing the square root behavior. Investigations of solutions of the heat equations of different dimension (analogously to Eq. (B.52)) showed that this $1/\sqrt{t}$ term only exists if the heat source and light mode have a lower dimension as the space in which the heat equation is solved.

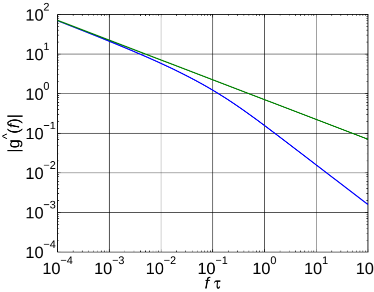

Fig. B.2: *The Fourier transform of a square root (green, Eq. (B.53)) and shifted square root impulse (blue, Eq. (B.54)). The first corresponds to zero thickness heat source and mode and the second to small finite thickness, which causes the transition from* $1/\sqrt{f}$ *to* $1/f$ *behavior.*

C. Derivations of equations

C.1 Derivation of Eq. (3.34)

By applying integration by parts n times in Eq. (3.32) one gets

$$H_n(\nu) = \int_{-\infty}^{\infty} T^{(n)}(\nu-\eta) \left(\int_{-\infty}^{\eta} \cdots \int_{-\infty}^{\eta_3} \int_{-\infty}^{\eta_2} K_{\mathrm{wms}}(\eta_1) \mathrm{d}\eta_1 \mathrm{d}\eta_2 \ldots \mathrm{d}\eta_n \right) \mathrm{d}\eta. \quad \text{(C.1)}$$

Note, that this uses the fact that K_{wms} is nonzero only over a finite range, and, hence, all of its antiderivatives vanish at $\pm\infty$. With help of Rodrigues' formula for the Chebyshev polynomials [78, chapter 22.11], i.e.,

$$\mathrm{T}_n(x) = \frac{\sqrt{\pi}}{(-1)^n 2^n \Gamma(n+1/2)} \sqrt{1-x^2} \frac{\mathrm{d}^n}{\mathrm{d}x^n} \left((1-x^2)^{n-1/2} \right) \quad \text{(C.2)}$$

the repeated integral in Eq. (C.1) can be solved in closed form. With

$$\underbrace{\int \cdots \int}_{n \text{ times}} \frac{\mathrm{T}_n(-x)}{\sqrt{1-x^2}} \mathrm{d}x_1 \cdots \mathrm{d}x_n = \frac{1}{1 \cdot 3 \cdot 5 \cdots (2n-1)} (1-x^2)^{n-1/2} \quad \text{(C.3)}$$

(where each integration starts at -1 and x is between -1 and 1) and $1 \cdot 3 \cdot 5 \cdots (2n-1) = (2n)!/(2^n n!)$ the following is obtained:

$$\int_{-\infty}^{\eta} \cdots \int_{-\infty}^{\eta_3} \int_{-\infty}^{\eta_2} K_{\mathrm{wms}}(\eta_1) \mathrm{d}\eta_1 \mathrm{d}\eta_2 \ldots \mathrm{d}\eta_n = \begin{cases} \frac{\epsilon_n 2^n n! (\nu_{\mathrm{a}}^2 - \eta^2)^n}{\pi (2n)! \nu_{\mathrm{a}}^n \sqrt{\nu_{\mathrm{a}}^2 - \eta^2}} & |\eta| \le \nu_{\mathrm{a}} \\ 0 & \text{otherwise} \end{cases}. \quad \text{(C.4)}$$

The normalization in $K_{\mathrm{wms}}^{\mathrm{der}}$ is obtained by

$$\int_{-\nu_a}^{\nu_a} \frac{\epsilon_n 2^n n! (\nu_{\mathrm{a}}^2 - \eta^2)^n}{\pi (2n)! \nu_{\mathrm{a}}^n \sqrt{\nu_{\mathrm{a}}^2 - \eta^2}} \mathrm{d}\eta = \frac{\epsilon_n \nu_{\mathrm{a}}^n}{2^n n!}. \quad \text{(C.5)}$$

C.2 Derivation of Eq. (3.37)

The zero mean property is a special case (with $i = 0$) of Eq. (3.38). See derivation C.3.

C.3 Derivation of Eq. (3.38)

First note that the orthogonality to monomials (or vanishing moments) is equivalent to vanishing derivatives of the Fourier transform around the origin:

$$\int_{-\infty}^{\infty} \nu^i H_n(\nu) \mathrm{d}\nu = 0, \text{ for } 0 \le i < n \Leftrightarrow \left. \frac{\mathrm{d}^i \widehat{H}_n(k)}{\mathrm{d}k^i} \right|_{k=0} = 0, \text{ for } 0 \le i < n. \quad \text{(C.6)}$$

From Eq. (3.36) it is known that

$$\widehat{H}_n(k) = \widehat{T}(k)\epsilon_n \mathrm{i}^n \, \mathrm{J}_n\left(2\pi\nu_\mathrm{a}k\right), \tag{C.7}$$

which, after i-th differentiation (Leibnitz' rule), results in

$$\widehat{H}_n^{(i)}(k) = \epsilon_n \mathrm{i}^n \sum_{j=0}^{i} \binom{i}{j} (2\pi\nu_\mathrm{a})^j \widehat{T}_n^{(i-j)}(k)\, \mathrm{J}_n^{(j)}(2\pi\nu_\mathrm{a}k). \tag{C.8}$$

Note that the j-th order derivative of the Bessel function can be expressed as sum of Bessel functions of order $n-j, \ldots, n+j$ [78, Eq. 9.1.31]. Because $j < n$ it follows that $\mathrm{J}_{n\pm j}(0) = 0$ and consequently $\mathrm{J}_n^{(j)}(0) = 0$ which proves the original statement.

C.4 Derivation of Eq. (3.39)

The following recursion property of the Bessel functions [78, Eq. 9.1.27] is known:

$$\mathrm{J}_{n+1}(x) = \frac{2n}{x}\mathrm{J}_n(x) - \mathrm{J}_{n-1}(x). \tag{C.9}$$

If $\mathrm{J}_n(x)$ is replaced by $K_\mathrm{wms}(k)$ (see Eq. (3.36)) and multiplied with the Fourier transform of the transmission $\widehat{T}(k)$, the following recursion formula for the Fourier transform of the n-th harmonic spectra is obtained:

$$\widehat{H}_{n+1}(k) = -\frac{n\epsilon_{n+1}}{\epsilon_n \nu_\mathrm{a} \mathrm{i}\pi k}\widehat{H}_n(k) + \frac{\epsilon_{n+1}}{\epsilon_{n-1}}\widehat{H}_{n-1}(k). \tag{C.10}$$

When transforming back the desired formula Eq. (3.39) is obtained. Multiplication with $1/(2\mathrm{i}\pi k)$ corresponds to an integration, because $n\widehat{H}_n(0)$ is zero for all n:

$$H_{n+1}(\nu) = -\frac{2n\epsilon_{n+1}}{\epsilon_n \nu_\mathrm{a}} \int_{-\infty}^{\nu} H_n(\nu)\mathrm{d}\nu + \frac{\epsilon_{n+1}}{\epsilon_{n-1}} H_{n-1}(\nu). \tag{C.11}$$

It is important to remark that for $n = 1$ prior to application of this formula the offset of the zeroth harmonic spectrum has to be removed. This is because for derivation to be valid $\widehat{H}_n$ may not contain a Dirac delta distribution.

C.5 Derivation of Eq. (3.40)

The first reconstruction formula is a special case (with $n = 0$) of Eq. (3.42). See derivation C.7. Alternatively it can be directly proven by the following property of the Bessel functions [78, Eq. 9.1.46]:

$$1 = \sum_{n=0}^{\infty} \epsilon_n \, \mathrm{J}_{2n}(x). \tag{C.12}$$

If the Bessel function is replaced by $K_\mathrm{wms}(k)$ (see Eq. (3.36)) and multiplied with the Fourier transform of the transmission the following is obtained (Note: $\widehat{H}_n(k) =$

$\widehat{T}_n(k)K_{\mathrm{wms}}(k))$:

$$\widehat{T}(k) = \sum_{n=0}^{\infty}(-1)^n \widehat{H}_n(k). \tag{C.13}$$

After applying the inverse Fourier transform the desired result is found.

C.6 Derivation of Eq. (3.41)

The implicit definition of harmonic spectra reads

$$T(\nu + \nu_a \cos(2\pi f_{\mathrm{m}} t)) = \sum_{n=0}^{\infty} H_n(\nu; \nu_{\mathrm{a}}) \cos(2\pi n f_{\mathrm{m}} t). \tag{C.14}$$

By substituting $\nu + \nu_{\mathrm{a}} \cos(2\pi f_{\mathrm{m}} t) = \eta$ it is obtained:

$$T(\eta) = \sum_{n=0}^{\infty} H_n(\nu; \nu_{\mathrm{a}}) \cos(n \arccos((\eta - \nu)/\nu_{\mathrm{a}})). \tag{C.15}$$

After exchanging the names of the variables ν and η and noting that $\cos(n \arccos(x))$ is equal to the Chebyshev polynomial $\mathrm{T}_n(x)$ the desired result is obtained. Note that the range of validity of the substitution (i.e., $|\eta - \nu| \leq \nu_{\mathrm{a}}$) is also the range of validity of the final formula.

C.7 Derivation of Eq. (3.42)

The first step is to compute the derivatives of Eq. (3.41), i.e.:

$$\frac{\mathrm{d}^k T(\nu)}{\mathrm{d}\nu^k} = \sum_{n=0}^{\infty} H_n(\eta) \frac{\mathrm{d}^k\, \mathrm{T}_n((\nu - \eta)/\nu_{\mathrm{a}})}{\mathrm{d}\nu^k}. \tag{C.16}$$

Since η is arbitrary it is possible choose $\eta = \nu$ in which case

$$\frac{\mathrm{d}^k T(\nu)}{\mathrm{d}\nu^k} = \sum_{n=0}^{\infty} H_n(\nu) \frac{1}{\nu_{\mathrm{a}}^k}\, \mathrm{T}_n^{(k)}(0) \tag{C.17}$$

is obtained. Using the explicit expression for the coefficients of the Chebyshev polynomials [78, Eq. 22.3.6] it is tedious but not difficult to derive an expression for $\mathrm{T}_n^{(k)}(0)$. This gives then the desired result Eq. (3.42).

C.8 Derivation of Eq. (3.45)

There is the general property of convolutions $||f * g||_\infty \leq ||f||_1 ||g||_\infty$, which is a special case of Young's inequality. Note, that the infinity norm is $||g||_\infty = \max_x |g(x)|$ and to obtain the result it is only necessary to compute $||K_{\mathrm{wms}}||_1$ and $||K_{\mathrm{wms}}^{\mathrm{der}}||_1$ for Eq. (3.45) and Eq. (3.46), respectively. Explicitly, the following integral values are needed:

$$\int_{-\nu_{\mathrm{a}}}^{\nu_{\mathrm{a}}} |K_{\mathrm{wms}}(\nu)| \mathrm{d}\nu, \qquad \int_{-\nu_{\mathrm{a}}}^{\nu_{\mathrm{a}}} |K_{\mathrm{wms}}^{\mathrm{der}}(\nu)| \mathrm{d}\nu. \tag{C.18}$$

This is equal to:

$$\int_{-1}^{1} \frac{\epsilon_n |\,\mathrm{T}_n(-x)\,|}{\pi\sqrt{1-x^2}} \mathrm{d}x, \qquad \int_{-1}^{1} \frac{4^n n!^2 (1-x^2)^n}{\pi (2n)! \sqrt{1-x^2}} \mathrm{d}x. \tag{C.19}$$

The latter integral has a value of 1, i.e., $||K_{\mathrm{wms}}^{\mathrm{der}}||_1 = 1$. The former integral is more difficult because of the alternating signs of the Chebyshev polynomials. For $n = 0$ both integrals are the same and also $||K_{\mathrm{wms}}||_1 = 1$ for $n = 0$ is obtained. For $n > 0$ the integrations thus have to be split at the Chebyshev nodes x_i (which are the zeros of $\mathrm{T}_n(x)$). Using the Chebyshev nodes in reverse order

$$x_i = \cos\left((2i-1)/(2n)\pi\right) \qquad i = 1, \ldots, n, \tag{C.20}$$

with the convention $x_0 = 1$ and $x_{n+1} = -1$ one obtains

$$\int_{-1}^{1} \frac{\epsilon_n |\,\mathrm{T}_n(-x)\,|}{\pi\sqrt{1-x^2}} \mathrm{d}x = -\sum_{i=0}^{n} (-1)^i \int_{x_i}^{x_{i+1}} \frac{\epsilon_n \mathrm{T}_n(x)}{\pi\sqrt{1-x^2}} \mathrm{d}x. \tag{C.21}$$

The factor $(-1)^i$ is to handle properly the regions with negative values. Substitution of $z = \arccos(x)$ gives

$$= \sum_{i=0}^{n} (-1)^i \int_{z_i}^{z_{i+1}} \frac{\epsilon_n}{\pi} \cos(nz)\,\mathrm{d}z = \frac{\epsilon_n}{n\pi} \sum_{i=0}^{n} (-1)^i (\sin(nz_{i+1}) - \sin(nz_i)) \tag{C.22}$$

Expanding the result yields $4/\pi$ and, hence, $||K_{\mathrm{wms}}||_1 = 4/\pi$ for $n > 0$.

C.9 Derivation of Eq. (3.57)

If the complex (two-sided) Fourier coefficients of two functions are given by

$$f(z) = \sum_{n=-\infty}^{\infty} \widetilde{F}_n \mathrm{e}^{\mathrm{i}nz}, \qquad g(z) = \sum_{n=-\infty}^{\infty} \widetilde{G}_n \mathrm{e}^{\mathrm{i}nz}, \tag{C.23}$$

the Fourier coefficients of the product are obtained by convolution of $\widetilde{F}_n$ and $\widetilde{G}_n$:

$$f(z)g(z) = \sum_{n=-\infty}^{\infty} \widetilde{K}_n \mathrm{e}^{\mathrm{i}nz} \qquad \widetilde{K}_n = \sum_{m=-\infty}^{\infty} \widetilde{F}_m \widetilde{G}_{n-m}. \tag{C.24}$$

For real valued functions the property $\widetilde{X}_n = \widetilde{X}^*_{-n}$ is always fulfilled and the one-sided Fourier coefficients X_n can be used instead $X_n = \epsilon_n \widetilde{X}_n$ $(n \geq 0)$. For the one-sided coefficients of a product one obtains

$$K_n = \frac{\epsilon_n}{2} \sum_{m=0}^{\infty} \frac{F_m G_{n-m}}{\epsilon_{n-m}} + \frac{F_m^* G_{n+m}}{\epsilon_{n+m}} \tag{C.25}$$

Note that the Fourier coefficients of $T(\nu_{\mathrm{L}}(t))$ are given by $H_n(\nu)\mathrm{e}^{-\mathrm{i}n\phi}$, i.e.

$$T(\nu_{\mathrm{L}}(t)) = \mathrm{Re}\left\{ \sum_{n=0}^{\infty} H_n(\nu) \mathrm{e}^{-\mathrm{i}n\phi} \mathrm{e}^{\mathrm{i}n2\pi f_m t} \right\}. \tag{C.26}$$

The last two equations then imply the desired result Eq. (3.57).

C.10 Derivation of Eq. (3.68)

It is most convenient to start with the convolution expression for $H_n(\nu)$:

$$H_n(\nu) = \int_{-\nu_\mathrm{a}}^{\nu_\mathrm{a}} T(\nu-\eta)\,\frac{\epsilon_n \,\mathrm{T}_n\left(-\eta/\nu_\mathrm{a}\right)}{\pi\sqrt{\nu_\mathrm{a}^2-\eta^2}}\mathrm{d}\eta. \tag{C.27}$$

Clearly, the result is the individual transform of each polynomial segment

$$\begin{aligned} H_n(\nu) &= \sum_{j=1}^{N}\int_{-\nu_\mathrm{a}}^{\nu_\mathrm{a}} p_j(\nu-\eta-\nu_{j-1})\chi_{[\nu_{j-1},\nu_j)}(\nu-\eta)\,\frac{\epsilon_n \,\mathrm{T}_n\left(-\eta/\nu_\mathrm{a}\right)}{\pi\sqrt{\nu_\mathrm{a}^2-\eta^2}}\mathrm{d}\eta && \text{(C.28)}\\ &= \sum_{j=1}^{N}\sum_{l=0}^{k} p_j^{(l)}(\nu-\nu_{j-1})\frac{\nu_\mathrm{a}^l\epsilon_n}{2^l l!\pi}\Big(f_n^l((\nu-\nu_{j-1})/\nu_\mathrm{a}) - f_n^l((\nu-\nu_j)/\nu_\mathrm{a})\Big) && \text{(C.29)}\end{aligned}$$

$$\text{with}\qquad f_n^j(w) = \int_{-1}^{w}\frac{(-2x)^j\,\mathrm{T}_n\left(-x\right)}{\sqrt{1-x^2}}\chi_{(-1,1)}(x)\mathrm{d}x. \tag{C.30}$$

Note that the polynomial segment p_j was expanded in its Taylor series around $\nu-\nu_{j-1}$. The remaining task is to find an analytical expression for $f_{n,j}(w)$. This is given by the following:

$$f_n^j(w) = \sqrt{1-w_\mathrm{C}^2}\sum_i(\boldsymbol{S}_n)_{ij}\,\mathrm{T}_i\left(-w_\mathrm{C}\right) + (\boldsymbol{r}_n)_j\left(\arcsin\left(w_\mathrm{C}\right)+\frac{\pi}{2}\right), \tag{C.31}$$

with the coefficients $\boldsymbol{S}_n$ and $\boldsymbol{r}_n$ as defined in Eq. (3.72) and w_C the number w limited to the range $[-1,1]$.

This can be shown as follows: First note, that repeated application of the recursion formula [78, Eq. 22.7.4] of the Chebyshev polynomials yields

$$(-2x)^j\,\mathrm{T}_n\left(-x\right) = \sum_{m=0}^{j}\binom{j}{m}\mathrm{T}_{|n+2m-j|}\left(-x\right). \tag{C.32}$$

Also note, that for $x\in[-1,1]$

$$\int\frac{\mathrm{T}_l\left(-x\right)}{\sqrt{1-x^2}}\mathrm{d}x = \begin{cases}\arcsin x & l=0\\ \frac{1}{l}\sqrt{1-x^2}\,\mathrm{U}_{l-1}\left(-x\right) & l>0\end{cases}, \tag{C.33}$$

with $\mathrm{U}_{l-1}\left(x\right) = \sin\left(l\arccos\left(x\right)\right)/\sqrt{1-x^2}$ the Chebyshev polynomial of the second kind. The identity is easily proved when $\mathrm{T}_l\left(-x\right) = \cos\left(l\arccos\left(-x\right)\right)$ is inserted and the substitution $y=\arccos\left(-x\right)$ is made to transform the integral to a solvable form. To convert the Chebyshev polynomial of the second kind to the first kind we have:

$$\mathrm{U}_{l-1}\left(-x\right) = \sum_{\substack{q=0\\ l-q\ \text{odd}}}^{l-1}\epsilon_q\,\mathrm{T}_q\left(-x\right). \tag{C.34}$$

Now all “ingredients” are present to derive the expressions for the $\boldsymbol{S}_n$ and $\boldsymbol{r}_n$ coefficients. This is achieved by inserting Eq. (C.32) in Eq. (C.30) and using Eq. (C.33) (with $l=|n+2m-j|$). Finally U_{l-1} is eliminated using Eq. (C.34). The resulting expression is of the form of Eq. (C.31) and the columns of $\boldsymbol{S}_n$ and $\boldsymbol{r}_n$ (i.e., for fixed j) are determined by equating coefficients.

C.11 Derivation of Eq. (3.84)

First note, that the total variance of noise on the spectrum $\sigma^2(y)$ is given by

$$\sigma^2(y) = RN/2\,\overline{S}_{yy}, \qquad \overline{S}_{yy} = \frac{2}{RN}\int_0^{RN/2} S_{yy}(f)\mathrm{d}f, \tag{C.35}$$

whereas the integration covers the positive Nyquist band with the sampling rate RN. It only covers the positive frequencies because the spectral density is in the one-sided engineering convention (i.e., the value is twice the value of the two-sided spectral density, which is used in theory). The elements w_{nm} of the $\boldsymbol{W}$ matrix are defined as covariance between the y_n and y_m normalized by $\sigma^2(y)$, i.e.,

$$w_{nm} = \frac{\operatorname{cov}\{y_n, y_m\}}{\sigma^2(y)}. \tag{C.36}$$

Since the errors on the y are of zero mean the covariance is the same as the correlation $\operatorname{cov}\{y_n, y_m\} = \mathrm{E}\{y_n y_m\}$. Due to stationarity $\mathrm{E}\{y_n y_m\} = \widetilde{R}_{yy}(n-m)$ with $\widetilde{R}_{xy}(k)$ being the autocorrelation function of the discrete process y_n. The discrete autocorrelation is equal to the sampled continuous autocorrelation $R_{yy}(\tau) = \mathrm{E}\{y(t)y(t+\tau)\}$, because of $y_n = y(n/(RN))$:

$$\widetilde{R}_{yy}(k) = R_{yy}(k/(RN)). \tag{C.37}$$

The continuous autocorrelation function is the inverse Fourier transform of the (two-sided) spectral density and hence one obtains

$$w_{nm} = \frac{2}{RN\,\overline{S}_{yy}}\int_{-RN/2}^{RN/2} \frac{1}{2} S_{yy}(|f|)\mathrm{e}^{\mathrm{i}2\pi f(n-m)/(RN)}\mathrm{d}f, \tag{C.38}$$

which is after a substitution of variables equal to Eq. (3.84).

C.12 Derivation of Eq. (3.88)

First define $\widetilde{\boldsymbol{f}}(\boldsymbol{\theta}) = \boldsymbol{W}^{-1/2}\boldsymbol{f}(\boldsymbol{\theta})$ and $\widetilde{\boldsymbol{y}} = \boldsymbol{W}^{-1/2}\boldsymbol{y}$. Then the least squares estimate is given by the minimum of the risk function $L(\boldsymbol{\theta})$:

$$\widehat{\boldsymbol{\theta}} = \operatorname*{argmin}_{\boldsymbol{\theta}} L(\boldsymbol{\theta}), \qquad L(\boldsymbol{\theta}) = (\widetilde{\boldsymbol{y}} - \widetilde{\boldsymbol{f}}(\boldsymbol{\theta}))^H(\widetilde{\boldsymbol{y}} - \widetilde{\boldsymbol{f}}(\boldsymbol{\theta})). \tag{C.39}$$

A necessary condition for the least squares estimate is that the risk function has a stationary point, i.e.,

$$\boldsymbol{0} = \nabla L(\boldsymbol{\theta}) = 2\operatorname{Re}\left\{\widetilde{\boldsymbol{F}}(\boldsymbol{\theta})^H(\widetilde{\boldsymbol{y}} - \widetilde{\boldsymbol{f}}(\boldsymbol{\theta}))\right\}, \qquad \text{for } \boldsymbol{\theta} = \widehat{\boldsymbol{\theta}}, \tag{C.40}$$

with $\widetilde{\boldsymbol{F}}(\boldsymbol{\theta}) = (\nabla\widetilde{\boldsymbol{f}}(\boldsymbol{\theta})^T)^T$ the Jacobian matrix of $\widetilde{\boldsymbol{f}}$. This equation implicitly defines $\widehat{\boldsymbol{\theta}}$. Let denote

$$\boldsymbol{Q}(\boldsymbol{\theta}, \widetilde{\boldsymbol{y}}) = \operatorname{Re}\left\{\widetilde{\boldsymbol{F}}(\boldsymbol{\theta})^H(\widetilde{\boldsymbol{y}} - \widetilde{\boldsymbol{f}}(\boldsymbol{\theta}))\right\}. \tag{C.41}$$

Applying implicit differentiation yields

$$\boldsymbol{Q}_{\boldsymbol{\theta}}(\boldsymbol{\theta},\widetilde{\boldsymbol{y}})\partial\boldsymbol{\theta}+\boldsymbol{Q}_{\widetilde{\boldsymbol{y}}}(\boldsymbol{\theta},\widetilde{\boldsymbol{y}})\partial\widetilde{\boldsymbol{y}}=\boldsymbol{0} \qquad \text{for } \boldsymbol{\theta}=\widehat{\boldsymbol{\theta}} \tag{C.42}$$

with $\boldsymbol{Q}_{\boldsymbol{\theta}}$ and $\boldsymbol{Q}_{\widetilde{\boldsymbol{y}}}$ the Jacobians of $\boldsymbol{Q}$ with respect to $\boldsymbol{\theta}$ and $\widetilde{\boldsymbol{y}}$. The first order perturbation is given by replacing the differentials with finite differences. By solving for $\Delta\boldsymbol{\theta}$,

$$\Delta\widehat{\boldsymbol{\theta}}=-\boldsymbol{Q}_{\boldsymbol{\theta}}^{+}\boldsymbol{Q}_{\widetilde{\boldsymbol{y}}}\Delta\widetilde{\boldsymbol{y}} \tag{C.43}$$

is obtained. Note, that the pseudoinverse $\boldsymbol{Q}_{\boldsymbol{\theta}}^{+}$ is the left inverse matrix if $\boldsymbol{Q}_{\boldsymbol{\theta}}$ has full rank (cf. section B.2), which is necessary for the least squares problem to have a unique solution. The remaining missing terms are given by:

$$\boldsymbol{Q}_{\widetilde{\boldsymbol{y}}}=\widetilde{\boldsymbol{F}}^{H}, \qquad \boldsymbol{Q}_{\boldsymbol{\theta}}=-\widetilde{\boldsymbol{F}}^{H}\widetilde{\boldsymbol{F}}+\partial\widetilde{\boldsymbol{F}}^{H}/\partial\boldsymbol{\theta}(\widetilde{\boldsymbol{y}}-\widetilde{\boldsymbol{f}}). \tag{C.44}$$

The term $\partial\boldsymbol{F}^{H}/\partial\boldsymbol{\theta}$ is a three dimensional object which results in a matrix when multiplied with a vector. If this second order model derivative is neglected or the point around which the perturbation is taken is exact (i.e., $\widetilde{\boldsymbol{y}}=\widetilde{\boldsymbol{f}}(\boldsymbol{\theta})$), the result is obtained

$$\Delta\widehat{\boldsymbol{\theta}}=(\widetilde{\boldsymbol{F}}^{H}\widetilde{\boldsymbol{F}})^{+}\widetilde{\boldsymbol{F}}^{H}\Delta\widetilde{\boldsymbol{y}}. \tag{C.45}$$

This is equivalent to Eq. (3.88) after back substitution.

C.13 Derivation of Eq. (3.91)

Eq. (3.91) can be proven for the important case of $\boldsymbol{F}$ with full rank. Without loss of generality $\boldsymbol{W}=\boldsymbol{I}$ is assumed (because $\boldsymbol{F}$ can be replaced by $\boldsymbol{W}^{-1/2}\boldsymbol{F}$). For clarity the dependence of $\boldsymbol{F}$ on the θ_j will be suppressed in the notation this paragraph. Let θ_i be a parameter which linearly enters the signal model and from which the first row of the Jacobian is independent. This is equivalent to

$$\frac{\partial\boldsymbol{F}}{\partial\theta_i}=\boldsymbol{F}\boldsymbol{D}, \qquad \boldsymbol{D}\text{ diagonal matrix, } D_{11}=0. \tag{C.46}$$

Note further, that $h(l)$ is just the first row of the pseudoinverse matrix $\boldsymbol{F}^{+}$, which is because $(\boldsymbol{F}^{H}\boldsymbol{F})^{-1}\boldsymbol{F}^{H}=\boldsymbol{F}^{+}$.

The derivative of the pseudoinverse matrix is given by [196, Eq. (4.12)]:

$$\frac{\partial\boldsymbol{F}^{+}}{\theta_i}=-\boldsymbol{F}^{+}\frac{\partial\boldsymbol{F}}{\partial\theta_i}\boldsymbol{F}^{+}+\boldsymbol{F}^{+}\boldsymbol{F}^{+H}\frac{\partial\boldsymbol{F}^{H}}{\partial\theta_i}(\boldsymbol{I}-\boldsymbol{F}\boldsymbol{F}^{+})+(\boldsymbol{I}-\boldsymbol{F}^{+}\boldsymbol{F})\frac{\partial\boldsymbol{F}^{H}}{\partial\theta_i}\boldsymbol{F}^{+H}\boldsymbol{F}^{+}.$$

Substituting the above expression for the derivative of $\partial\boldsymbol{F}/\partial\theta_i$ into this equation and observing that for $\boldsymbol{F}$ of full rank $\boldsymbol{F}^{+}\boldsymbol{F}=\boldsymbol{I}$ and $\boldsymbol{F}^{H}\boldsymbol{F}^{+H}\boldsymbol{F}^{H}=\boldsymbol{F}^{H}$,

$$\frac{\partial\boldsymbol{F}^{+}}{\theta_i}=-\boldsymbol{D}\boldsymbol{F}^{+} \tag{C.47}$$

is obtained. Because of $D_{11}=0$,

$$\frac{\partial h(l)}{\partial\theta_i}=0 \tag{C.48}$$

follows, which shows that the impulse response $h(l)$ of the filter model is independent on the value of a linear parameter θ_i.

Abbreviations and Symbols

Abbreviations

DFB	Distributed feed-back
FRS	Faraday rotation spectrometry
FSR	Free Spectral Range
FWHM	Full-width at half-maximum
HCF	Hollow capillary fiber
HITRAN	High resolution transmission molecular absorption line database
HWHM	Half-width at half-maximum
LMR	Laser magnetic resonance
OPD	Optical path length difference (physical length times refractive index)
QCL	Quantum cascade laser
SATP	Standard ambient temperature and pressure, $T = 25\,^{\circ}\mathrm{C}, p = 1\,\mathrm{bar}$
TDLAS	Tunable diode laser absorption spectrometry
VCSEL	Vertical-cavity surface-emitting laser
WMS	Wavelength modulation spectrometry
ZMS	Zeeman modulation spectrometry

Math Symbols

$\boldsymbol{A}^{+}$	The Moore-Penrose pseudoinverse to matrix $\boldsymbol{A}$, *p. 143*
$A_n(x, m)$	Arndt's formula (harmonic spectrum for an unsaturated Lorentzian line), *p. 49*
δ_n	Kronecker delta, $\delta_n = 1$ for $n = 0$ and $\delta_n = 0$ otherwise.
ϵ_n	Fourier series factor, 1 for $n = 0$ and 2 for $n \neq 0$
$\mathrm{J}_n\left(x\right)$	Bessel function of order n [78, chapter 9]
$\sigma(x)$	Standard deviation of random variable x
$\sigma^2(x)$	Variance of random variable x

$\mathrm{T}_n(x)$	Chebyshev polynomial of degree n [78, chapter 22]
$\chi_I(x)$	Characteristic function, 1 for $x \in I$ and 0 otherwise.

Symbols

$\lambda_\mathrm{L}(t)$	Instantaneous laser emission wavelength, *p. 12*	μm
$\nu_\mathrm{L}(t)$	Instantaneous laser emission frequency, *p. 12*	Hz or cm^{-1}
α	Absorption coefficient, $\alpha = A/L$, *p. 39*	1/cm
A	Absorbance, $A = -\log T$, *p. 39*	1
A	Amplitude of the optical interference (unit of absorbance), *p. 40*	1
$\boldsymbol{a}^{[i]}$	Incident power waves in junction for waveguide i, *p. 43*	1
$\alpha_\mathrm{pk,mol}$	The target gas peak absorption coefficient, *p. 68*	1/cm
a_mol	The target gas absorbance (same as θ_1),$a_\mathrm{mol} = C_\mathrm{mol}\alpha_\mathrm{pk}L$, *p. 68*	1
$\boldsymbol{b}^{[i]}$	Outgoing power waves from junction for waveguide i, *p. 43*	1
$\beta_p^{[i]}$	Propagation constant of mode p in waveguide i, *p. 42*	1/m
C_mol	The target gas concentration, $C_\mathrm{mol} = a_\mathrm{mol}/(\alpha_\mathrm{pk}L)$, *p. 68*	1
η_D	FM response parameter for distance of active region and heat-sink , *p. 19*	1
η_e	Laser (external) differential quantum efficiency, *p. 13*	1
$\eta_{e,\mathrm{S}}(I, T_\mathrm{S}, f)$	Laser differential quantum efficiency at constant heat-sink temperature, *p. 12*	1
$\boldsymbol{E}_{p,\mathrm{t}}^{[i]}$	Tangential electric field of mode p in waveguide i, *p. 42*	V/m
η_R	FM response parameter for radius of light mode and heat source, *p. 19*	1
η_Z	FM response parameter for thickness of light mode and heat source, *p. 19*	1
ϕ	Laser FM phase-shift	rad
$F(L_\mathrm{OPD})$	Fringe response, *p. 98*	1
$\boldsymbol{f}(\boldsymbol{\theta})$	Model function (describes analytic part of measurement $\boldsymbol{y}$), *p. 70*	1
G	Observation factor, $G = \sigma(\widehat{a}_\mathrm{mol}) \cdot (R\overline{S}_{yy}/2)^{-1/2}$, *p. 97*	1
$h(l)$	Impulse response of the curve-fitting filter model, *p. 73*	1
$H_\mathrm{chip}(f)$	FM response of chip-submount tuning, *p. 17*	1
$H_n(\nu; \nu_\mathrm{a})$	n-th harmonic transmission spectrum (WMS), *p. 47*	1

$H_{\mathrm{pl}}(f)$	FM response of plasma effect tuning, *p. 17*	1
$\boldsymbol{H}_{p,\mathrm{t}}^{[i]}$	Tangential magnetic field of mode p in waveguide i, *p. 42*	A/m
$H_{\mathrm{thm}}(f)$	FM response of intrinsic thermal tuning, *p. 17*	1
$h_{\mathrm{thm}}(t)$	FM impulse response of intrinsic thermal tuning, *p. 19*	1/s
I	Laser injection current	mA
$I_{\mathrm{L}}(t)$	Instantaneous laser injection current, *p. 12*	mA
I_a	WMS current modulation amplitude, *p. 57*	A
I_{th}	Laser threshold current, *p. 13*	mA
k_{chip}	DC coefficient of chip-submount tuning, *p. 17*	nm/mA or GHz/mA
$k_{\lambda}(I, T_{\mathrm{S}}, f)$	Laser tuning coefficient, *p. 12*	nm/mA or GHz/mA
k_{pl}	DC coefficient of plasma effect tuning, *p. 17*	nm/mA or GHz/mA
k_{thm}	DC coefficient of intrinsic thermal tuning, *p. 17*	nm/mA or GHz/mA
$K_{\mathrm{wms}}^{\mathrm{der}}(\nu)$	Convolution kernel for the n-th harmonic spectrum (WMS), *p. 50*	1
$K_{\mathrm{wms}}(\nu)$	Convolution kernel for the n-th harmonic spectrum (WMS), *p. 50*	1
L	The sensors optical path length	cm
$\lambda(I, T_{\mathrm{S}})$	Steady state laser emission wavelength characteristic, *p. 11*	µm
L_{OPD}	Optical path length difference, $L_{\mathrm{OPD}} = c/\nu_{\mathrm{fsr}}$	m
$M(x, y, z)$	Laser internal light mode distribution, *p. 18*	$1/\mathrm{m}^3$
N	Number of points per spectral scan, *p. 69*	1
ν_{a}	Frequency modulation amplitude (WMS), *p. 47*	Hz or cm^{-1}
ν_{fsr}	Free spectral range of a resonance, $\nu_{\mathrm{fsr}} = c/L_{\mathrm{OPD}}$	Hz
n_{mol}	The target gas number density ($n_{\mathrm{mol}} = p/kTC_{\mathrm{mol}}$), *p. 68*	$1/\mathrm{cm}^3$
p	Gas pressure	bar
$P(I, T_{\mathrm{S}})$	Steady state laser output power characteristic, *p. 11*	W
$P_{\mathrm{L}}(t)$	Instantaneous laser output power, *p. 12*	mW
P_n	n-th harmonic amplitude of $P_{\mathrm{L}}(t)$, w.r.t frequency f_{m} (complex), *p. 57*	W
$Q(x, y, z)$	Laser internal heat source distribution, *p. 18*	$1/\mathrm{m}^3$
R	Measurement rate (repetition rate of measurements), *p. 69*	Hz

$R_d(I, T_\mathrm{S}, f)$	Laser differential impedance, *p. 12*	Ω
R_M	Transversal extent (radius) of laser internal light mode, *p. 18*	m
R_Q	Transversal extent (radius) of laser internal heat source, *p. 18*	m
R_thm	Internal laser thermal resistance, *p. 27*	K/W
$S_D(t)$	Instantaneous received detector power signal, *p. 57*	W
S_n	n-th harmonic amplitude of $S_\mathrm{D}(t)$, w.r.t frequency f_m (complex), *p. 57*	W
$\overline{S}_{yy}$	Average noise spectral density on measured spectrum y, *p. 71*	1/Hz
$S_{yy}(f)$	Noise spectral density on measured spectrum y, *p. 71*	1/Hz
T	Gas temperature	T
$\boldsymbol{\theta}$	The vector of unknown model parameters, $\boldsymbol{\theta} = (\theta_1, \ldots, \theta_P)^T$, *p. 69*	n/a
$\widehat{\boldsymbol{\theta}}$	Estimates for the unknown parameters ("Fit results"), *p. 72*	n/a
$T(\nu)$	Optical transmission	1
$T(\nu)$	Transmission or transmittance, $T = P/P_0$, *p. 39*	1
T_cav	Internal laser average cavity temperature, *p. 13*	K
θ_i	The i-th unknown model parameter, *p. 69*	n/a
T_jcn	Internal laser average junction (active region) temperature, *p. 13*	K
T_S	Laser heat-sink temperature	K
$U(I, T_\mathrm{S})$	Steady state laser voltage characteristic, *p. 11*	V
$U_\mathrm{L}(t)$	Instantaneous laser voltage, *p. 12*	V
$\boldsymbol{W}$	Noise covariance structure matrix for $\boldsymbol{y}$, *p. 70*	1
$\boldsymbol{y}$	The vector of one measurement spectrum, $\boldsymbol{y} = (y_1, \ldots, y_N)^T$, *p. 69*	1
y_i	The i-th (of N total) spectrum sample, *p. 69*	1
Z_M	Longitudinal extent (thickness) of laser internal light mode, *p. 18*	m
Z_Q	Longitudinal extent (thickness) of laser internal heat source, *p. 18*	m

References

[1] International Union of Pure and Applied Chemistry, *IUPAC Compendium of Chemical Terminology – the Gold Book*. Published online, Mar. 2012, version 2.3.1. DOI: `10.1351/goldbook`.

[2] J. Fraunhofer, “VIII. Bestimmung des Brechungs- und Farbenzerstreuungs-Vermögens verschiedener Glasarten, in Bezug auf die Vervollkommnung achromatischer Fernröhre”, German, in *Denkschriften der königlichen Akademie der Wissenschaften zu München für die Jahre 1814 und 1815*. 1817, vol. 5, pp. 193–226. DOI: `10.3931/e-rara-3769`.

[3] Fraunhofer Gesellschaft, *Fraunhofer in Benediktbeuern - Glashütte und Werkstatt*, Online, `http://www.fraunhofer.de/content/dam/zv/de/publikationen/broschueren/FraunhoferinBenediktbeuern.pdf`, 2011.

[4] M. Born and R. Oppenheimer, “Zur Quantentheorie der Molekeln”, *Annalen der Physik*, vol. 389, no. 20, pp. 457–484, 1927. DOI: `10.1002/andp.19273892002`.

[5] J. Brown and A. Carrington, *Rotational Spectroscopy of Diatomic Molecules*, ser. Cambridge Molecular Science Series. Cambridge University Press, 2003.

[6] L. Rothman *et al.*, “The HITRAN 2008 molecular spectroscopic database”, *J. Quant. Spectrosc. Radiat. Transfer*, vol. 110, no. 9-10, pp. 533–572, 2009. DOI: `10.1016/j.jqsrt.2009.02.013`.

[7] M. I. Nathan *et al.*, “Stimulated emission of radiation from GaAs p-n junctions”, *Appl. Phys. Lett.*, vol. 1, no. 3, pp. 62–64, 1962. DOI: `10.1063/1.1777371`.

[8] R. N. Hall *et al.*, “Coherent light emission from GaAs junctions”, *Phys. Rev. Lett.*, vol. 9, pp. 366–368, 9 Nov. 1962. DOI: `10.1103/PhysRevLett.9.366`.

[9] E. D. Hinkley, “High-resolution infrared spectroscopy with a tunable diode laser”, *Appl. Phys. Lett.*, vol. 16, no. 9, pp. 351–354, 1970. DOI: `10.1063/1.1653222`.

[10] E. D. Hinkley and P. L. Kelley, “Detection of air pollutants with tunable diode lasers”, *Science*, vol. 171, no. 3972, pp. 635–639, 1971. DOI: `10.1126/science.171.3972.635`.

[11] H. Kogelnik and C. V. Shank, “Coupled-wave theory of distributed feedback lasers”, *J. Appl. Phys.*, vol. 43, no. 5, pp. 2327–2335, 1972. DOI: `10.1063/1.1661499`.

[12] H. Soda, K. Iga, C. Kitahara, and Y. Suematsu, “GaInAsP/InP surface emitting injection lasers”, *Jpn. J. Appl. Phys.*, vol. 18, no. 12, pp. 2329–2330, 1979. DOI: `10.1143/JJAP.18.2329`.

[13] M. Nakamura, K. Aiki, J. Umeda, and A. Yariv, “Cw operation of distributed-feedback GaAs-GaAlAs diode lasers at temperatures up to 300 K”, *Appl. Phys. Lett.*, vol. 27, no. 7, pp. 403–405, 1975. DOI: `10.1063/1.88492`.

[14] T. Matsuoka *et al.*, “CW operation of DFB-BH GaInAsP/InP lasers in 1.5 μm wavelength region”, *Electron. Lett.*, vol. 18, no. 1, pp. 27–28, 1982. DOI: `10.1049/el:19820020`.

[15] S. R. Darvish *et al.*, “Room-temperature, high-power, and continuous-wave operation of distributed-feedback quantum-cascade lasers at $\lambda \sim 9.6\mu$m”, *Appl. Phys. Lett.*, vol. 88, no. 20, 201114, p. 201 114, 2006. DOI: `10.1063/1.2205730`.

[16] C. J. Chang-Hasnain *et al.*, “Low threshold buried heterostructure vertical cavity surface emitting laser”, *Appl. Phys. Lett.*, vol. 63, no. 10, pp. 1307–1309, 1993. DOI: `10.1063/1.109713`.

[17] M. Ortsiefer *et al.*, “Low-threshold index-guided 1.5 μm long-wavelength vertical-cavity surface-emitting laser with high efficiency”, *Appl. Phys. Lett.*, vol. 76, pp. 2179–2181, 2000. DOI: `10.1063/1.126290`.

[18] A. Bachmann *et al.*, “Single-mode continuous wave operation of electrically pumped 2.25 μm GaSb-based VCSEL”, *20th International Conference on Indium Phosphide and Related Materials, Versailles, France*, May 2008. DOI: `10.1109/ICIPRM.2008.4703030`.

[19] L. Rothman *et al.*, “The HITRAN 2004 molecular spectroscopic database”, *J. Quant. Spectrosc. Radiat. Transfer*, vol. 96, pp. 139–204, 2005. DOI: `10.1016/j.jqsrt.2004.10.008`.

[20] J. Reid and D. Labrie, “Second-harmonic detection with tunable diode lasers - comparison of experiment and theory”, *Appl. Phys. B: Lasers Opt.*, vol. 26, pp. 203–210, Nov. 1981. DOI: `10.1007/BF00692448`.

[21] A. Hangauer, J. Chen, and M.-C. Amann, “Vertical-cavity surface-emitting laser light-current characteristic at constant internal temperature”, *IEEE Photon. Technol. Lett.*, vol. 23, no. 18, pp. 1295–1297, Sep. 2011. DOI: `10.1109/LPT.2011.2160389`.

[22] A. Hangauer, J. Chen, R. Strzoda, and M.-C. Amann, “The frequency modulation response of vertical-cavity surface-emitting lasers: experiment and theory”, *IEEE J. Sel. Topics Quantum Electron.*, vol. 17, pp. 1584–1593, Nov. 2011. DOI: `10.1109/JSTQE.2011.2110640`.

[23] A. Hangauer, J. Chen, and M. C. Amann, “Comparison of plasma-effect in different InP-based VCSELs”, in *Conference on Lasers and Electro Optics (CLEO)*, San Jose, USA, 2010, CMO4.

[24] A. Hangauer, J. Chen, R. Strzoda, and M.-C. Amann, “High-speed tuning in vertical-cavity surface-emitting lasers”, in *CLEO Europe - EQEC 2009*, Jun. 2009, CB13.5. DOI: `10.1109/CLEOE-EQEC.2009.5193616`.

[25] A. Hangauer, J. Chen, and M.-C. Amann, “Square-root law thermal response in VCSELs: experiment and theoretical model”, in *Conference on Lasers and Electro Optics (CLEO)*, May 2008, JThA27.

[26] J. Chen, A. Hangauer, R. Strzoda, and M. C. Amann, “Resolution limits of laser spectroscopic absorption measurements with hollow glass waveguides”, *Appl. Opt.*, vol. 49, no. 28, pp. 5254–5261, Oct. 2010. DOI: `10.1364/AO.49.005254`.

[27] J. Hodgkinson, D. Masiyano, and R. P. Tatam, “Using integrating spheres as absorption cells: path-length distribution and application of Beer’s law”, *Appl. Opt.*, vol. 48, no. 30, pp. 5748–5758, Oct. 2009. DOI: `10.1364/AO.48.005748`.

[28] J. Chen, A. Hangauer, R. Strzoda, and M.-C. Amann, “Laser spectroscopic oxygen sensor using diffuse reflector based optical cell and advanced signal processing”, *Appl. Phys. B: Lasers Opt.*, vol. 100, pp. 417–425, 2010. DOI: `10.1007/s00340-010-3956-3`.

[29] R. Engelbrecht *et al.*, "Line shapes of near-infrared DFB and VCSEL diode lasers under the influence of system back reflections", *Appl. Phys. B: Lasers Opt.*, pp. 1–12, DOI: `10.1007/s00340-012-5097-3`.

[30] M. Van Uffelen *et al.*, "Comparison of gamma and proton-induced radiation damage in long-wavelength VCSELs", in *Radiation and Its Effects on Components and Systems, 2007. RADECS 2007. 9th European Conference on*, Sep. 2007, pp. 1–4. DOI: `10.1109/RADECS.2007.5205463`.

[31] P. Teng *et al.*, "Radiation hardness and lifetime studies of the VCSELs for the ATLAS SemiConductor Tracker", *Nucl. Instrum. Methods Phys. Res., Sect. A*, vol. 497, no. 2-3, pp. 294–304, 2003. DOI: `10.1016/S0168-9002(02)01922-8`.

[32] L. A. Coldren and S. W. Corzine, *Diode Lasers and Photonic Integrated Circuits*. John Wiley & Sons, 1995.

[33] B. Weigl *et al.*, "High-performance oxide-confined GaAs VCSELs", *IEEE J. Sel. Topics Quantum Electron.*, vol. 3, no. 2, pp. 409–415, Apr. 1997. DOI: `10.1109/2944.605686`.

[34] J. Chen, A. Hangauer, and M.-C. Amann, "Simplified model of the dynamic thermal tuning behavior of VCSELs", *IEEE Photon. Technol. Lett.*, vol. 20, pp. 1082–1084, Jul. 2008. DOI: `10.1109/LPT.2008.924296`.

[35] G. Böhm *et al.*, "Growth of InAs-containing quantum wells for InP-based VCSELs emitting at 2.3 μm", *J. Cryst. Growth*, vol. 301, pp. 941–944, Apr. 2007. DOI: `10.1016/j.jcrysgro.2006.11.098`.

[36] M. Ortsiefer *et al.*, "Electrically pumped room temperature CW VCSELs with 2.3 μm emission wavelength", *Electron. Lett.*, vol. 42, no. 11, pp. 640–641, 25 May 2006. DOI: `10.1049/el:20061096`.

[37] H. E. Li and K. Iga, Eds., *Vertical-Cavity Surface-Emitting Laser Devices*, 1st ed. Springer-Verlag, 2003.

[38] J. Piprek, D. I. Babic, and J. E. Bowers, "Simulation and analysis of 1.55 μm double-fused vertical-cavity lasers", *J. Appl. Phys.*, vol. 81, no. 8, pp. 3382 –3390, Apr. 1997. DOI: `10.1063/1.365033`.

[39] M.-C. Amann and J. Buus, *Tunable Laser Diodes*. Norwood: Artech House publishers, 1998.

[40] K. Petermann, *Laser Diode Modulation and Noise*. Kluwer, 1988.

[41] C. Henry, "Theory of the linewidth of semiconductor lasers", *IEEE J. Quantum Electron.*, vol. 18, no. 2, pp. 259–264, Feb. 1982. DOI: `10.1109/JQE.1982.1071522`.

[42] J. Huang and L. W. Casperson, "Gain and saturation in semiconductor lasers", *Opt. Quantum. Electron.*, vol. 25, no. 6, pp. 369–390, Jun. 1993. DOI: `10.1007/BF00420579`.

[43] J. Gustavsson *et al.*, "Dynamic behavior of fundamental-mode stabilized VCSELs using a shallow surface relief", *IEEE J. Quantum Electron.*, vol. 40, no. 6, pp. 607–619, Jun. 2004. DOI: `10.1109/JQE.2004.828273`.

[44] Y. Liu, W.-C. Ng, B. Klein, and K. Hess, "Effects of the spatial nonuniformity of optical transverse modes on the modulation response of vertical-cavity surface-emitting lasers", *IEEE J. Quantum Electron.*, vol. 39, no. 1, pp. 99–108, Jan. 2003. DOI: `10.1109/JQE.2002.806205`.

[45] A. V. Oppenheim, R. W. Schafer, and J. R. Buck, *Discrete-time signal processing*, 2nd. Upper Saddle River, NJ, USA: Prentice-Hall, Inc., 1999.

[46] M. Grabherr, D. Wiedenmann, R. Jaeger, and R. King, "Fabrication and performance of tunable single-mode VCSELs emitting in the 750 to 1000 nm range", *Proc. SPIE 5737*, vol. 5737, pp. 120–128, Mar. 2005. DOI: `10.1117/12.590178`.

[47] M.-C. Amann and M. Ortsiefer, "Long-wavelength ($\lambda \geq 1.3$ μm) InGaAlAs-InP vertical-cavity surface-emitting lasers for applications in optical communication and sensing", *Phys. Status Solidi A*, vol. 203, pp. 3538–3544, Aug. 2006. DOI: `10.1002/pssa.200622380`.

[48] A. Bachmann *et al.*, "Continuous-wave operation of electrically pumped GaSb-based vertical cavity surface emitting laser at 2.3 μm", *Electron. Lett.*, vol. 44, no. 3, pp. 202–203, Jan. 2008. DOI: `10.1049/el:20083430`.

[49] H. Shalom *et al.*, "On the various time constants of wavelength changes of a DFB laser under direct modulation", *IEEE J. Quantum Electron.*, vol. 34, pp. 1816–1822, 1998. DOI: `10.1109/3.720212`.

[50] I. Roudas *et al.*, "Accurate model of the semiconductor laser nonuniform FM response for the study of coherent optical systems", *IEEE Photon. Technol. Lett.*, vol. 6, no. 11, pp. 1389–1391, Nov. 1994. DOI: `10.1109/68.334849`.

[51] K. Iga, "Surface emitting lasers", *Opt. Quantum. Electron.*, vol. 24, pp. 97–104, 1992.

[52] A. Hangauer, J. Chen, and M.-C. Amann, "Modeling of the n-th harmonic spectra used in wavelength modulation spectroscopy and their properties", *Appl. Phys. B: Lasers Opt.*, vol. 90, no. 2, pp. 249–254, Feb. 2008. DOI: `10.1007/s00340-007-2902-5`.

[53] J. Chen, A. Hangauer, R. Strzoda, and M. C. Amann, "Tunable diode laser spectroscopy with optimum wavelength scanning", *Appl. Phys. B: Lasers Opt.*, vol. 100, pp. 331–339, 2010. DOI: `10.1007/s00340-010-3973-2`.

[54] J. Chen, A. Hangauer, R. Strzoda, and M.-C. Amann, "VCSEL-based calibration-free carbon monoxide sensor at 2.3 μm with in-line reference cell", *Appl. Phys. B: Lasers Opt.*, vol. 102, pp. 381–389, 2010. DOI: `10.1007/s00340-010-4011-0`.

[55] A. Hangauer *et al.*, "Compact VCSEL-based CO_2 and H_2O sensor with inherent wavelength calibration for safety and air-quality applications", in *Conference on Lasers and Electro Optics (CLEO)*, San Jose, USA, May 2010, JThB3.

[56] D. Herriott, H. Kogelnik, and R. Kompfner, "Off-axis paths in spherical mirror interferometers", *Appl. Opt.*, vol. 3, pp. 523–526, 1964. DOI: `10.1364/AO.3.000523`.

[57] J. U. White, "Long paths of large aperture", *J. Opt. Soc. Am.*, vol. 32, no. 5, p. 285, 1942. DOI: `10.1364/JOSA.32.000285`.

[58] S. M. Chernin and E. G. Barskaya, "Optical multipass matrix systems", *Appl. Opt.*, vol. 30, no. 1, pp. 51–58, Jan. 1991. DOI: `10.1364/AO.30.000051`.

[59] D. Masiyano, J. Hodgkinson, and R. P. Tatam, "Use of diffuse reflections in tunable diode laser absorption spectroscopy: implications of laser speckle for gas absorption measurements", *Appl. Phys. B: Lasers Opt.*, vol. 90, pp. 279–288, Feb. 2008. DOI: `10.1007/s00340-007-2896-z`.

[60] G. C. Bjorklund, "Frequency-modulation spectroscopy: a new method for measuring weak absorptions and dispersions", *Opt. Lett.*, vol. 5, no. 1, pp. 15–17, Jan. 1980. DOI: `10.1364/OL.5.000015`.

[61] D. T. Cassidy and J. Reid, "Harmonic detection with tunable diode lasers-two-tone modulation", *Appl. Phys. B: Lasers Opt.*, vol. 29, pp. 279–285, Dec. 1982. DOI: `10.1007/BF00689188`.

[62] L. Richman, "ELDS - enhanced laser diode spectroscopy", Senscient Ltd., Tech. Rep., `http://www.senscient.com/downloads/SenscientTutorialPaperISA.pdf`.

[63] H. S. Müller, F. Schlöder, J. Stutzki, and G. Winnewisser, "The Cologne database for molecular spectroscopy, CDMS: a useful tool for astronomers and spectroscopists", *J. Mol. Struct.*, vol. 742, no. 1-3, pp. 215–227, 2005. DOI: `10.1016/j.molstruc.2005.01.027`.

[64] H. Pickett *et al.*, "Submillimeter, millimeter, and microwave spectral line catalog", *J. Quant. Spectrosc. Radiat. Transfer*, vol. 60, no. 5, pp. 883 –890, 1998. DOI: `10.1016/S0022-4073(98)00091-0`.

[65] N. Jacquinet-Husson *et al.*, "The 2009 edition of the GEISA spectroscopic database", *J. Quant. Spectrosc. Radiat. Transfer*, vol. 112, no. 15, pp. 2395–2445, 2011. DOI: `10.1016/j.jqsrt.2011.06.004`.

[66] M. Born and E. Wolf, *Principles of Optics: Electromagnetic Theory of Propagation, Interference and Diffraction of Light*, 7th ed. Cambridge University Press, 1999.

[67] W. C. Chew, *Waves and fields in inhomogeneous media.* Van Nostrand Reinhold, 1990.

[68] J. Kong, *Electromagnetic wave theory*, ser. Wiley-Interscience publication. Wiley, 1986.

[69] Y. Saad, *Iterative Methods for Sparse Linear Systems*, 2nd ed. Society for Industrial and Applied Mathematics, 2003.

[70] P. Kluczynski, J. Gustafsson, Åsa M. Lindberg, and O. Axner, "Wavelength modulation absorption spectrometry – an extensive scrutiny of the generation of signals", *Spectrochim. Acta, Part B*, vol. 56, no. 8, pp. 1277–1354, 2001. DOI: `10.1016/S0584-8547(01)00248-8`.

[71] R. Arndt, "Analytical line shapes for Lorentzian signals broadened by modulation", *J. Appl. Phys.*, vol. 36, no. 8, pp. 2522–2524, 1965. DOI: `10.1063/1.1714523`.

[72] A. N. Dharamsi, "A theory of modulation spectroscopy with applications of higher harmonic detection", *J. Phys. D: Appl. Phys.*, vol. 29, pp. 540–549, Mar. 1996. DOI: `10.1088/0022-3727/29/3/009`.

[73] G. V. H. Wilson, "Modulation broadening of NMR and ESR line shapes", *J. Appl. Phys.*, vol. 34, no. 11, pp. 3276–3285, 1963. DOI: `10.1063/1.1729177`.

[74] R. Engelbrecht, "A compact NIR fiber-optic diode laser spectrometer for CO and CO_2: analysis of observed 2f wavelength modulation spectroscopy line shapes", *Spectrochim. Acta, Part A*, vol. 60, no. 14, pp. 3291–3298, 2004. DOI: `10.1016/j.saa.2003.11.033`.

[75] T. Asakawa, N. Kanno, and K. Tonokura, “Diode laser detection of greenhouse gases in the near-infrared region by wavelength modulation spectroscopy: pressure dependence of the detection sensitivity”, *Sensors*, vol. 10, no. 5, pp. 4686–4699, 2010. DOI: `10.3390/s100504686`.

[76] T. Fernholz, H. Teichert, and V. Ebert, “Digital, phase-sensitive detection for *in situ* diode-laser spectroscopy under rapidly changing transmission conditions”, *Appl. Phys. B: Lasers Opt.*, vol. 75, pp. 229–236, 2 2002. DOI: `10.1007/s00340-002-0962-0`.

[77] A. Hangauer, J. Chen, and M.-C. Amann, “Straightforward modeling of the nth harmonic signals used in wavelength modulation spectroscopy and their mathematical properties”, in *Book of Abstracts, 6th International Conference on Tunable Diode Laser Spectroscopy*, Reims, France, 2007, pp. D–15.

[78] M. Abramowitz and I. A. Stegun, Eds., *Handbook of Mathematical Functions*, 9th. New York: Dover, 1970.

[79] A. M. Russell and D. A. Torchia, “Harmonic analysis in systems using phase sensitive detectors”, *Rev. Sci. Instrum.*, vol. 33, no. 4, pp. 442–444, 1962. DOI: `10.1063/1.1717875`.

[80] C. B. Carlisle and D. E. Cooper, “Tunable diode laser frequency modulation spectroscopy through an optical fiber: high-sensitivity detection of water vapor”, *Appl. Phys. Lett.*, vol. 56, no. 9, pp. 805–807, 1990. DOI: `10.1063/1.102669`.

[81] P. C. D. Hobbs, “Ultrasensitive laser measurements without tears”, *Appl. Opt.*, vol. 36, no. 4, pp. 903–920, Feb. 1997. DOI: `10.1364/AO.36.000903`.

[82] K. L. Haller and P. C. D. Hobbs, “Double-beam laser absorption spectroscopy: shot noise-limited performance at baseband with a novel electronic noise canceler”, in *Proc. SPIE 1435*, B. L. Fearey, Ed., vol. 1435, Los Angeles, CA, USA: SPIE, 1991, pp. 298–309. DOI: `10.1117/12.44253`.

[83] O. Axner, P. Kluczynski, and A. M. Lindberg, “A general non-complex analytical expression for the nth Fourier component of a wavelength-modulated Lorentzian lineshape function”, *J. Quant. Spectrosc. Radiat. Transfer*, vol. 68, no. 3, pp. 299–317, Feb. 2001. DOI: `10.1016/S0022-4073(00)00032-7`.

[84] I. Linnerud, P. Kaspersen, and T. Jaeger, “Gas monitoring in the process industry using diode laser spectroscopy”, *Appl. Phys. B: Lasers Opt.*, vol. 67, pp. 297–305, 3 1998. DOI: `10.1007/s003400050509`.

[85] J. Westberg, P. Kluczynski, S. Lundqvist, and O. Axner, “Analytical expression for the nth Fourier coefficient of a modulated Lorentzian dispersion lineshape function”, *J. Quant. Spectrosc. Radiat. Transfer*, vol. 112, no. 9, pp. 1443 –1449, 2011. DOI: `10.1016/j.jqsrt.2011.02.007`.

[86] L. C. Philippe and R. K. Hanson, “Laser diode wavelength-modulation spectroscopy for simultaneous measurement of temperature, pressure, and velocity in shock-heated oxygen flows”, *Appl. Opt.*, vol. 32, pp. 6090–6103, Oct. 1993. DOI: `10.1364/AO.32.006090`.

[87] T. Gardiner *et al.*, “A lightweight near-infrared spectrometer for the detection of trace atmospheric species”, *Rev. Sci. Instrum*, vol. 81, no. 8, p. 083 102, 2010. DOI: `10.1063/1.3455827`.

[88] D. Rojas, P. Ljung, and O. Axner, “An investigation of the 2f-wavelength modulation technique for detection of atoms under optically thin as well as thick

conditions", *Spectrochim. Acta, Part B*, vol. 52, no. 11, pp. 1663–1686, 1997. DOI: `10.1016/S0584-8547(97)00056-6`.

[89] G. Cazzoli and L. Dore, "Lineshape measurements of rotational lines in the millimeter-wave region by second harmonic detection", *J. Mol. Spectrosc.*, vol. 141, no. 1, pp. 49–58, 1990. DOI: `10.1016/0022-2852(90)90277-W`.

[90] D. C. Hovde, J. T. Hodges, G. E. Scace, and J. A. Silver, "Wavelength-modulation laser hygrometer for ultrasensitive detection of water vapor in semiconductor gases", *Appl. Opt.*, vol. 40, no. 6, pp. 829–839, Feb. 2001. DOI: `10.1364/AO.40.000829`.

[91] R. D. May and C. R. Webster, "Data processing and calibration for tunable diode laser harmonic absorption spectrometers", *J. Quant. Spectrosc. Radiat. Transfer*, vol. 49, no. 4, pp. 335–347, 1993. DOI: `10.1016/0022-4073(93)90098-3`.

[92] J. A. Silver, "Frequency-modulation spectroscopy for trace species detection: theory and comparison among experimental methods", *Appl. Opt.*, vol. 31, no. 6, pp. 707–717, Feb. 1992. DOI: `10.1364/AO.31.000707`.

[93] R. Chaux and B. Lavorel, "Relative line intensity measurement in absorption spectra using a tunable diode laser at 1.6 μm: application to the determination of $^{13}CO_2/^{12}CO_2$ isotope ratio", *Appl. Phys. B: Lasers Opt.*, vol. 72, pp. 237–240, 2 2001. DOI: `10.1007/s003400000440`.

[94] K. Uehara, "Dependence of harmonic signals on sample-gas parameters in wavelength-modulation spectroscopy for precise absorption measurements", *Appl. Phys. B: Lasers Opt.*, vol. 67, pp. 517–523, 4 1998. DOI: `10.1007/s003400050537`.

[95] P. Kluczynski, A. M. Lindberg, and O. Axner, "Wavelength modulation diode laser absorption signals from Doppler broadened absorption profiles", *J. Quant. Spectrosc. Radiat. Transfer*, vol. 83, pp. 345–360, Feb. 2004. DOI: `10.1016/S0022-4073(02)00377-1`.

[96] B. D. Shaw, "Analytical evaluation of the Fourier components of wavelength-modulated Gaussian functions", *J. Quant. Spectrosc. Radiat. Transfer*, vol. 109, no. 17-18, pp. 2891–2894, 2008. DOI: `10.1016/j.jqsrt.2008.08.002`.

[97] B. W. M Moeskops, S. M. Cristescu, and F. J. M Harren, "Sub-part-per-billion monitoring of nitric oxide by use of wavelength modulation spectroscopy in combination with a thermoelectrically cooled, continuous-wave quantum cascade laser", *Opt. Lett.*, vol. 31, no. 6, pp. 823–825, Mar. 2006. DOI: `10.1364/OL.31.000823`.

[98] S. Schäfer *et al.*, "Sensitive detection of methane with a 1.65μm diode laser by photoacoustic and absorption spectroscopy", *Appl. Phys. B: Lasers Opt.*, vol. 66, pp. 511–516, 4 1998. DOI: `10.1007/s003400050426`.

[99] M. D. Rosa *et al.*, "On the measurement of pressure induced shift by diode lasers and harmonic detection", *Opt. Commun.*, vol. 147, no. 1-3, pp. 55–60, 1998. DOI: `10.1016/S0030-4018(97)00548-8`.

[100] E. D. Tommasi, A. Castrillo, G. Casa, and L. Gianfrani, "An efficient approximation for a wavelength-modulated 2nd harmonic lineshape from a Voigt absorption profile", *J. Quant. Spectrosc. Radiat. Transfer*, vol. 109, no. 1, pp. 168–175, 2008. DOI: `10.1016/j.jqsrt.2007.06.001`.

[101] M. Peric and H. J. Halpern, “Fitting of the derivative Voigt ESR line under conditions of modulation broadening”, *J. Magn. Reson., Ser A*, vol. 109, no. 2, pp. 198–202, Jan. 1994. DOI: `10.1006/jmra.1994.1155`.

[102] J. Evans, P. Morgan, and R. Renaud, “Simulation of electron spin resonance spectra by fast Fourier transform”, *Anal. Chim. Acta*, vol. 103, pp. 175–187, Jan. 1978. DOI: `10.1016/S0003-2670(01)84037-X`.

[103] ——, “Simulation of electron spin resonance spectra by fast Fourier transform”, *J. Magn. Reson.*, vol. 52, pp. 529–531, Jan. 1983. DOI: `10.1016/0022-2364(83)90182-8`.

[104] L. Dore, “Using fast Fourier transform to compute the line shape of frequency-modulated spectral profiles”, *J. Mol. Spectrosc.*, vol. 221, no. 1, pp. 93–98, 2003. DOI: `10.1016/S0022-2852(03)00203-0`.

[105] M. Shaw and J. F. Traub, “On the number of multiplications for the evaluation of a polynomial and some of its derivatives”, *J. ACM*, vol. 21, no. 1, pp. 161–167, Jan. 1974. DOI: `10.1145/321796.321810`.

[106] T. Iguchi, “Modulation waveforms for second-harmonic detection with tunable diode lasers”, *J. Opt. Soc. Am. B: Opt. Phys.*, vol. 3, pp. 419–423, Mar. 1986. DOI: `10.1364/JOSAB.3.000419`.

[107] J. Gustafsson, N. Chekalin, and O. Axner, “Improved detectability of wavelength modulation diode laser absorption spectrometry applied to window-equipped graphite furnaces by 4th and 6th harmonic detection”, *Spectrochim. Acta, Part B*, vol. 58, no. 1, pp. 111–122, 2003. DOI: `10.1016/S0584-8547(02)00220-3`.

[108] A. N. Dharamsi, P. C. Shea, and A. M. Bullock, “Reduction of effects of Fabry-Perot fringing in wavelength modulation experiments”, *Appl. Phys. Lett.*, vol. 72, pp. 3118–3120, Jun. 1998. DOI: `10.1063/1.121565`.

[109] G. Rao, C. Gudipaty, and D. Martin, “Higher harmonic detection employing wavelength modulation spectroscopy and near infrared diode lasers: an undergraduate experiment”, *American Journal of Physics*, vol. 77, no. 9, pp. 821–825, 2009. DOI: `10.1119/1.3141043`.

[110] V. Liger, “Optical fringes reduction in ultrasensitive diode laser absorption spectroscopy”, *Spectrochim. Acta, Part A*, vol. 55, pp. 2021–2026, Sep. 1999. DOI: `doi:10.1016/S1386-1425(99)00074-8`.

[111] A. N. Dharamsi and A. M. Bullock, “Measurements of density fluctuations by modulation spectroscopy”, *Appl. Phys. Lett.*, vol. 69, pp. 22–24, Jul. 1996. DOI: `10.1063/1.118105`.

[112] A. N. Dharamsi and Y. Lu, “Sensitive density-fluctuation measurements using wavelength-modulation spectroscopy with high-order-harmonic detection”, *Appl. Phys. B: Lasers Opt.*, vol. 62, pp. 273–278, Mar. 1996. DOI: `10.1007/BF01080955`.

[113] ——, “High-resolution spectroscopy using high-order derivative techniques”, *Appl. Phys. Lett.*, vol. 65, pp. 2257–2259, Oct. 1994. DOI: `10.1063/1.112736`.

[114] J. McManus *et al.*, “Comparison of cw and pulsed operation with a TE-cooled quantum cascade infrared laser for detection of nitric oxide at 1900 cm^{-1}”, *Appl. Phys. B: Lasers Opt.*, vol. 85, pp. 235–241, 2 2006. DOI: `10.1007/s00340-006-2407-7`.

[115] J. Reid, M. El-Sherbiny, B. K. Garside, and E. A. Ballik, “Sensitivity limits of a tunable diode laser spectrometer, with application to the detection of NO_2 at

the 100-ppt level", *Appl. Opt.*, vol. 19, no. 19, pp. 3349–3353, Oct. 1980. DOI: `10.1364/AO.19.003349`.

[116] H. C. Sun and E. A. Whittaker, "Novel étalon fringe rejection technique for laser absorption spectroscopy", *Appl. Opt.*, vol. 31, no. 24, pp. 4998–5002, 1992.

[117] S.-Q. Wu, T. Kimishima, H. Kuze, and N. Takeuchi, "Efficient reduction of fringe noise in trace gas detection with diode laser multipass absorption spectroscopy", *Jpn. J. Appl. Phys.*, vol. 39, pp. 4034–4040, Jul. 2000. DOI: `10.1143/JJAP.39.4034`.

[118] H. Schiff, G. Mackay, and J. Bechara, "Air monitoring by spectroscopic techniques", in, M. Sigrist, Ed., ser. Chemical Analysis: A Series of Monographs on Analytical Chemistry and Its Applications. Wiley, 1994, ch. The Use of Tunable Diode Laser Absorption Spectroscopy for Atmospheric Measurements, pp. 239–333.

[119] S.-Q. Wu *et al.*, "Reduction of fringe noise in wavelength modulation spectroscopy using a one-dimensional focal plane array", *Optical Review*, vol. 9, pp. 189–192, Sep. 2002. DOI: `10.1007/s10043-002-0189-7`.

[120] X. Zhu and D. T. Cassidy, "Modulation spectroscopy with a semiconductor diode laser by injection-current modulation", *J. Opt. Soc. Am. B: Opt. Phys.*, vol. 14, no. 8, pp. 1945–1950, Aug. 1997. DOI: `10.1364/JOSAB.14.001945`.

[121] Philips Technologie GmbH U-L-M Photonics, *760±1/±3 nm single mode VCSEL*, Online: `http://www.ulm-photonics.com/components/com_products/datasheets/VCSEL-ULM760-SingleMode.pdf`, 2012.

[122] Nanoplus GmbH, *DFB laser diodes from 750 nm to 830 nm*, Online: `http://www.nanoplus.com/download/750_830nm_01.pdf`, 2012.

[123] ——, *DFB laser diodes from 1900 nm to 2200 nm*, Online: `http://www.nanoplus.com/download/1900_2200nm_02.pdf`, 2012.

[124] P. Werle *et al.*, "Signal processing and calibration procedures for in situ diode-laser absorption spectroscopy", *Spectrochim. Acta, Part A*, vol. 60, no. 8-9, pp. 1685–1705, 2004. DOI: `10.1016/j.saa.2003.10.013`.

[125] D. S. Bomse and D. J. Kane, "An adaptive singular value decomposition (SVD) algorithm for analysis of wavelength modulation spectra", *Appl. Phys. B: Lasers Opt.*, vol. 85, no. 2, pp. 461–466, 2006. DOI: `10.1007/s00340-006-2316-9`.

[126] C. Rao and H. Toutenburg, *Linear Models: Least Squares and Alternatives*, ser. Springer Series in Statistics. Springer, 1999.

[127] G. Seber and C. J Wild, *Nonlinear Regression*. Wiley-Interscience, 1988.

[128] A. S. Goldberger, "Best linear unbiased prediction in the generalized linear regression model", *Journal of the American Statistical Association*, vol. 57, no. 298, pp. 369–375, 1962. DOI: `10.2307/2281645`.

[129] A. Hangauer *et al.*, "Fire detection with a compact, 2.3 μm VCSEL-based carbon monoxide sensor", in *Conference on Lasers and Electro Optics (CLEO)*, Baltimore, USA, Jun. 2009, CTuA3.

[130] A. Hangauer, J. Chen, R. Strzoda, and M.-C. Amann, "Laser wavelength stabilization using gases with complex spectral fingerprint", in *International Conference on Field Laser Applications in Industry and Research*, Garmisch-Partenkirchen, Germany, 2009, p. 44.

[131] A. Hangauer, J. Chen, R. Strzoda, and M.-C. Amann, "Multi-harmonic detection in wavelength modulation spectroscopy systems", *Appl. Phys. B: Lasers Opt.*, 2012. DOI: `10.1007/s00340-012-5049-y`.

[132] A. Hangauer, J. Chen, R. Strzoda, and M.-C. Amann, "Feasibility study of Zeeman modulation spectrometry with a hollow capillary fiber based gas cell", *Opt. Lett.*, vol. 37, no. 7, pp. 1265–1267, Apr. 2012. DOI: `10.1364/OL.37.001265`.

[133] P. Werle *et al.*, "Near- and mid-infrared laser-optical sensors for gas analysis", *Optics and Lasers in Engineering*, vol. 37, pp. 101–114, Feb. 2002. DOI: `10.1016/S0143-8166(01)00092-6`.

[134] W. Demtröder, *Laser Spectroscopy - Basic Concepts and Instrumentation*, 3rd ed. Springer, 2003.

[135] J. Chen *et al.*, "Compact carbon monoxide sensor using a continuously tunable 2.3 μm single-mode VCSEL", in *The 21st Annual Meeting of The IEEE Lasers & Electro-Optics Society*, Newport Beach, Nov. 2008, pp. 721–722. DOI: `10.1109/LEOS.2008.4688822`.

[136] J. Liu, J. Jeffries, and R. Hanson, "Wavelength modulation absorption spectroscopy with 2f detection using multiplexed diode lasers for rapid temperature measurements in gaseous flows", *Appl. Phys. B: Lasers Opt.*, vol. 78, pp. 503–511, 3 2004. DOI: `10.1007/s00340-003-1380-7`.

[137] A. A. Kosterev, Y. Bakhirkin, R. F. Curl, and F. K. Tittel, "Quartz-enhanced photoacoustic spectroscopy", *Opt. Lett.*, vol. 27, no. 21, pp. 1902–1904, 2002. DOI: `10.1364/OL.27.001902`.

[138] J. A. Silver and D. S. Bomse, *Wavelength modulation spectroscopy with multiple harmonic detection*, Patent US6356350, Jul. 1999.

[139] T. Svensson *et al.*, "VCSEL-based oxygen spectroscopy for structural analysis of pharmaceutical solids", *Appl. Phys. B: Lasers Opt.*, vol. 90, pp. 345–354, 2 2008. DOI: `10.1007/s00340-007-2901-6`.

[140] W. Urban and W. Herrmann, """Zeeman modulation spectroscopy" with spin-flip Raman laser", *Applied Physics A: Materials Science & Processing*, vol. 17, pp. 325–330, 4 1978. DOI: `10.1007/BF00886200`.

[141] A. Kaldor, W. B. Olson, and A. G. Maki, "Pollution monitor for Nitric Oxide: a laser device based on the Zeeman modulation of absorption", *Science*, vol. 176, no. 4034, pp. 508–510, 1972. DOI: `10.1126/science.176.4034.508`.

[142] G. Litfin, C. R. Pollock, J. R. F. Curl, and F. K. Tittel, "Sensitivity enhancement of laser absorption spectroscopy by magnetic rotation effect", *J. Chem. Phys.*, vol. 72, no. 12, pp. 6602–6605, 1980. DOI: `10.1063/1.439117`.

[143] R. Lewicki *et al.*, "Ultrasensitive detection of nitric oxide at 5.33 μm by using external cavity quantum cascade laser-based Faraday rotation spectroscopy", *Proc. Natl. Acad. Sci. USA*, vol. 106, no. 31, pp. 12 587–12 592, 2009. DOI: `10.1073/pnas.0906291106`.

[144] P. B. Davies, "Laser magnetic resonance spectroscopy", *J. Phys. Chem.*, vol. 85, no. 18, pp. 2599–2607, 1981. DOI: `10.1021/j150618a006`.

[145] W. T. McLyman, *Transformer and Inductor Design Handbook*. Dekker Inc., 2004.

[146] R. George and J. Harrington, “Infrared transmissive, hollow plastic waveguides with inner Ag–AgI coatings”, *Appl. Opt.*, vol. 44, no. 30, pp. 6449–6455, Oct. 2005. DOI: `10.1364/AO.44.006449`.

[147] Doko Engineering, *Capillary waveguide specifications*, Downloaded from http://do-ko.jp/specs.html (Feb 20, 2012).

[148] R. J. Brecha, L. M. Pedrotti, and D. Krause, “Magnetic rotation spectroscopy of molecular oxygen with a diode laser”, *J. Opt. Soc. Am. B: Opt. Phys.*, vol. 14, no. 8, pp. 1921–1930, Aug. 1997. DOI: `10.1364/JOSAB.14.001921`.

[149] A. Hangauer *et al.*, “Wavelength modulation spectroscopy with a widely tunable InP-based 2.3 μm vertical-cavity surface-emitting laser”, *Opt. Lett.*, vol. 33, no. 14, pp. 1566–1568, 2008. DOI: `10.1364/OL.33.001566`.

[150] E. Moyer *et al.*, “Design considerations in high-sensitivity off-axis integrated cavity output spectroscopy”, *Appl. Phys. B: Lasers Opt.*, vol. 92, pp. 467–474, 3 2008. DOI: `10.1007/s00340-008-3137-9`.

[151] J. Chen, A. Hangauer, and M.-C. Amann, “TDLS sensor performance prediction: theory and experiment”, in *Field Laser Applications in Industry and Research (FLAIR)*, Murnau, Germany, 2011, pp. II–12.

[152] B. Lins, P. Zinn, R. Engelbrecht, and B. Schmauss, “Simulation-based comparison of noise effects in wavelength modulation spectroscopy and direct absorption TDLAS”, *Appl. Phys. B: Lasers Opt.*, vol. 100, pp. 367–376, 2 2010. DOI: `10.1007/s00340-009-3881-5`.

[153] P. Werle and F. Slemr, “Signal-to-noise ratio analysis in laser absorption spectrometers using optical multipass cells”, *Appl. Opt.*, vol. 30, no. 4, pp. 430–434, Feb. 1991. DOI: `10.1364/AO.30.000430`.

[154] M. Gabrysch, C. Corsi, F. Pavone, and M. Inguscio, “Simultaneous detection of CO and CO_2 using a semiconductor DFB diode laser at 1.578 μm”, *Appl. Phys. B: Lasers Opt.*, vol. 65, pp. 75–79, 1 1997. DOI: `10.1007/s003400050253`.

[155] S. Jie *et al.*, “Absorption measurements for highly sensitive diode laser of CO_2 near 1.3μm at room temperature”, *Chinese Physics*, vol. 14, no. 3, p. 482, 2005. DOI: `10.1088/1009-1963/14/3/009`.

[156] H. Riris *et al.*, “Signal processing strategies in tunable diode laser spectrometers”, *Spectrochim. Acta, Part A*, vol. 52, no. 8, pp. 843 –849, 1996. DOI: `10.1016/0584-8539(95)01605-8`.

[157] S. Hunsmann *et al.*, “Absolute, high resolution water transpiration rate measurements on single plant leaves via tunable diode laser absorption spectroscopy (TDLAS) at 1.37 μm”, *Appl. Phys. B: Lasers Opt.*, vol. 92, pp. 393–401, 3 2008. DOI: `10.1007/s00340-008-3095-2`.

[158] K. Song *et al.*, “Application of laser photoacoustic spectroscopy for the detection of water vapor near 1.38 μm”, *Microchem. J.*, vol. 80, no. 2, pp. 113–119, 2005. DOI: `10.1016/j.microc.2004.07.026`.

[159] R. Jiménez *et al.*, “Ozone detection by differential absorption spectroscopy at ambient pressure with a 9.6 μm pulsed quantum-cascade laser”, *Appl. Phys. B: Lasers Opt.*, vol. 78, pp. 249–256, 2 2004. DOI: `10.1007/s00340-003-1358-5`.

[160] I. Mappe-Fogaing *et al.*, “Wavelet denoising for infrared laser spectroscopy and gas detection”, *Appl. Spectrosc.*, vol. 66, no. 6, pp. 700–710, 2012. DOI: `10.1366/11-06459`.

[161] B. Lins, R. Engelbrecht, and B. Schmauss, “Software-switching between direct absorption and wavelength modulation spectroscopy for the investigation of ADC resolution requirements”, *Appl. Phys. B: Lasers Opt.*, vol. 106, pp. 999–1008, 4 2012. DOI: `10.1007/s00340-011-4827-2`.

[162] J. Chen, A. Hangauer, R. Strzoda, and M.-C. Amann, “Tunable diode laser spectroscopy with optimum nonlinear wavelength scanning”, in *Book of Abstracts, 7th Conference on Tunable Diode Laser Spectroscopy (TDLS)*, Zermatt, Switzerland, 2009, pp. D–4.

[163] M. Arndt and M. Sauer, “Spectroscopic carbon dioxide sensor for automotive applications”, in *Proceedings of IEEE Sensors, 2004*, Oct. 2004, 252–255 vol.1. DOI: `10.1109/ICSENS.2004.1426149`.

[164] A. Nelson and A. Kouznetsov, “A 4.26-μm RCLED and a fast low-power CO_2 sensor”, in *Society of Photo-Optical Instrumentation Engineers (SPIE) Conference Series*, vol. 7231, Feb. 2009. DOI: `10.1117/12.809293`.

[165] K. Kaneyasu *et al.*, “A carbon dioxide gas sensor based on solid electrolyte for air quality control”, *Sens. Actuators, B*, vol. 66, no. 1-3, pp. 56–58, 2000. DOI: `10.1016/S0925-4005(99)00411-6`.

[166] D. D. Nelson *et al.*, “New method for isotopic ratio measurements of atmospheric carbon dioxide using a 4.3 μm pulsed quantum cascade laser”, *Appl. Phys. B: Lasers Opt.*, vol. 90, pp. 301–309, Feb. 2008. DOI: `10.1007/s00340-007-2894-1`.

[167] J. A. Silver and W. R. Wood, “Miniature gas sensor for monitoring biological space environments”, in *Diode Lasers and Applications in Atmospheric Sensing*, A. Fried, Ed., vol. 4817, Seattle, WA, USA: SPIE, 2002, pp. 82–87. DOI: `10.1117/12.452092`.

[168] P. S. Burge, “Sick building syndrome”, *Occup. Environ. Med.*, vol. 61, pp. 185–190, 2004. DOI: `10.1136/oem.2003.008813`.

[169] American Conference of Governmental Industrial Hygienists, *2005 Threshold Limit Values and Biological Exposure Indices.* American Conference of Governmental Industrial Hygienists, 2005.

[170] Center for Disease Control and Prevention, *Carbon Monoxide Poisoning: Fact Sheet*, Online electronic publication, web page, 2007.

[171] S.-J. Chen, C. Hovde, K. A. Peterson, and A. Marshal, “Fire detection using smoke and gas sensors”, *Fire Safety Journal*, vol. 42, no. 8, pp. 507–515, 2007. DOI: `10.1016/j.firesaf.2007.01.006`.

[172] R. Pohle *et al.*, “Fire detection with low power FET gas sensors”, *Sens. Actuators, B*, vol. 120, no. 2, pp. 669–672, 2007. DOI: `10.1016/j.snb.2006.03.040`.

[173] A. A. Kosterev and F. K. Tittel, “Advanced quartz-enhanced photoacoustic trace gas sensor for early fire detection”, *SAE International Journal of Aerospace*, vol. 1, pp. 331–336, Apr. 2009.

[174] D. S. Bomse, D. C. Hovde, S.-J. Chen, and J. A. Silver, “Early fire sensing using near-IR diode laser spectroscopy”, in *Diode Lasers and Applications in Atmospheric Sensing*, A. Fried, Ed., SPIE, 2002, pp. 73–81. DOI: `10.1117/12.452097`.

[175] J. Chen, A. Hangauer, R. Strzoda, and M.-C. Amann, “Erratum to: VCSEL-based calibration-free carbon monoxide sensor at 2.3μm with in-line reference cell”,

Appl. Phys. B: Lasers Opt., vol. 102, pp. 425–425, 2 2011. DOI: `10.1007/s00340-010-4352-8`.

[176] European Standard, *EN54-7: Fire detection and fire alarm systems - Part 7: Smoke detectors - point detectors using scattered light, transmitted light or ionization.* Berlin: Beuth, 2001.

[177] ——, *EN54-15: Fire detection and fire alarm systems - Part 15: Point detectors using a combination of detected fire phenomena.* Berlin: Beuth, 2006.

[178] ——, *EN54-26: Fire detection and fire alarm systems - Part 26: Point fire detectors using carbon monoxide sensors.* Berlin: Beuth, 2008.

[179] S. W. Sharpe *et al.*, "Gas-phase databases for quantitative infrared spectroscopy", *Appl. Spectrosc.*, vol. 58, pp. 1452–1461, Dec. 2004. DOI: `10.1366/0003702042641281`.

[180] A. Hangauer, J. Chen, R. Strzoda, and M.-C. Amann, "Analysis of dynamic tuning effects in vertical-cavity surface-emitting lasers", in *Proceedings of the Fifth Joint Symposium on Opto- & Microelectronic Devices and Circuits (SODC)*, Beijing, China, 2009, pp. 28–31.

[181] ——, "Accurate measurement of the wavelength modulation phase shift of tunable vertical cavity surface-emitting lasers (vcsels)", in *Programme and Abstracts, Conference on Semiconductor and Integrated Optoelectronics*, 2008, p. 38.

[182] T. Paoli, "A new technique for measuring the thermal impedance of junction lasers", *IEEE J. Quantum Electron.*, vol. 11, no. 7, pp. 498–503, Jul. 1975. DOI: `10.1109/JQE.1975.1068661`.

[183] H. Moench *et al.*, "Advanced characterization techniques for high power VCSELs", *Proc. SPIE 7615*, vol. 76150G, 2010. DOI: `10.1117/12.839953`.

[184] H. Carslaw and J. Jaeger, *Conduction of Heat in Solids.* Clarendon Press, Oxford, U.K., 1990.

[185] M. Amir Khan, K. Mohan, and A. Dharamsi, "Optical pathlength saturation signatures in wavelength modulation spectroscopy signals of atmospheric molecular oxygen", *Appl. Phys. B: Lasers Opt.*, vol. 99, pp. 363–369, 1 2010. DOI: `10.1007/s00340-009-3814-3`.

[186] J. M. Supplee, E. A. Whittaker, and W. Lenth, "Theoretical description of frequency modulation and wavelength modulation spectroscopy", *Appl. Opt.*, vol. 33, pp. 6294–6302, Sep. 1994. DOI: `10.1364/AO.33.006294`.

[187] L. Fox and I. B. Parker, *Chebyshev polynomials in numerical analysis.* Oxford University Press, 1968.

[188] A. Albert, *Regression and the Moore-Penrose Pseudoinverse*, ser. Mathematics in Science and Engineering. Academic Press, 1972.

[189] G. P. M. Poppe and C. M. J. Wijers, "Algorithm 680: evaluation of the complex error function", *ACM Trans. Math. Softw.*, vol. 16, no. 1, p. 47, Mar. 1990. DOI: `10.1145/77626.77630`.

[190] ——, "More efficient computation of the complex error function", *ACM Trans. Math. Softw.*, vol. 16, no. 1, pp. 38–46, Mar. 1990. DOI: `10.1145/77626.77629`.

[191] D. W. Allan, "Statistics of atomic frequency standards", *Proc. IEEE*, vol. 54, no. 2, pp. 221–230, Feb. 1966. DOI: `10.1109/PROC.1966.4634`.

[192] P. Werle, R. Muecke, and F. Slemr, “The limits of signal averaging in atmospheric trace gas monitoring by tunable diode-laser absorption spectroscopy”, *Appl. Phys. B: Lasers Opt.*, vol. 57, pp. 131–139, 1993. DOI: `10.1007/BF00425997`.

[193] J. A. Barnes *et al.*, “Characterization of frequency stability”, *IEEE Trans. Instrum. Meas.*, vol. IM-20, no. 2, pp. 105–120, May 1971. DOI: `10.1109/TIM.1971.5570702`.

[194] J. Hespanha, *Linear Systems Theory*. Princeton University Press, 2009.

[195] G. Pandian and S. Dilwali, “On the thermal FM response of a semiconductor laser diode”, *IEEE Photon. Technol. Lett.*, vol. 4, no. 2, pp. 130–133, Feb. 1992. DOI: `10.1109/68.122338`.

[196] G. H. Golub and V. Pereyra, “The differentiation of pseudo-inverses and nonlinear least squares problems whose variables separate”, *SIAM Journal on Numerical Analysis*, vol. 10, no. 2, pp. 413–432, 1973. DOI: `10.1137/0710036`.

[197] A. Hangauer *et al.*, “Laser spectroscopic oxygen sensor for real time combustion optimization”, in *Proceedings of the Eurosensors XXIII conference*, vol. 1, 2009, pp. 955 –958. DOI: `DOI:10.1016/j.proche.2009.07.238`.

[198] S. Arafin *et al.*, “Comprehensive analysis of electrically-pumped GaSb-based VCSELs”, *Opt. Express*, vol. 19, no. 18, pp. 17 267–17 282, Aug. 2011. DOI: `10.1364/OE.19.017267`.

[199] G. Böhm *et al.*, “Comparison of InP- and GaSb-based vcsels emitting at 2.3 μm suitable for carbon monoxide detection”, *J. Cryst. Growth*, vol. 323, no. 1, pp. 442–445, 2011. DOI: `10.1016/j.jcrysgro.2010.11.174`.

[200] J. Chen, A. Hangauer, R. Strzoda, and M.-C. Amann, “Low-level and ultra-low volume hollow waveguide based carbon monoxide sensor”, *Opt. Lett.*, vol. 35, no. 21, pp. 3577–3579, Oct. 2010. DOI: `OL.35.003577`.

[201] J. Chen, A. Hangauer, R. Strzoda, and M.-C. Amann, “Accurate extraction method for the FM response of tunable diode lasers based on wavelength modulation spectroscopy”, *Appl. Phys. B: Lasers Opt.*, vol. 90, pp. 243–247, 2 2008. DOI: `10.1007/s00340-007-2848-7`.

[202] J. Chen, A. Hangauer, R. Strzoda, and M.-C. Amann, “Experimental characterization of the frequency modulation behavior of vertical cavity surface emitting lasers”, *Appl. Phys. Lett.*, vol. 91, no. 14, 141105, pp. 141 105–141 108, 2007. DOI: `10.1063/1.2794406`.

[203] A. Hangauer, J. Chen, R. Strzoda, and M.-C. Amann, “Zeeman modulation spectroscopy with a hollow capillary fiber based gas cell”, in *Field Laser Applications in Industry and Research (FLAIR)*, Murnau, Germany, 2011, pp. II–11.

[204] A. Hangauer, J. Chen, and M.-C. Amann, “Wavelength modulation spectroscopy with multi-harmonic detection”, in *Field Laser Applications in Industry and Research (FLAIR)*, Murnau, Germany, 2011, pp. I–18.

[205] J. Chen, A. Hangauer, R. Strzoda, and M.-C. Amann, “Laser optical breath analysis using hollow fibers and VCSELs”, in *Field Laser Applications in Industry and Research (FLAIR)*, Murnau, Germany, 2011, pp. III–4.

[206] M. Ortsiefer *et al.*, “Long-wavelength VCSELs for sensing applications”, in *SPIE Photonics West 2012*, San Francisco, Jan. 2012, pp. 8276–9. DOI: `10.1117/12.909876`.

[207] R. Strzoda, J. Chen, A. Hangauer, and M. Fleischer, "Highly sensitive laser based gas sensors", in *Proceeding of 40th Freiburg Infrared Colloquium*, Freiburg, Feb. 2011, pp. 1–2.

[208] M. Ortsiefer *et al.*, "GaSb and InP-based VCSELs at 2.3 μm emission wavelength for tuneable diode laser spectroscopy of carbon monoxide", in *SPIE Photonics West 2011*, San Francisco, Jan. 2011. DOI: `10.1117/12.871561`.

[209] J. Chen *et al.*, "Sensitivity limits for near- infrared gas sensing with suspended-core PCFs directly coupled with VCSELs", in *Conference on Laser Electro-Optics (CLEO)*, San Jose, USA, 2010, JThB7.

[210] A. Hangauer, J. Chen, and M.-C. Amann, "Vertical-cavity surface-emitting laser *P*-*I*-characteristic at constant internal temperature", in *Proceedings of the Sixth Joint Symposium on Opto- & Microelectronic Devices and Circuits (SODC)*, Berlin, Germany, 2010.

[211] J. Chen, A. Hangauer, R. Strzoda, and M.-C. Amann, "Fiber sensor using hollow capillary fiber directly coupled with VCSELs", in *Proceedings of the Sixth Joint Symposium on Opto- & Microelectronic Devices and Circuits (SODC)*, Berlin, Germany, 2010.

[212] A. Hangauer *et al.*, "Laser-spectroscopic, ultra low volume and low level carbon monoxide sensor", in *Proceedings of Eurosensors XXIV*, Linz, Austria, Sep. 2010. DOI: `10.1016/j.proeng.2010.09.341`.

[213] J. Chen *et al.*, "CO and CH_4 sensing with single mode 2.3 μm GaSb-based VCSEL", in *Conference on Lasers and Electro Optics (CLEO)*, Baltimore, USA, Jun. 2009, CThI2.

[214] J. Chen *et al.*, "VCSEL-based oxygen sensor for combustion optimization in gas/oil furnaces", in *Conference on Laser Electro-Optics (CLEO)*, Baltimore, USA, Jun. 2009, CTuA4.

[215] J. Chen, A. Hangauer, R. Strzoda, and M.-C. Amann, "Simultaneous CH_4 and CO sensing with 2.3 μm vertical surface emitting lasers and their application", in *Proceedings of the Fifth Joint Symposium on Opto- & Microelectronic Devices and Circuits (SODC)*, Beijing, China, 2009, pp. 58–61.

[216] J. Chen *et al.*, "Miniaturized laser spectroscopic CO sensor for industrial and safety applications", in *Proceedings of the Eurosensors XXIII conference*, vol. 1, 2009, pp. 1383 –1386. DOI: `10.1016/j.proche.2009.07.345`.

[217] J. Chen *et al.*, "Near-infrared gas sensing using hollow waveguides and PCFs directly coupled to VCSELs", in *International Conference on Field Laser Applications in Industry and Research*, Garmisch-Partenkirchen, Germany, 2009, p. 93.

[218] J. Chen, A. Hangauer, R. Strzoda, and M.-C. Amann, "Oxygen sensor with diffuse reflector employed in harsh conditions for concentration and pressure measurements", in *Book of Abstracts, 7th Conference on Tunable Diode Laser Spectroscopy (TDLS)*, Zermatt, Switzerland, 2009, E–16.

[219] A. Hangauer, J. Chen, R. Strzoda, and M.-C. Amann, "Miniaturized sensor without separate reference cell for carbon-monoxide detection at 2.3 μm", in *Book of Abstracts, 7th Conference on Tunable Diode Laser Spectroscopy (TDLS)*, Zermatt, Switzerland, 2009, pp. C–4.

[220] ——, “Comparison of GaSb- and InP-based VCSELs at 2.3 μm”, in *Book of Abstracts, 7th Conference on Tunable Diode Laser Spectroscopy (TDLS)*, Zermatt, Switzerland, 2009, E–4.

[221] ——, “Analysis of thermal tuning in vertical-cavity surface-emitting lasers”, in *European Semiconductor Laser Workshop*, Eindhoven, The Netherlands, 2008, p. 20.

[222] J. Chen *et al.*, “CO and CH_4 sensing with electrically pumped 2.3μm GaSb-based vertical-cavity surface-emitting laser”, in *European Semiconductor Laser Workshop*, Eindhoven, The Netherlands, 2008, p. 20.

[223] J. Chen, A. Hangauer, R. Strzoda, and M.-C. Amann, “Dynamic wavelength tuning behavior of vertical-cavity surface-emitting lasers”, in *Programme and Abstracts, Conference on Semiconductor and Integrated Optoelectronics*, 2008, p. 39.

[224] M. Ortsiefer *et al.*, “Extended near-infrared wavelength VCSELs for optical sensing”, in *IEEE/LEOS International Semiconductor Laser Conference*, Sorrento, Italy, Sep. 2008, pp. 167–168. DOI: `10.1109/ISLC.2008.4636062`.

[225] A. Hangauer, J. Chen, R. Strzoda, and M.-C. Amann, “Reconstruction of the transmission from n-th harmonic spectra”, in *Book of Abstracts Field Laser Applications in Industry and Research (FLAIR)*, Florence, Italy, 2007, post–deadline.

[226] J. Chen, A. Hangauer, R. Strzoda, and M.-C. Amann, “New method based on wavelength modulation spectroscopy for measurement and characterization of the current to wavelength tuning frequency response of VCSELs”, in *Book of Abstracts, 6th International Conference on Tunable Diode Laser Spectroscopy*, Reims, France, 2007, pp. C–15.

List of Publications

Awards and recognitions

- Kaiser-Friedrich Research Award in 2009
- Nomination for the International SENSOR Innovation Award, AMA Fachverband für Sensorik in 2009
- Best Poster Award (first place), Eurosensors conference, Lausanne:
  A. Hangauer *et al.*, "Laser spectroscopic oxygen sensor for real time combustion optimization", in *Proceedings of the Eurosensors XXIII conference*, vol. 1, 2009, pp. 955 –958. DOI: `DOI:10.1016/j.proche.2009.07.238`
- Newsdesk article on optics.org: VCSEL extends its reach to detect CO, 2008
- Exhibition of the CO_2 sensor in the "Science Express" train in Germany, 2009
- Invitation for a SPIE newsroom article on the CO_2 and H_2O air-quality sensor.

Journal publications

- A. Hangauer, J. Chen, R. Strzoda, and M.-C. Amann, "Multi-harmonic detection in wavelength modulation spectroscopy systems", *Appl. Phys. B: Lasers Opt.*, 2012. DOI: `10.1007/s00340-012-5049-y`
- A. Hangauer, J. Chen, R. Strzoda, and M.-C. Amann, "Feasibility study of Zeeman modulation spectrometry with a hollow capillary fiber based gas cell", *Opt. Lett.*, vol. 37, no. 7, pp. 1265–1267, Apr. 2012. DOI: `10.1364/OL.37.001265`
- S. Arafin, A. Bachmann, K. Vizbaras, A. Hangauer, J. Gustavsson, J. Bengtsson, A. Larsson, and M.-C. Amann, "Comprehensive analysis of electrically-pumped GaSb-based VCSELs", *Opt. Express*, vol. 19, no. 18, pp. 17 267–17 282, Aug. 2011. DOI: `10.1364/OE.19.017267`
- A. Hangauer, J. Chen, and M.-C. Amann, "Vertical-cavity surface-emitting laser light-current characteristic at constant internal temperature", *IEEE Photon. Technol. Lett.*, vol. 23, no. 18, pp. 1295–1297, Sep. 2011. DOI: `10.1109/LPT.2011.2160389`
- A. Hangauer, J. Chen, R. Strzoda, and M.-C. Amann, "The frequency modulation response of vertical-cavity surface-emitting lasers: experiment and theory", *IEEE J. Sel. Topics Quantum Electron.*, vol. 17, pp. 1584–1593, Nov. 2011. DOI: `10.1109/JSTQE.2011.2110640`
- G. Böhm, A. Bachmann, J. Rosskopf, M. Ortsiefer, J. Chen, A. Hangauer, R. Meyer, R. Strzoda, and M.-C. Amann, "Comparison of InP- and GaSb-based vcsels emitting at 2.3 μm suitable for carbon monoxide detection", *J. Cryst. Growth*, vol. 323, no. 1, pp. 442–445, 2011. DOI: `10.1016/j.jcrysgro.2010.11.174`

- J. Chen, A. Hangauer, R. Strzoda, and M.-C. Amann, "Low-level and ultra-low volume hollow waveguide based carbon monoxide sensor", *Opt. Lett.*, vol. 35, no. 21, pp. 3577–3579, Oct. 2010. DOI: `OL.35.003577`
- J. Chen, A. Hangauer, R. Strzoda, and M. C. Amann, "Resolution limits of laser spectroscopic absorption measurements with hollow glass waveguides", *Appl. Opt.*, vol. 49, no. 28, pp. 5254–5261, Oct. 2010. DOI: `10.1364/AO.49.005254`
- J. Chen, A. Hangauer, R. Strzoda, and M. C. Amann, "Tunable diode laser spectroscopy with optimum wavelength scanning", *Appl. Phys. B: Lasers Opt.*, vol. 100, pp. 331–339, 2010. DOI: `10.1007/s00340-010-3973-2`
- J. Chen, A. Hangauer, R. Strzoda, and M.-C. Amann, "Erratum to: VCSEL-based calibration-free carbon monoxide sensor at 2.3μm with in-line reference cell", *Appl. Phys. B: Lasers Opt.*, vol. 102, pp. 425–425, 2 2011. DOI: `10.1007/s00340-010-4352-8`
- J. Chen, A. Hangauer, R. Strzoda, and M.-C. Amann, "VCSEL-based calibration-free carbon monoxide sensor at 2.3 μm with in-line reference cell", *Appl. Phys. B: Lasers Opt.*, vol. 102, pp. 381–389, 2010. DOI: `10.1007/s00340-010-4011-0`
- J. Chen, A. Hangauer, R. Strzoda, and M.-C. Amann, "Laser spectroscopic oxygen sensor using diffuse reflector based optical cell and advanced signal processing", *Appl. Phys. B: Lasers Opt.*, vol. 100, pp. 417–425, 2010. DOI: `10.1007/s00340-010-3956-3`
- A. Hangauer, J. Chen, R. Strzoda, M. Ortsiefer, and M.-C. Amann, "Wavelength modulation spectroscopy with a widely tunable InP-based 2.3 μm vertical-cavity surface-emitting laser", *Opt. Lett.*, vol. 33, no. 14, pp. 1566–1568, 2008. DOI: `10.1364/OL.33.001566`
- J. Chen, A. Hangauer, and M.-C. Amann, "Simplified model of the dynamic thermal tuning behavior of VCSELs", *IEEE Photon. Technol. Lett.*, vol. 20, pp. 1082–1084, Jul. 2008. DOI: `10.1109/LPT.2008.924296`
- J. Chen, A. Hangauer, R. Strzoda, and M.-C. Amann, "Accurate extraction method for the FM response of tunable diode lasers based on wavelength modulation spectroscopy", *Appl. Phys. B: Lasers Opt.*, vol. 90, pp. 243–247, 2 2008. DOI: `10.1007/s00340-007-2848-7`
- A. Hangauer, J. Chen, and M.-C. Amann, "Modeling of the n-th harmonic spectra used in wavelength modulation spectroscopy and their properties", *Appl. Phys. B: Lasers Opt.*, vol. 90, no. 2, pp. 249–254, Feb. 2008. DOI: `10.1007/s00340-007-2902-5`
- J. Chen, A. Hangauer, R. Strzoda, and M.-C. Amann, "Experimental characterization of the frequency modulation behavior of vertical cavity surface emitting lasers", *Appl. Phys. Lett.*, vol. 91, no. 14, 141105, pp. 141 105–141 108, 2007. DOI: `10.1063/1.2794406`

Conference publications

- A. Hangauer, J. Chen, R. Strzoda, and M.-C. Amann, "Zeeman modulation spectroscopy with a hollow capillary fiber based gas cell", in *Field Laser Applications in Industry and Research (FLAIR)*, Murnau, Germany, 2011, pp. II–11
- A. Hangauer, J. Chen, and M.-C. Amann, "Wavelength modulation spectroscopy with multi-harmonic detection", in *Field Laser Applications in Industry and Research (FLAIR)*, Murnau, Germany, 2011, pp. I–18
- J. Chen, A. Hangauer, R. Strzoda, and M.-C. Amann, "Laser optical breath analysis using hollow fibers and VCSELs", in *Field Laser Applications in Industry and Research (FLAIR)*, Murnau, Germany, 2011, pp. III–4
- J. Chen, A. Hangauer, and M.-C. Amann, "TDLS sensor performance prediction: theory and experiment", in *Field Laser Applications in Industry and Research (FLAIR)*, Murnau, Germany, 2011, pp. II–12
- M. Ortsiefer, J. Rosskopf, *et al.*, "Long-wavelength VCSELs for sensing applications", in *SPIE Photonics West 2012*, San Francisco, Jan. 2012, pp. 8276–9. DOI: `10.1117/12.909876`
- R. Strzoda, J. Chen, A. Hangauer, and M. Fleischer, "Highly sensitive laser based gas sensors", in *Proceeding of 40th Freiburg Infrared Colloquium*, Freiburg, Feb. 2011, pp. 1–2
- M. Ortsiefer, C. Neumeyr, J. Rosskopf, S.Arafin, G. Boehm, A. Hangauer, J. Chen, R. Strzoda, and M. C. Amann, "GaSb and InP-based VCSELs at 2.3 μm emission wavelength for tuneable diode laser spectroscopy of carbon monoxide", in *SPIE Photonics West 2011*, San Francisco, Jan. 2011. DOI: `10.1117/12.871561`
- J. Chen, A. Hangauer, R. Strzoda, T. Euser, J. Chen, M. Scharrer, P. Russell, and M.-C. Amann, "Sensitivity limits for near- infrared gas sensing with suspended-core PCFs directly coupled with VCSELs", in *Conference on Laser Electro-Optics (CLEO)*, San Jose, USA, 2010, JThB7
- A. Hangauer, J. Chen, K.-U. Seemann, P. Karge, R. Strzoda, and M.-C. Amann, "Compact VCSEL-based CO_2 and H_2O sensor with inherent wavelength calibration for safety and air-quality applications", in *Conference on Lasers and Electro Optics (CLEO)*, San Jose, USA, May 2010, JThB3
- A. Hangauer, J. Chen, and M. C. Amann, "Comparison of plasma-effect in different InP-based VCSELs", in *Conference on Lasers and Electro Optics (CLEO)*, San Jose, USA, 2010, CMO4
- A. Hangauer, J. Chen, and M.-C. Amann, "Vertical-cavity surface-emitting laser P-I-characteristic at constant internal temperature", in *Proceedings of the Sixth Joint Symposium on Opto- & Microelectronic Devices and Circuits (SODC)*, Berlin, Germany, 2010
- J. Chen, A. Hangauer, R. Strzoda, and M.-C. Amann, "Fiber sensor using hollow capillary fiber directly coupled with VCSELs", in *Proceedings of the Sixth Joint Symposium on Opto- & Microelectronic Devices and Circuits (SODC)*, Berlin, Germany, 2010
- A. Hangauer, J. Chen, R. Strzoda, M. Fleischer, and M.-C. Amann, "Laser-spectroscopic, ultra low volume and low level carbon monoxide sensor", in *Pro-*

ceedings of Eurosensors XXIV, Linz, Austria, Sep. 2010. DOI: `10.1016/j.proeng.2010.09.341`

- J. Chen, A. Hangauer, A. Bachmann, T. Lim, K. Kashani, R. Strzoda, and M.-C. Amann, “CO and CH_4 sensing with single mode 2.3 μm GaSb-based VCSEL”, in *Conference on Lasers and Electro Optics (CLEO)*, Baltimore, USA, Jun. 2009, CThI2
- J. Chen, A. Hangauer, R. Strzoda, M. Fleischer, and M.-C. Amann, “VCSEL-based oxygen sensor for combustion optimization in gas/oil furnaces”, in *Conference on Laser Electro-Optics (CLEO)*, Baltimore, USA, Jun. 2009, CTuA4
- J. Chen, A. Hangauer, R. Strzoda, and M.-C. Amann, “Simultaneous CH_4 and CO sensing with 2.3 μm vertical surface emitting lasers and their application”, in *Proceedings of the Fifth Joint Symposium on Opto- & Microelectronic Devices and Circuits (SODC)*, Beijing, China, 2009, pp. 58–61
- A. Hangauer, J. Chen, R. Strzoda, M. Fleischer, and M.-C. Amann, “Fire detection with a compact, 2.3 μm VCSEL-based carbon monoxide sensor”, in *Conference on Lasers and Electro Optics (CLEO)*, Baltimore, USA, Jun. 2009, CTuA3
- A. Hangauer, J. Chen, R. Strzoda, and M.-C. Amann, “Analysis of dynamic tuning effects in vertical-cavity surface-emitting lasers”, in *Proceedings of the Fifth Joint Symposium on Opto- & Microelectronic Devices and Circuits (SODC)*, Beijing, China, 2009, pp. 28–31
- J. Chen, A. Hangauer, R. Strzoda, M. Fleischer, and M.-C. Amann, “Miniaturized laser spectroscopic CO sensor for industrial and safety applications”, in *Proceedings of the Eurosensors XXIII conference*, vol. 1, 2009, pp. 1383 –1386. DOI: `10.1016/j.proche.2009.07.345`
- A. Hangauer, A. Spitznas, J. Chen, R. Strzoda, H. Link, and M. Fleischer, “Laser spectroscopic oxygen sensor for real time combustion optimization”, in *Proceedings of the Eurosensors XXIII conference*, vol. 1, 2009, pp. 955 –958. DOI: `DOI:10.1016/j.proche.2009.07.238`
- A. Hangauer, J. Chen, R. Strzoda, and M.-C. Amann, “Laser wavelength stabilization using gases with complex spectral fingerprint”, in *International Conference on Field Laser Applications in Industry and Research*, Garmisch-Partenkirchen, Germany, 2009, p. 44
- J. Chen, A. Hangauer, R. Strzoda, T. Euser, J. Chen, M. Scharrer, P. Russell, and M.-C. Amann, “Near-infrared gas sensing using hollow waveguides and PCFs directly coupled to VCSELs”, in *International Conference on Field Laser Applications in Industry and Research*, Garmisch-Partenkirchen, Germany, 2009, p. 93
- A. Hangauer, J. Chen, R. Strzoda, and M.-C. Amann, “High-speed tuning in vertical-cavity surface-emitting lasers”, in *CLEO Europe - EQEC 2009*, Jun. 2009, CB13.5. DOI: `10.1109/CLEOE-EQEC.2009.5193616`
- J. Chen, A. Hangauer, R. Strzoda, and M.-C. Amann, “Tunable diode laser spectroscopy with optimum nonlinear wavelength scanning”, in *Book of Abstracts, 7th Conference on Tunable Diode Laser Spectroscopy (TDLS)*, Zermatt, Switzerland, 2009, pp. D–4
- J. Chen, A. Hangauer, R. Strzoda, and M.-C. Amann, “Oxygen sensor with

diffuse reflector employed in harsh conditions for concentration and pressure measurements", in *Book of Abstracts, 7th Conference on Tunable Diode Laser Spectroscopy (TDLS)*, Zermatt, Switzerland, 2009, E–16

- A. Hangauer, J. Chen, R. Strzoda, and M.-C. Amann, "Miniaturized sensor without separate reference cell for carbon-monoxide detection at 2.3 μm", in *Book of Abstracts, 7th Conference on Tunable Diode Laser Spectroscopy (TDLS)*, Zermatt, Switzerland, 2009, pp. C–4
- A. Hangauer, J. Chen, R. Strzoda, and M.-C. Amann, "Comparison of GaSb- and InP-based VCSELs at 2.3 μm", in *Book of Abstracts, 7th Conference on Tunable Diode Laser Spectroscopy (TDLS)*, Zermatt, Switzerland, 2009, E–4
- J. Chen, A. Hangauer, R. Strzoda, M. Ortsiefer, M. Fleischer, and M.-C. Amann, "Compact carbon monoxide sensor using a continuously tunable 2.3 μm single-mode VCSEL", in *The 21st Annual Meeting of The IEEE Lasers & Electro-Optics Society*, Newport Beach, Nov. 2008, pp. 721–722. DOI: `10.1109/LEOS.2008.4688822`
- A. Hangauer, J. Chen, R. Strzoda, and M.-C. Amann, "Analysis of thermal tuning in vertical-cavity surface-emitting lasers", in *European Semiconductor Laser Workshop*, Eindhoven, The Netherlands, 2008, p. 20
- J. Chen, A. Hangauer, A. Bachmann, T. Lim, K. Kashani, R. Strzoda, and M.-C. Amann, "CO and CH_4 sensing with electrically pumped 2.3μm GaSb-based vertical-cavity surface-emitting laser", in *European Semiconductor Laser Workshop*, Eindhoven, The Netherlands, 2008, p. 20
- J. Chen, A. Hangauer, R. Strzoda, and M.-C. Amann, "Dynamic wavelength tuning behavior of vertical-cavity surface-emitting lasers", in *Programme and Abstracts, Conference on Semiconductor and Integrated Optoelectronics*, 2008, p. 39
- A. Hangauer, J. Chen, R. Strzoda, and M.-C. Amann, "Accurate measurement of the wavelength modulation phase shift of tunable vertical cavity surface-emitting lasers (vcsels)", in *Programme and Abstracts, Conference on Semiconductor and Integrated Optoelectronics*, 2008, p. 38
- M. Ortsiefer, J. Rosskopf, *et al.*, "Extended near-infrared wavelength VCSELs for optical sensing", in *IEEE/LEOS International Semiconductor Laser Conference*, Sorrento, Italy, Sep. 2008, pp. 167–168. DOI: `10.1109/ISLC.2008.4636062`
- A. Hangauer, J. Chen, and M.-C. Amann, "Square-root law thermal response in VCSELs: experiment and theoretical model", in *Conference on Lasers and Electro Optics (CLEO)*, May 2008, JThA27
- A. Hangauer, J. Chen, R. Strzoda, and M.-C. Amann, "Reconstruction of the transmission from n-th harmonic spectra", in *Book of Abstracts Field Laser Applications in Industry and Research (FLAIR)*, Florence, Italy, 2007, post–deadline
- J. Chen, A. Hangauer, R. Strzoda, and M.-C. Amann, "New method based on wavelength modulation spectroscopy for measurement and characterization of the current to wavelength tuning frequency response of VCSELs", in *Book of Abstracts, 6th International Conference on Tunable Diode Laser Spectroscopy*, Reims, France, 2007, pp. C–15

- A. Hangauer, J. Chen, and M.-C. Amann, “Straightforward modeling of the nth harmonic signals used in wavelength modulation spectroscopy and their mathematical properties”, in *Book of Abstracts, 6th International Conference on Tunable Diode Laser Spectroscopy*, Reims, France, 2007, pp. D–15

Acknowledgement

The research presented in this dissertation has been conducted during my time at the Siemens Corporate Research and Technologies laboratories in Munich and at the Walter Schottky institute in Garching, Germany.

The work would not have been successful with the help of numerous people. Specifically I would like to express my gratitude to,

- Prof. M.-C. Amann for supervising the thesis, many stimulating discussions and his patience. I am grateful for his knowledge and intuition on countless topics and for providing answers to my questions nobody else could. He always believed in my abilities which encouraged me to overcome difficulties.
- Prof. Maximilian Fleischer at Siemens for sharing with me his enormous experience and knowledge on gas sensing and continuous encouragement and interest in a field that is not his main topic. I am also grateful for his patience and time even very late in the evening.
- Rainer Strzoda my second advisor at Siemens for sharing with me his enormous experience on laser gas spectroscopic sensing and optics design. I would like to acknowledge the fruitful discussions and the creative freedom I had during this time.
- Dr. Jia Chen for the extremely productive cooperation and mutual encouragement during our joint work. Without her, the work would not exist in the present form and I am glad for the complementary addition of our skills.
- Dr. Markus Ortsiefer and Jürgen Rosskopf of VERTILAS for the cooperation and the providing of lasers.
- Dr. Alexander Bachmann, Dr. Shamsul Arafin, Kaveh Kashani (†13.06.2009), Gerhard Böhm and Christian Grasse for the coperation and the one or another interesting evening.
- Prof. Gerard Wysocki for the offer and bringing the fringe insensitivity of Zeeman and Faraday spectroscopy to my attention.
- Dr. David Nelson and Dr. Barry McManus from Aerodyne Research for many interesting discussions about laser spectroscopic sensors.
- Dr. Ralf Meyer for his continuous teaching of presentation skills and proof-reading of this thesis.
- My father for proof-reading and valuable comments and providing an exterior view on many things.
- Daniela Huber for her support in administrative things and the always interesting conversations.
- The numerous persons who were involved in the sensor electronics development, D. Bergmann, C. Tump, S. Hain, Dr. A. Luzbhinin and G. Metz.
- Björn Hellenkamp for his help with creation of the automated measurement set-up.

- My former colleagues at Siemens and the Walter Schottky Institute for the excellent and cooperative working atmosphere.
- Lixin Zuo for the delicious food.
- My family for their continuous support and encouragement throughout the full time of my education.
- Luise for the great time.